Multiscale Modeling of Protein Systems Integrating QM/MM Simulation, Enhanced Sampling, and Machine Learning

Zur Erlangung des akademischen Grades eines

DOKTORS DER NATURWISSENSCHAFTEN
(Dr. rer. nat.)

von der KIT-Fakultät für Chemie und Biowissenschaften
des Karlsruher Instituts für Technologie (KIT)

genehmigte

DISSERTATION

von

M.Sc. Julian Böser

aus Karlsruhe

1. Referent:	Prof. Marcus Elstner
2. Referent:	PD Dr. Sebastian Höfener
Tag der mündlichen Prüfung:	03.02.2026

There is a story about two friends, who were classmates in high school, talking about their jobs. One of them became a statistician and was working on population trends. He showed a reprint to his former classmate. The reprint started, as usual, with the Gaussian distribution and the statistician explained to his former classmate the meaning of the symbols for the actual population, for the average population, and so on. His classmate was a bit incredulous and was not quite sure whether the statistician was pulling his leg. "How can you know that?" was his query. "And what is this symbol here?" "Oh," said the statistician, "this is pi." "What is that?" "The ratio of the circumference of the circle to its diameter." "Well, now you are pushing your joke too far," said the classmate, "surely the population has nothing to do with the circumference of the circle."

E. P. Wigner (1960) The unreasonable effectiveness of mathematics in the natural sciences. Communications on Pure and Applied Mathematics 13, 1–14.

Acknowledgment

I am grateful to my Professor Marcus Elstner for the opportunity to carry out my PhD research in his group and for the guidance. In the same breath, I thank Dr. Tomáš Kubař for his guidance, for the discussions that deepened my understanding of key concepts, and for his technical assistance with servers and software. A special thanks goes to Dr. Van-Quan Vuong. Working with you was a genuine pleasure. I learned a great deal, and the experience was both productive and enjoyable. I am also thankful to Dr. Katharina Spies and Lena Eichinger, my office mates, for the many valuable moments we shared. I appreciated both the challenging project-related discussions we worked through together and the lighter and funny moments that made the workdays more enjoyable. To Lukas Petersen and Dr. Christian Schmidt, thank you for discussing the disulfide project and for always being available whenever I had detailed questions about machine learning and code implementation. Finally, I would like to thank all my colleagues. I greatly appreciated the collaborative atmosphere within the group. I wish each of you the very best for your future journeys, and I look forward to seeing you again.

Abstract

Proteins operate across a broad hierarchy of spatial and temporal scales, and their local chemical reactivity, long-range noncovalent interactions, and conformational dynamics are coupled. Capturing this complexity on multiple scales requires methods that combine chemical accuracy with the sampling efficiency. The quantum mechanics/molecular mechanics (QM/MM) framework achieves this by treating the reactive region quantum mechanically while modeling the surrounding environment with molecular mechanics. Its reliability depends on how the system is partitioned, how reactive events are modeled, and how conformational ensembles are sampled. This thesis addressed these challenges by integrating three complementary research directions. Together, they show how QM/MM methods can be refined for specific applications, enabling more accurate descriptions of reactive processes in dynamic protein environments on multiple scales.

First, in Chapter 6, noncovalent interactions in hydrogen-bonded complexes were evaluated using the QM/MM framework for pairs of small molecules. The results show that errors in interaction energies stem mainly from the QM/MM interface, especially when van der Waals parameters distort short-range behavior. Charge transfer is minor in neutral dimers but becomes substantial in ionic systems, where reliable energetics require that the QM region fully captures the charge-transfer. These findings clarify guidelines for constructing more robust QM/MM partitions.

Second, in Chapter 7, the QM/MM framework was applied to elucidate the mechanism of thiol–disulfide exchange (TDE) catalyzed by *Homo sapiens* glutaredoxin (Grx). Because sulfur chemistry requires an accurate electronic description, two previously developed approaches were employed: a specific reaction parametrization for semi-empirical density functional tight binding (DFTB) and a Δ-machine learning correction trained to reproduce higher level reference energies. In combination with metadynamics (MTD) sampling, these methods enabled the construction of free-energy surfaces (FESs) for successive reaction steps and reproduced the experimentally observed regioselectivity. The computed barriers support the proposed catalytic pathway and reveal how many-body effects can influence the accuracy of the calculated barriers.

Third, in Chapter 8, a strategy was developed to extend the accessible timescales of QM/MM simulations by coupling a reactive coordinate to a machine-learned collective variable (CV). Linear dimensionality-reduction methods were used to extract critical torsional modes from a dynamic disulfide bridge, as low-dimensional descriptors. When applied in two-dimensional QM/MM MTD, these variables improved conformational sampling. The simulations revealed that local disulfide motions are coupled to shifts in global protein geometry and that only a subset of conformations are preorganized for reaction. This points to a conformational filtering mechanism that governs reactivity and demonstrates the utility of data-driven variables for probing coupled reactive–dynamic processes.

Zusammenfassung

Proteine zeigen eine Hierarchie räumlicher und zeitlicher Skalen, in der lokale chemische Reaktivität, langreichweitige nichtkovalenten Wechselwirkungen und konformationellen Dynamiken miteinander gekoppelt sind. Die Erfassung dieser Mehrskaligkeit erfordert Methoden, die chemische Genauigkeit mit effizientem Sampling verbinden. Der QM/MM-Ansatz erreicht dies, indem die reaktive Region quantenmechanisch beschrieben wird, während die umgebende Umgebung mittels Molekülmechanik modelliert wird. Seine Verlässlichkeit hängt davon ab, wie das System partitioniert wird, wie reaktive Ereignisse modelliert werden und wie konformationelle Ensembles gesampled werden. Diese Dissertation adressiert diese Herausforderungen durch die Integration dreier komplementärer Forschungsrichtungen. Gemeinsam zeigen sie, wie QM/MM-Methoden für spezifische Anwendungen verfeinert werden können und dadurch genauere Beschreibungen reaktiver Prozesse in dynamischen Proteinumgebungen über mehrere Skalen hinweg ermöglichen.

Kapitel 6 untersucht nichtkovalente Wechselwirkungen in wasserstoffbrückengebundenen Komplexen mittels QM/MM, wobei Paare kleiner Moleküle als Modellsysteme dienen. Die Ergebnisse zeigen, dass Fehler in den Wechselwirkungsenergien hauptsächlich an der QM/MM-Grenzfläche entstehen, insbesondere durch unoptimierte van-der-Waals-Parameter für kurze Bindungsabständen. Ladungstransfer ist in neutralen Dimeren gering, wird jedoch in ionischen Systemen bedeutsam. Diese Befunde liefern Leitlinien für den Aufbau geeigneter QM/MM-Partitionen.

In Kapitel 7 wird QM/MM angewendet, um den Mechanismus der Thiol-Disulfide Austausch zu untersuchen, die von Glutaredoxin katalysiert wird. Da Schwefelchemie eine besonders genaue elektronische Beschreibung erfordert, wurden zwei zuvor entwickelte Ansätze eingesetzt: eine reaktionsspezifische Parametrisierung für DFTB sowie eine Δ-Machine-Learning-Korrektur, trainiert auf höherwertige Referenzenergien. In Kombination mit MTD-Sampling ermöglichten diese Methoden die Konstruktion von freie Enerie Flächen für aufeinanderfolgende Reaktionsschritte und reproduzierten die experimentell beobachtete Regioselektivität. Die berechneten Barrieren stützen den vorgeschlagenen katalytischen Mechanismus und zeigen, wie Vieleffekte die Genauigkeit der berechneten Barrieren beeinflussen können.

In Kapitel 8 wird eine Strategie entwickelt, um die zugänglichen Zeitskalen von QM/MM-Simulationen zu erweitern, indem eine reaktive Koordinate mit einer maschinell gelernten CV gekoppelt wird. Lineare dimensionsreduzierende Methoden wurden eingesetzt, um kritische Torsionsmoden einer dynamischen Disulfidbrücke als niederdimensionale Deskriptoren zu extrahieren. In zweidimensionalen QM/MM-MTD-Simulationen verbesserten diese Variablen das konformationelle Sampling. Die Simulationen zeigten, dass lokale Bewegungen der Disulfidbrücke mit globalen Strukturänderungen des Proteins gekoppelt sind und dass nur ein Teil der Konformationen für die Reaktion vororganisiert ist. Dies weist auf einen konformationellen Filtermechanismus hin, der die Reaktivität steuert, und demonstriert den Nutzen datengetriebener Variablen zur Untersuchung gekoppelter reaktiver und dynamischer Prozesse.

List of Publications

Journal articles

- **Julian Böser** et al. "Reduction pathway of glutaredoxin 1 investigated with QM/MM molecular dynamics using a neural network correction". In: *The Journal of Chemical Physics* (2022), p. 154104.
- Sani Idris Alhassan, Tomáš Kubař, Marcus Elstner, **Julian Böser**. "Multiscale Computational Workflow to Determine Stability of Disulfide Bridges in Proteins-Application to IgG Antibodies". In: *Journal of Chemical Information and Modeling* (2025), pp. 11187–11202.
- **Julian Böser** et al. "Non-covalent Interactions at the QM–MM Interface in the Semi-Empirical and Density-Functional Limit". In: *Journal of Chemical Theory and Computation* (2026), 22, 1, pp. 678–695.

Contents

List of Figures

List of Tables

Acronyms

1D	one-dimensional
2D	two-dimensional
ACSF	atom-centered symmetry function
ANN	artificial neural network
CT	charge transfer
CV	collective variable
CVs	collective variables
Cys	cysteine
DFT	density functional theory
DFTB	semi-empirical density functional tight binding
FF	force field
FES	free-energy surface
GAFF	General Amber Force Field
GMM	Gaussian Mixture Model
Grx	*Homo sapiens* glutaredoxin
GSSG	glutathione disulfide
GSH	glutathione
H-bond	hydrogen bond
HK	Hohenberg-Kohn
HDNNP	high-dimensional neural network potential
Hma	HMA4n
KS	Kohn-Sham
LCAO	linear combination of atomic orbitals
LDA	local density approximation
LJ	Lennard-Jones
MD	molecular dynamics

MTD metadynamics

ML machine learning

MM molecular mechanics

MLP machine-learning potential

NVE constant energy isochoric ensemble

NVT isothermal-isochoric ensemble

NPT isothermal-isobaric ensemble

PCA principal component analysis

PE potential energy

QM/MM quantum mechanics/molecular mechanics

SASA solvent-accessible surface area

SCC self-consistent charge

SCF self-consistent field

SE semiempirical

SRP specific reaction parameterization

TDE thiol–disulfide exchange

TS transition state

tICA time lagged independent component analysis

t-SNE t-distributed Stochastic Neighbor Embedding

XC exchange-correlation

Part I.

Introduction

1. Calculability of Proteins on Multiple Scales

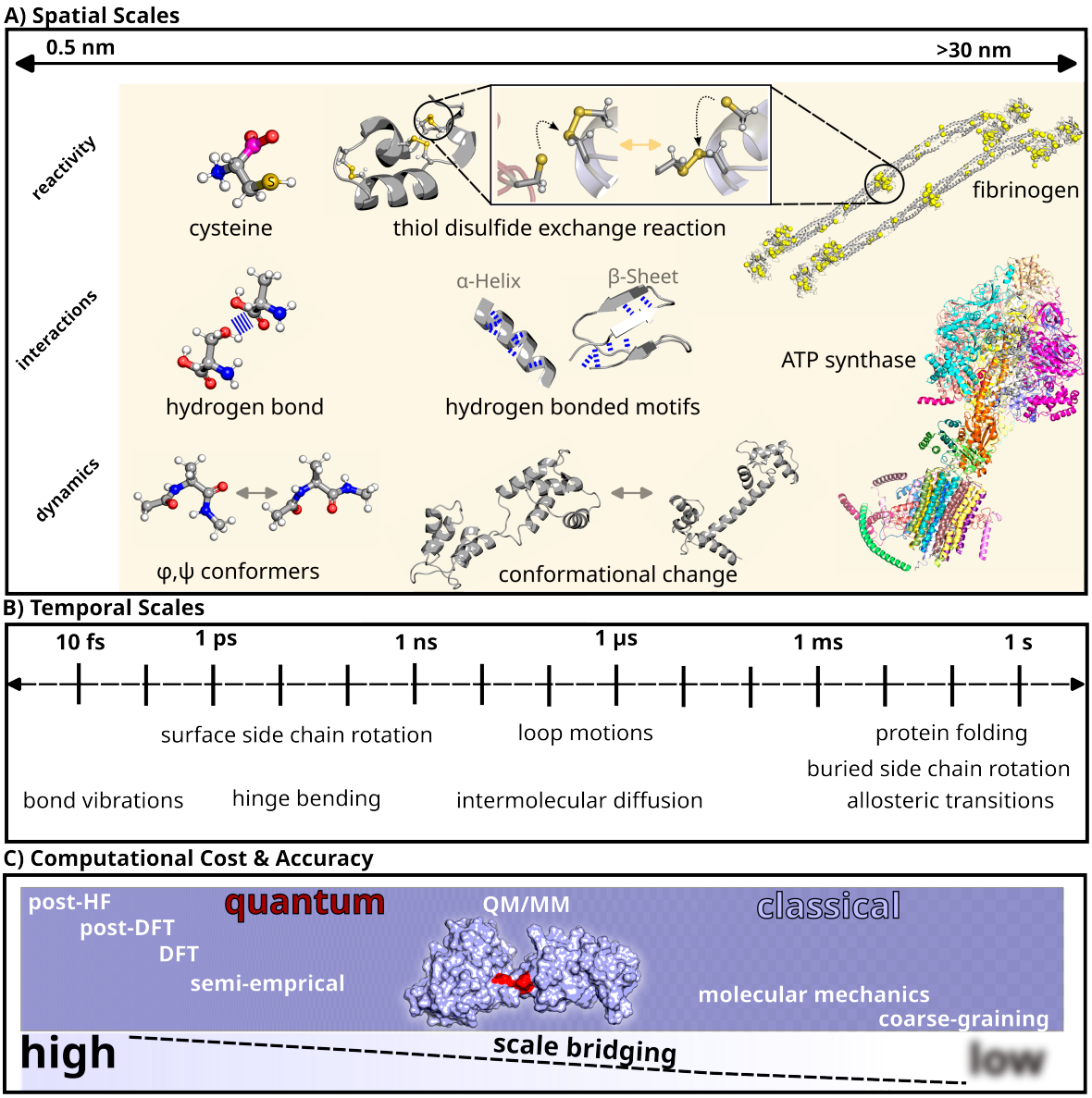

Figure 1.1.: Multiscale nature of protein systems and the trade-off between computational cost and accuracy. A) Spatial scales range from subnanometer-sized molecules to supramolecular assemblies, illustrating how reactivity, nonbonded interactions, and conformational dynamics manifest across different structural scales. ATP synthase exemplifies a complex molecular machine whose function relies on large-scale conformational transitions and coordinated hydrogen-bonding networks that enable proton translocation and catalytic ATP synthesis. B) Temporal scales span more than twelve orders of magnitude, from femtosecond bond vibrations to second timescale conformational transitions, reflecting the range of molecular motions. C) Computational methods vary in accuracy and cost, from high-level quantum treatments to classical and coarse-grained models. Hybrid QM/MM approaches occupy the intermediate computational regime and provide a practical strategy for bridging scales in complex systems.

In 1925, Gilbert Adair provided one of the first quantitative thermodynamic models of protein function through his analysis of hemoglobin's oxygen binding curves.[1,2] By introducing a binding polynomial formalism, he was able to calculate successive equilibrium constants and describe cooperative binding in quantitative terms. This approach represented a critical advance in demonstrating that proteins could be treated quantitatively as physical systems. After atomic-resolution structures became available in the 1950s,[3] computational predictive methods began shifting toward molecular properties such as secondary structure propensities,[4] marking the transition from macroscopic thermodynamics toward sequence- and structure-based developments. In parallel with these advances, the first molecular dynamics simulation of a condensed-phase system was performed by Alder and Wainwright in 1957.[5] Since then, molecular dynamics has evolved into a central computational technique for studying the structure, dynamics, and function of biomolecular systems.[6]

The structural organization of proteins arises from the assembly of the twenty-two proteinogenic amino acids that serve as their fundamental building blocks.[7] Their sequence and chemical properties guide the folding of these polymers into three-dimensional structures and govern their stability and function.[8–10] Each amino acid contributes distinct chemical characteristics that enable specific interactions at the residue level, and biological systems leverage this diversity when assembling peptides and proteins. As residues are incorporated into higher-order architectures, their individual properties converge into coordinated interaction networks that organize both structure and dynamic behavior.[11–13]

Figure 1.1A exemplifies how biomolecular structure and function emerge across multiple spatial scales. Disulfide bridges formed between pairs of cysteine residues represent a pervasive structural motif in small peptides and large macromolecular assemblies, such as fibrinogen, where they contribute to mechanical stability and structural integrity.[14–16] Beyond their structural role, cysteine residues can also undergo chemical reactions. Thiol–disulfide exchange (TDE) may occur and reorganize existing cross-links, reflecting an interplay between local chemical events and broader structural adaptations that can propagate through distant regions of a protein or protein complex.[17–19] Noncovalent interactions influence protein function by modulating ligand binding, intermolecular complex formation, molecular recognition, and enzymatic activity.[20] At the residue level, hydrogen bonds (H-bonds) stabilize local structure through directional interactions between backbone and side-chain groups and can accumulate to stabilize higher-order motifs such as α-helices and β-sheets. Networks of H-bonds provide essential stability while permitting the plasticity required for functional conformational changes across spatial scales.[21] Protein dynamics span a wide range of motions, from local φ, ψ dihedral rotations that modulate backbone geometry to large-scale conformational rearrangements that enable functional transitions.[22,23] ATP synthase exemplifies this principle as a complex molecular machine whose activity depends on extensive conformational changes and organized hydrogen-bonding networks that couple proton translocation to catalytic ATP synthesis.[24,25]

Although proteins can be large and complex, their functions often arise from a set of localized functional sites such as ligand-binding pockets, catalytic residues, allosteric switches, post-translational modification sites, prosthetic groups, and chromophores.[26] The activity of these regions is influenced by molecular motions, which span a wide range of temporal scales.[27,28] Figure 1.1B illustrates the broad timescales over which biomolecular motions occur. Fast events such as bond vibrations and picosecond backbone fluctuations enable rapid local adjustments within protein structures. Nanosecond side-chain rotations and microsecond loop motions support conformational rearrangements and regulate access to functional sites. Slower millisecond-to-second processes, including domain rearrangements, allostery, and protein folding, reshape global structure and govern higher-level functional transitions.[29,30]

Confronted with the inherent complexity of biological systems, the choice of computational method must balance the required level of accuracy with the spatial and temporal scales relevant to the process under study. Figure 1.1C highlights this trade-off by illustrating how different methods vary in both computational cost and attainable accuracy. High-level quantum chemical approaches provide detailed electronic descriptions but exhibit steep scaling with system size. Density-functional theory typically scales as $\mathcal{O}(N^3)$–$\mathcal{O}(N^4)$, while correlated methods such as MP2, CCSD, and CCSD(T) scale as $\mathcal{O}(N^5)$, $\mathcal{O}(N^6)$, and $\mathcal{O}(N^7)$. This steep scaling limits their routine use to small systems or short trajectories.[31] Semiempirical (SE) quantum-mechanical models reduce computational cost by several orders of magnitude through approximations, typically achieving $\mathcal{O}(N^2)$–$\mathcal{O}(N^3)$ scaling but with reduced accuracy.[32] This trend continues for classical molecular mechanics,[30] which offers near-linear to quadratic scaling, $\mathcal{O}(N)$–$\mathcal{O}(N^2)$, through the use of empirical potentials. Coarse-grained models[33] further approach linear scaling by mapping groups of atoms onto single effective particles, enabling simulations of large biomolecular assemblies at even lower computational cost.

The use of classical potentials enables efficient simulations of very large biomolecular assemblies over microsecond to millisecond timescales, though at the expense of chemical accuracy. Such models cannot capture changes in electron structure, including bond rearrangements, charge transfer, or proton-transfer that are central to many biological reactions. Hybrid quantum mechanics/-molecular mechanics (QM/MM)[34] approaches address this limitation by treating a localized site quantum mechanically while modeling the surrounding protein environment classically. This division reflects the organization of many biological systems, in which functional activity is concentrated in spatially confined regions. As shown in Figure 1.1C, QM/MM embeds a small quantum region (red) within a much larger classical system. This class of models approaches chemical accuracy while reducing computational cost, thereby expanding the spatial and temporal scales that can be explored. This capability underpins its prominent role in scale-bridging strategies for complex biomolecular systems, where access to extended and accurately described scales is essential. Decades of development have established QM/MM as a powerful and widely adopted framework that can be tailored to the specific process under investigation.[35–38]

Scope of this Thesis

This thesis explores and applies the QM/MM approach for scale-bridging in the protein domain along three key directions, drawing on recent methodological advances, as briefly outlined below.

Hydrogen Bonding. Chapter 6, Non-covalent Interactions at the QM-MM Interface in the Semi-Empirical and Density-Functional Limit, investigates how the QM–MM interface affects the accuracy of hydrogen-bond descriptions in neutral and ionic dimers, addressing an often neglected challenge. This systematic analysis clarifies how the interface can introduce artifacts that reduce reliability and identifies practical ways to mitigate these issues.

Thiol–Disulfide Reaction. Chapter 7, Reduction Pathway of Glutaredoxin 1 Investigated with QM/MM Molecular Dynamics Using a Neural Network correction, applies the QM/MM framework to investigate the reaction mechanism of *Homo sapiens* glutaredoxin (Grx), a class of enzymes that catalyze TDE. Sulfur chemistry imposes stringent demands on QM/MM models because it requires an accurate treatment of electron correlation, long-range electrostatic interactions, and inclusion of many-body effects. The study evaluates two previously developed strategies: (1) a specific reaction parameterization (SRP) for semi-empirical density functional tight binding (DFTB) and (2) an artificial neural network (ANN)-based Δ-ML correction to refine the underlying quantum chemical description between the DFTB baseline and CCSD(T) target method.

Coupling Reactivity and Dynamics. Chapter 8, Transferring Collective Variables from Molecular Dynamics Simulations to QM/MM Simulations for Reactivity Exploration in Dynamic Systems, introduces a novel strategy to extend the accessible timescales in QM/MM simulations. The approach couples a canonical reaction coordinate within the quantum region, such as an asymmetric distance coordinate, with a machine-learned collective variable (CV) designed to accelerate the conformational sampling of the surrounding protein environment. This approach captures the coupling between reactivity and the dynamically evolving protein environment, thereby enabling more efficient sampling in systems with many states and dynamic behavior that modulates reactivity.

1.1. Biomolecular Context

The following section introduces the biomolecular structures and dynamics relevant to the studies in this work, with a focus on hydrogen bonding and thiol–disulfide exchange in proteins.

1.1.1. Thiol–Disulfide Exchange in Proteins

Post-translational modifications, including the formation of intramolecular disulfide bonds between cysteine (Cys) residues, are central to physiological and biochemical processes.[39–41] Early studies recognized the high reactivity of Cys and the substantial structural stabilization provided by disulfide bonds.[42,43] Beyond their structural role, Cys residues undergo reversible chemical

modifications, can act as nucleophilic catalysts,[44] or participate directly in substrate recognition and binding.[45] Recent work emphasizes the functional plasticity of disulfide bonds, highlighting their dynamic roles alongside their classical structural contributions.[46] Through reversible redox reactions, disulfide bonds can be cleaved and reformed, enabling dynamic regulation of protein structure and function. At the core of this chemistry lies thiol–disulfide exchange (TDE), which establishes the mechanistic basis for reversible disulfide exchange and enables molecular modeling of the regulatory and pathological processes driven by dynamic disulfide rearrangements.[47–49]

Figure 1.2 depicts two sequential TDE steps that proceed as nucleophilic substitutions, each yielding a distinct disulfide linkage. In the first step, nucleophilic attack generates a mixed disulfide intermediate. The subsequent substitution then forms a new disulfide bond between the two cysteines that were initially unpaired. In each step, the reactive thiolate species initiates an S_N2 attack on the disulfide bond.[50] Thiolate formation through deprotonation and subsequent reprotonation completes the reaction cycle. The detailed course of the mechanism is determined by its free-energy surface (FES) and depends on the nature of the attacking thiolate, the leaving group, the electrophilicity of the sulfur atoms and their substituents, and on the environment in which the reaction takes place. TDE is a reversible equilibrium reaction in small-molecule systems. In proteins, however, subsequent irreversible events such as denaturation or proteolysis can disrupt this reversibility.[51] As a result, TDEs introduce non-equilibrium dynamic processes in cells that depend on the local environment. TDE may occur spontaneously[52] or be catalyzed by enzymes.[53] Noncatalyzed reactions proceed with relatively small rate constants on the order of 0.1–10 L mol^{-1} s^{-1}, whereas enzymatic catalysis accelerates the process to 10^4–10^6 L mol^{-1} s^{-1}.[51] Enzymatic control is therefore essential for maintaining TDE within the functional range required for cellular homeostasis.[51]

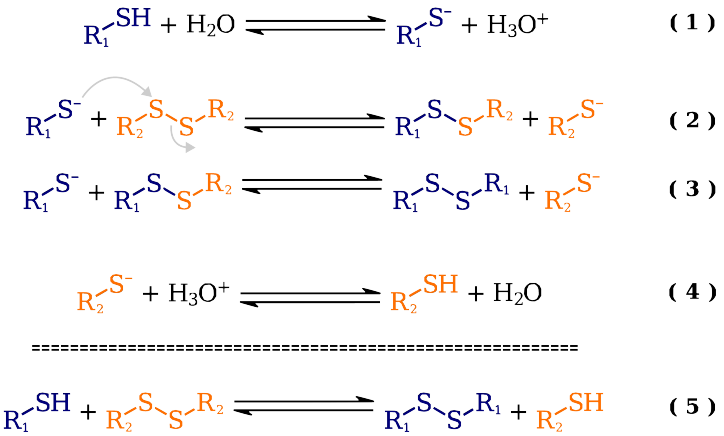

Figure 1.2.: Reaction scheme for thiol–disulfide exchange. (1) Cysteine is deprotonated to form a reactive thiolate. (2) The nucleophilic thiolate attacks the sulfur atom of a pre-existing disulfide, forming a new S–S bond while the second sulfur acts as the leaving group. (3) Repetition of this reaction leads to sequential disulfide scrambling among different thiolates. (4) The thiolate is subsequently protonated to regenerate cysteine. (5) Continued exchange among multiple thiol–disulfide pairs yields fully mixed disulfides.[54]

Several enzymes are known that catalyze TDE. These encompass thioredoxins (Trx), protein disulfide isomerases, the disulfide bond protein family A–D (DsbA–D), and glutaredoxins.[41,55] Their function relies on an active site that features a conserved Cys-X-X-Cys motif, whose vicinal thiols undergo reversible oxidation to a disulfide. The N-terminal cysteine is solvent-exposed, has an unusually low pK_a,[56] and initiates nucleophilic attacks on target disulfides.[51,57] Structural features near the active site, such as the cis-proline motif in Grx that facilitates glutathione (GSH) binding, further tune specificity.[58] Trx-like proteins adopt a characteristic fold with a β-sheet core flanked by α-helices that mediate protein interactions and redox activity.[59]

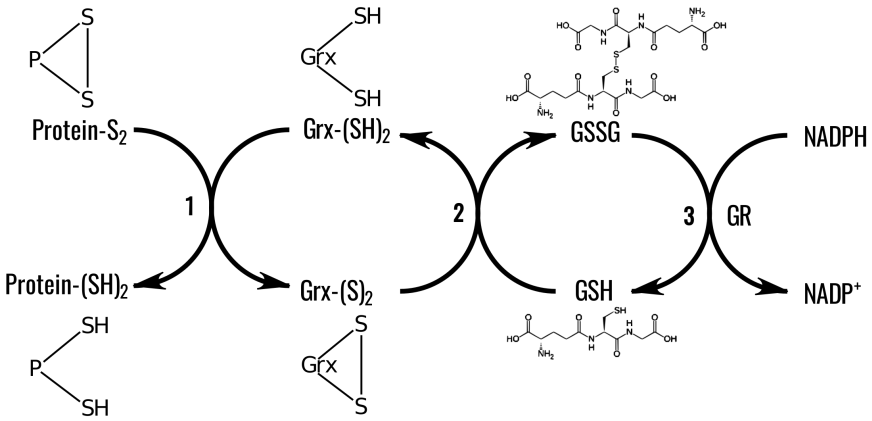

Figure 1.3.: General mechanism of the cellular glutaredoxin system. The glutaredoxin system is composed of NADPH, the flavoprotein glutathione reductase (GR), Glutathione, and Glutaredoxin. In step one, a protein disulfide is reduced to its dithiol form, and Grx is oxidized to a disulfide. In step two, the Grx disulfide is reduced by GSH to regenerate its thiol form, and two GSH are oxidized to from GSSG. In step three, GSH is regenerated by electrons provided from NADPH, catalyzed by GR.

For example, the activity of Grx is coupled to the concentration of the tripeptide GSH, the most abundant cellular low-molecular-weight thiol.[58] As illustrated in Figure 1.3, reduced Grx cleaves disulfide bonds in substrate proteins, and becomes oxidized during the reaction.[60] The efficiency of this catalytic cycle depends on the redox environment established by the intracellular glutathione pool. The ratio of GSH to glutathione disulfide (GSSG) is a major contributor to the cellular redox potential, and it shifts with physiological context, including differences among cell types and stages of the cell cycle.[61] This ratio determines whether oxidized Grx can be reconverted to its active dithiol form, which in turn controls the rate at which protein substrates are reduced. Oxidative stress increases GSSG levels when reactive oxygen species convert GSH to its disulfide form. Conversely, glutathione reductase restores reduced glutathione by reducing GSSG at the expense of NADPH. These reactions underscore the tight coupling between glutathione buffering and Grx-catalyzed protein disulfide reduction. Through this central role in redox homeostasis, Grx contributes to processes such as cell development, metabolism, stress adaptation, redox sensing, signaling, oxidative protein folding, maintenance of protein thiol function, and apoptosis.[62,63]

Computational and experimental studies indicate that TDE typically proceeds through an in-line S_N2 attack, with a near-linear trisulfide-like transition state in which charge is delocalized between the terminal sulfurs.[64–66] This charge distribution favors nonpolar environments, lowering

activation barriers.[50] Although addition–elimination pathways with stable trisulfide intermediates have been proposed, solvation and steric effects generally shift the mechanism toward classical S_N2 behavior under physiological conditions.[64,65,67] In proteins, local structural features modulate this chemistry. Hydrophobic pockets can accelerate exchange, conformational strain alters disulfide lability, and cysteine pK_a values and nucleophilicity depend on sequence context, electrostatics, and solvent accessibility.[51,68,69] Disulfide shuffling, therefore, represents a multiscale process in which complex sulfur chemistry couples to protein dynamics.

1.1.2. Hydrogen Bonds in Proteins

H-bonds interactions constitute one of the essential noncovalent forces that govern the structure, stability, and function of proteins.[70–73] They influence ligand binding affinities, guide molecular recognition processes, and shape both the energetics and kinetics of enzymatic reactions.[73] Their interaction energy arises from a combination of electrostatics, polarization, exchange repulsion, charge transfer (CT), dispersion and coupling between these components.[74,75] In simplified terms, a hydrogen bond can be viewed as a directional attraction between a hydrogen donor and an electronegative acceptor, typically oxygen or nitrogen.[76]

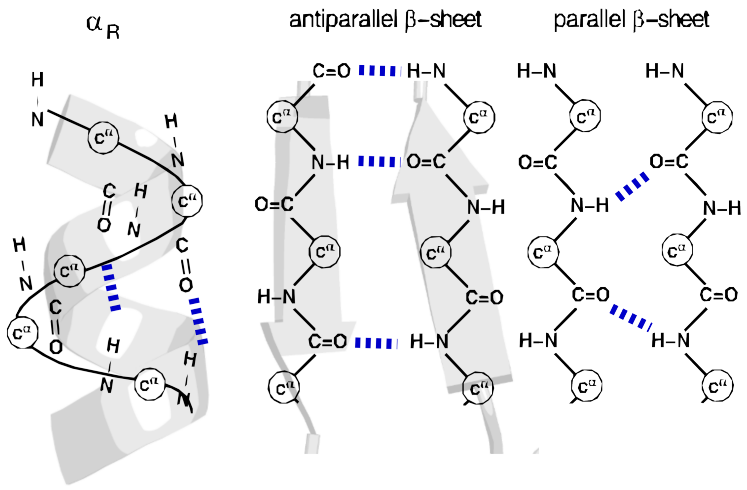

Figure 1.4.: Schematic representations of an α_R helix, an antiparallel β-sheet, and a parallel β-sheet (from left to right). The blue dashed lines represent the hydrogen bonds. The α_R helix is defined by dihedral angles of approximately $\phi \approx -57°$ and $\psi \approx -47°$, which generate a regular helical pitch stabilized by characteristic intrachain hydrogen bonds oriented roughly parallel to the helix axis. In contrast, β-sheets extend the polypeptide chain, with antiparallel β-strands typically adopting $\phi \approx -139°$ and $\psi \approx +135°$ and parallel β-strands adopting $\phi \approx -119°$ and $\psi \approx +113°$, each stabilized by interstrand hydrogen bonding. Reproduced with permission from Tamar Schlick. *Molecular Modeling and Simulation: An Interdisciplinary Guide.* 2nd ed. New York: Springer, 2010.

H-bonds interactions stabilize secondary structures and modulate dynamic properties that are critical for biochemical function. Furthermore, they contribute to the organization of tertiary and quaternary structures by mediating interactions among side-chain functional groups, between

distinct protein domains, and across protein–protein interfaces.[77,78] Figure 1.4 illustrates the geometry and stabilizing role of hydrogen bonds in the formation of α-helices and β-sheets as fundamental protein secondary-structure elements.

H-bonds interactions contribute through multiple mechanisms to the catalytic power of enzymes.[79,80] Their directional and cooperative nature allows enzymes to pre-organize substrates and catalytic residues within the active site, reducing conformational freedom and enforcing precise proximity and orientation.[78] Hydrogen bonds also facilitate general acid–base chemistry by stabilizing charges during proton transfer,[81] tuning the pK_a values of catalytic groups,[82] and supporting the prototropic shifts essential to many enzymatic pathways.[83] Within the preorganized electrostatic environment of the active site, these interactions further polarize bonds,[84] stabilize high-energy intermediates, and, in some cases, give rise to unusually strong low-barrier hydrogen bonds that significantly enhance transition-state stabilization.[78] Figure 1.5 illustrates the contribution of H-bonds interactions to the catalytic triad of serine proteases.[85]

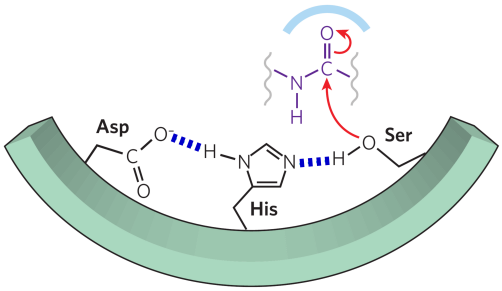

Figure 1.5.: Hydrogen-bond–mediated catalytic assistance in a serine protease active site. Hydrogen bonds are shown as blue dashed lines. Hydrogen bonds between Asp, His, and Ser align and activate the nucleophile, while additional hydrogen bonds in the pocket help stabilize the developing oxyanion during peptide-bond cleavage. Reproduced with permission from Elinor Erez, Deborah Fass, and Eitan Bibi. "How intramembrane proteases bury hydrolytic reactions in the membrane". In: *Nature* 459.7245 (May 2009), pp. 371–378. Copyright 2009 Springer Nature Limited.

H-bond networks can assemble into cooperative architectures that influence biomolecular organization and dynamics across multiple spatial scales. These networks not only stabilize local structural motifs but also mediate long-range communication within proteins, enabling dynamic coupling between distant sites. Such connectivity can underlie forms of allosteric regulation, where subtle rearrangements in H-bond patterns propagate through the protein matrix to modulate activity at remote functional centers.[21,86–90] Figure 1.6 shows an example of a H-bond network in human lysozyme.[91]

The central importance of hydrogen bonding in proteins underscores the need for computationally efficient and sufficiently accurate methods. CCSD(T)/CBS calculations are considered the gold standard reference but remain computationally expensive.[92] More efficient, though less accurate, approaches such as DFT and SE methods therefore rely on explicit corrections to noncovalent energy contributions.[93]

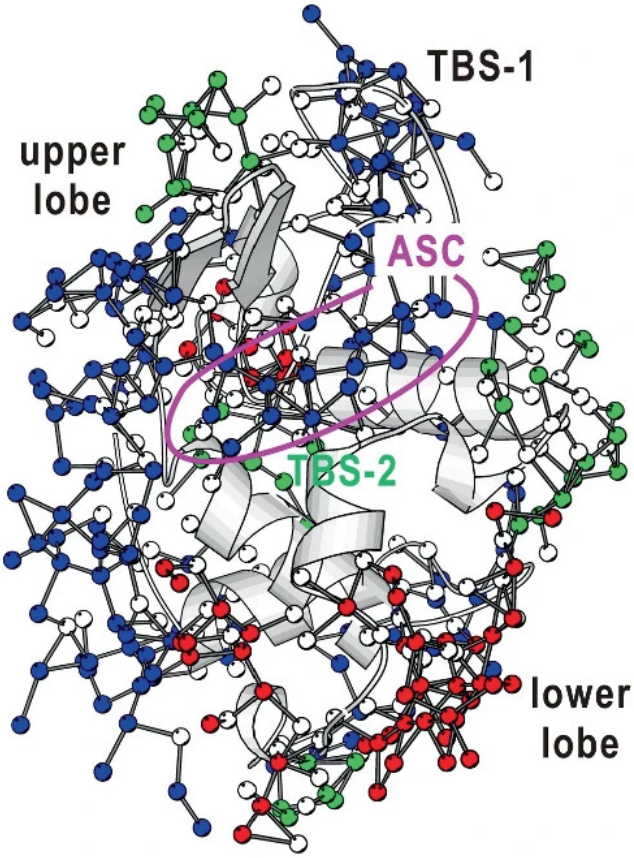

Figure 1.6.: Network of hydrogen bonds in human lysozyme. Colored clusters depict three distinct hydrogen-bonded regions spanning the upper and lower lobes, with tight-binding water sites (TBS-1 and TBS-2) and the active-site cleft (ASC) marked to illustrate how structured hydration organizes the protein's H-bond network. Reproduced with permission from Masayoshi Nakasako. "Network of Hydrogen Bonds Around Proteins". In: *Hydration Structures of Proteins*. Ed. by Masayoshi Nakasako. Soft and Biological Matter. Springer, 2021, pp. 163–182.

Part II.

Theoretical Background

2. Potential Energy Functions and Molecular Models

A central aspect of molecular modeling is to describe how the potential energy (PE) of a system varies with its molecular configuration and the electronic or chemical state. PEs provide the foundation for predicting equilibrium structures, conformational changes, reaction pathways, and spectroscopic properties. Strategies for constructing these functions span classical force fields, hybrid approaches, and quantum-mechanical formalisms based on first-principles methods. Multiscale modeling aims to select the appropriate level of theory for a given problem by balancing accuracy and computational cost. It further requires accounting for system size, environmental effects, and the sampling needed to capture relevant molecular behavior.

2.1. Molecular Mechanics

Molecular mechanics (MM) is a framework for molecular modeling that uses classical mechanics to approximate atomic interactions. In this approach, the PE is represented as an explicit analytical function of the atomic coordinates. It is computationally inexpensive and can be applied to systems containing millions of atoms, which enables simulations of proteins, membranes, and materials on microsecond to millisecond timescales. The main limitation of MM is that it cannot model changes in electron structure, which prevents the description of bond breaking, charge transfer, and electronic polarization, and can lead to inaccuracies in the description of weak or highly directional noncovalent interactions.

2.1.1. Force Fields

When MM is used to evaluate the PE of a molecular system, the mathematical form of the energy, together with the parameters assigned to different atom types and interactions, defines an atomistic Force field (FF). Constructing such models is nontrivial because numerous parameters are required to represent the variety of atomic environments and interaction types. A detailed introduction to FF is provided in Part IV of Ref. [94]. The energy of a FF is expressed as a sum of bonded and nonbonded contributions, as shown in Equation 2.1. Bonded terms typically account for bond stretching, angle bending, and torsional rotations. Nonbonded contributions describe

van der Waals and electrostatic interactions. Each term quantifies how the energy varies as the molecular structure changes.[95,96]

$$\begin{aligned} V_{\text{Force Field}} &= V_{\text{bonded}} + V_{\text{non-bonded}} \\ &= V_{\text{bonds}} + V_{\text{angles}} + V_{\text{tors.}} + V_{\text{vdW}} + V_{\text{coul.}} \end{aligned} \tag{2.1}$$

The PE of a system changes when the bond length r between two atoms is varied. The bond–stretch contribution V_{bond} is modeled by a harmonic potential where the energy increases with the squared deviation of r from its equilibrium value r_0, with the force constant k_r determining the stiffness. The energy thus increases symmetrically upon compression or extension of the bond. To reproduce the correct asymptotic behavior at large interatomic distances when bond dissociation must be represented, a Morse potential can be used. The angle term V_{angle} is likewise described by a harmonic potential, analogous to bond stretching, and its curvature is determined by the force constant k_θ when the angle θ formed by atoms A–B–C deviates from its equilibrium value θ_0. In contrast, the torsional term $V_{\text{tors.}}$ is modeled as a periodic function of the dihedral angle ω, typically expressed as a Fourier series of cosine terms. The dihedral ω is defined by the angle of planes formed by A–B–C and B–C–D in the sequence A–B–C–D. In this expression, V_n is the barrier height for term n, n denotes the periodicity, and γ is the phase. The total energy for the bonded interactions can then be written as follows.[95,96]

$$V_{bonded} = \frac{1}{2}\sum_{i}^{bonds} k_i^r (r_i - r_i^0)^2 + \frac{1}{2}\sum_{j}^{angles} k_j^\theta (\theta_j - \theta_j^0)^2 + \sum_{k}^{tors.}\sum_{n}\frac{V_n}{2}\Big[1+\cos(n\omega_k - \gamma_n)\Big]. \tag{2.2}$$

Nonbonded interactions comprise two contributions, each expressed as a function of the interatomic distance r_{ij}. The first contribution is the van der Waals term, typically modeled by the Lennard–Jones potential, whose repulsive (Pauli) component scales as r_{ij}^{-12} and whose attractive dispersion component scales as r_{ij}^{-6}. The combined potential is strongly positive at short separations, crosses zero at $r_{ij} = \sigma_{ij}$, reaches its minimum value $-\varepsilon_{ij}$ at $r_{ij} = 2^{1/6}\sigma_{ij}$, and approaches zero as $r_{ij} \to \infty$. The second contribution is the electrostatic interaction, represented by the Coulomb term, which depends on the atomic charges q_i and q_j and decays as $1/r_{ij}$. The total energy for the nonbonded interactions can then be written as[95,96]

$$V_{non-bonded} = \sum_{i\neq j}^{vdW} 4\epsilon_{ij}\left(\left(\frac{\sigma_{ij}}{r_{ij}}\right)^{12} - \left(\frac{\sigma_{ij}}{r_{ij}}\right)^{6}\right) + \sum_{i\neq j}^{coul.}\frac{q_i q_j}{4\pi\epsilon_0 r_{ij}}. \tag{2.3}$$

Electrostatic interactions are intrinsically long ranged, so many pairwise terms must be evaluated, and the computational cost increases accordingly. The number of evaluations can be reduced by applying a distance cutoff, which neglects interactions beyond a prescribed threshold. In periodic systems, the Particle Mesh Ewald method incorporates all electrostatic interactions by performing the long-range summation in Fourier space.[95,96]

After specifying the analytical form of the potential, one determines numerical parameters (e.g., k_r, k_θ, V_n) for specific atom and interaction types. Atom typing classifies atoms by element and chemical context, including bond order, hybridization, aromaticity, and typical bonding partners. Parameters are obtained by fitting to reference data generated with high-level quantum chemical methods.The design of FF relies on a strictly local view of molecular structure, in which each atom and its directly bonded neighbors define a transferable pattern of parameters. For example, a C–C single bond exhibits a characteristic length and stiffness associated with that specific bonded pair. This illustrates the broader principle that comparable atom–partner combinations tend to display similar structural and energetic properties, enabling systematic parameter transfer across molecules.[95,96] This rationale underlies atom typing and the use of locally defined parameters. In practice, a force field is the pair consisting of the selected functional form and its associated parameter set.[95,96]

FF can adopt diverse functional forms and weigh physical effects differently. Beyond standard bonded and nonbonded terms, some include cross terms that couple internal coordinates, e.g., bond–angle couplings (Urey–Bradley potentials[97]) or torsion–torsion couplings (CMAP[98,99]). Representative FF include AMBER[100], CHARMM[101], and OPLS, which are widely used fixed-charge models for biomolecular simulations. The molecular-mechanics framework can be extended to more sophisticated formulations such as AMOEBA[102] for polarizable interactions and ReaxFF[103] for chemically reactive systems. Conversely, it can also be simplified for coarse-grained modeling, as exemplified by MARTINI[104].

Water plays an important role in biomolecular simulations, typically constituting the majority of particles and strongly influencing electrostatics, conformational dynamics, and protonation equilibria. Numerous explicit water models exist. The choice of water model should match the target properties, the electrostatics treatment[105–109], and the FF[110].

2.2. Quantum Chemistry

2.2.1. Density Functional Theory

In density functional theory (DFT), the many-electron wave function, which depends on $3N$ spatial and N spin variables, is reformulated in terms of electron density $\rho(\mathbf{r})$. Because $\rho(\mathbf{r})$ depends only on three spatial variables, the electronic structure problem can be reformulated. Its conceptual foundation rests on the seminal work of Hohenberg and Kohn[111], whose 1964 paper introduced the two theorems that established the modern framework of density functional theory. The following discussion draws on Sections 4 and 5 of Ref. [112], which provide additional details on the foundations of DFT. The first Hohenberg-Kohn (HK) theorem states that the external potential $V_S(\mathbf{r})$ is a unique functional of $\rho(\mathbf{r})$. Since the Hamiltonian $\hat{H}$ is defined by $V_S(\mathbf{r})$, the

many-particle ground state Ψ_0 is also a unique functional of $\rho(\mathbf{r})$. Therefore, the ground-state energy and its components can be written as

$$E[\rho] = E_{Ne}[\rho(\mathbf{r})] + \quad E_{ee}[\rho(\mathbf{r})] + T[\rho(\mathbf{r})]. \tag{2.4}$$

where T is the kinetic energy, E_{ee} the electron–electron interaction energy, and E_{Ne} the nuclear–electron interaction energy. The electron density ρ thus determines all ground-state observables. Equation 2.4 separates the total energy into a system-dependent contribution arising from the nuclear–electron interaction and universal terms that do not depend on the nuclear configuration. The former is explicitly functional form, whereas the universal contributions define the HK functional F_{HK}

$$E[\rho] = \int \rho(\mathbf{r}) V_{Ne} d\mathbf{r} \quad + \quad F_{HK}[\rho(\mathbf{r})]. \tag{2.5}$$

The second HK theorem establishes that the ground-state density satisfies a variational principle. However, approximating the kinetic energy directly from the density yields an overly simplistic relation between the spatial distribution of electrons and their velocities, which is insufficient for quantitative calculations. In orbital-free DFT, finding a functional of the kinetic energy $T[\rho(\mathbf{r})]$ remains an open challenge. Kohn and Sham introduced a non-interacting reference system constructed from orbitals to evaluate the kinetic energy. This non-interacting kinetic term T_S already accounts for most of the true kinetic energy in an interacting system, so only a small residual contribution must be approximated. This leads to

$$F_{HK}[\rho(\mathbf{r})] = T_S[\rho(\mathbf{r})] + J[\rho(\mathbf{r})] + E_{\mathrm{XC}}[\rho(\mathbf{r})], \tag{2.6}$$

where $J[\rho(\mathbf{r})]$ is the classical Coulomb functional describing electron–electron repulsion and $E_{\mathrm{XC}}[\rho(\mathbf{r})]$ captures the exchange-correlation (XC) energy, which includes all non-classical contributions to electron–electron interactions together with the remaining part of the exact kinetic energy not represented by T_S. The explicit form of $E_{\mathrm{XC}}[\rho(\mathbf{r})]$ is unknown and must therefore be approximated.

The kinetic energy of a non-interacting system can be calculated from one electron orbitals ϕ

$$T_S = -\frac{1}{2} \sum_{i}^{N} \langle \phi_i | \nabla^2 | \phi_i \rangle \,. \tag{2.7}$$

These orbitals are determined by iteratively solving the Kohn-Sham (KS) eigenvalue equation

$$\hat{f}^{KS} \phi_i = \epsilon_i \phi_i, \tag{2.8}$$

with the one-electron KS operator defined as

$$\hat{f}^{KS} = -\frac{1}{2} \nabla^2 \quad + \quad V_S(\mathbf{r}), \tag{2.9}$$

resulting in

$$\begin{aligned} E[\rho(\mathbf{r})] &= T_S[\rho] + J[\rho] + E_{\mathrm{XC}}[\rho] + E_{Ne}[\rho] \\ &= T_S[\rho] + \frac{1}{2}\iint \frac{\rho(\mathbf{r}_1)\,\rho(\mathbf{r}_2)}{r_{12}}\,d\mathbf{r}_1 d\mathbf{r}_2 + E_{\mathrm{XC}}[\rho] + \int V_{Ne}(\mathbf{r})\,\rho(\mathbf{r})\,d\mathbf{r} \\ &= -\frac{1}{2}\sum_{i=1}^{N}\left\langle \phi_i \middle| \nabla^2 \middle| \phi_i \right\rangle + \frac{1}{2}\sum_{i=1}^{N}\sum_{j=1}^{N}\iint \frac{|\phi_i(\mathbf{r}_1)|^2\,|\phi_j(\mathbf{r}_2)|^2}{r_{12}}\,d\mathbf{r}_1 d\mathbf{r}_2 \\ &\quad + E_{\mathrm{XC}}[\rho] - \sum_{i=1}^{N}\sum_{A=1}^{M}\int \frac{Z_A}{r_{1A}}\,|\phi_i(\mathbf{r}_1)|^2\,d\mathbf{r}_1 \end{aligned} \tag{2.10}$$

for the total energy of the system.[112]

To solve Eq. 2.10, a crucial step is to construct the effective potential $V_S(\mathbf{r})$ such that the electron density of the non-interacting system $\rho_S(\mathbf{r})$ corresponds to the density $\rho(\mathbf{r})$ of the interacting system

$$\rho_s(\mathbf{r}) = \sum_{i=1}^{N} |\phi_i|^2 = \rho(\mathbf{r}). \tag{2.11}$$

The KS potential

$$V_{KS} = \int \frac{\rho(\mathbf{r}_2)}{r_{12}} d\mathbf{r}_2 - \sum_{A}^{M} \frac{Z_A}{r_{1A}} + V_{XC}(\mathbf{r}_1) \tag{2.12}$$

satisfies this condition. Here, V_{XC} denotes the potential associated with the XC energy E_{XC} and is defined as

$$V_{XC} = \frac{\delta E_{XC}[\rho(\mathbf{r})]}{\delta \rho(\mathbf{r})}. \tag{2.13}$$

It can be used to construct the KS operator in Eq. 2.9 to solve the KS eigenvalue equation in Eq. 2.8, which yields the orbitals. Thus, the ground-state energy and ground-state density can be calculated. As V_{KS} depends on the density, the equation must be solved iteratively.

The central goal of modern DFT is to devise reliable approximations for the XC functional, as the formalism introduced above does not provide an exact expression for E_{XC}. Numerous approximations of varying complexity have therefore been proposed, and Jacob's ladder offers a systematic framework for organizing these approaches. The ladder comprises five rungs that illustrate how progressively sophisticated concepts can be incorporated to improve predictive performance and guide the development of methods toward chemical accuracy.[113,114]

- **Rung 1: Local Density Approximation (LDA).** Relies solely on the local electron density and models each point in space as a locally homogeneous electron gas.[113]

- **Rung 2: Generalized Gradient Approximation (GGA).** Extends local density approximation (LDA) by incorporating the loal density gradient $\nabla\rho(\mathbf{r})$, enabling a more realistic description of inhomogeneous systems.
- **Rung 3: Meta-GGA.** Introduces additional semi-local ingredients such as the kinetic energy density $\tau(\mathbf{r})$ and the Laplacian of the density $\nabla^2\rho(\mathbf{r})$.
- **Rung 4: Hybrid Functional.** Mixes semi-local exchange with a fraction of exact Hartree–Fock exchange. Global hybrids apply a fixed mixing ratio, whereas range-separated hybrids use a distance-dependent partitioning of short- and long-range exchange contributions.
- **Rung 5: Double Hybrid.** Enhance hybrid functionals by adding a perturbative correlation term (e.g., MP2-like contributions), achieving higher accuracy at an even increased computational cost.

2.2.2. Density-Functional Tight-Binding

semi-empirical density functional tight binding (DFTB) is a semiempirical method that employs several approximations and a number of element-specific parameters, thereby achieving significant computational efficiency. The approximations include the two-center integral approximation for Hamiltonian matrix elements, the monopole approximation for charge–charge interactions, and the use of a confined minimal atomic basis set. These approximations limit the method's accuracy, particularly for non-covalent interactions, where the monopole treatment underestimates attractive forces, and the minimal basis set underestimates Pauli repulsion and polarizability.[115] The method is 2–3 orders of magnitude faster than DFT, while showing comparable accuracy,[116] which allows for efficient sampling of large systems such as biomolecules.

The DFTB methodology originated from adapting the basic concepts of the tight-binding model in solid-state physics to KS-DFT.[117] Here, the electrons are tightly bound to their atoms, and they interact only weakly with the potentials of neighboring atoms. The electron density is mainly localized near the nuclei, and only a minor portion of the valence electrons contributes to changes in the local electron density. Consequently, the electron density ρ of a molecule can be approximated by constructing a reference density ρ_0 as a superposition of neutral atomic densities ρ_0^a,

$$\rho_0(\mathbf{r}) = \sum_a \rho_0^a(\mathbf{r}). \tag{2.14}$$

To account for the response of the valence electrons to the chemical environment, the density fluctuation $\delta\rho$ refines the approximation,

$$\rho(\mathbf{r}) = \rho_0(\mathbf{r}) + \delta\rho(\mathbf{r}). \tag{2.15}$$

The key concept of DFTB is to use the approximate electron density ρ in the KS scheme. The expression for the total energy of the system in Eq. 2.10 is then expanded around the reference density by a Taylor series up to third order,[116,118]

$$\begin{aligned} E[\rho^0+\delta\rho] &= -\frac{1}{2}\int\frac{\rho^0(\mathbf{r})\rho^0(\mathbf{r}')}{|\mathbf{r}-\mathbf{r}'|}\,d\mathbf{r}\,d\mathbf{r}' - \int V_{XC}[\rho^0]\rho^0(\mathbf{r})\,d\mathbf{r} + E_{XC}[\rho^0] + E_{nn} \\ &+ \sum_i \langle\Psi_i|\hat{H}[\rho^0]|\Psi_i\rangle \\ &+ \frac{1}{2}\int\int\left(\frac{1}{|\mathbf{r}-\mathbf{r}'|} + \frac{\delta^2 E_{XC}[\rho]}{\delta\rho(\mathbf{r})\,\delta\rho(\mathbf{r}')}\bigg|_{\rho^0}\right)\delta\rho(\mathbf{r})\,\delta\rho(\mathbf{r}')\,d\mathbf{r}\,d\mathbf{r}' \\ &+ \frac{1}{6}\int\int\int\frac{\delta^3 E_{XC}[\rho]}{\delta\rho(\mathbf{r})\,\delta\rho(\mathbf{r}')\,\delta\rho(\mathbf{r}'')}\bigg|_{\rho^0}\delta\rho(\mathbf{r})\,\delta\rho(\mathbf{r}')\,\delta\rho(\mathbf{r}'')\,d\mathbf{r}\,d\mathbf{r}'\,d\mathbf{r}'', \end{aligned} \tag{2.16}$$

where the colors indicate the order of the Taylor terms as assigned in Eq. 2.17. Here V_{XC} is the XC potential, E_{XC} the XC energy, and E_{nn} the nuclear repulsion energy. The equation can be rewritten as

$$E[\rho] = E^{(0)}[\rho_0] + E^{(1)}[\rho_0,\delta\rho] + E^{(2)}[\rho_0,(\delta\rho)^2] + E^{(3)}[\rho_0,(\delta\rho)^3]. \tag{2.17}$$

One can distinguish between DFTB1,[119] DFTB2,[120] and DFTB3[116] according to the highest order of the Taylor series included in the model. The second-order terms are essential for accounting for partial charge-transfer processes, and the third-order terms are important for accurately describing charged molecules.[116] DFTB3 with parameter set 3ob is recommended for standard biomolecular applications.[116]

DFTB1. The red terms in Eq. 2.17 depend only on the reference density ρ_0. They contain the interactions involving the core electrons and can be represented as the repulsive potential E_{rep}, which is typically expressed as a sum of pairwise repulsive terms V_{ab}^{rep},

$$E_{\text{rep}} = \frac{1}{2}\sum_{ab} V_{ab}^{\text{rep}}. \tag{2.18}$$

The values of V_{ab}^{rep} are determined from DFT–GGA calculations using the PBE functional. The orange term in Eq. 2.17 is used to construct the Hamiltonian matrix from the KS Hamiltonian $\hat{H}[\rho^0]$ for a hypothetical molecule described by the reference density. The KS operator and orbitals are adapted using the linear combination of atomic orbitals (LCAO) ansatz with an atom-specific minimal basis set for the valence shell to account for the tight-binding approximation.[119] The KS orbitals within the LCAO approach are written as

$$\Psi_i(\mathbf{r}) = \sum_\mu c_{\mu i}\,\phi_\mu(\mathbf{r}) \tag{2.19}$$

where $c_{i\mu}$ are the molecular orbital coefficients in the atomic orbital basis. The total energy is minimized with respect to the orbital coefficients, leading to the corresponding KS equation

$$\sum_{\nu} c_{\nu i}(H^0_{\mu\nu} - \epsilon_i S_{\mu\nu}) = 0, \tag{2.20}$$

with the Hamiltonian matrix element

$$H^0_{\mu\nu} = \langle \phi_\mu | \hat{H}^0 | \phi_\nu \rangle \tag{2.21}$$

and the overlap matrix elements

$$S_{\mu\nu} = \langle \phi_\mu | \phi_\nu \rangle . \tag{2.22}$$

The total energy for DFTB1 is then given by

$$E^{\mathrm{DFTB1}} = \frac{1}{2}\sum_{ab} V^{\mathrm{rep}}_{ab} + \sum_i \sum_{\mu\nu} n_i \, c_{\mu i} c_{\nu i} H^0_{\mu\nu} \tag{2.23}$$

where n_i are the occupation numbers of the KS orbitals. Precalculated values of $S_{\mu\nu}$ and $H^0_{\mu\nu}$ are stored in tables and read during runtime. In DFTB1, the KS equations are solved only once. Therefore, DFTB1 is about 5–10 times faster than DFTB2 and DFTB3 because a self-consistent solution of the eigenvalue problem is required in the latter methods.[119,121]

DFTB2. In the second-order term (blue in Eq. 2.16), the density fluctuations are constructed as a superposition of atomic contributions

$$\delta\rho(\mathbf{r}) = \sum_a \delta\rho_a(\mathbf{r}). \tag{2.24}$$

The atomic-like density fluctuations are approximated by

$$\delta\rho_a(\mathbf{r}) \approx \Delta q_a \frac{\tau_a}{8\pi} e^{-\tau_a |\mathbf{r}-\mathbf{R}_a|}, \tag{2.25}$$

in the monopole approximation.[120] The fluctuating charges Δq_a are calculated from the partial charges q_a and the parameters τ_a are chosen such that the function γ_{ab} adequately reproduces the atomic chemical hardness. This leads to an analytical function γ that solves the Coulomb interaction between spherical atomic density contributions analytically. The partial charges Δq_a are derived by subtracting the Mulliken charges

$$q_a = \sum_i n_i \sum_{\mu\in a} \sum_{\nu} c_{\mu i} \, c_{\nu i} \, S_{\mu\nu}, \tag{2.26}$$

$$\Delta q_a = q_a - q^0_a, \tag{2.27}$$

from the reference atomic charges. The matrix elements must be calculated in a modified form

$$H_{\mu\nu} = \langle\varphi_\mu|\hat{H}_0|\varphi_\nu\rangle + \frac{1}{2}S_{\mu\nu}\sum_{c=1}^{N}(\gamma_{ac}+\gamma_{bc})\,\Delta q_c = H^0_{\mu\nu} + H^{DFTB2}_{\mu\nu}, \tag{2.28}$$

and the solution is obtained iteratively, which is referred to as self-consistent charge (SCC). The total energy is written as

$$E^{\mathrm{DFTB2}} = \frac{1}{2}\sum_{ab}V^{\mathrm{rep}}_{ab} + \sum_i\sum_{\mu\nu} n_i\, c_{\mu i}c_{\nu i}H^0_{\mu\nu} + \frac{1}{2}\sum_{ab}\Delta q_a\Delta q_b\gamma_{ab} \tag{2.29}$$

DFTB3. The third-order term (green in Eqn. 2.16) incorporates a new parameter that describes the chemical hardness derivative U^d_a.[122] This results in a new function Γ_{ab} as the derivative of the γ-function with respect to charge and is used to refine the charge dependencies of the model. Again, the matrix elements must be calculated in a modified form

$$H_{\mu\nu} = H^0_{\mu\nu} + S_{\mu\nu}\sum_c \Delta q_c\left(\frac{1}{2}(\gamma_{ac}+\gamma_{bc}) + \frac{1}{3}(\Delta q_a\Gamma_{ac}+\Delta q_b\Gamma_{bc}) + \frac{\Delta q_c}{6}(\Gamma_{ca}+\Gamma_{cb})\right), \tag{2.30}$$

and solved as SCC. The Hamilton matrix elements depend on the Mulliken charges, which are dependent on the molecular orbital coefficients $c_{\mu i}$. The total energy of the DFTB3 model can be written as

$$E^{\mathrm{DFTB3}} = \frac{1}{2}\sum_{ab}V^{\mathrm{rep}}_{ab} + \sum_i\sum_{\mu\nu} n_i\, c_{\mu i}c_{\nu i}H^0_{\mu\nu} + \frac{1}{2}\sum_{ab}\Delta q_a\Delta q_b\gamma_{ab} + \frac{1}{3}\sum_{ab}\Delta q_a^2\Delta q_b\Gamma_{ab}. \tag{2.31}$$

With the 3ob parameter set, DFTB3 achieves accuracy suitable for biochemical applications while remaining approximately two to three orders of magnitude faster than standard DFT.[123–126] This balance of cost and accuracy makes it an effective choice for large-scale simulations of chemically reactive processes in complex molecular environments. Extensive sampling is essential for characterizing biomolecular dynamics.[127] Semi-empirical QM methods are therefore well suited for quantum mechanics/molecular mechanics (QM/MM) simulations because they maintain reasonable accuracy without incurring prohibitive computational cost.[32,128] In this dissertation, DFTB serves as the method of choice for the QM region,[129] enabling long-timescale QM/MM simulations that can reach the nanosecond timescales.[130–135]

2.3. Hybrid QM/MM Approach

QM/MM simulations offer an efficient alternative to treating an entire system at the quantum-chemical level. The method was first introduced in 1976 by Warshel and Levitt[34] in a seminal study, and its significance was later acknowledged by the 2013 Nobel Prize in Chemistry. These simulations aim to retain the accuracy of a quantum chemical description in relevant regions while

leveraging the lower computational demands of classical molecular mechanics. In this approach, the system is partitioned into a QM region and an MM region, as shown in Figure 2.1. The MM region contains atoms that are sufficiently represented by classical force fields, whereas the QM region includes atoms whose behavior requires an explicit electronic description. Phenomena that involve substantial changes in electronic structure, such as charge transfer, electronic excitation, or chemical reactivity, cannot be captured accurately within a purely classical framework. For this reason, the atoms participating directly in these processes are assigned to the QM part of the system. The QM region is selected to be small enough to ensure manageable computational cost and large enough to capture the essential chemistry of interest.[136,137]

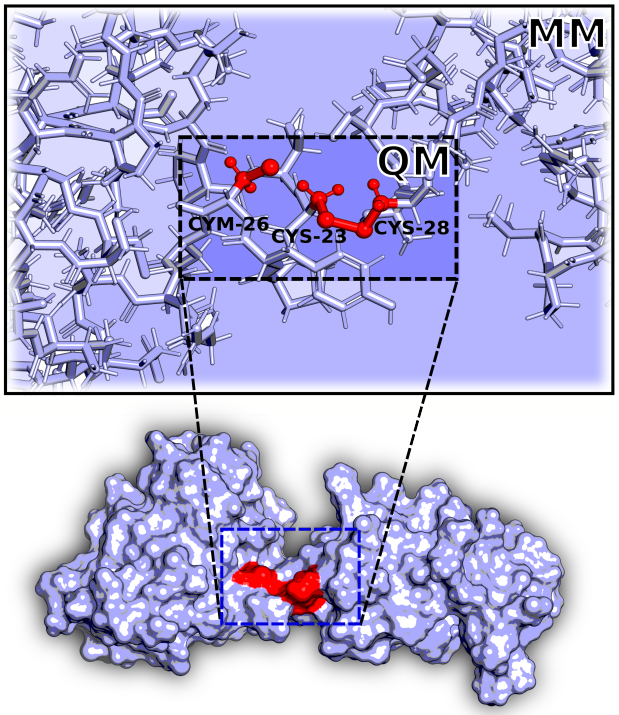

Figure 2.1.: QM/MM partitioning in a protein. The protein is shown with the reactive residues highlighted in red. The QM subsystem comprises three residues (CYS-23, CYS-28, and Cym-26) that participate in the thiol–disulfide exchange (TDE) reaction. This QM region interacts with the surrounding MM environment, with the form of the QM–MM coupling determined by the chosen interface treatment.

In the additive QM/MM framework, the total energy of the system is expressed as the sum of the QM contribution E_{QM}, the MM contribution E_{MM}, and the interactions between the two subsystems $E_{\mathrm{QM/MM}}$,

$$E_{\mathrm{total}} = E_{\mathrm{QM}} + E_{\mathrm{MM}} + E_{\mathrm{QM/MM}}. \tag{2.32}$$

The QM/MM interaction term comprises three components

$$E_{\mathrm{QM/MM}} = E^{\mathrm{elec}}_{\mathrm{QM/MM}} + E^{\mathrm{vdW}}_{\mathrm{QM/MM}} + E^{\mathrm{bonded}}_{\mathrm{QM/MM}}. \tag{2.33}$$

Here, $E^{\text{elec}}_{\text{QM/MM}}$ denotes the electrostatic interactions between QM and MM subsystem, $E^{\text{vdW}}_{\text{QM/MM}}$ represents their van der Waals interactions, and $E^{\text{bonded}}_{\text{QM/MM}}$ describes interactions across covalent linkages that connect the two subsystems. The Quality of description of these contributions can significantly affect the overall accuracy of a QM/MM calculation. A careful and appropriate treatment of the QM–MM boundary is therefore essential, as discussed in the following.[136,137]

Bonded Interaction. When covalent bonds cross the QM–MM interface, specific complications arise because the QM region cannot terminate abruptly at a bonded atom.[35,138,139] A naive partitioning would leave the QM subsystem with an unsatisfied valence and distort the electronic structure at the boundary. To address this, several strategies have been developed for a consistent treatment of boundary-spanning bonds. The most common approach employs a link atom, typically hydrogen, together with a redistribution of MM charges.[140] Variants such as double–link and tuned–link atoms seek to refine the description of the cut bond. More advanced alternatives include local self-consistent field methods, pseudo-bond approaches, frozen-orbital and generalized hybrid-orbital formulations, and Yin–Yang atom schemes, each designed to preserve a chemically consistent electronic environment across the QM–MM boundary.[38]

Short-Range Interactions. The van der Waals interactions act over short distances, so they mainly affect regions in which QM and MM atoms are in close proximity. These interactions are usually treated with classical force-field parameters as in Eq. 2.3. In this approach, Lennard–Jones parameters are assigned to the QM atoms, and the corresponding interactions are evaluated using the MM force field.[139] However, this treatment can introduce non-negligible errors. At short intermolecular separations, the original force-field parameterization may no longer be reliable, leading to progressively less accurate interaction energies. A more rigorous approach is to reparameterize the relevant van der Waals terms specifically for QM/MM applications, ensuring that they remain valid in the chemical environment surrounding the QM region.[138,141]

Long-Range Interactions. There are several schemes that can be used to couple the electrostatic components of the QM/MM model and to calculate $E^{\text{elec}}_{\text{QM/MM}}$.

Mechanical Embedding. The simplest coupling scheme is mechanical embedding. In this approach, the electrostatic interactions between the QM and MM subsystems are evaluated entirely at the MM level using atom-centered point charges for all atoms. The QM–MM interactions are therefore represented as classical Coulomb interactions using the FF, as in Eq. 2.3. A notable limitation of this scheme is that it neglects any polarization of the QM subsystem by the MM environment. As a result, mechanical embedding cannot account for the modification of the QM electronic structure induced by the surrounding classical region.[139]

Electrostatic Embedding. In contrast, electrostatic embedding includes the polarization effect of the MM on the QM subsystem. The QM Hamiltonian incorporates one-electron operators for these interactions

$$H^{\text{Total}} = H^{\text{QM}} - \sum_{i=1}^{N}\sum_{j=1}^{M} \frac{e^2 Q_j}{4\pi\epsilon_0 |\mathbf{r}_i - \mathbf{R}_j|}, \tag{2.34}$$

where $\mathbf{r}_i$ and $\mathbf{R}_j$ denote the positions of electron i and MM atom j, respectively. H^{QM} represents the unmodified Hamiltonian operator acting on the QM region. The QM zone contains N electrons, while M MM atoms carry point charges Q_j.[139] Thus, MM charges directly affect the charge distribution in the QM part through polarization. However, MM charges remain fixed point charges and therefore cannot be polarized by the QM electron density. Improvements to the MM charge density can be achieved by smearing the point charges into a Gaussian distribution[142,143] or by employing Gaussian electrostatic models,[144] which adapt the charge-fitting procedure to parameterize Gaussian charge distributions directly. For DFTB3 as a QM method, electrostatic embedding with point charges modifies the charge-dependent matrix elements in Eq. 2.30 by adding the term

$$H_{\mu\nu}^{\mathrm{QM/MM}} = S_{\mu\nu} \cdot \frac{1}{2} \left(\Phi_a + \Phi_b \right). \tag{2.35}$$

It can be calculated from

$$\Phi_a = \sum_{A \in \mathrm{MM}} \frac{Q_A}{|\mathbf{R}_A - \mathbf{r}_a|}, \tag{2.36}$$

which is the electrostatic potential generated by all MM charges.[145]

Polarizable Embedding. Polarization embedding enables the MM region to become polarized in response to the QM electron density. This can be achieved by employing polarizable FFs, based on Drude oscillators, fluctuating charges, or induced point dipoles.[146] For induced–dipole models, the electrostatic QM/MM interaction term $E_{\mathrm{QM/MM}}^{\mathrm{elec}}$ is extended by two additional contributions,

$$E_{\mathrm{QM/MM}}^{\mathrm{pol}} = \frac{1}{2} \sum_i \left(\alpha_i^{-1} \mu_i^2 + \sum_{j \neq i} \mu_i \mathcal{T}_{ij} \mu_j \right) - \sum_i \mu_i \left(E_i^{\mathrm{MM}} + E_i^{\mathrm{QM}} \right), \tag{2.37}$$

which reflects the self-energy of the induced dipoles and their dipole–dipole interactions. Here, μ_i is the induced dipole on atom i, α_i is the corresponding polarizability, and $\mathcal{T}_{ij}$ denotes the effective dipole–field interaction tensor.[146] This introduces a mutual dependence between the QM electron density and the induced dipoles of the MM environment. This coupling represents a major advantage of polarizable embedding, as the classical environment can dynamically respond to changes in the QM region. At the same time, it introduces a nonlinear QM/MM interaction that requires the self-consistent field (SCF) and induced–dipole equations to be solved iteratively to achieve a self-consistent description of the combined system.[146]

Adaptive Embedding. The choice of QM region size remains a critical determinant of accuracy and efficiency in QM/MM simulations. Larger QM regions may be required when the reaction involves pronounced charge transfer (CT) or environmental polarization effects extend beyond the immediate active site. Recent developments in adaptive QM/MM schemes[147–156] aim to address this challenge by dynamically adjusting the QM region in response to changes in the chemical environment.

3. Molecular Dynamics Simulations

Molecular dynamics (MD) simulations sample the phase space defined by a chosen interaction model and its Hamiltonian. The resulting data points are time-correlated configurations obtained by numerically integrating the equations of motion. If the space of molecular configurations are sampled sufficiently well, the underlying partition function $Q_R(\xi)$, where ξ is a coordinate in the reduced phase space (typically called the reaction coordinate), can be estimated from the resulting distribution. $Q_R(\xi)$ is of interest because (1) it determines key thermodynamic quantities and (2) its direct calculation via phase-space integration is infeasible for complex systems.[96]

In statistical mechanics, $Q_R(\xi)$ for a classical continuous system is given by

$$Q_R(\xi) = \frac{\int \delta\Big(\xi(\mathbf{q}) - \xi\Big) \exp\Big(-\beta H(\mathbf{q},\mathbf{p})\Big)\, d^3q_1 \cdots d^3q_N\, d^3p_1 \cdots d^3p_N}{\int \exp\Big(-\beta H(\mathbf{q},\mathbf{p})\Big)\, d^3q_1 \cdots d^3q_N\, d^3p_1 \cdots d^3p_N}, \tag{3.1}$$

where N is the number of particles, h is Planck's constant, δ is the Dirac delta function, $\beta = 1/(k_\mathrm{B}T)$, and $H(\mathbf{q},\mathbf{p})$ denotes the Hamiltonian as a function of all particle positions $\mathbf{q}$ and momenta $\mathbf{p}$. The phase-space volume elements d^3q_i and d^3p_i integrate over the Cartesian components of position and momentum, respectively. This defines the free energy

$$F(\xi) = -k_\mathrm{B}T \ln Q_R^{NVT}(\xi), \tag{3.2}$$

and the free enthalpy

$$G(\xi) = -k_\mathrm{B}T \ln Q_R^{NPT}(\xi), \tag{3.3}$$

of the reduced space defined by ξ. Both quantities are referred to as potentials of mean force, to distinguish them from the free energy expression derived directly from the unrestricted partition function.[157,158]

If the trajectory generated by the MD simulations eventually visits all relevant states regardless of the initial condition, Birkhoff's ergodic theorem[159] implies

$$Q_R(\xi) = \lim_{T\to\infty} \frac{1}{T} \int_0^T \delta\Big(\xi[t] - \xi\Big)\, dt. \tag{3.4}$$

It expresses the equivalence between the ensemble average over all microstates in Eq. 3.1 and the time average obtained from a sufficiently long trajectory. As a consequence, $Q_R(\xi)$ can be estimated from the distribution of ξ obtained from the MD data, for example by histogramming or

by related density-estimation techniques. However, sufficient sampling is a critical and nontrivial requirement, as further discussed in Section 4 Enhanced Sampling.

Molecular dynamics simulations rely on a collection of algorithms that enable stable and efficient calculations. For an in-depth overview of the underlying principles, the reader is referred to Refs. [157, 158, 160]. The simulation workflow, which is an essential aspect of practical MD simulations, is well summarized in Refs. [30, 161]. The following sections focus on central methodological components. Specifically, Section 3.1 introduces the numerical integrator used to solve the equations of motion, and Section 3.1.1 discusses the algorithms used to generate non-standard ensembles that are essential in many applications.

3.1. Finite Difference Methods

MD simulations sample the phase space of a model system by explicitly integrating its equations of motion. Once a potential energy function has been defined (Section 2), the forces acting on each particle follow directly from the gradient of the energy function. For a force field (FF), the force acting on the i-th particle is given by

$$\mathbf{F}_i = -\nabla_i V_{\mathrm{FF}}(\mathbf{r}_1, \ldots, \mathbf{r}_n), \tag{3.5}$$

where $\mathbf{r}_i$ denotes the particle coordinates. A system of N particles obeys Newton's second law of motion

$$\mathbf{F}_i = m_i \mathbf{a}_i = m_i \frac{d^2 \mathbf{r}_i}{dt^2}, \tag{3.6}$$

a relation that provides $3N$ linear second-order differential equations that cannot be solved analytically for complex systems. Instead, numerical integration is used to propagate forward in time and thereby generate trajectories. A variety of algorithms, collectively referred to as integrators, are available to perform this task with differing levels of accuracy, stability, and energy conservation.[162] A well-behaved integrator is one that yields a set of trajectories that approximates the exact analytical solution within the limits of the system's correlation time for the property of interest.[162,163]

Integrators propagate the system through discrete time steps. Starting from the positions $\mathbf{r}_i$, velocities $\mathbf{v}_i$, and accelerations $\mathbf{a}_i$ of all atoms at time t, the dynamics are obtained by iteratively jumping to the next time point $t + \Delta t$ using information from the previous step or steps. The Verlet integrator[164]

$$\mathbf{r}(t + \Delta t) = 2\,\mathbf{r}(t) - \mathbf{r}(t - \Delta t) + \Delta t^2\,\mathbf{a}(t) \tag{3.7}$$

can be derived by summation of the Taylor expansions of the atom position in the forward and backward time directions

$$\mathbf{r}(t+\Delta t) = \mathbf{r}(t) + \Delta t\,\mathbf{v}(t) + \tfrac{1}{2}\Delta t^2\,\mathbf{a}(t) \tag{3.8}$$

$$\mathbf{r}(t-\Delta t) = \mathbf{r}(t) - \Delta t\,\mathbf{v}(t) + \tfrac{1}{2}\Delta t^2\,\mathbf{a}(t). \tag{3.9}$$

An adaptation, the velocity Verlet integrator,

$$\mathbf{r}_{i+1} = \mathbf{r}_i + \mathbf{v}_i\,\Delta t + \tfrac{1}{2}\,\mathbf{a}_i\,\Delta t^2 \tag{3.10}$$

$$\mathbf{v}_{i+1} = \mathbf{v}_i + \tfrac{1}{2}\,(\mathbf{a}_i + \mathbf{a}_{i+1})\,\Delta t, \tag{3.11}$$

renders the algorithm more stable and conceptually more physically grounded, which in turn facilitates extensions such as coupling to an external heat bath.[157,163] Acceleration is calculated from $\mathbf{a}_i = -\nabla_i V_{\mathrm{FF}}(\mathbf{r}_1,\ldots,\mathbf{r}_n)/m_i$. Initial velocities $\mathbf{v}_i$ are drawn from the Maxwell–Boltzmann distribution at the reference temperature using Box–Muller–generated random numbers.[157] The native ensemble generated by these integrators is the constant energy isochoric ensemble (NVE), characterized by constant particle number, volume, and energy. Algorithms that control temperature and pressure to generate the isothermal-isochoric ensemble (NVT) and isothermal-isobaric ensemble (NPT) ensembles, respectively, are discussed in the next section.

Critical factors for integration efficiency are (1) the computational cost of evaluating the forces $\mathbf{F}_i = -\nabla V_{\mathrm{FF}}(\mathbf{r}_1,\ldots,\mathbf{r}_n)$ and (2) the size of the time step Δt. The first factor can be optimized by avoiding a full force evaluation at every time step. Instead, the integrator can be advanced for several steps using an approximate $\mathbf{a}_i$, after which the forces are recalculated to correct the trajectory. This class of schemes is known as predictor–corrector methods.[163] Additional cost reductions arise from using cutoff functions to limit the evaluation of short-range nonbonded interactions, Ewald-based mesh methods for efficient treatment of long-range electrostatics,[165] and neighbor lists that buffer the set of interacting particle pairs over multiple time steps, thereby avoiding a full pair search at every step.[166]

Optimization of (2), the time step, can be achieved by removing fast vibrational components through the introduction of constraints. On short timescales, typically around 10 fs, high-frequency H-bond vibrations behave as approximately harmonic and are irrelevant for many observables. However, they limit the numerical stability of the integrator and restrict the time step to about 1 fs. These modes can be eliminated by holonomic constraints introduced through the Lagrange formalism, for example by fixing H-bond lengths at their equilibrium values. For three-point water models, the modified equations of motion can be solved analytically using the SETTLE algorithm.[167] For general molecular systems, however, the constraint equations must be solved numerically, requiring an additional correction step after each unconstrained integration update. Common algorithms include SHAKE,[168] RATTLE, and LINCS.[169] These constraints allow the time step to be increased to approximately 2 fs, and can be extended further to 4 fs by also constraining hydrogen bond angles.[170]

3.1.1. Constant Temperature and Constant Pressure Ensembles

Additional algorithms have been developed to regulate temperature and pressure, referred to as thermostats and barostats, respectively. These methods are essential for establishing the NVT and NPT, which generate thermodynamic ensembles encountered in experimental settings. These ensembles require algorithms that modify the equations of motion to regulate temperature or pressure.[158] The following section outlines the basic idea, while Ref. [161] provides an overview of commonly used algorithms.

Thermostats. A thermostat couples the system to an external heat bath and ensures that the temperature

$$T = \frac{2}{(3N - N_{\text{constr.}})\, k_{\text{B}}} \mathbb{E}[E_{\text{kin}}(\mathbf{v})], \tag{3.12}$$

with $N_{\text{constr.}}$ constraints in the system, fluctuates around a target value T_0. The Berendsen thermostat[171] imposes weak first-order relaxation toward the reference temperature T_0,

$$\frac{dT}{dt} = \frac{T_0 - T}{\tau_T}, \tag{3.13}$$

which yields the velocity–rescaling factor

$$\lambda = \sqrt{1 + \frac{\Delta t}{\tau_T}\left(\frac{T_0}{T} - 1\right)}. \tag{3.14}$$

Applied uniformly to all particle velocities, λ drives the system smoothly and asymptotically toward T_0. Its value is determined by the instantaneous deviation of T from the target temperature and by the coupling constant τ_T, which controls the rate of thermal relaxation. This method provides efficient temperature control but does not generate the canonical ensemble. Nosé–Hoover[172] dynamics extends the phase space by an additional variable that regulates kinetic energy. This emulates coupling to an external heat bath and rigorously generates a canonical ensemble.

Barostats. The Berendsen barostat[171] regulates the system pressure P by scaling the simulation cell volume toward a target pressure P_0. The scaling factor is

$$\mu = \sqrt[3]{1 - \kappa \frac{\Delta t}{\tau} (P - P_0)}, \tag{3.15}$$

where κ denotes the isothermal compressibility and τ is the pressure-coupling time constant. This scheme provides smooth and efficient pressure relaxation, although it does not rigorously generate the NPT ensemble. In contrast, the Parrinello–Rahman barostat[173] employs an extended-Lagrangian description of the simulation cell, and when combined with a Nosé–Hoover thermostat, it yields samples rigorously drawn from the NPT ensemble.[157]

4. Enhanced Sampling

The use of sampling methods to estimate average values is very widespread in numerical mathematics and computational physics. A historical illustration is Buffon's needle experiment[174], which demonstrates how random sampling can be used to approximate π. Analogously, random samples (with replacement) can be used to estimate the ratio of the area of an inscribed circle to that of its enclosing square. Figure 4.1 illustrates how such sampling provides accurate estimates in low dimensions but loses efficiency as dimensionality increases. Improvements are achieved by increasing the number of samples, although increasing the number of samples comes at a higher computational cost. This challenge, often referred to as the sampling problem, motivates the development of more systematic and efficient sampling strategies.[175]

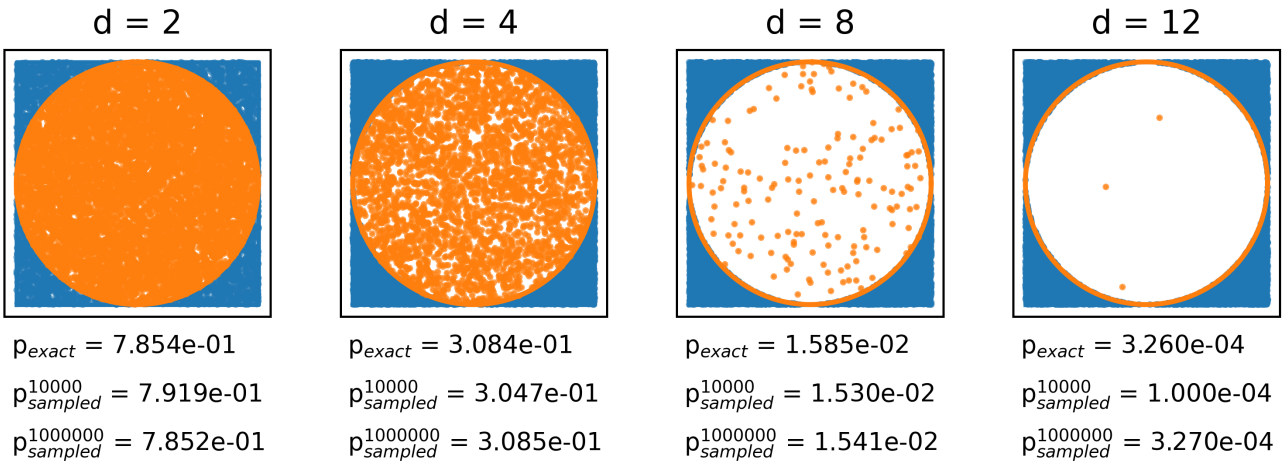

Figure 4.1.: Estimation of the volume ratio between a d-dimensional hypersphere and its enclosing hypercube by random sampling. For each dimension, orange points indicate sampled configurations that fall inside the hypersphere, while blue points lie outside. The exact analytical ratio p_{exact} is shown together with numerical estimates obtained using 10^4 and 10^6 uniformly drawn random samples. In low dimensions, a substantial fraction of the samples fall inside the sphere, producing accurate estimates. As the dimension increases, sampled points inside the hypersphere become undersampled. Achieving an accurate estimate requires more than two orders of magnitude more samples to obtain a sufficient number of interior points, which greatly increases the computational cost.

When trying to estimate ensemble averages of molecular systems, MD simulations provide an efficient way to sample. Instead of drawing samples from an independent random distribution, they systematically generate configurations from the Boltzmann distribution defined by the potential energy function (Section 2). This focuses the sampling to the most relevant regions of phase

space, such as local minima and the surrounding low-energy configurations, while energetically unfavorable, nonphysical structures are avoided.[176]

However, important regions can still remain undersampled if high barriers hamper exploration.[177] When the system approaches such a barrier, gradients in the potential energy oppose the motion toward the barrier and drive the system back. The average kinetic energy per degree of freedom is $k_\mathrm{B}T/2$, which implies that crossing a barrier becomes increasingly unlikely as its height grows, especially when it is significantly larger than $k_\mathrm{B}T$.[176] Sufficient sampling of all relevant regions is therefore not guaranteed. For example, if a protein undergoes a conformational change, it must first overcome a high free energy barrier, making the event rare. Proteins may spend a very long time in one metastable state before transitioning to another, due to high free energy barriers or entropic bottlenecks.[178] Such incomplete sampling exhibits quasi-nonergodic behavior, indicating that ergodicity (Eq. 3.4) could in principle be achieved only by extending the simulation time to an unknown and likely impractically long duration. This obstacle is commonly known as the timescale problem.

Enhanced sampling[179,180] methods address the timescale problem by improving sampling efficiency without requiring impractically long simulation times. In principle, sampling can be accelerated by the following strategies. (1) Modifying the dynamics, while keeping the potential energy surface unchanged, to enhance motion along slow degrees of freedom. (2) Deforming the free energy landscape to increase the likelihood of barrier crossing. (3) Extending the dimensionality of the phase space to bypass such barriers. (4) Perturbing the forces to promote broader configurational exploration. (5) Reducing the number of degrees of freedom through an appropriate coarse-graining. (6) Employing multi-copy or replica-based strategies.[176] Within this spectrum of approaches, methods based on collective variables (CVs) and bias potentials are widely used. Examples include metadynamics (MTD)[181–184], umbrella sampling[185–187], adaptive biasing force[188], and variationally enhanced sampling[189]. The following sections concentrate on this class of CV-based methods. The underlying concepts of CVs and bias potentials will be introduced in Sections 4.1 and 4.2.

4.1. Collective Variables

If states are undersampled due to high barriers, resulting in imprecise estimates from Eq. 3.1, enhanced sampling methods can be applied to bias the system along selected collective variables (CVs) toward the relevant states.[179,180] The mechanism by which such a bias is applied, and its influence on the dynamics and sampling, will be explained in Section 4.2. For now, the definition of a CV is introduced and its properties are discussed. In principle, a CV is a d-dimensional[177] function of the $3N$ coordinates $\mathbf{q}$ of the system

$$\mathbf{CV}(\mathbf{q}) = \Big(S_1(\mathbf{q}), \ldots, S_d(\mathbf{q})\Big). \tag{4.1}$$

For clarity, the CV used in enhanced sampling does not need to be identical to the coordinate $\xi(\mathbf{q})$ used for evaluation. Strictly speaking, these two roles of biasing and evaluation can differ. This distinction is often ignored in practice and the terms CV and reaction coordinate are used interchangeably. For example, studies of protein folding often examine the system on a two-dimensional free-energy surface (FES) constructed from the radius of gyration and the root-mean-square deviation (RMSD). However, the CV used for biasing can differ from the coordinates employed for analysis.

CVs may be defined from geometric constructions such as distances, angles, coordination numbers, or RMSD. More abstract CVs can involve functional forms that offer little intuitive interpretation. [190] The design of such abstract CVs is an active area of research, often relying on machine-learning techniques. Section 5.2 Machine Learning for Enhanced Sampling will discuss this option in more detail.

To be suitable for enhanced sampling, a CV should satisfy the following properties. (1) The CV must take distinguishable values for the initial, metastable, transition, and final states. Its predictive power increases when it resolves the correct number of states and captures their connectivity accurately. Otherwise, projection errors[191] can severely impair sampling, as illustrated in Figure 4.2.[177] (2) The CV must incorporate the slowest relevant motion involved in the process. Otherwise, a significant free energy barrier remains unbiased and continues to hinder sampling.[177] (3) A CV is preferable if it provides a low-dimensional reduction of the system, has components that are approximately orthogonal, and exhibits minimal degeneracy. In this case, the effective phase space becomes more compact and can be sampled more efficiently.[192] (4) A CV is preferable when it can be infered from the system's dynamics, and (5) a CV is preferable if it is maximally predictive of the system's future evolution.[192]

4.2. Importance Sampling Based on Bias and Collective Variables

In CV-based sampling, the system dynamics are biased to promote exploration of undersampled regions. This is achieved by adding a bias potential V_{bias} to the potential energy (PE),

$$V_{\text{eff}} = V_{\text{PE}} + V_{\text{bias}}, \tag{4.2}$$

to form an effective potential V_{eff} for the system. This modification leads to an additional bias force,

$$\mathbf{F}_{\text{bias}} = -\frac{\partial V_{\text{bias}}}{\partial CV}\frac{\partial CV}{\partial \mathbf{q}}, \tag{4.3}$$

acting on the coordinates from which the collective variables (CVs) are constructed. The resulting dynamics follow a modified, non-Boltzmann distribution that enables the system to cross higher free energy barriers and access relevant states more efficiently. The bias potential can be applied in different ways. For example, umbrella sampling uses a stratification of static bias potentials

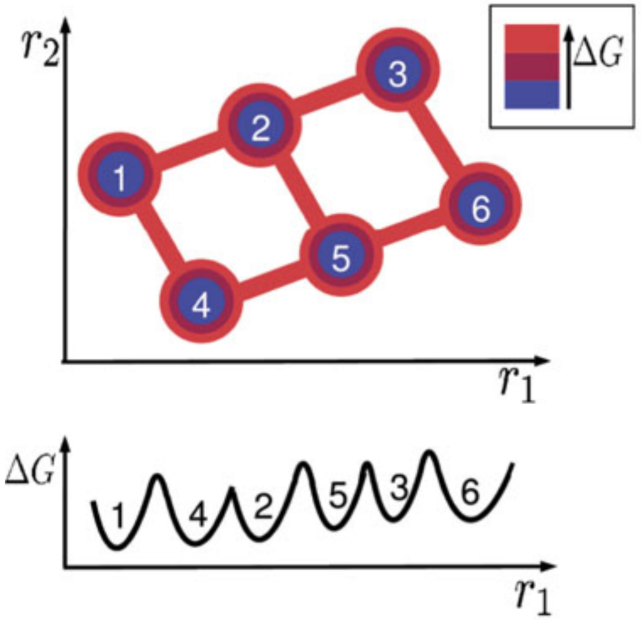

Figure 4.2.: Schematic illustration of projection errors arising from an inadequate choice of CVs. **Top** A 2D setup using two CVs distinguishes all states with correct connectivity. **Bottom** A 1D setup using a single CV reproduces the correct number of minima but fails to resolve the connectivity, thereby projecting distinct pathways into a single coordinate. For example, states 2 and 4 are not connected in the underlying 2D landscape, but the 1D projection suggests a pathway between them. Such projection errors occur when a CV does not capture the correct state topology, and they can severely hamper sampling. Reproduced with permission from Alexandros Altis et al. "Construction of the free energy landscape of biomolecules via dihedral angle principal component analysis". In: *The Journal of Chemical Physics* 128.24 (June 2008), p. 245102.

applied in multiple independent replica simulations, whereas metadynamics (MTD) constructs a time-dependent bias that can be shared across parallel replicas. The following section illustrates the core principles of the bias potential in MTD.

4.2.1. Metadynamics

To improve sampling efficiency, Parrinello and co-workers introduced MTD.[181] The central idea is to incorporate a form of local memory into the simulation, such that the system is discouraged from revisiting regions of phase space it has already explored. It was designed to overcome the time-scale problem by frequently adding a bias potential during the simulation. As a result, the bias pushes the system over free energy barriers and promotes exploration of new areas of the free-energy surface (FES). The bias potential V_{bias} builds up over the course of the simulation, and once the bias has converged, the underlying FES can be reconstructed from the accumulated V_{bias}.

Standard Metadynamics. The standard MTD method continuously builds up a bias potential during the course of a simulation. At regular time intervals τ_G, Gaussian functions are instantaneously added to the PE at the most recent point in CV space, defined by the current value of

the CV. Consequently, the deposited Gaussian functions accumulate to form a time-dependent bias potential

$$V_{\text{bias}}(\mathbf{CV}, t) = \sum_{i=1}^{\lfloor t/\tau_G \rfloor} W_G \prod_{k=1}^{N_{\text{CV}}} \exp\left[-\frac{(CV_k - CV_k(t_i))^2}{2\sigma_k^2} \right]. \tag{4.4}$$

Here, W_G is the constant Gaussian height, $CV_k(t_i)$ is the CV value at the deposition time t_i, σ_k is the Gaussian width associated with the k-th CV, and t is the current simulation time. The quantity N_{CV} denotes the dimensionality of CVs included, which specifies the dimensionality of the MTD setup. When running a simulation, the parameters W_G, σ_k, and τ_G must be specified beforehand. The amount of bias added per unit time is determined by the deposition rate $\omega = W_G/\tau_G$. The higher the deposition rate, the faster the MTD will progress. However, it is important to allow the system sufficient time to relax and respond to the added bias. A typical choice for W_G is on the order of $k_{\text{B}}T/2$. The parameter τ_G depends on the typical autocorrelation time of the CV.[182] The width σ_k needs to be set for each CV and should be small enough to resolve all relevant features of the landscape. The operating principle of MTD is often paraphrased as "filling the free energy wells with computational sand". Figure 4.3 illustrates the accumulation of bias potential as the simulation progresses in a one-dimensional MTD simulation.

Interestingly, MTD also generates an estimate of the underlying FES. As shown in Figure 4.3, as soon as the simulation reaches convergence, the sum of all deposited Gaussians reconstructs a negative image of the underlying FES.

However, in standard MTD, the leveling of the landscape is difficult to achieve due to the large height of the continuously added Gaussians. The resulting FES estimate carries larger uncertainties and exhibits fluctuations. This limitation can be addressed by reducing the effective Gaussian height as the bias builds up. This is achieved in well-tempered MTD, a method that will be introduced next.

Well-Tempered Metadynamics. Incorporates a modification that improves convergence and suppresses sampling of nonphysical high free energy states by limiting the maximal accumulable bias.[177,183] In well-tempered MTD, the Gaussian height is scaled down as the bias potential increases. The constant value W_G in Eq. 4.4 is replaced by a time-dependent height of the Gaussians,

$$G(\mathbf{CV}, t) = W_G \exp\left[-\frac{V_{\text{bias}}(\mathbf{CV}, t)}{k_{\text{B}}\Delta T} \right], \tag{4.5}$$

where W_G is the initial Gaussian height, ΔT is a parameter with dimensions of temperature, and V_{bias} is the bias potential evaluated at the same point where the Gaussian is centered. Consequently, the Gaussian height is smaller in regions where a high bias potential has already been deposited. With this rescaling of the Gaussian height, the bias potential smoothly converges in the long-time limit, and the FES can be estimated more accurately as the sum of the bias added as Gaussians

$$\lim_{t\to\infty} V_{\text{bias}}(\mathbf{CV}, t) = -\frac{\Delta T}{T + \Delta T} F(\mathbf{CV}) + C. \tag{4.6}$$

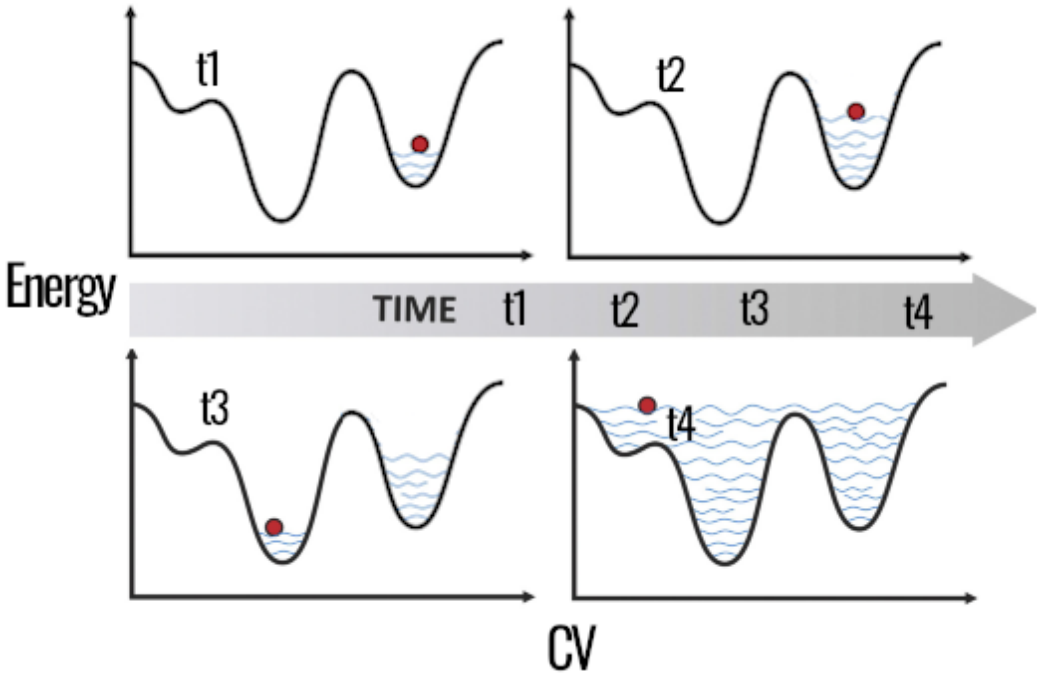

Figure 4.3.: Accumulation of time-dependent bias potential in MTD. This example illustrates the one-dimensional case. The FES of the unbiased system is indicated by the black line, forming a characteristic landscape. At the beginning, the system is trapped in a deep metastable basin, indicated by the red ball at time t_1. The MTD simulation has already started to add a bias potential to the FES, as shown by the blue wavy lines. As the simulation progresses to time t_2, the added potential increasingly compensates for the well of this metastable state. The basin becomes "filled", discouraging revisits to previously sampled CV configurations. Consequently, the likelihood of transitions to other states increases. At time t_3, the system has reached another basin. As the simulation continues, transitions between states occur more frequently. Finally, at time t_4, the bias potential effectively compensates for the features of the landscape, which becomes nearly flattened. At this stage, the states of the system are sampled more uniformly, regardless of the initial basin depths. Reproduced with permission from Rafael C. Bernardi, Marcelo C.R. Melo, and Klaus Schulten. "Enhanced Sampling Techniques in Molecular Dynamics Simulations of Biological Systems". In: *Biochimica et Biophysica Acta (BBA) - General Subjects* 1850.5 (2015-05), pp. 872–877.

The parameter ΔT controls the magnitude of smoothing and is often expressed in terms of the bias factor,

$$\gamma = \frac{T + \Delta T}{T}. \tag{4.7}$$

As a consequence of this formulation, the CVs are explored at an effective temperature of $T + \Delta T$. For $\gamma \to \infty$, standard MTD is recovered. For $\gamma = 1$, unbiased sampling is recovered.

5. Machine Learning for Molecular Dynamics Simulations

Machine learning (ML) is rapidly transforming natural sciences by providing effective solutions where conventional approaches fail or become computationally prohibitive. In molecular dynamics (MD) simulations, its application has progressed primarily along two directions. One is the construction of collective variables (CVs) for enhanced sampling.[195–197] The other is the development of machine-learned potentials to represent molecular interactions.[198–201] More broadly, ML contributes to MD through three complementary functions. It accelerates simulations by replacing costly electronic-structure evaluations with learned force fields. It enhances sampling by providing data-driven collective variables and adaptive biasing strategies. It also extract physical understanding by means of unsupervised analysis and model reduction. For an overview of fundamental machine learning concepts, see Goodfellow et al.[202] and Hastie et al.[203]

5.1. Machine-Learned Molecular Potentials

Machine-learning potentials (MLPs) learn the mapping between atomic configurations and potential energy surfaces from reference QM data, achieving near-QM accuracy at only a fraction of the computational cost.[198,200,201,204] They can be formulated using kernel-based approaches or neural-network architectures, which differ mainly in scalability and data efficiency.[198] Early MLPs relied on simple descriptors, such as the symmetry functions introduced in the Behler–Parrinello framework,[205,206] whereas modern architectures, such as graph neural networks[207,208] and equivariant transformers,[199,209] learn molecular representations directly and encode physical symmetries, including translational, rotational, and permutational invariance.[198–201] MLPs can serve as stand-alone models, fully replacing physical models with data-driven predictions of energies and forces, or as correction potentials[210,211] where they compensate for the deficiencies of approximate baseline methods. The Δ-ML approach, which adopts this corrective concept, is discussed in more detail in Section 5.1.1.

5.1.1. Δ-ML Potential

Despite recent advances in MLPs, the application of stand-alone models remains limited due to their complex architectures, demanding training procedures, and costly evaluation.[212,213]

Moreover, MLPs struggle with transferability beyond their training domain and exhibit insufficient treatment of long-range electrostatic interactions, leading to imbalances in predicted interactions.[198,214] Physics-informed ML has been shown to improve robustness and data efficiency by embedding physical constraints.[215–217] The Δ-ML approach leverages physical principles by learning the difference between two levels of theory. In principle, this should reduce complexity, as the model focuses on systematic errors rather than reproducing the entire potential energy surface. This method has been successfully applied to enhance PM6 toward CCSD(T) accuracy,[213] and to improve the description of long-range interactions between the QM and MM regions in QM/MM simulations.[218,219]

Zhu et al.[220] introduced a Δ-ML correction scheme for DFTB, which was subsequently extended by Gómez et al.[221] into a proprietary Δ-ML model tailored for thiol–disulfide exchange (TDE) in QM/MM simulations. This model corrects the qualitative deficiencies of the standard semi-empirical density functional tight binding (DFTB) description of the TDE reaction, which stem from its limited treatment of electronic correlation.[222] As a result, DFTB overestimates S–S bond distances and leads to inadequate transition states, introducing errors of up to 5 kcal mol^{-1}.[52,222] Fundamentally, these inaccuracies are intrinsic to the sulfur bonding region and can therefore be addressed independently of the environment. This makes it reasonable to train the ML correction on a minimal gas-phase system while ensuring its transferability to more complex environments.[221] It also improves quantitative accuracy by including many-body interactions.[220,221,223] This Δ-ML model was employed in the study presented in Chapter 7 to investigate TDE in the catalytic cycle of monothiol *Homo sapiens* glutaredoxin (Grx). The following section therefore introduces this model in greater detail to provide the necessary theoretical context.

The model architecture is based on the second-generation Behler–Parrinello artificial neural network (ANN).[205,206] This architecture is also known under the term high-dimensional neural network potential (HDNNP). The DFTB-3OB method[123,124] was used as the baseline and CCSD(T)/aug-cc-pVTZ[224,225] as the target method. The model was constructed to learn the energy difference

$$\Delta E = E_{\mathrm{CCSD(T)}} - E_{\mathrm{DFTB}}. \tag{5.1}$$

The calculations were performed on the minimal reactive model comprising the geometrical ensemble of the TDE between methylthiolate and dimethyldisulfide, containing a total of 15 atoms. This model closely resembles the QM region used in the QM/MM simulations, in which one methyl hydrogen is substituted to form the covalent bond with the protein backbone. All 15 atoms were used as inputs to the ANN.[221] Distinct components of the network comprise the atomic coordinate representation (embedding), neural-layer architecture, optimization strategy, and the treatment of modified forces, each of which is discussed in the following sections. For implementation details and the construction of the training dataset, the reader is referred to the original source in Ref. [221].

Embedding. The atomic coordinates are first transformed into atom-centered symmetry function (ACSF) that serve as the input descriptors for the neural network. This representation is

motivated by the need for feature vectors that remain unchanged under rotation, translation, and permutation of identical atoms, which ensures physically consistent energy predictions. The functions are designed to depend smoothly on the atomic coordinates, which provides continuous potential energy surfaces and well-defined forces suitable for molecular dynamics simulations.[205,206] As a result, the predicted atomic contributions to the total energy remain invariant under global transformations of the molecular system.[215] The symmetry functions are constructed from interatomic distances R_{ij} and angles θ_{ijk}, yielding radial and angular terms that encode the local environment of each atom. Each term is multiplied by a cutoff function $f_c(R_{ij})$ that restricts its influence to neighbors within a radius R_c. This cutoff length defines the spatial extent of the interactions that affect the atomic environment and must be large enough to capture all energetically relevant contributions. In practical applications, cutoff values between 6 and 10 Å provide reliable potential energy surfaces.[206]

The radial symmetry functions

$$G_{i,\mu}^{\mathrm{rad}} = \sum_{\substack{j\neq i \\ R_{ij}\leq R_\mathrm{c}}} \exp\left[-\eta(R_{ij}-R_s)^2\right] f_c(R_{ij}) \tag{5.2}$$

characterize the coordination shells surrounding each atom by summing over all neighbors within the cutoff radius. The summation accounts for the cumulative contribution of atoms located inside this spatial region. Radial ACSFs are defined by two parameters: the width parameter η, which controls the spatial extent of the Gaussian, and the shift parameter R_s, which allows the Gaussian center to be displaced from the reference atom. The effects of varying these parameters are illustrated in Figure 5.1a and b. Radial functions describe neighbor distances but cannot distinguish geometries with identical radial distributions, such as tetrahedral and square-planar environments. This limitation motivates the introduction of angular symmetry functions.

The angular terms

$$G_{i,\mu}^{\mathrm{ang}} = 2^{1-\zeta} \sum_{\substack{j\neq i \\ k\neq i,j}} \left(1+\lambda\cos\theta_{ijk}\right)^{\zeta} \exp\left[-\eta\left(R_{ij}^2+R_{ik}^2+R_{jk}^2\right)\right] f_c(R_{ij}) f_c(R_{ik}) f_c(R_{jk}) \tag{5.3}$$

capture the three-body geometric relationships within the local environment. Additional many-body correlations are incorporated through the nonlinear transformations of the neural network.[206] Angular ACSFs are defined by three parameters that determine their shape, as illustrated in Figure 5.1c. The exponent ζ controls the angular resolution, the parameter η modulates the width of the Gaussian term, and the parameter λ, which takes values of $+1$ or -1, enforces the required symmetry conditions.[206] A cutoff function is applied to each pair distance.

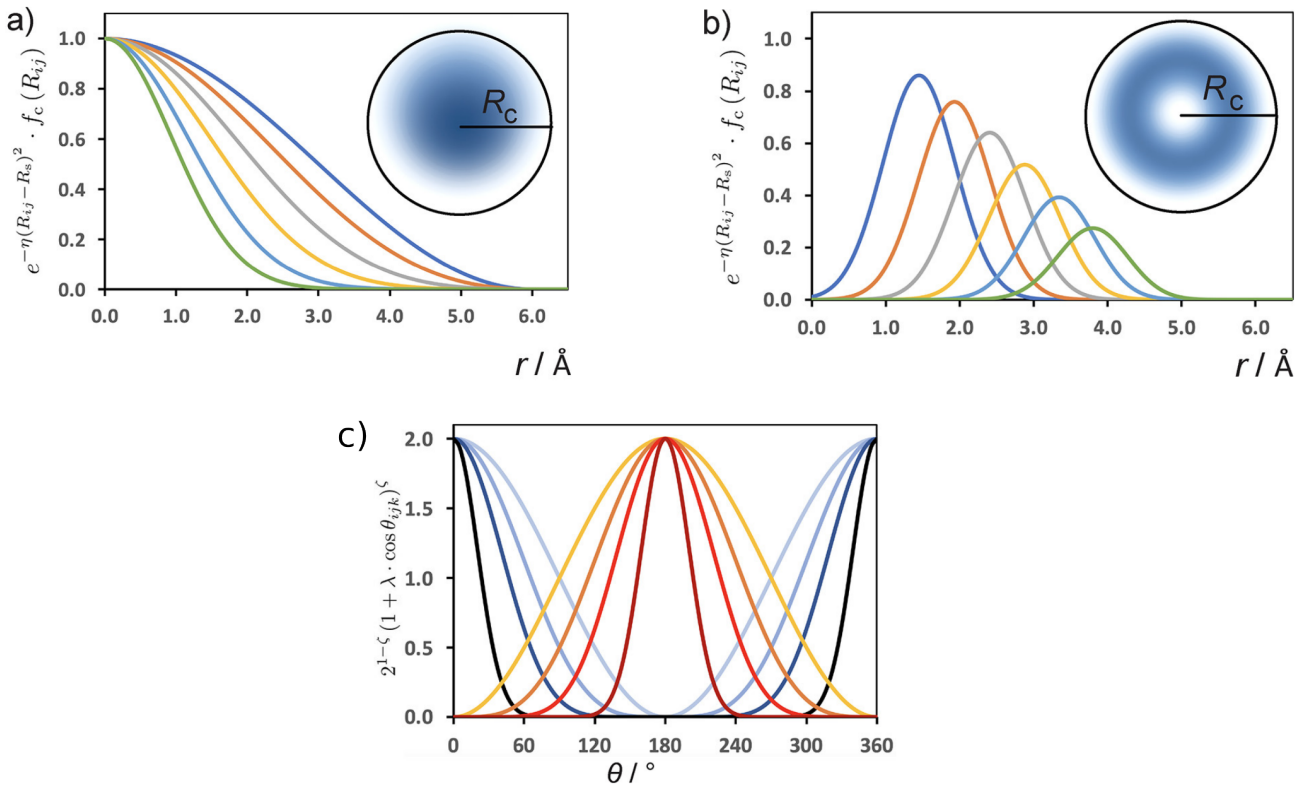

Figure 5.1.: Radial and angular ACSFs with parameters. (a) Radial functions with $R_s = 0$ Å and η values of 0.0, 0.03, 0.08, 0.16, 0.3, and 0.5 Å^{-2} for a cutoff radius of 6 Å, resulting in approximately equidistant turning points between 1 Å and R_c. (b) Shifted radial functions with $\eta \neq 0$ and R_s values of 1.5, 2.0, 2.5, 3.0, 3.5, and 4.0 Å. (c) Angular terms $2^{1-\zeta}(1+\lambda\cos\theta_{ijk})^\zeta$ used in the angular symmetry functions. Curves with $\lambda = +1$ are shown in blue to black and those with $\lambda = -1$ in orange to brown, with exponents $\zeta = 1, 2, 4$, and 16 from light to dark tones. Reproduced with permission from Jörg Behler. "Four Generations of High-Dimensional Neural Network Potentials". In: *Chem. Rev.* 121.16 (2021), pp. 10037–10072.

The atomic environment centered on each atom is described by a set of radial and angular symmetry functions. The minimal representation includes one radial ACSF for each element pair and one angular ACSF for each element triple, yielding

$$N_{\text{sym}} = \frac{N_{\text{elem}}(N_{\text{elem}}+1)}{2} + N_{\text{elem}}. \tag{5.4}$$

In practice, a larger number of ACSFs is employed to obtain an adequate and detailed description of the atomic environment. A crucial step in constructing the embedding is selecting appropriate parameters for the ACSFs. One approach is to optimize the parameters in a data-driven manner by fitting them directly to the training data, although this often compromises transferability.[206,226,227] Alternatively, the parameters can be defined in a more systematic and unbiased way. A common strategy is to construct six radial functions per element pair, positioning their centers evenly between the minimum expected interatomic distance and the cutoff radius. For the angular functions, all distinct combinations of two neighboring element types around the central atom are

considered, with ζ values of 1, 2, 4, and 16 combined with $\lambda = +1$ and $\lambda = -1$ serving as suitable initial choices.[206] Parameter optimization can also involve the use of genetic algorithms[228] or iterative fitting procedures based on short preliminary ANN training runs.[229] Once the parameters are defined, each atom is represented by a fixed-length vector of ACSFs, ensuring that the dimensionality of the atomic descriptor remains constant regardless of the number of neighbors within the cutoff in the local environment.

Neural Networks.

Figure 5.2 illustrates the second-generation Behler–Parrinello ANN architecture.[205,206] The design is founded on the locality approximation, which assumes that atomic interactions can be described as functions of each atom's local environment encoded through the corresponding ACSFs.

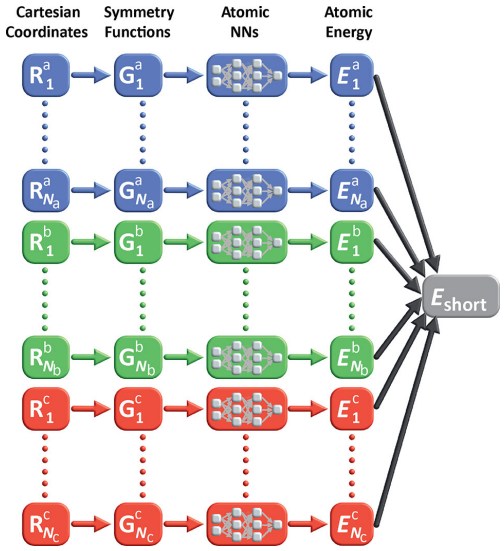

Figure 5.2.: Structure of a second-generation high-dimensional neural network potential (HDNNP) as proposed by Behler and Parrinello.[205] Each color represents a different chemical element (a, b, c) with N_a, N_b, and N_c atoms, respectively. For each atom i of element μ, the Cartesian coordinates R_i^μ are transformed into a vector of symmetry functions G_i^μ, describing its local environment within the cutoff radius. This vector serves as input to an element-specific neural network that predicts the atomic energy E_i^μ. The total short-range energy E_{short} is obtained as the sum of all atomic contributions. Reproduced with permission from Jörg Behler. "Four Generations of High-Dimensional Neural Network Potentials". In: *Chem. Rev.* 121.16 (2021), pp. 10037–10072. Copyright 2021 American Chemical Society.

As a direct consequence of the locality approximation, the total potential energy of the system

$$E_{\text{total}} = \sum_{j=1}^{N_{\text{elem}}} \sum_{i=1}^{N_{\text{atom}}^j} E_i^j \tag{5.5}$$

can be expressed as the sum of local atomic energy contributions. Here, N_{elem} is the number of elements present in the system and N_{atom}^j is the number of atoms of element j. This decomposition is reflected in the ANN architecture, which employs a separate feed-forward neural network for each element type, applied identically to all atoms of that element. Each subnetwork consists of

multiple layers, where every node applies a nonlinear activation function h. The output of a node is given by

$$y_j = h\left(b_j + \sum_{i=1}^{n} w_{ij}\, x_i\right), \tag{5.6}$$

where w_{ij} are the connection weights, b_j is the bias term, and x_i are the inputs from the preceding layer. The individual atomic energy contributions are summed to obtain the total energy of the system. Adding an atom introduces an additional evaluation of the corresponding element-specific subnetwork, whereas removing an atom eliminates that evaluation.

Modified Forces.

To enable the Δ-ML model for thiol–disulfide exchange (TDE) to correct not only total energies but also provide consistent forces for QM/MM simulations on an augmented potential energy surface, the force acting on atom $\hat{\imath}$ in direction α is defined as

$$F^{\hat{\imath}\alpha}_{\text{DFTB-NN}} = F^{\mu\alpha}_{\text{DFTB}} + F^{\hat{\imath}\alpha}_{\text{corr}}, \tag{5.7}$$

where $F^{\hat{\imath}\alpha}_{\text{DFTB}}$ denotes the baseline DFTB forces and $F^{\text{corr}}_{\hat{\imath}\alpha}$ is the ANN-derived force correction. This correction follows from the derivative of the total ANN energy

$$\begin{aligned} F^{\hat{\imath}\alpha}_{\text{corr}} &= -\frac{\partial E_{\text{total}}}{\partial R_{\hat{\imath}\alpha}} \\ &= -\sum_{j=1}^{N_{\text{elem}}} \sum_{i=1}^{N^j_{\text{atom}}} \frac{\partial E^j_i}{\partial R_{\hat{\imath}\alpha}} \\ &= -\sum_{j=1}^{N_{\text{elem}}} \sum_{i=1}^{N^j_{\text{atom}}} \sum_{k=1}^{N^i_{\text{sym}}} \frac{\partial E^j_i}{\partial G^j_{ik}} \frac{\partial G^j_{ik}}{\partial R_{\hat{\imath}\alpha}}. \end{aligned} \tag{5.8}$$

Here, $R_{\hat{\imath}\alpha}$ denotes the Cartesian coordinates of atom $\hat{\imath}$ in direction α. The terms $\partial E^i_j / \partial G^i_{jk}$ are the derivatives of the atomic neural networks determined by the network architecture, and $\partial G^i_{jk} / \partial R_{\mu\alpha}$ are the analytical derivatives of the ACSFs with respect to the Cartesian coordinates.

5.2. Machine Learning for Enhanced Sampling

The concept of collective variables (CVs) was introduced in Section 4.1, together with the basic methodological considerations underlying their use in enhanced sampling. The definition of suitable CVs is often central in a MD study, as they provide a reduced representation of the system's essential degrees of freedom – the reaction mechanism. However, identifying them is inherently challenging due to a "chicken-and-egg" dilemma: one must know the relevant CVs to locate the transition pathways; however, such pathways cannot be observed without first sampling them.

This circular dependence naturally suggests an iterative workflow, where preliminary CVs are refined based on new data points. A typical starting point involves geometric constructions derived from chemical intuition, such as bond distances, angles, or dihedral combinations. However, these predefined CVs may not adequately capture the complexity and true dimensionality of the underlying conformational space. This is where machine learning becomes a powerful tool. ML-based approaches can infer optimal low-dimensional representations directly from simulation data, revealing hidden CVs that are difficult to define a priori.[230]

Unsupervised learning techniques are employed with the goal of reducing the dimensionality of molecular dynamics data. In a typical workflow, MD trajectories are represented in a high-dimensional space (e.g., interatomic distances or internal coordinates), from which the algorithm seeks a low-dimensional projection (latent space) that defines new CVs.[231] Common approaches include principal component analysis (PCA)[232–234] and time lagged independent component analysis (tICA)[235], which identify latent coordinates that maximize variance or autocorrelation, respectively.[191] The optimization metric can be chosen with different objectives in mind, thereby setting different emphasis in the construction of the resulting CVs. For instance, in the Spectral Gap Optimization of Order Parameters (SGOOP) method[236], the CV is learned to maximize the path entropy as a linear or nonlinear combination of inputs.

In contrast, supervised ML aims to identify the features that define metastable states by learning discriminative functions.[195,197,230] In this case, configurations are labeled according to their metastable assignment, often derived from clustering or kinetic modeling. Then, a classifier, such as a neural network or support vector machine[197,203], is trained to distinguish these states in feature space. The optimized network serves as a CV that not only separates metastable basins but also provides a smooth interpolation between them. Once established, such data-driven CVs can be iteratively refined and applied in subsequent simulations to accelerate sampling and improve convergence.[230]

Both strategies have been explored using classical ML and deep neural network approaches. Deep learning architectures offer substantial representational capacity, enabling the automatic extraction of nonlinear dependencies and hierarchical features from large data sets. However, they require extensive data, careful hyperparameter optimization, and often lack interpretability.[195,197,230] In contrast, this work employs unsupervised classical ML algorithms, PCA and tICA, which provide transparent and computationally efficient models that are easier to interpret.[191,230,231] Both algorithms are complementary in nature. While PCA is biased toward identifying directions of maximum variance, tICA focuses on capturing the system's slowest dynamical modes, representing the two principal metrics commonly used in dimensionality reduction.[198] These methods are described in the following section.

5.2.1. Principal Component Analysis

PCA is a widely used dimensionality reduction method and a cornerstone of multivariate data analysis across scientific disciplines.[237] It is a linear dimensionality reduction technique that identifies orthogonal components capturing the maximum variance within a dataset. It serves as an example of how dimensionality reduction operates. Given a collection of data points $\{x^{(1)}, \ldots, x^{(m)}\} \in \mathbb{R}^n$, the goal of PCA is to transform each $x^{(i)}$ from the original n-dimensional space into a lower-dimensional representation $c^{(i)} \in \mathbb{R}^l$ with $l < n$. To find this transformation, PCA considers the reverse mapping $x_*^{(i)} = g(c^{(i)})$, where $x_*^{(i)}$ exhibits information loss relative to $x^{(i)}$ (lossy transformation). PCA requires minimizing the reconstruction error measured by the L_2 norm

$$\text{error}_{l \to n} = \arg\min_c \|x - g(c)\|_2^2. \tag{5.9}$$

The objective is to minimize the distance between the input point x and its reconstruction $g(c)$ obtained from a lower-dimensional space. This optimization problem is solved under orthogonality and unit-norm constraints imposed on the columns of the transformation matrix that defines $g(c)$. By applying the method of Lagrange multipliers, that optimal transformation matrix is defined by the first eigenvectors of the covariance matrix of the input data. Thus, the solution is obtained through the eigendecomposition of the covariance matrix.[202]

Starting from an MD trajectory, a d-dimensional discrete time series $\{\mathbf{x}_t\}$ represents the evolution of a molecular system. From this data, the covariance matrix $\mathbf{C}$ is constructed, with its elements defined by the individual coordinates r_i as

$$\mathbf{C}_{ij} = \langle (r_i - \langle r_i \rangle)(r_j - \langle r_j \rangle) \rangle, \quad i, j = 1, \ldots, d. \tag{5.10}$$

Diagonalizing the covariance matrix

$$\mathbf{C} = \mathbf{V}\mathbf{\Lambda}\mathbf{V}^{-1} \tag{5.11}$$

yields the eigenvector matrix $\mathbf{V}$ and the diagonal eigenvalue matrix $\mathbf{\Lambda}$. The eigenvectors $\mathbf{v}_i$ describe the directions of the principal motions. When sorted in descending order according to their associated eigenvalues λ_i, the eigenvectors describe progressively smaller contributions to the variance of the system.[191,238,239] The explained variance of the i-th principal component is given by

$$p_i = \frac{\lambda_i}{\sum_{j=1}^{d} \lambda_j}. \tag{5.12}$$

A low dimensional representation of the original MD data $\{\mathbf{x}_t\}$ can be constructed by projecting it onto a subset of eigenvectors

$$z_i(t) = \Big(\mathbf{x}_t - \langle \mathbf{x} \rangle\Big) \cdot \mathbf{v}_i. \tag{5.13}$$

The result of the dimensionality reduction is a smaller set of z_i that can be employed for further analyses, such as the construction of free energy landscapes[240] or as collective variables (CV) in

enhanced sampling simulations.[238] Eigenvectors $\mathbf{v}_i$ that contribute only marginally to the total variance can be discarded.

5.2.2. Time Lagged Independent Component Analysis

Time lagged independent component analysis (tICA) is linear dimensionality reduction algorithm. For the data points $\{\mathbf{x}_t\}$ in an MD trajectory, the centered coordinates at time t can be denoted as a vector in bra–ket notation, $|\mathbf{x}_t\rangle$. The following discussion is based on Ref. [235, 241, 242].

tICA constructs uncorrelated components $|\alpha_i\rangle$ that maximize their autocorrelation,

$$f(|\alpha_i\rangle) = \frac{\mathbb{E}[\langle\alpha_i|\mathbf{x}_t\rangle\langle\alpha_i|\mathbf{x}_{t+\tau}\rangle]}{\mathbb{E}[\langle\alpha_i|\mathbf{x}_t\rangle\langle\alpha_i|\mathbf{x}_t\rangle]}. \tag{5.14}$$

The parameter τ defines a fixed lag time, representing the temporal interval between two configurations along the trajectory. By applying standard linear algebra operations, this expression simplifies to

$$f(|\alpha_i\rangle) = \frac{\langle\alpha_i|\mathbf{C}^\tau|\alpha_i\rangle}{\langle\alpha_i|\mathbf{C}|\alpha_i\rangle}, \tag{5.15}$$

where $\mathbf{C}^\tau$ denotes the time-lagged covariance matrix and $\mathbf{C}$ represents the instantaneous covariance matrix.

The algorithm begins by solving for the first time-lagged component $|\alpha_0\rangle$ while constraining its variance to unity, $\langle\alpha_0|\mathbf{C}|\alpha_0\rangle = 1$. This simplifies Eq. 5.15 to

$$\max_{|\alpha_0\rangle} f(|\alpha_0\rangle) = \max_{|\alpha_0\rangle} \langle\alpha_0|\mathbf{C}^\tau|\alpha_0\rangle. \tag{5.16}$$

The optimal solution can be obtained using the method of Lagrange multipliers. Subsequently, the next component $|\alpha_1\rangle$ is determined by solving

$$\max_{|\alpha_1\rangle} f(|\alpha_1\rangle) = \max_{|\alpha_1\rangle} \langle\alpha_1|\mathbf{C}^\tau|\alpha_1\rangle, \tag{5.17}$$

subject to the unit-variance constraint $\langle\alpha_1|\mathbf{C}|\alpha_1\rangle = 1$ and the additional condition $\langle\alpha_1|\mathbf{C}|\alpha_0\rangle = 0$, which ensures that $|\alpha_1\rangle$ is uncorrelated with $|\alpha_0\rangle$. By repeating this procedure, higher-order components can be systematically constructed.

The set of components $|\alpha_i\rangle$ can be ordered according to their corresponding eigenvalues λ_i, such that those associated with the slowest dynamical processes (largest characteristic time scales) appear first. This relation is given by

$$\begin{aligned} f(|\alpha_i\rangle) &= \langle\alpha_i|\mathbf{C}^\tau|\alpha_i\rangle && (5.18)\\ &= \langle\alpha_i|\lambda_i\mathbf{C}|\alpha_i\rangle && (5.19)\\ &= \lambda_i\langle\alpha_i|\mathbf{C}|\alpha_i\rangle && (5.20)\\ &= \lambda_i. && (5.21) \end{aligned}$$

Each component $|\alpha_i\rangle$ is assigned an implied time scale,

$$t_i = -\frac{\tau}{\log(\lambda_i)}. \tag{5.22}$$

Time-lagged components α_i associated with smaller eigenvalues can be discarded, since they encode only rapidly decorrelating fluctuations. The result of this dimensionality reduction is a smaller set of slow coordinates, represented by the remaining α_i, which correspond to the dominant dynamical modes of the system and can be employed as CVs.

Part III.

Contributions

6. Non-covalent Interactions at the QM-MM Interface in the Semi-Empirical and Density-Functional Limit

Chapter 6 is reproduced from publication with permission from ACS Publishing:

- Accepted manuscript: **Julian Böser** et al. "Non-covalent Interactions at the QM–MM Interface in the Semi-Empirical and Density-Functional Limit", *Journal of Chemical Theory and Computation* (2025).

6.1. Introduction

In molecular simulations, extensive sampling is essential to capture rare yet functional events such as substrate binding, conformational rearrangements, photochemical reactions, and enzyme catalysis, which span multiple timescales.[35,36,243] An accurate description of these processes requires consideration of localized electronic rearrangements, bond-making and bond-breaking within the active site, and conformational motions of the surrounding environment. In principle, one could model the entire system using a quantum-mechanical (QM) method, but the prohibitive cost of QM for large systems like biomolecules precludes routine application. Hybrid quantum mechanics/molecular mechanics (QM/MM) approaches[34,139] address this challenge by treating the reactive core quantum mechanically while embedding it in a computationally efficient classical environment.

Typically, QM/MM divides a system of interest into two parts: (1) a smaller region in which changes of electronic structure occur, such as chemical reactions or photoexcitation, and (2) a larger surrounding environment that retains its initial electronic structure. The smaller region is described with a QM method, capable of simulating the change of electronic structure, while the larger region is treated at the MM level to keep the computational cost affordable. Despite the clarity of the QM/MM conceptual blueprint, its setup requires rigor and scrutiny to balance interatomic and intermolecular interactions.[38,244–249] The issue is that QM/MM inherently creates an interface between the two subsystems, affecting the interactions between them, especially, preventing any charge transfer (CT) between the subsystems and limiting the mutual polarization. In additive embedding, an explicit coupling term $E_{\text{QM-MM}}$ must be added to the classical energy

of the MM region E_{MM} and the quantum mechanical energy E_{QM} of the QM region to reconcile the integrity of the system, $E_{\mathrm{Total}} = E_{\mathrm{QM}} + E_{\mathrm{MM}} + E_{\mathrm{QM\text{-}MM}}$.

For systems lacking covalent bonds between subsystems, the coupling term simplifies to only noncovalent interactions (NCIs). Accurate modeling of these interactions is the central aim of the development of embedding schemes. Mechanical embedding (ME), electrostatic embedding (EE), and polarizable embedding (PE) each offer different trade-offs between accuracy and cost.[148] While PE accounts for mutual polarization and is advantageous for spectroscopy or photoexcitation,[250–254] its higher computational cost does not universally translate to improved performance, even though polarization can contribute 10–20% of total interaction energy.[255–257]

Despite significant advances in the development and optimization of embedding methods, the size of the QM region remains critical for mitigating said deficiencies. An appropriately designed QM region can help avoid interface artifacts where the embedding scheme may poorly capture key electronic effects.[151] Minimal QM regions suffice in systems like chorismate mutase, where charge transfer is negligible,[256] but defining them in more complex systems is less straightforward. In catechol-O-methyltransferase (COMT), where substrates span a large, solvent-exposed active site, charge shift analysis showed that residues often selected by proximity or intuition were unnecessary, while typically overlooked nonpolar residues were essential, favoring data-driven over intuition-based selection.[258] Thus, the construction of the QM region and the selection of the method must balance the accuracy against the computational cost for each specific system.

Unlike QM/MM studies on complex systems, which are computationally intensive and often difficult to generalize, the benchmarking of smaller, prototypical systems plays a central role in the development and validation of accurate QM/MM models. Benchmarking quantum chemical methods against high-level reference interaction energies is a well-established practice for assessing and improving computational accuracy. Focusing on NCIs is important, as such interactions are fundamental to the structure and function of molecules. NCIs are generally weaker than covalent bonds, with binding energies ranging from -0.5 to -50 kcal mol^{-1}[20], allowing for the flexibility and dynamic behavior of molecular structures, but are highly dependent on geometric parameters.[259,260]. In spite of the importance of NCI and the usefulness of QM/MM, systematic studies of NCIs using QM/MM setups have been strikingly scarce. To the best of the authors' knowledge, existing comparisons of non-covalent interaction (NCI) components have been limited to specific systems and small datasets. However, a systematic evaluation of NCIs within QM/MM frameworks has not yet been reported in the literature.[141,246,261–272].

In this work, we aim to fill this gap in the field by investigating NCIs at the QM–MM interface. The analysis was carried out within the frameworks of density functional theory (DFT) and semiempirical quantum chemistry (SQM), using ωB97X-V and DFTB as the respective representative methods. To evaluate how QM/MM captures non-bonded interaction energies relative to higher-level references, two contrasting structural models were employed: small-molecule dimers in vacuum ("pair models") and protein–ligand clusters embedded in their native-like environments ("microenvironment models"). Interaction energy profiles are computed for neutral

(HB375x10) and ionic (IHB100x10) hydrogen-bonded complexes from the Noncovalent Interactions Atlas (NCIA)[273]. The focus on H-bonds is motivated by their role in relevant phenomena such as stabilizing molecular structures[274], molecular recognition[275], and catalysis[276,277]. The dominant contributors to hydrogen bonding are electrostatics, polarization and charge transfer interactions.[260] However, depending on the balance of all underlying energy components[75], H-bonding spans a spectrum[76] of interactions broadly categorized as conventional and unconventional, making it sensitive to the intricate interplay between these components. This is particularly relevant in the context of QM/MM calculations, as the QM–MM interface inevitably perturbs the balance between electrostatics, polarization, exchange repulsion, and charge transfer, as well as their coupling. For example, omitting polarization in the modeling of hydrogen bonds, by using unperturbed MM charges, can lead to incorrect intramolecular hydrogen bonding[278] and underestimated cooperative effects in proteins[279]. Additionally employed was a set of larger models from the "Protein–Ligand Refined EXperiment" benchmark (PL-REX),[280] comprising ten protein–ligand complexes (with 10–30 ligands per protein) derived from well-characterized protein targets with interaction energies computed using DFT as reference. Considering such different datasets makes it possible to evaluate how environmental context and model type influence the accuracy of QM/MM calculations. This may provide a foundation for understanding and improving the treatment of hydrogen bonding at the QM–MM interface in applications to realistic biomolecular systems.

6.2. Methodology

6.2.1. Benchmark Data

Pair Models. The benchmark for the small-molecule dimer systems is based on the HB375x10 and IHB100x10 datasets. The noncovalent complexes in these datasets are designed to test the performance of computational methods across a broad range of interaction types. Each complex includes a 10-point dissociation curve sampled from the equilibrium geometry, with interaction energies extrapolated to the CCSD(T)/CBS limit using large basis sets. The intracomplex distance along the dissociation curve is characterized by the distance scaling factor f_{dscaling}. To test neutral hydrogen-bonded and ionic hydrogen-bonded structures, we used the HB375x10 and IHB100x10 datasets, respectively.[273] The interaction strength and the number of components per class are summarized in Table A.1. Notably, the IHB100x10 dataset is less dense; some bond types encompass as few as one to six complexes. Structural details can be explored in the database, which is conveniently accessible at www.nciatlas.org.

Microenvironment Models. The benchmark for the protein–ligand cluster models is based on the PL-REX dataset[280], which comprises ten receptor–ligand systems derived from well-characterized protein targets, with interaction energies computed using the ωB97X-D3(BJ) functional as reference. This dataset was curated to assess protein–ligand binding affinity. Each system

includes a receptor structure trimmed from the entire protein and paired with a representative set of ligands, resulting in models containing between 753 and 1,096 atoms. These trimmed models are characterized by variations in the number of retained water molecules, presence of zinc cations and halogens, and differences in ligand topology, pK_a, and similarity. Of the ten systems available in PL-REX, eight were selected for this study: Systems 1, 2, 3, 5, 6, 7, 9, and 10, see Table A.7 for system names and number of ligands. A note on systems 1 and 10, which involve interactions between a zinc cation and coordinating ligands: pilot force-field calculations revealed that the use of standard General Amber Force Field (GAFF) parameters and AMBER parameters results in substantial overestimation of interaction energies in all models. Apparently, more specialized parameter sets, such as ZAFF,[275] would be more appropriate in these cases. Consequently, Systems 1 and 10 are excluded from the calculations.

6.2.2. QM/MM Model

We employed electrostatic embedding (EE) in our QM/MM setup. In EE, the QM region is explicitly polarized by the surrounding MM environment, allowing the electronic structure of the QM subsystem to dynamically respond to changes in the environmental charge distribution. This can be achieved by incorporating MM point charges directly into the QM Hamiltonian as one-electron terms[35] as introduced in Eq. 2.34. The QM zone contains N electrons, while M MM atoms carry point charges Q_j. Additionally, our implementation introduces a charge scaling factor, λ, which modulates the magnitude of the QM-MM electrostatic interactions. To evaluate the sensitivity of the benchmark results to variations in the MM charge distribution, we systematically varied λ over the range 0.80 to 2.00 and assessed its impact on accuracy. Since the systems studied here consist of isolated noncovalent complexes, there was no need to account for covalent bonds crossing the QM/MM interface. Although earlier studies emphasized the potential importance of parameterizing QM/MM van der Waals terms specifically for quantum atoms[281,282], in practice, most contemporary QM/MM implementations employ Lennard–Jones parameters directly from widely used force fields. Following this convention, we adopted the AMBER/GAFF parameters for the QM atoms, ensuring consistency across both the QM/MM models and the GAFF reference models.

MM Parameters and Charge Model. To parameterize the components of the MM region, we used the general AMBER force field (GAFF) following the Antechamber workflow to assign bonded and nonbonded parameters.[283–285] Atomic charges were generated through restrained electrostatic potential (RESP) fitting. The following operations were performed in GAUSSIAN 09[286]. Initially, the structures were optimized using the B3LYP functional and the 6-31G* basis set. Subsequently, a population analysis was carried out at the Hartree–Fock level (HF/6-31G*, Pop=MK, IOp(6/33=2)) to obtain electrostatic potential-derived charges based on the Merz–Singh–Kollman scheme.[100] The final RESP fitting was completed in the Antechamber using single conformers and without constraints for the charge symmetry between symmetric atom groups. The GAFF1 parameters were used for all systems in HB375x10 and IHB100x10. For PL-REX, the systems were

built using standard parameters from the AMBER99SB-ILDN force field (FF) for the receptor and the GAFF1 FF for the ligand.

Binding Energy Calculations and Analyses. The interaction energy was calculated as the difference between the QM/MM energy for the whole complex and the sum of the QM and MM energies for the isolated subsystems A and B, defined as

$$\Delta E_{\text{int}} = E_{\text{QM/MM}}(\text{A,B}) - E_{\text{QM}}(\text{A}) - E_{\text{MM}}(\text{B}). \tag{6.1}$$

Our calculations included ωB97X-V/ma-def2-TZVPP[287], DFTB[120,122,288], GAFF, and both QM/MM partitionings. For PL-REX, ωB97X-V/ma-def2-TZVPP calculations were excluded due to convergence difficulties in the self-consistent field (SCF) calculations. The partitioning into the QM and MM regions always kept all molecules whole, therefore avoiding the need for the QM–MM boundary to cross any covalent bonds. In HB375x10 and IHB100x10, the first compound (left) interacts as an H-donor and the second compound (right) interacts as an H-acceptor. Accordingly, the system "QM/MM" incorporates the H-donor in its QM region, while the system "MM/QM" incorporates the H-acceptor in its QM region. In PL-REX, the receptor or ligand was included as a QM region. The third-order DFTB calculations used the 3OB[123–126] parameter set and a Fermi temperature of 300 K. To improve the description of noncovalent interactions, γ-damping hydrogen bond correction (exponent $\zeta = 4.0$)[123] and D3 dispersion correction with Becke–Johnson (BJ) damping ($s_8 = 3.209$, $a_1 = 0.746$, and $a_2 = 4.191$)[126] were applied. The calculations on the pairwise models did not include the three-body term in D3(BJ) as its effects had been shown to be negligible in small complexes, although they become increasingly important in larger ones.[289] For that reason, we included the three-body contribution in the large PL-REX complexes, and also compared the results to those obtained without the three-body contribution. The electrostatic interactions were calculated without a cutoff. All calculations were performed as single-point evaluations using our local implementation of QM/MM in GROMACS 2020.2[290] and DFTB+,[291] which is available from a public repository.[292,293] We additionally tested DFTB-CPE/GAFF models using a local implementation of the chemical-potential equalization model (DFTB-CPE).[294–297] These calculations used the parameterization by Vuong et al.[115] Calculations employing ωB97X-V/ma-def2-TZVPP were performed using our local QM/MM implementation in GROMACS 2020.2 interfaced with ORCA 5.0.3.[298]

Reference calculations for CT were performed at the PBE-D3(BJ)/def2-SVP, PBE-D3(BJ)/ma-def2-TZVPP, and ωB97X-V/ma-def2-TZVPP levels of theory. The extent of CT was determined by calculating the net change in total monomer charge upon complex formation. Specifically, the atomic charges of each monomer were summed once in the isolated (vacuum) state and once from the QM calculation of the complex; the difference between these two totals defines the amount of CT. Mulliken charges were used for DFTB calculations, while natural bond orbital (NBO) charges were used for all other methods. The latter calculations were carried out using GROMACS 2020.2, interfaced with ORCA 5.0.3, which was patched with NBO6[299]. To generate reference values for monomer polarization, we employed the same levels of theory used for CT

analysis. For DFTB calculations, dipole moments were computed from Mulliken charges after centering each monomer at its center of mass (COM). For all other methods, dipole moments were derived directly from the electron density, also centered at the COM. Dipole moments were calculated for both isolated monomers in vacuum and monomers embedded within their MM environment at $f_{\text{dscaling}} = 1.0$. All analyses used the following reference data: CCSD(T)/CBS values from the HB375x10 and IHB100x10 datasets and ωB97X-D3(BJ)/DZVP results from the PL-REX dataset. The metrics used to evaluate model performance are detailed in Section A. We evaluated the accuracy using the root mean squared error (RMSE) and assessed systematic error using the mean signed error (MSE). To make possible an unbiased comparison between strong and weak hydrogen bond (H-bond) interaction types, we also compared the error normalized by the mean interaction strength.

6.3. Results and Discussion

Our assessment of interaction energies in hydrogen-bonded complexes is based on pairwise models of noncovalent dimer complexes provided in the HB375x10 and IHB100x10 datasets, as well as microenvironment models obtained from the PL-REX dataset. For each complex, we report interaction energies for the QM/MM and MM/QM models, corresponding to swapped QM and MM regions, in addition to the interaction energies for the MM and QM models. Our calculations used either the GAFF (small compound/ligand) or the AMBER99SB-ILDN (receptor) FF for the MM region. The QM region was treated using either DFTB or ωB97X-V. The calculated interaction energies were compared to the CCSD(T)/CBS reference from the HB375x10 and IHB100x10 datasets and the ωB97X-D3(BJ)/DZVP reference from the PL-REX dataset. Additionally, we also quantified charge transfer and monomer polarity within each complex to assess the models. Computational protocols and modeling details are provided in the Methods section. The discussion is organized in three parts. Section 6.3.1 examines trends across neutral and ionic hydrogen bonds in the pairwise models and discusses implications for practical applications. Section 6.3.2 extends this analysis to microenvironment models, evaluating how environmental context influences QM/MM accuracy. Finally, Section 6.3.3 investigates the effect of scaling QM–MM electrostatic interactions across all datasets. To clarify terminology, we define a "QM/MM model" or "MM/QM model" as a specific partitioning of QM and MM regions (e.g., DFTB/GAFF or GAFF/DFTB). In contrast, "QM/MM models" refers collectively to both partitionings of a given pairing (e.g., ωB97X-V/GAFF and GAFF/ωB97X-V). It should be emphasized that, in the notation "**QM**/*MM*" and "**MM**/*QM*" notation, the method (region) **on the left** is always associated with the **hydrogen-bond donor** and the one *on the right* with the *hydrogen-bond acceptor*. Accordingly, "QM/MM" has the H-donor in its QM region, while "MM/QM" has the H-acceptor in its QM region. This notation is used consistently throughout the text, with the exception of group 7 in HB375, which does not involve hydrogen bonding.

6.3.1. Pairwise Models

Interaction energies were computed along the dissociation curves for the complexes included in the HB375x10 and IHB100x10. For the analysis, we proceeded in two stages: (1) examining interaction energies for structures at which each corresponding method exhibits a minimum of energy, and the energies from the reference. These results are discussed below under "Equilibrium". The distributions of deviations from the reference equilibrium distances are shown in the App. Section A. (2) Extending the analysis to the full dissociation curves for the combined dataset. The details are given below under "Dissociation Energy Curves".

6.3.1.1. Neutral Hydrogen Bonds

Equilibrium. For HB375x10, DFTB and GAFF exhibit comparable accuracy. As shown in Figure 6.1, GAFF gives a slightly lower RMSE of 1.5 kcal/mol compared to 1.7 kcal/mol of DFTB. Although the RMSE is quite low, the accuracy in terms of relative error remains significant, at approximately 30%. These errors stem from systematic underbinding, which is evident from positive MSE values shown in Figure A.1. DFTB/GAFF models perform comparably to the DFTB and GAFF references, with only moderate increases in error overall.

The introduction of the QM/MM interface contributes an additional error of up to 0.5 kcal/mol. Transitioning from DFTB to the DFTB/GAFF and GAFF/DFTB models increases the RMSE by ca. 0.1 kcal/mol and 0.5 kcal/mol, respectively. The accuracy of QM/MM models is remarkable considering that the other SQM methods, such as PM6, exhibit significantly higher RMSE of 2.99 kcal/mol, while GFN2-xTB shows a RMSE of 1.22 kcal/mol.[273] For ab initio methods like SCS-MP2/CBS, the RMSE is 0.81 kcal/mol, and the RMSE of PBE-D3(BJ)/def2-QZVP is 0.49 kcal/mol. The increased error observed in the DFTB/GAFF models, relative to DFTB and GAFF, can be rationalized by the fundamental differences in how polarity, CT, and dispersion interactions are treated. First, while the DFTB model accounts for CT across the entire system, the QM/MM framework imposes a strict boundary at the QM–MM interface, excluding charge delocalization between subsystems. Second, DFTB handles the dispersion interactions via the D3JB correction, which is well established for accurately modeling nonbonded interactions, whereas the QM/MM approach used here relies on Lennard-Jones parameters from the FF. In contrast to DFTB, the GAFF model resembles QM/MM in that it similarly precludes CT and uses the same Lennard-Jones implementation for dispersion. Finally, the key distinction between DFTB and the DFTB/GAFF partitionings lies in the capabilities to treat the polarization of the individual molecules and the CT between them.

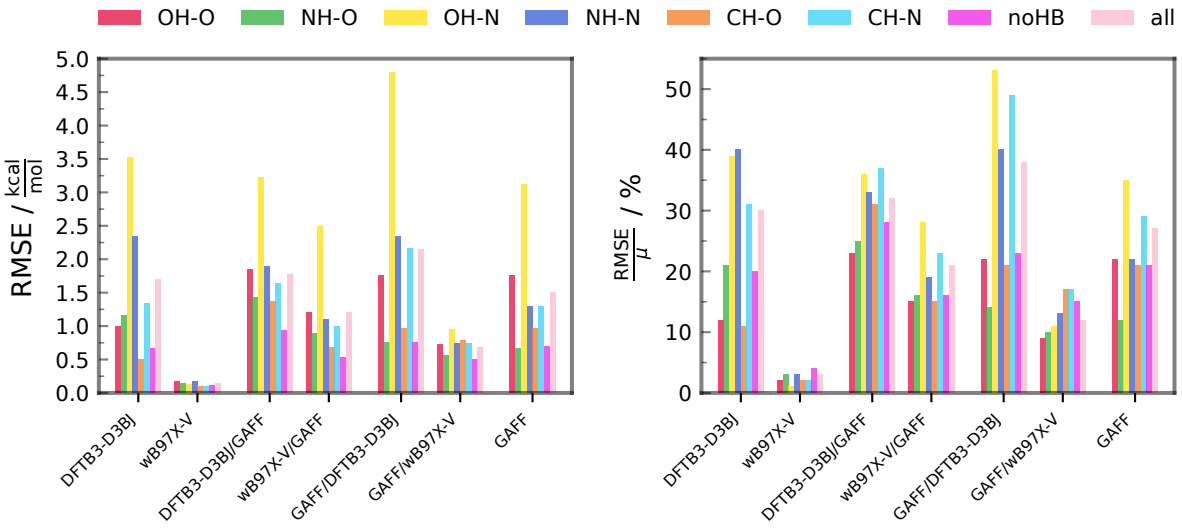

Figure 6.1.: RMSE (left) and RMSE/μ (right) for ΔE_{int} per method and H-bond type in HB375x10. DFTB and ωB97X-V as QM, and GAFF as MM. CCSD(T)/CBS as reference

The lower errors reported for DFTB in some of the previous benchmarks originate from a smaller emphasis on polar hydrogen bonds in those datasets and possibly also from the specific parametrization of the dispersion correction. For instance, DFTB-D3 yielded RMSE/MSE values of 1.5/0.7 kcal/mol on the S22 dataset, and 1.1/0.4 kcal/mol on S66. The DFTB-D3H4 variant performed 0.1–0.3 kcal/mol better at the cost of reduced transferability.[32] Unlike S66, which includes systems with stronger dispersion contributions, HB375x10 focuses on directional hydrogen bonds involving nitrogen and oxygen. Notably, DFTB has well-documented limitations in describing noncovalent interactions due to its monopole approximation.[32,115,296] It does not allow for out-of-plane polarization, and fails to capture the directionality and polarizability of lone pairs perpendicular to the molecular plane. These deficiencies are particularly severe for nitrogen-containing species and introduce a negative bias in benchmarks that include such systems in larger numbers. This difference, along with the fact that D3 is parametrized on S66x8, likely explains the slightly higher errors observed for HB375.[273] Passing to a better description of electrostatics and polarization, multipole-extended DFTB was shown to reduce the RMSE to 1.07 kcal/mol for HB375.[300]. On the other hand, neither the choice of the dispersion correction nor of the hydrogen correction influences the results for QM/MM interaction energies, as they only apply to the QM zone.

To understand the connection between CT and electrostatic interactions with the errors, we analyzed charge transfer as well as the magnitude of the DFTB point charges and compared them to the GAFF point charges. The DFTB charge redistribution was validated by comparing the intermolecular DFTB CT to the results obtained via natural bond orbital (NBO) analysis using ωB97X-V/ma-def2-TZVPP. As shown in the left panel of Figure 6.2, the amount of intermolecular CT is small, and there is no discernible correlation between the degree of CT and the error between both DFTB/GAFF models and the DFTB reference in the HB375 dataset. The results, provided

in Figure A.6, confirm that DFTB closely reproduces the amount of CT compared to the ωB97X-V reference. The comparable performance between DFTB and the DFTB/GAFF models, as well as GAFF, can be attributed to the subordinate role of CT in the interaction. Considering the polarity or the magnitude of the point charges, Figure 6.2 (right) shows an observed strong correlation between the DFTB charges and the GAFF charges, but generally smaller DFTB charges compared to the magnitude of the GAFF charges. This difference in charge distribution can be attributed to the different charge models employed: DFTB utilizes Mulliken charges derived from minimal basis sets, which leads to a systematic underestimation of electrostatic interactions in hydrogen bonds. In contrast, GAFF uses RESP charges obtained from the HF method, which, by design, have greater polarity.[100] The stronger polarity of GAFF's charges enhances electrostatic interactions and binding energies in GAFF for HB375. Employing a more advanced charge model, such as CM3,[301] could improve the description of electrostatic interactions. This advancement would be beneficial to explore in the future development of DFTB/MM.

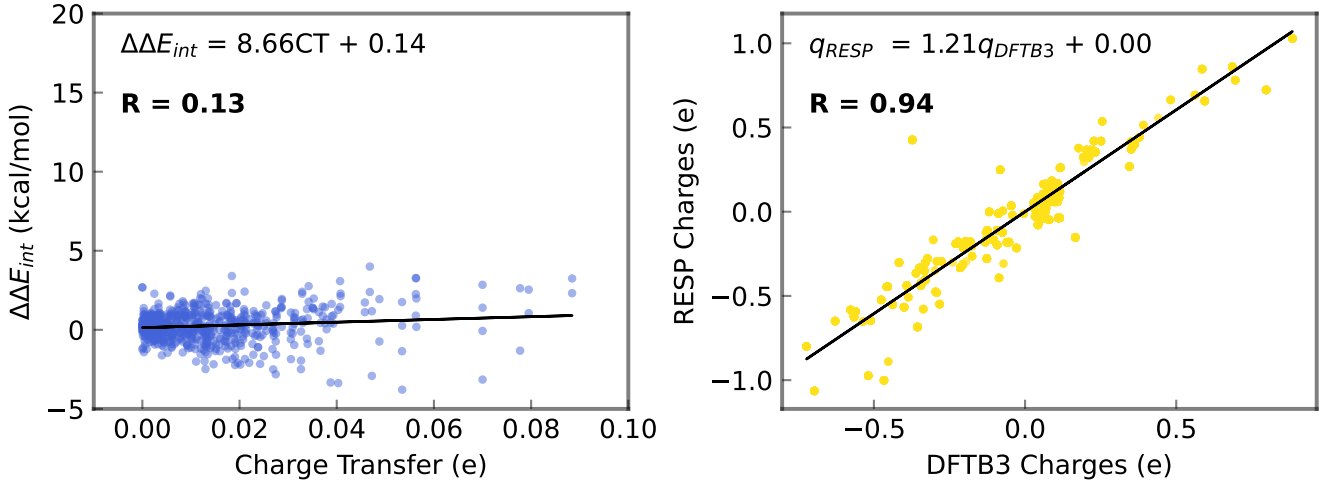

Figure 6.2.: Correlation between the amount of CT and the error of QM/MM to DFTB in HB375 (left). Correlation between the atom charges of GAFF (RESP) and the atom charges of DFTB (Mulliken) in HB375 (right).

Hydrogen bonding is sensitive to the charge model, as observed by replacing GAFF's more polar charges with less polar DFTB charges, which weakens the binding and increases RMSE values. This highlights the need to investigate how DFTB accounts for the polarity of the compounds. In principle, the accuracy of the QM/MM energies depends on both monomer polarity and their polarization response. To evaluate both aspects, we compared vacuum dipole moments from DFTB with ωB97X-V references and assessed the polarization response by subtracting the vacuum dipole from the dipole of the monomer in the complex in both DFTB/GAFF models. For the results, each group of four candlesticks in Figure 6.3 displays vacuum dipoles (first two) and polarization responses (last two) for each bond type. Vacuum dipoles exhibit slightly positive median deviations across many H-bond types, with a noticeable spread extending into negative values. Underestimated polarity was found for nitrogen acceptors and dispersion-dominated (noHB) systems, both of which show negative median deviations. In contrast, polarization responses are consistently

underestimated, as indicated by candlesticks falling below the zero line. Due to its semiempirical nature, DFTB is prone to underestimating both monomer polarity and polarization effects. However, our analysis indicates that the underestimation is particularly pronounced for polarization effects, especially in systems involving nitrogen H-bond acceptors, which had already drawn attention in Figure 6.1 due to elevated errors in the GAFF/DFTB model. This is further supported by additional calculations using PBE-D3(BJ)/def2-SVP and PBE-D3(BJ)/ma-def2-TZVPP, which show a gradual improvement in agreement with the ωB97X-V reference, particularly in capturing polarization effects, see SI Figures A.2, A.3 and A.4.

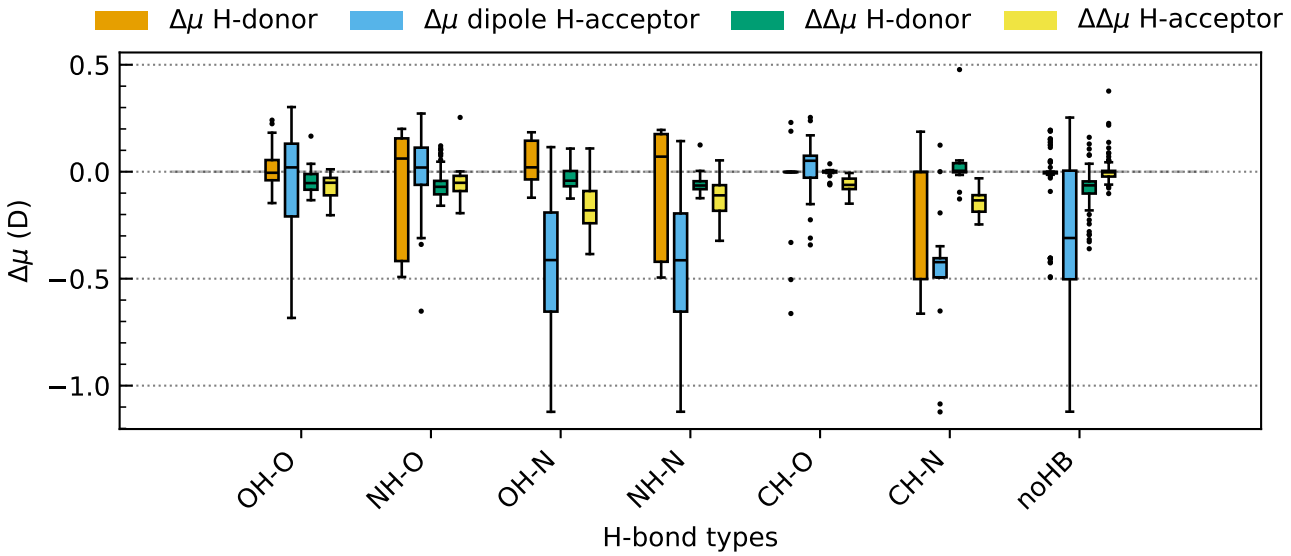

Figure 6.3.: The box plot displays the dipole differences, denoted as $\Delta\mu$, between monomers in vacuum calculated using DFTB and ωB97X-V. Additionally, it shows $\Delta\Delta\mu$, which represents the differences in polarization response of the monomers in the QM regions of the DFTB/GAFF models relative to their polarization response in the ωB97X-V/GAFF models. Dipoles (first two) and polarization responses (last two) of each group of four candlesticks per bond type in HB375. Negative values indicate underestimation in DFTB. The polarization response was calculated as difference between the dipole of the monomer in vacuum and in the complex $\mu^{\text{monomer}}_{\text{response}} = \mu^{\text{monomer}}_{\text{complex}} - \mu^{\text{monomer}}_{\text{vacuum}}$.

We further assessed the performance of the ωB97X-V/GAFF models as a hybrid electron density/-point charge model to determine the extent to which the QM–MM interface may limit accuracy, even when a high-level QM method is employed. Applied to ωB97X-V/GAFF and GAFF/ωB97X-V, it reduces the MSE to 0.2 and 0.0 kcal/mol, respectively, as shown in Figure A.1, and lowers the RMSE to 1.2 and 0.7 kcal/mol, respectively, as shown in Figure 6.1. Slightly negative MSEs are now observed in bond types OH · · · O, NH · · · O, and NH · · · N. Overall, ωB97X-V still gives very accurate results when combined with GAFF. The elevated errors for nitrogen acceptors in GAFF/DFTB are not observed in the GAFF/ωB97X-V model, indicating improved polarization in this model. Smaller improvements in ωB97X-V/GAFF highlight error contributions from the GAFF. Exploring the use of a polarizable FF may offer a potential solution to address these limitations, especially for the nitrogen H-bond acceptors in GAFF.

Dissociation Energy Curves. We extended the analysis beyond equilibrium points using the HB375x10 dataset. The resulting RMSEs and MSEs are shown in the upper panels of Figure 6.4 and Figure A.12. In the region around the scaling factor of 1.0, both methods show comparable accuracy; however, DFTB performs increasingly better at shorter distances, whereas GAFF shows a slight advantage at larger distances. This behavior is consistent with the inherent capacity of DFTB to adapt its charges in response to the local environment through polarization, thereby offering a more accurate description of short-range interactions. A similar plot for the MSE values is provided in the App. SectionA.

Similarly, the differences in polarizability and polarity govern the performance gap between DFTB/GAFF and GAFF/DFTB, with polarizability playing a dominant role at short distances and polarity becoming more relevant at longer separations. This can be rationalized by the properties of the monomers involved in complexes with nitrogen H-bond acceptors shown in Figure 6.3. In these cases, H-donors have higher polarity and higher polarizability than the H-acceptors, showing that the QM region in GAFF/DFTB is less polar and less polarizable than in DFTB/GAFF. (Recall the notation: the monomer on the left is the H-bond donor, and the one on the right is the H-bond acceptor). As shown in Figure 6.4 (panels A and B), DFTB/GAFF, with greater dipoles in the QM zone, yields lower RMSE than GAFF/DFTB at larger distances, falling between DFTB and GAFF. The DFTB/GAFF model shows the highest RMSE among all models for distances smaller than 1.1, whereas GAFF/DFTB already for distances below 1.25, indicated by the shaded regions in panels A and B. For GAFF/DFTB, this region is broader, reflecting the influence of a less polarizable QM zone, most notably nitrogen H-acceptors (yellow candlesticks). This limitation is further evident when comparing the QM/MM models constructed with ωB97X-V and DFTB. As shown by the blue curves in panels C and D, the RMSE difference of these models displays a distinct maximum between f_{dscaling} 1.1 and 1.2, highlighting the benefit of improved polarization in the QM region provided by ωB97X-V. This effect is less pronounced for DFTB/GAFF, where the more polarizable QM zone reduces the error compared to the DFTB and the GAFF calculation. Gray shading in panels A and B highlights areas in which the DFTB/GAFF models introduce an additional error compared to the DFTB and GAFF calculations, and apparently this additional error is smaller for DFTB/GAFF than for GAFF/DFTB.

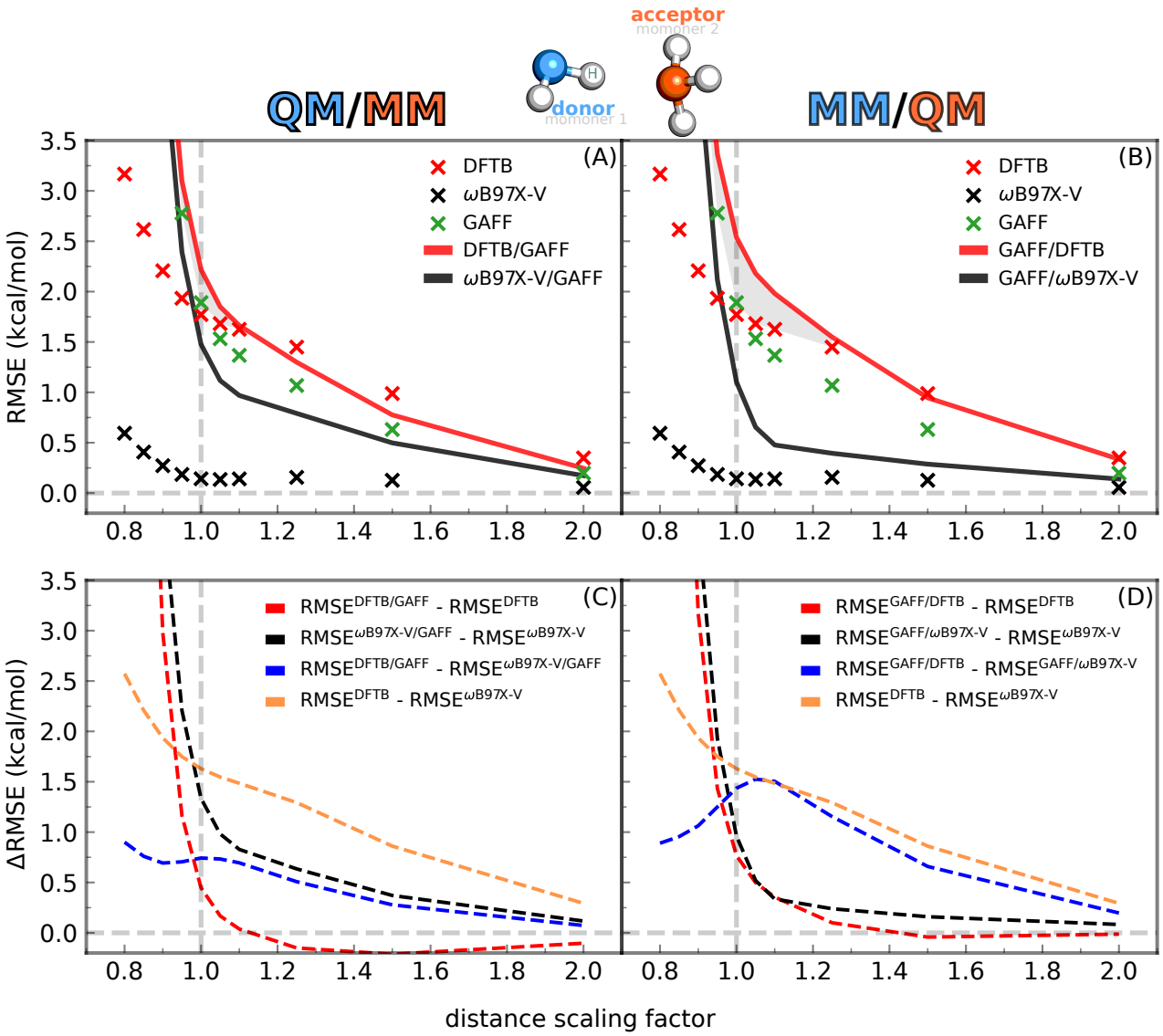

Figure 6.4.: RMSE along the entire dissociation curves in HB375x10. Results are shown for both partitioning schemes: QM/GAFF (left) and GAFF/QM (right), using CCSD(T)/CBS as the reference. QM/MM treats the H-bond donor (monomer 1 in blue) at the QM level and the H-bond acceptor (monomer 2 in orange) at the MM level. MM/QM reverses this assignment. The upper row shows RMSEs between the respective QM or QM/MM methods and the reference. Gray-shaded regions indicate areas where the DFTB/GAFF models introduce additional error compared to the DFTB and GAFF calculations. The panels in the lower row display RMSEs for the differences between the curves shown in the upper row. For visual clarity, the y-axis is limited to 3.5 kcal/mol; the full range for the RMSE and the MSE is shown in Figures A.15 and A.16.

Comparing the QM/MM results obtained with ωB97X-V and DFTB helps to understand the limitations of QM/MM models. The accuracies of ωB97X-V/GAFF and DFTB/GAFF are comparable, whereas the performance gap between GAFF/ωB97X-V and GAFF/DFTB is more evident, as illustrated by the red and black curves in panels A and B. Consistently, the RMSE difference

between ωB97X-V and ωB97X-V/GAFF, shown by the black curve in Figure 6.4C, increases immediately with decreasing distance. In contrast, the corresponding error for GAFF/ωB97X-V in panel D remains small until $f_{\mathrm{dscaling}} \approx 1.1$. These results indicate that the treatment of the H-bond acceptor requires particular attention in QM/MM models. The difference between DFTB/GAFF and ωB97X-V/GAFF, shown by the blue curve in panel C, arises from two factors; (1) a better performance of DFTB/GAFF due to a better description of the H-bond donor in DFTB than for the H-bond acceptor, and (2) a poorer performance of ωB97X-V/GAFF caused by the GAFF description of the H-bond acceptor (Recall the notation: the monomer on the left is the H-bond donor, and the one on the right is the H-bond acceptor). Conversely, the performance gap is larger between the GAFF/QM models, as shown by the blue curve in panel D, which reflects the insufficient description of H-bond acceptors in DFTB. At shorter distances, however, all QM/GAFF models display comparable performance, as evidenced by the similarly rising black and red curves and the gently sloping blue curves in panels C and D of Figure 6.4. This trend underscores the limitations imposed by the QM–MM interface, which persist even when higher-level QM methods are employed.

6.3.1.2. Ionic Hydrogen Bonds

Equilibrium. For biological systems, one central question is how the presence of net charges leads to qualitative differences in the performance of methods compared to neutral complexes. This is of high practical relevance, as biomolecules such as DNA, RNA, and proteins carry significant charges essential to their function. For that reason, we included the structures from the IHB100x10 dataset, composed of various ionic hydrogen bonds; the resulting RMSEs and MSEs are shown in Figure 6.5 and Figure A.7. Overall, DFTB describes ionic H-bonds quite well with an RMSE of 3.96 kcal/mol, corresponding to an RMSE/μ of 20%. While the RMSE is significantly larger compared to its RMSE for the neutral hydrogen bonds, the relative error is smaller than that of the neutral hydrogen bonds, which is ca. 30%. The method outperforms PM6, which showed 5.21 kcal/mol, and is comparable to GFN2-xTB with 3.34 kcal/mol.[273] Higher-level methods were reported to show significantly lower RMSEs, with MP2/CBS at 0.45 kcal/mol and DSD-BLYP-D3 at around 1.3 kcal/mol. Our calculations show ωB97X-V further improved accuracy with an RMSE of 0.38 kcal/mol. Unlike the case of HB375x10, IHB100x10 reveals a clearer performance gap between the QM and QM/MM results. Transitioning from DFTB to DFTB/GAFF increases the RMSE by 2.75 kcal/mol, while transitioning from ωB97X-V to ωB97X-V/GAFF increases by 5.62 kcal/mol. The RMSEs for the ωB97X-V/GAFF models lie between 5.0 and 6.0 kcal/mol, higher than those of DFTB and close to the DFTB/GAFF models with around 6.7 kcal/mol. This contrasts with the case of HB375x10, where ωB97X-V/GAFF models outperform DFTB, DFTB/GAFF, GAFF/DFTB, and GAFF. The calculation showed that GAFF is comparable to that of all QM/GAFF models tested, with the RMSE of 7.35 kcal/mol. We found that DFTB systematically overestimates anionic interactions involving CH H-bond donors or $\mathrm{OH}\cdots\mathrm{O}^-$ H-bonds. (Recall the notation: the monomer on the left is the H-bond donor, and the one on the right

is the H-bond acceptor). This tendency is even more pronounced for ωB97X-V/GAFF, as shown in Figure A.7. As shown below in Section 6.3.2 (PL-REX dataset), in protein environments, this overestimation becomes notable in regions rich in anions, such as the carboxylate group, forming multiple anionic H-bonds.

Our calculations showed that the capability to describe CT significantly enhances the accuracy of DFTB relative to GAFF and the DFTB/GAFF models. This is evidenced by the notably lower RMSE of ca. 4.0 kcal/mol for DFTB compared to values near 7.0 kcal/mol for the alternative DFTB/GAFF models, as shown in Figure 6.5. A similar trend is reflected in the MSE, where DFTB achieves 1.7 kcal/mol, while the other methods exhibit MSEs ranging from 5 to 6 kcal/mol, see Figure A.7. The better performance of DFTB is further supported by a stronger correlation between the magnitude of CT and model error in both DFTB and GAFF, as illustrated in Figure 6.6 (right). Again, reference calculations for CT within each complex via natural bond orbital (NBO) analysis using ωB97X-V/ma-def2-TZVPP validated the results obtained with DFTB. The results, provided in the Figure A.8, confirm that DFTB closely reproduces the amount of CT compared to the ωB97X-V reference.

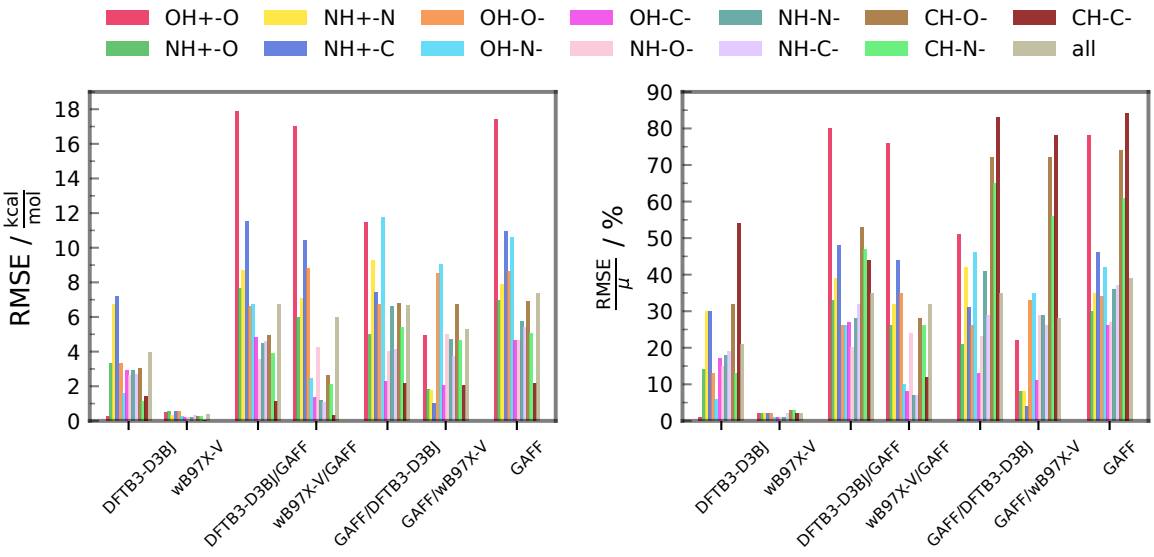

Figure 6.5.: RMSE (left) and RMSE/μ (right) for ΔE_{int} per method and H-bond type in IHB100x10. DFTB and ωB97X-V as QM, and GAFF as MM. CCSD(T)/CBS as reference

Comparison between the methods that do not include CT moves the focus to the charge model. In HB375x10, slightly higher RMSE and MSE values are observed for the DFTB/GAFF models, which potentially relate to less polar DFTB charges compared to the GAFF charges (Figure 6.2, left). In IHB100x10, the trend subtly shifts, with the QM/MM models showing marginally smaller error than GAFF (Figure 6.5). This shift is consistent with a reduced polarity difference for charged species: linear fits of DFTB versus GAFF charges yield slopes of 1.21 in HB375x10 and 1.09 in IHB100x10 (Figure 6.6, left), and even decrease to 1.03 for charged systems only.

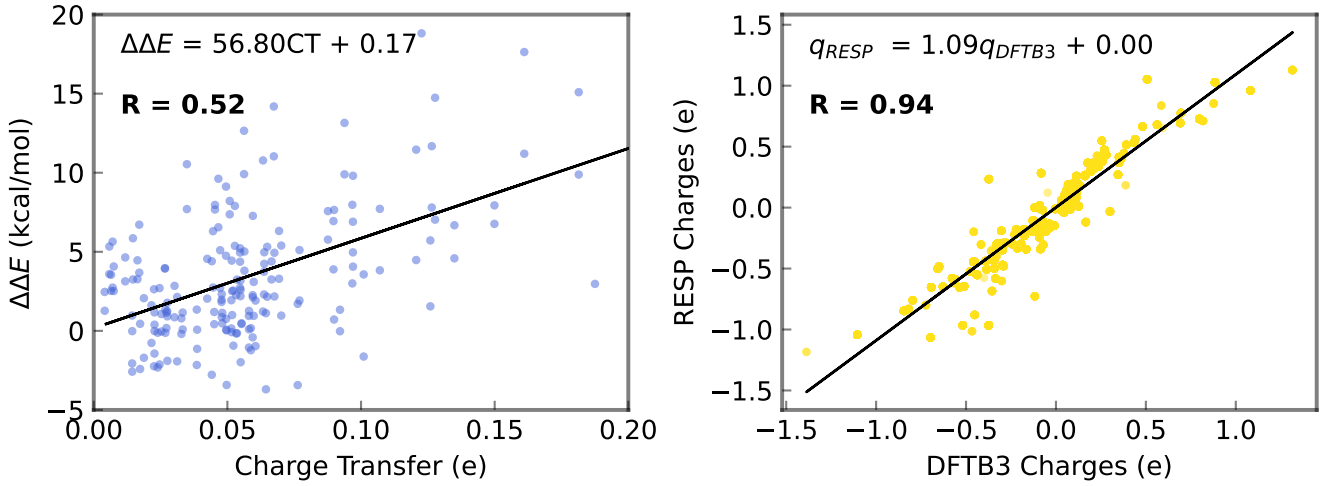

Figure 6.6.: Correlation between the amount of CT and the error of QM/MM to DFTB in IHB100 (left). Correlation between the atom charges of GAFF (RESP) and the atom charges of DFTB (Mulliken) in IHB100 (right).

Similar to our analysis for HB375, we examined vacuum dipoles and polarization responses for each bond type in IHB100, using ωB97X-V as the reference. (Recall the notation: the monomer on the left is the H-bond donor, and the one on the right is the H-bond acceptor). Each group of four candlesticks in Figure 6.7 displays the vacuum dipoles (first two) and polarization responses (last two) for the respective monomers. In contrast to HB375, IHB100 shows overestimated vacuum dipoles for anionic H-bond acceptors. Moreover, the strongest underestimations in polarization response are observed for H-bond acceptors interacting with cationic H-bond donors, most notably in the $NH^+ \cdots O$ and $NH^+ \cdots N$ interactions. The polarizability of cations is described fairly well. Vacuum dipoles and polarization responses can be improved by using PBE-D3(BJ)/def2-SVP and PBE-D3(BJ)/ma-def2-TZVPP, which show gradually improved agreement with the ωB97X-V reference (Figures A.9-A.11). Note that the bond types involving nitrogen and carbon anions, in fact, contain a single H-acceptor, the cyanide ion interacting with several different H-donors. The cyanide species is a notoriously difficult case for DFTB as well as SQM in general, for instance, systematically overestimating the vacuum dipole. Therefore, the apparent poor performance for these bond types merely reflects this specific problem, and shall not be generalized to more diverse chemical environments.

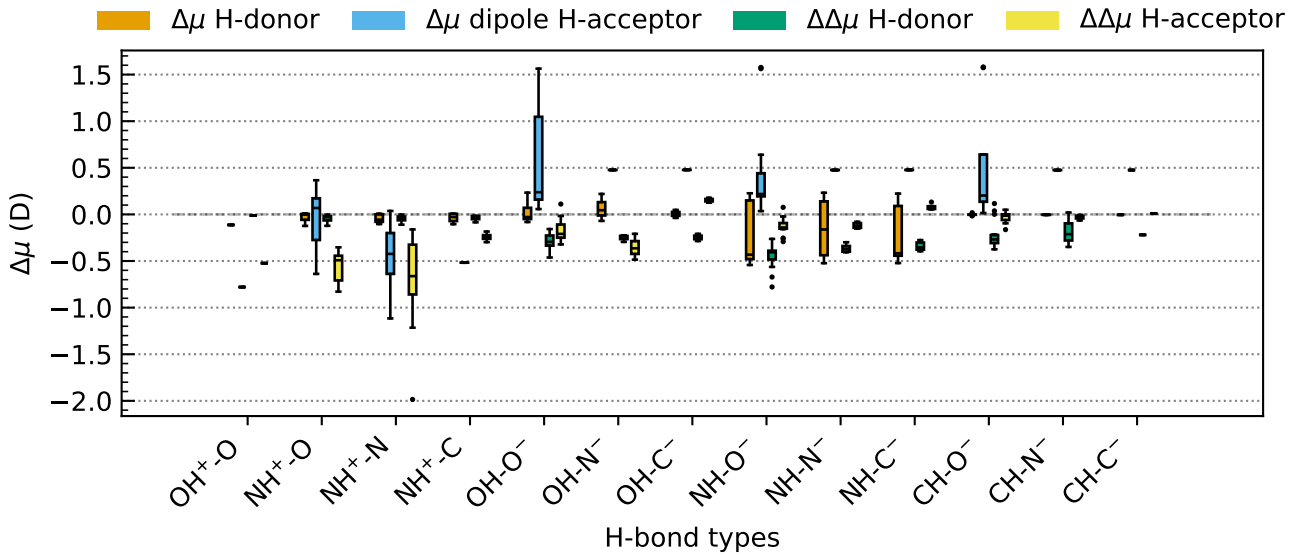

Figure 6.7.: The box plot displays the dipole differences, denoted as $\Delta\mu$, between monomers in vacuum calculated using DFTB and ωB97X-V. Additionally, it shows $\Delta\Delta\mu$, which represents the differences in polarization response of the monomers in the QM regions of the DFTB/GAFF models relative to their polarization response in the ωB97X-V/GAFF models. Dipoles (first two) and polarization responses (last two) of each group of four candlesticks per bond type in IHB100. Negative values indicate underestimation in DFTB. The polarization response was calculated as difference between the dipole of the monomer in vacuum and in the complex $\mu^{\text{monomer}}_{\text{response}} = \mu^{\text{monomer}}_{\text{complex}} - \mu^{\text{monomer}}_{\text{vacuum}}$.

The ωB97X-V/GAFF models provide only modest improvements over GAFF in the IHB100x10 set, in contrast to the more substantial improvements observed for HB375x10. While the enhancement in accuracy arises from improved electrostatic interactions, the model does not account for missing CT, which limits its performance in IHB100x10. The RMSE for all tested QM/MM models falls between the two ωB97X-V/GAFF models at ca. 5.5 kcal/mol and the highest at 7.4 kcal/mol for GAFF. A more notable reduction is observed in MSE (Figure A.7), which decreases from 6.0 kcal/mol in GAFF to 1.7 and 3.2 kcal/mol in the ωB97X-V/GAFF models. ωB97X-V/GAFF shows overestimated interactions in the $\mathrm{OH}\cdots\mathrm{O}^-$ and $\mathrm{NH}\cdots\mathrm{O}^-$ bond types, with MSE of −3.2 and −3.7 kcal/mol, respectively (Figure A.7). (Recall the notation: the monomer on the left is the H-bond donor, and the one on the right is the H-bond acceptor). In these systems, the QM region includes the H-donor surrounded by the MM charges of the O^- H-bond acceptor. Notably, this overestimation is absent in calculations using GAFF and ωB97X-V (see App., Figure A.7). ωB97X-V exhibits stronger electrostatics than DFTB (Figures A.9–A.11), which may increase its susceptibility to being influenced by adjacent point charges in the MM region.

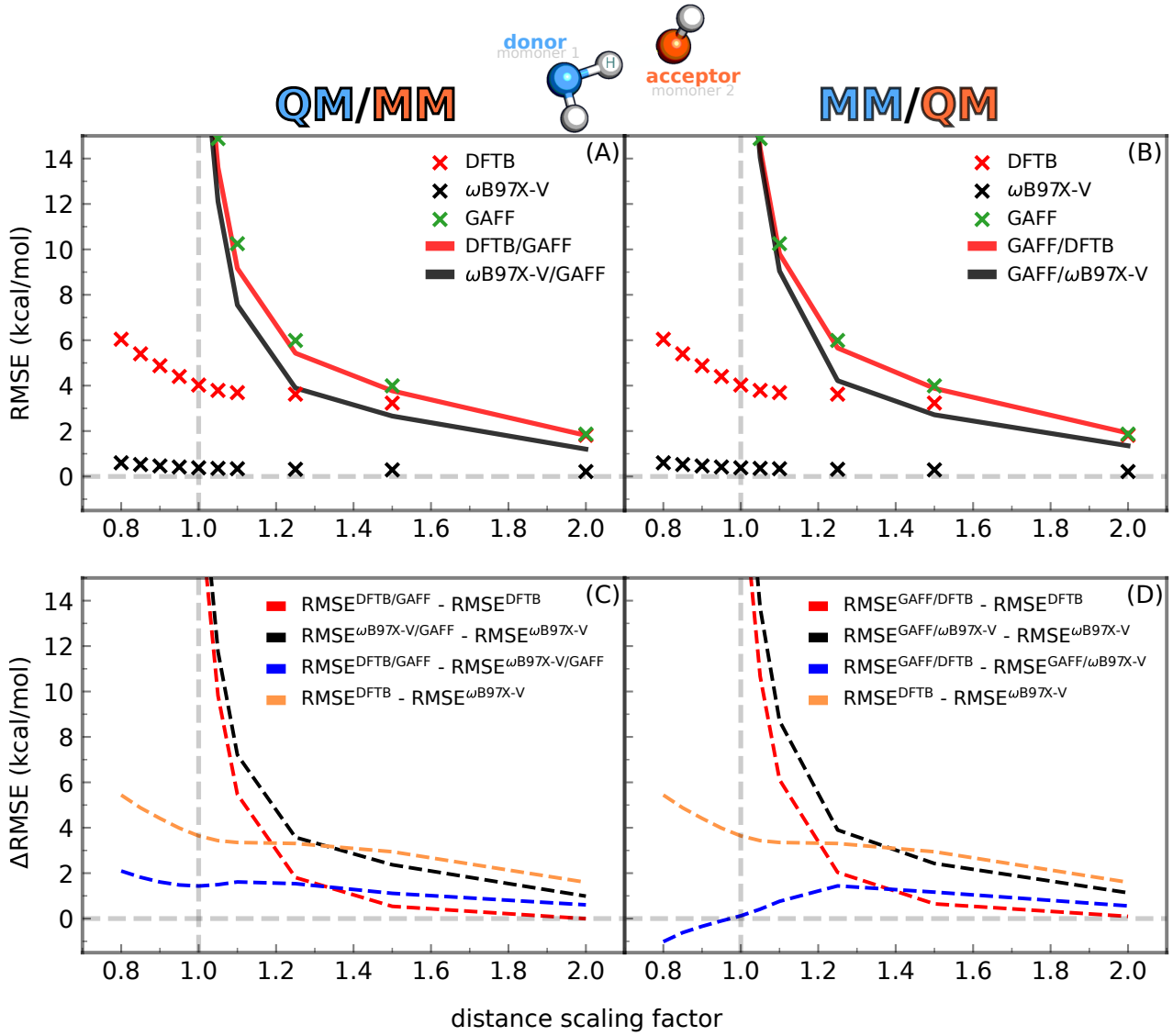

Figure 6.8.: RMSE along the entire dissociation curves in IHB100x10. Results are shown for both partitioning schemes: QM/GAFF (left) and GAFF/QM (right), using CCSD(T)/CBS as the reference. QM/MM treats the H-bond donor (monomer 1 in blue) at the QM level and the H-bond acceptor (monomer 2 in orange) at the MM level. MM/QM reverses this assignment. The upper row shows RMSEs between the respective QM (QM/MM) methods and the reference. The lower row shows the differences between the curve in the upper row. For visual clarity, the vertical axis is limited to 15 kcal/mol; the full range for the RMSE and the MSE is shown in Figures A.21 and A.22.

Dissociation Energy Curves. We extended the analysis beyond the equilibrium structures by using the IHB100x10 dataset. The resulting RMSEs and MSEs are shown in the panels A–B of Figure 6.8 and Figure A.18. Additionally, we monitored the differences in these measures between pairs of models, which are shown in panels C–D. At $f_{\text{dscaling}} = 1.0$, both QM models exhibit RMSE values comparable to those reported at equilibrium points (Figure 6.5). All QM/GAFF models show RMSEs in the range of 22–24 kcal/mol at $f_{\text{dscaling}} = 1.0$. As shown by the red and black lines in the lower panels, both DFTB/GAFF and ωB97X-V/GAFF models exhibit a comparable increase in RMSE relative to the corresponding QM models. In contrast, the RMSE difference

between the DFTB/GAFF and ωB97X-V models, shown as the blue line in the lower panel, remains below 2 kcal/mol over the entire range of distances, which is especially remarkable at short distances where both RMSE are in the order of 100s kcal/mol. Interestingly, this difference closely follows the RMSE difference between ωB97X-V and DFTB, shown as the orange line in panels C–D. (Note that the blue curve is a small difference of two large values, which thus carries a considerable statistical uncertainty, and so merely a qualitative agreement with the orange curve is sought.) This suggests that the QM/MM models featuring both QM methods carry an error due the presence of the QM–MM boundary, which is of a very similar magnitude. Further, they appear to especially underperform at shorter distances. Any inaccuracy caused by the QM method of choice, such as when passing from ωB97X-V/GAFF to DFTB/GAFF, is very minor compared to the error due to the QM–MM interface.

The extremely large average error of the QM/MM methods observed at short distances can be attributed to the lack of CT and limited polarization, or using inappropriate Lennard-Jones (LJ) potential parameters for (typically short) ionic hydrogen bonds. To identify the source of the error, we decomposed the interaction energies yielded by the QM/MM models into the contributions from the LJ potential and all other interactions, and analyzed their respective contributions to the RMSE. The results shown in Figure A.19 reveal that at short distances, the LJ potential dominates the RMSE of all QM/MM models entirely. An extended analysis in the App. Section A provides more details including the identification of the complexes in which this failure occurs to the largest extent. This illustrates how the employed LJ parameters, developed typically for interactions of electro-neutral molecules, are inappropriate for short ionic hydrogen bonds. It appears that it might be beneficial to reoptimize the LJ parameters for the description of ionic H-bonds here.

The similarity between the DFTB/GAFF models and ωB97X-V/GAFF models in IHB100x10 highlights the reduced role of polarization and the increased relevance of the missing CT. In HB375x10, weak polarizability of individual monomers leads to increased error for the DFTB/-GAFF calculations relative to DFTB and GAFF starting at distances $f_{\mathrm{dscaling}} < 1.1$ and 1.25, respectively, see Figure 6.4 A-B. This feature is absent in IHB100x10; instead, both QM/MM models display elevated RMSEs at short distances relative to their QM counterparts starting at $_{\mathrm{dscaling}} = 1.25$, suggesting a dominant error contribution from missing charge transfer. Supporting this, the RMSE difference between the DFTB/MM models and ωB97X-V/MM models remains nearly constant at 2.0 kcal/mol in IHB100x10 (Figure 6.8 C-D, blue curves), whereas a gradual increase in error was observed at shorter distances in HB375x10 (Figure 6.4).

6.3.2. Microenvironment Models

Some features of NCI cannot be captured in datasets consisting of isolated dimers, such as those discussed above. In particular, such pairwise models cannot cover any solvent, cooperative, and many-body effects that are prevalent in the condensed phase.[302] To explore this in the context of our study, we considered a subset of six receptor–ligand complexes from the PL-REX dataset, which comprises truncated active sites from several different proteins with ligand molecules bound.[280] Our computations include FF calculations with AMBER and GAFF, QM calculations with DFTB, as well as both possible DFTB/MM partitionings ("AMBER/DFTB" – receptor is MM region, ligand is QM region; "DFTB/GAFF" – receptor is QM region, ligand is MM region).For DFTB, the D3(BJ) dispersion correction was considered either with or without the three-body term to assess the significance of many-body dispersion interactions in the condensed phase. This section does not include any new ωB97X-V or ωB97X-V/MM data, because of SCF convergence failures observed in pilot calculations. Instead, the interaction energies taken from the PL-REX paper, which were obtained on the level ωB97X-D3(BJ)/DZVP, are considered as reference. Interaction energies are reported for individual ligands per system, and the results are exemplified in Figure 6.9 for system 5. In addition, Table 6.1 summarizes the RMSE and MSE values for the interaction energies across all systems.

The overall RMSE values of all models range from 4 to 7 kcal/mol, corresponding to a maximum relative error of 7.4%. DFTB exhibits an RMSE of 7.3 kcal/mol, which is larger than those of all other models: 5.7, 3.8, and 5.8 kcal/mol for AMBER/GAFF, DFTB/GAFF, and AMBER/DFTB, respectively. Particularly for systems 2 and 5, DFTB yields RMSEs ca. 4 kcal/mol higher than those of AMBER/GAFF. For comparison, DFTB exhibited RMSE of 1.7 kcal/mol with a relative error of 30% on the HB375x10 dataset and 4.0 kcal/mol with a 20% error on IHB100x10. This indicates that certain interactions in these systems may not be accurately described by DFTB. Additionally, DFTB is the only method that systematically predicts stronger interactions than the reference, with an overall MSE of –4.5 kcal/mol. This behavior contrasts with the results obtained from pairwise models, which predominantly underestimate interaction energies. Many-body dispersion interactions become more relevant in the condensed phase. Consistent with this trend, including the three-body term of the D3(BJ) correction in DFTB reduces systematic overbinding across all systems, lowering the MSE from −4.5 to −1.8 kcal/mol and the RMSE from 7.3 to 5.9 kcal/mol.

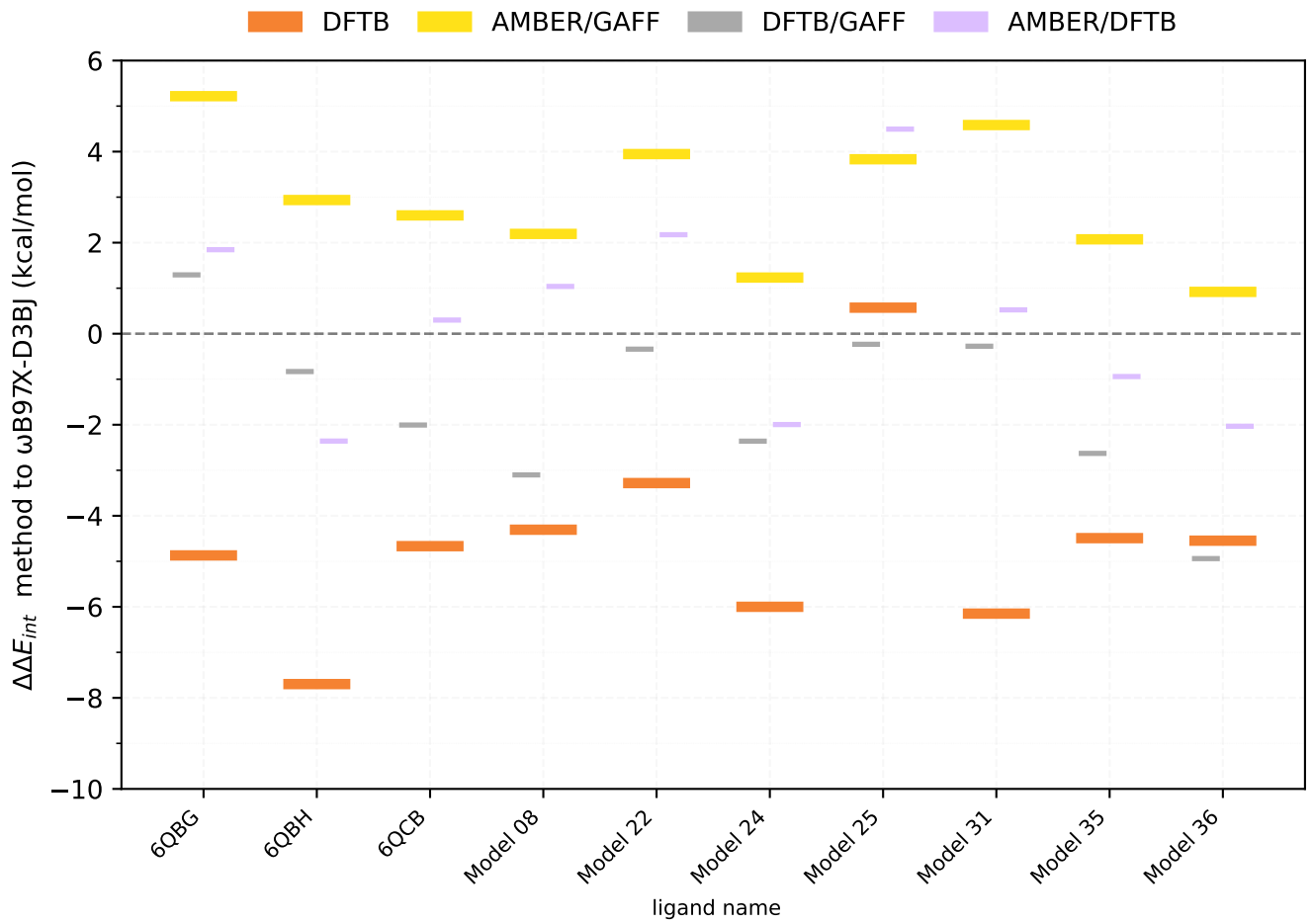

Figure 6.9.: Interaction energies for individual ligands in system 05-Cath-D (human cathepsin D) from the PL-REX dataset. The receptor charge is −2 and the charge for all ligands is 0. $\Delta\Delta E_{\text{int}}$ values were computed as the difference between the binding energy ΔE_{int} obtained from each method and the corresponding ωB97X-D3(BJ) reference from PL-REX. The reference interaction energies vary from −150 to −113 kcal/mol. The DFTB calculations involve the three-body contribution to the D3(BJ) correction.

A word of caution is warranted regarding the use of the PL-REX in our study. The structures in PL-REX are derived from protein environments; the data exhibit greater heterogeneity and less systematic variation compared to the data from NCIA. For example, ligands bound to the same receptor can carry different net charges, including both neutral and charged species within a single set. Even among neutral ligands, differences in binding pose can lead to substantial variations in electrostatic contributions, and the QM/MM partitioning may cross multiple hydrogen bridges. These factors limit the generalization of trends due to the non-systematic selection of systems. Nonetheless, the results enable evaluation of model performance.

As it turns out, the individual complexes in the PL-REX dataset do in fact differ in the amount of hydrogen bonding, as reflected by the mean numbers of hydrogen bonding contacts that are shown in Table A.8. There are two distinct groups of systems in the PL-REX dataset: The first group (consisting of systems 2, 5, and 6) is characterized by, on average, eight hydrogen bond donors and acceptors. Notably, these complexes consistently exhibit a systematic overestimation of interaction

Table 6.1.: Summary of interaction energies compared to ωB97X-D3(BJ)/DZVP for all microenvironment models.

	System	2	3	5	6	7	9	All
RMSE (kcal/mol)	DFTB[a]	9.54	8.31	7.15	10.09	2.97	3.29	7.29
	DFTB[b]	6.52	7.00	5.00	7.18	4.72	4.65	5.90
	AMBER/GAFF	5.63	6.77	3.25	7.79	3.51	5.00	5.65
	DFTB/GAFF	3.40	5.37	2.31	3.52	3.87	3.44	3.76
	AMBER/DFTB	3.92	6.41	2.11	7.23	4.34	6.85	5.76
MSE (kcal/mol)	DFTB[a]	-8.87	-6.96	-6.86	-9.32	1.69	0.88	-4.46
	DFTB[b]	-5.58	-5.20	-4.54	-6.15	4.03	3.47	-1.83
	AMBER/GAFF	4.23	4.58	2.95	4.32	-1.90	0.96	2.54
	DFTB/GAFF	0.79	3.90	-1.54	-1.47	-1.34	-0.82	-0.01
	AMBER/DFTB	-1.26	4.47	0.30	-4.08	2.02	5.38	1.61
RMSE/μ (%)	DFTB[a]	6.2	16.0	5.3	15.4	3.1	3.7	7.4
	DFTB[b]	4.2	13.5	3.7	11.0	4.9	5.2	6.0
	AMBER/GAFF	3.6	13.1	2.4	11.9	3.6	5.6	5.7
	DFTB/GAFF	2.2	10.4	1.7	5.4	4.0	3.9	3.8
	AMBER/DFTB	2.5	12.4	1.5	11.0	4.5	7.7	5.9

[a] Using D3(BJ) without three-body contribution. [b] Using D3(BJ) with three-body contribution.

(negative MSEs) by DFTB, resulting in the highest RMSE. By contrast, the second group (systems 3, 7, and 9) only has a mean number of hydrogen bond donors and acceptors of three. Within this group, systems 7 and 9 exhibit the lowest RMSE for DFTB among all interaction models and positive MSEs. The fact that System 3 deviates from this trend – by DFTB showing the highest RMSE within the group – is likely due to the presence of several halogen bonds, which constitute a known limitation in DFTB and other SQM.[32] This observation prompted a closer analysis of ionic hydrogen bonds relevant to protein systems. Two types proved most informative, as shown in the previous analysis, see Figure A.7: (1) CH or OH donors binding to Asp/Glu carboxylates, which tend to cause overestimation, and (2) NH donors binding to Asp/Glu carboxylates or O/N acceptors binding to Lys/Arg ammonium groups, which lead to underestimation. Our analysis reveals that the overestimation of DFTB is correlated with the occurrence of the first bond type, see Table A.8. While the second type of H-bond contributes to the underestimation of DFTB. These trends explain the opposing signs of DFTB MSEs for systems 2, 5, and 6 compared to systems 7 and 9. The DFTB/MM, on the other hand, mitigates the overestimation resulting from error cancellation caused by adding an underestimation introduced by the QM/MM interface as discussed above.

For the DFTB/MM models, a crucial feature is that both partitionings employ identical van der Waals parameters. Consequently, any observed differences in E_{int} between the two partitionings

for a given system arise exclusively from differences in electrostatic interactions, which are governed by the charge distributions in the MM region and the polarity as well as the polarizability of the QM region. Differences in charge distribution can emerge from differences in GAFF, AMBER, and DFTB-derived charges, as well as the net charge assigned to the compounds. For example, System 6, which has the largest charges in the dataset, has charges of +5 for the receptor and +1 for the ligand. Here, the two DFTB/GAFF partitionings exhibit the largest RMSE difference, amounting to 3.7 kcal/mol. The decomposition of interaction energy reveals that electrostatic interactions are weakly attractive, contributing ca. 3 to 6 kcal/mol, while van der Waals interaction dominates the interaction profile, see Table A.8. Given the extreme charge conditions, it is plausible that this system is more prone to generating variations in charge distributions between the partitionings.

The lower RMSE observed for the DFTB/GAFF models compared to the MM and DFTB calculations may result from error compensation between subsystems. DFTB calculations overestimate the interaction energy while AMBER/GAFF underestimates it on average, as indicated by the opposite signs of the corresponding MSE values. DFTB/MM calculations with both partitionings yield results that are closer to the target on average, and this is accompanied by a smaller RMSE. We evaluated CT on the level of DFTB, which turned out to not deviate from the higher-level reference (Section 6.3.1). For PL-REX, no significant correlation was found between the extent of charge transfer.

6.3.3. Scaling of the QM-MM Electronic Interaction

Our analysis highlighted the importance of accurate electrostatic components, indicated by errors introduced by CT and polarization. The "quick and dirty" way to influence the magnitude of the electrostatic interactions is to scale the entire interaction by means of a factor λ introduced in Equation 2.34. The effect of this scaling is proportional to electrostatic interactions in the system, as shown in Figure A.35. In fact, approaches based on scaling electrostatics were previously introduced to mitigate various problems in both purely classical and QM/MM simulations. (i) One is the missing electronic polarizability of the MM surroundings of charged particles, which can be compensated for by scaling the charges of the ions by the inverse square root of the optical dielectric constant of the medium.[303,304] (ii) Another is the over-polarization or artificial charge transfer near the QM/MM boundary, especially for charged QM regions, brought about by the nearby MM charges. Some previous solutions relied on special treatments in the QM region, such as a method developed to describe phosphate chemistry with DFTB.[141] Still, the general underlying idea is to reduce the strength of the QM–MM interactions.

We applied scaling factors λ ranging from 0.80 to 1.80. The effects of scaling on the dissociation curve in HB375x10 and IHB100x10 are shown in the Section A of the App. Applying a charge scaling factor of 1.30 can improve the RMSE by ca. 0.5 and 2.0 kcal/mol for HB375x10 and IHB100x10, respectively. The subset of best performing scaling factors lies in the range of $\lambda = 1.25 - 1.40$. The order may vary slightly along the full curves, as shown in Section A of

the App. Table 6.2 summarizes the effects of scaling on equilibrium energies, while the effects on individual H-bond types in HB375x10 and IHB100x10 are shown in Figures A.33 and A.34, respectively. Overbinding appears in certain bond types of both DFTB/GAFF models, despite being completely absent in the unscaled cases. At equilibrium energies, scaling up the QM-MM electronic interaction can reduce the RMSE of DFTB/GAFF or GAFF/DFTB by 0.36-0.5 kcal/-mol and 0.78-1.39 kcal/mol for the HB375x10 and IHB100x10 datasets, respectively. Nevertheless, scaling the interaction applied to the ωB97X-V/GAFF models did not improve RMSE or MSE for HB375x10 and IHB100x10 (Table A.9-A.12). This suggests that scaling is only effective for models with systematic underestimation or overestimation, particularly in terms of polarity and polarization. The lack of improvement indicates a potential limit to the benefits of scaling when applied to an already well-polarized model. As the QM/MM interface does not allow CT, these models clearly require correction for CT effects for further improvements.

Table 6.2.: Subset of MM charge scaling factors λ that optimize RMSE and MSE in HB375x10 and IHB100x10.

λ	RMSE, kcal/mol	RMSE, relative (%)	MSE, kcal/mol	MSE, relative (%)
HB375x10				
		DFTB		
	1.70	24.83	1.16	18.85
		DFTB/GAFF		
1.00	1.78	29.27	1.40	25.54
1.25	1.28	21.85	0.42	10.63
1.30	1.33	21.73	0.22	7.48
		GAFF/DFTB		
1.00	2.14	30.84	1.41	24.19
1.25	1.78	26.49	0.46	9.33
1.30	1.81	26.91	0.26	6.15
IHB100x10				
		DFTB		
	3.98	24.96	1.71	6.32
		DFTB/GAFF		
1.00	6.72	33.98	5.35	30.11
1.20	5.81	23.66	1.54	10.18
1.25	5.94	22.36	0.36	4.13
		GAFF/DFTB		
1.00	6.70	39.93	5.18	31.28
1.20	5.31	34.69	1.78	14.89
1.25	5.41	34.78	0.85	10.48

Finally, it turned out impossible to identify an optimal range of λ values for the scaling of QM-MM interactions in the PL-REX subset. As shown in Table 6.3, the optimal scaling factors for the individual systems were generally lower, and there were even several systems for which the unscaled calculations ($\lambda = 1$) performed the best. This is consistent with our findings for the ωB97X-V/GAFF models for the pairwise models. Here, we demonstrated no benefit from charge scaling, which we attributed to the model's more accurate electrostatics. A similar explanation may apply here; the improved polarization in the cluster models has probably diminished the need for scaling. These results caution against transferring λ values optimized for pairwise models to condensed-phase systems.

Table 6.3.: QM–MM electronic interaction scaling applied to PL-REX subset. RMSE for standard QM/MM calculation, optimal λ, and achieved improvements Δ in kcal/mol.

	System	2	3	5	6	7	9
RMSE (kcal/mol)	DFTB/GAFF	3.40	4.8	2.31	1.76	3.87	3.44
	λ	1.0	1.1	1.0	0.9	1.0	1.0
	Δ	0.0	−0.57	0.0	−1.76	0.0	0.0
	AMBER/DFTB	3.92	4.29	2.11	3.50	4.25	4.10
	λ	1.0	1.2	1.0	0.85	1.05	1.1
	Δ	0.0	−2.12	0.0	−3.73	0.09	−2.75

6.4. Summary and Conclusion

We investigated non-covalent interactions in neutral and ionic hydrogen-bonded complexes to assess the limitations imposed by the QM–MM interface on model accuracy. ωB97X-V and DFTB are chosen as representative methods for DFT and SQM, respectively. On the side of the MM force field, GAFF is employed for small molecules, while AMBER is used for proteins.

For neutral complexes in the HB375x10 dataset, interaction energies computed using GAFF, DFTB, and DFTB/GAFF models yield comparable RMSEs, and relative errors around 30%, ranging from 1.5 kcal/mol for GAFF to 2.1 kcal/mol for DFTB/GAFF. Among all tested approaches, the GAFF/ωB97X-V model achieves the lowest RMSE of 0.7 kcal/mol, establishing a practical upper bound for the accuracy of QM/MM models employing GAFF. The observed small magnitude of charge-transfer (CT) and its weak correlation with the errors suggest that the discrepancies are more likely attributable to differences in model polarity and polarizability.

In contrast to the neutral complexes, the ionic complexes in IHB100x10 show more significant amounts of CT and a clear correlation between QM/MM error and the extent of CT in the system. Accurate treatment of these systems requires that CT be included within the QM region, and that the QM–MM boundary does not cross the hydrogen bond. This necessity is evident from the sharp

increase in RMSE when transitioning from QM to QM/MM models. For example, at equilibrium geometry, the ωB97X-V model yields an RMSE of 0.4 kcal/mol, while the GAFF/ωB97X-V model rises to 5.3 kcal/mol. DFTB/GAFF models perform comparably, with RMSEs around 7.0 kcal/mol. At $f_{\mathrm{dscaling}} = 1.0$, RMSEs reach up to 20 kcal/mol, underscoring the importance of charge redistribution in capturing equilibrium interactions.

Consistently across both datasets, the choice of the QM method has a limited impact on the performance of the QM/MM models for shorter distances, which tend to yield comparable E_{int}. The poor performance of QM/MM methods at shorter interatomic distances originates primarily from unoptimized LJ parameters, as the analysis of results revealed that the LJ term dominates the overall error. These findings challenge the common practice of directly adopting unmodified FF LJ parameters in QM/MM calculations and highlight the need to refine them to better describe short-range interactions. The patterns in RMSE values suggest that including the H-bond acceptor in the QM region is more critical than including the donor. Generally, the absence of charge transfer and the underestimation of polarization emerged as the dominant sources of error in the evaluated QM/MM models. To assess the sensitivity of electrostatic embedding, we applied QM–MM electronic interaction scaling, resulting in RMSE reductions of up to 0.5 kcal/mol for HB375x10 and 2.0 kcal/mol for IHB100x10 in DFTB-based models. Optimal scaling factors ($\lambda = 1.25 - 1.35$) were consistent across distances, although overbinding was observed in specific H-bond types. In contrast, scaling had no benefit for ωB97X-V/GAFF models, indicating its limited usefulness when electrostatic interactions are already well-represented.

To further assess the performance of QM/MM models, we extended our analysis to a small subset of cluster-type microenvironment systems from the PL-REX dataset, which represent realistic ligand–receptor interactions. In contrast to pairwise models, these systems feature a QM region embedded within a densely populated molecular environment, often involving multiple H-bond donors and acceptors. The increased system size results in a more extensive QM–MM interface, where atoms from both regions are positioned in close proximity to each other. Despite this added complexity, studied models yielded reasonable RMSEs ranging from 4 to 7 kcal/mol, with a maximum relative error of only 7.4%. This is notably lower than the >30% relative errors observed for the HB375x10 and IHB100x10 datasets. However, the structural heterogeneity within the PL-REX set complicates the identification of systematic trends, as discussed in detail in Section 6.3.2.

Previous studies by others highlighted the limitations of methods parametrized for pairwise models when applied to condensed-phase systems, primarily due to the exclusion of cooperative effects such as non-classical many-body responses.[302] For many-body force fields derived from gas-phase data, the neglect of polarization–exchange coupling has been shown to result in overpolarization in condensed environments[305], while the omission of CT effects leads to underpolarization[306]. The extent to which these two phenomena interact and counterbalance each other appears to depend strongly on the system's structural conformation.[306] Importantly, it was demonstrated that while SQM methods generally underestimate binding energies in the gas phase, they tend to overestimate those in solution.[93] Our current results show a significant difference between pairwise

and microenvironment-based models. For instance, DFTB tends to underestimate H-bonds for the pairwise systems but occasionally overestimates interaction energies in PL-REX systems, similar to Ref. [93]. Attempts to improve accuracy by applying QM–MM scaling factors optimized for pairwise systems did not yield any improvements for the PL-REX structures. In light of this observation, it can be said that greater attention should be paid to the question of transferability when models developed under vacuum conditions are applied to condensed-phase environments.

It is worth noting that our analysis focuses on the binding energy, while in practical applications, the most relevant quantity is the binding free energy. The accuracy in predicting binding free energy values can benefit from enthalpy–entropy compensation effects[307], which could reduce some of the systematic errors observed in the binding energy. This raises the possibility that errors in QM/MM binding free energies may be smaller than what is suggested by errors in binding energies. To this end, the use of free energy perturbation or reweighting schemes to explore perturbations between MM and QM levels represents an interesting direction for future work.[37,135]

Apart from model selection and evaluation criteria, further progress in the development of QM/MM stems from improved, physics grounded frameworks, which can help mitigate boundary artifacts and better capture polarization effects.[38] These are especially the polarizable embedding [146,254,308,309] and adaptive QM/MM schemes.[149,150,156] In any new development, greater standardization of QM/MM protocols may facilitate methodological progress by mitigating inconsistencies among different implementations.[247,248] Furthermore, systematic evaluation strategies, such as charge-shift analysis,[310] can guide the adjustment of the QM region size according to the extent of charge transfer between regions. An additional promising avenue for future development lies in using machine learning models to refine the QM/MM coupling rather than merely correcting internal QM energies. Here, several strategies have been developed to incorporate electrostatic embedding into ML-based QM/MM frameworks for short- and mid-range interactions. Recent advances include range-corrected deep learning potentials, which refine short-range QM and QM-MM interactions to achieve higher accuracy,[214,219,311] as well as (QM)ML/MM schemes that integrate electrostatic embedding and polarization corrections.[211,218,312–314] These models exhibit transferability, delivering near-ab initio accuracy for condensed-phase and biomolecular systems and reducing computational cost.

A question to ask is to what extent the charge distribution and polarizability in DFTB can be improved to achieve a better description of hydrogen bridging. There have been at least two recent attempts for this. Firstly, the DFTB-CPE approach utilizes an augmented representation of electron density, which is beneficial for describing intermolecular interactions. Previously, in the context of DFTB, it showed that an appropriately parametrized CPE calculation slightly improves the description of hydrogen bridging: Comparing to standard DFTB/3OB calculations, the RMSE of interaction energies reduced from 1.65 to 1.34 kcal/mol on the HB375 set, and from 4.04 to 3.41 kcal/mol on IHB100.[115] The present work, however, shows that employing DFTB-CPE as the QM component in QM/MM approaches yields no improvement, as evidenced by Tables A.2 & A.3. This is because the current DFTB-CPE/MM implementation lacks the coupling between the

MM charges and the CPE's augmented charges. As a result, the indirect effect of MM charges via the traditional MM–DFTB electrostatic interaction on the QM-only CPE appears to be negligible. To conduct a more thorough evaluation, a fully supported DFTB-CPE/MM that incorporates the coupling is needed. We anticipate that the full DFTB-CPE/MM would also require additional parameters to screen the MM–CPE charge interactions at short range. Despite this complexity, it offers a promising approach for more accurately capturing the polarization of QM atoms by the MM environment. A more elaborate approach that also offers potential improvements in several different application areas is to extend the representation of atomic electron density in DFTB by including atom-centered dipoles and quadrupoles. The model called mDFTB performs remarkably better than the usual DFTB for hydrogen bridging, reducing the RMSE of interaction energies from 1.69 to 0.69 kcal/mol on the HB375 set, and from 3.98 to 2.08 kcal/mol on IHB100.[300] Incorporating mDFTB within the QM/MM framework could be a promising direction for future development.

As hinted in the results with ωB97X-V, the mere existence of a QM–MM interface constitutes another source of error that cannot be mitigated by an improvement of the QM method (or, of the MM force field). A particularly illustrative example showing the need for a balanced description of intermolecular interactions is the sensitive structural patterns in the active center of bacteriorhodopsin as discussed in Ref. [315]. These patterns collapsed in force field simulations, arguably because of the lack of polarizability in the model. The description improved when applying QM/MM models with increasing QM region size; however, the imbalance between the hydrogen bridges in the QM and MM regions, as well as those crossing the boundary, can lead to instabilities, especially during dynamics simulations. It was discussed that the (already large) QM region might need to be made even larger. Clearly, there will always be cases in which such a solution is untractable, be it due to the unacceptable computational cost of the corresponding QM calculation, or for more fundamental reasons, such as the possibly overestimated delocalization of electrons that may occur in large QM regions with methods based on DFT.

The errors stemming from an unbalanced description of NCI at the QM–MM interface can significantly worsen the overall performance of QM/MM models, in addition to any inaccuracy of the QM and MM methods. Other studies demonstrated that increasing QM regions may not always lead to a single-sided improvement.[316] Employing a larger QM region inevitably brings about a larger QM–MM interface, which can accumulate errors. This was highlighted, on the one hand, in cases where extended QM-MM interfaces cross multiple covalent bonds, with each of the bonds contributing to the error.[247] On the other hand, when considering NCI, errors might similarly accumulate due to a large number of hydrogen-bonding contacts crossing the QM-MM interface.

Based on our analysis, we can identify situations stemming from a particular construction of the QM region that bring on the most significant errors, and thus should be avoided. The QM region should be extended so that (1) the interface does not cross ionic hydrogen bonds, (2) any NCI contacts exhibiting sizable CT are included in the QM region, and (3) including the H-bond acceptor within the QM region is more critical than including the donor, in general. (4)

Also, the LJ potentials for short QM–MM interatomic contacts, particularly any ionic hydrogen bonds, should be carefully evaluated and, if necessary, reparameterized. The selection of the QM region in practical applications should be guided by an understanding of the strengths and limitations inherent to each method. Informed use of SQM methods, acknowledging their inherent limitations, can be leveraged to enhance the reliability of computed interaction energies. This generally reinforces efforts toward improved embedding schemes and selection algorithms.[38]

7. Reduction Pathway of Glutaredoxin 1 Investigated with QM/MM Molecular Dynamics Using a Neural Network correction

Chapter 7 is reproduced in modified form from publication Ref. [223] with permission from AIP Publishing:

- Julian Böser et al. "Reduction pathway of glutaredoxin 1 investigated with QM/MM molecular dynamics using a neural network correction". In: *The Journal of Chemical Physics* (2022), p. 154104.

Author Contributions:
Julian Böser performed all classical and QM/MM simulations using both the DFTB/SRP and DFTB/Δ-ML setups. The QM/MM metadynamics simulations performed with DFTB/SRP were initialized using preliminary data generated during Julian Bösers's master's thesis [317]. These data have been extensively expanded in the present work through additional simulations, refined analysis and extended by the DFTB/Δ-ML approach. Julian Böser also conducted the analysis of the free energy surfaces and the regioselectivity. Denis Maag performed the model evaluation, which is only summarized in the following.

7.1. Introduction

Homo sapiens glutaredoxins (Grxs) are thiol–disulfide oxidoreductases that play a central role in maintaining cellular redox homeostasis and regulating signaling processes under oxidative stress.[57,63] Their catalytic function relies on the reversible thiol–disulfide exchange (TDE) of disulfide bonds within protein substrates, a reaction tightly coupled to the intracellular redox balance of glutathione (GSH) and glutathione disulfide (GSSG). The relative abundance of these co-substrates governs the efficiency of protein glutathionylation and deglutathionylation, thereby modulating both enzyme activity and substrate reactivity.[54] Structurally, Grxs are classified according to the number of active-site cysteines: dithiol Grxs possess a Cys–X–X–Cys motif, whereas monothiol Grxs contain a single catalytic cysteine (Cys–X–X–Ser) as shown in Figure 7.1A. Experimental mutagenesis of the second cysteine to serine in dithiol Grxs has revealed that the monothiol mechanism can achieve higher catalytic efficiency than the dithiol route.[62,318–320] Detailed kinetic analyses of Homo sapiens HsGrx1 illustrate this divergence. In a study employing

the metal-binding domain HMA4n (Hma) as a substrate and GSH/GSSG as co-substrates (see Figure 7.1B and C), electrospray ionization mass spectrometry identified intermediates consistent with parallel catalytic cycles. The wild-type enzyme (Cys–Pro–Tyr–Cys) was capable of operating through both monothiol and dithiol routes, whereas the Cys–Pro–Tyr–Ser mutant was restricted to the monothiol pathway as proposed in Figure 7.1D. Both mechanisms proceed via sequential TDE, yet the dithiol route incurs an additional intramolecular rearrangement between the two cysteines, reducing overall catalytic efficiency.[62] Although these findings support a nucleophilic attack by the Grx thiolate on the substrate disulfide as the initiating step, alternative models propose that glutathione initiates the reaction, first forming a glutathionylated substrate intermediate.[54,321,322] The persistence of such competing hypotheses underscores that the precise sequence of events governing Grx catalysis remains an active topic of mechanistic investigation.

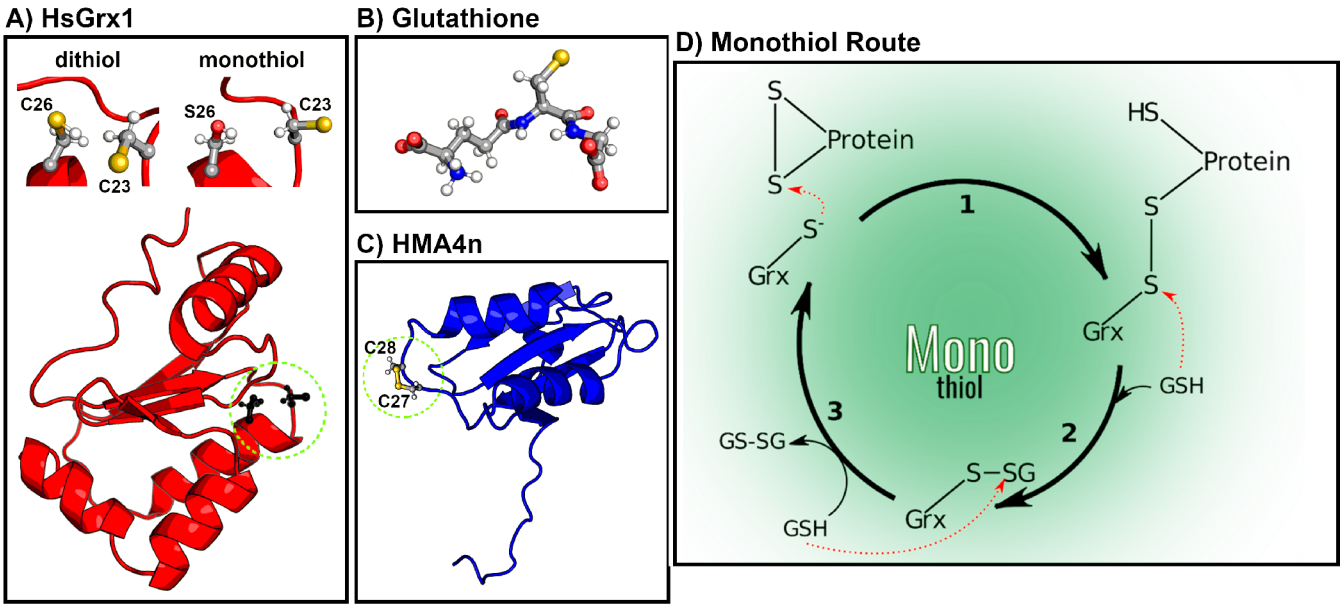

Figure 7.1.: (A) Active-site configurations of the dithiol (Cys23–Pro–Tyr–Cys26) and monothiol (Cys23–Pro–Tyr–Ser26) variants of HsGrx1 (PDB ID: 1JHB[323]). (B) Molecular structure of the co-substrate GSH. (C) Metal-binding domain Hma, used as a model substrate containing a Cys27–Cys28 disulfide bridge.[324] (D) Proposed monothiol catalytic mechanism showing the sequence of TDE reactions: (1) nucleophilic attack of the HsGrx1 thiolate on the reduced Hma to generate a mixed disulfide intermediate, (2) subsequent attack of GSH on the disulfide bridge to release the reduced form of Hma and form a glutathionylated Grx intermediate, and (3) reduction of the glutathionylated Grx by a second GSH molecule, thereby regenerating the active Grx and completing the catalytic cycle.[62]

Computational approaches offer a compelling route to disentangle mechanistic hypotheses in enzyme chemistry. In the context of HsGrx1 reactivity, one might first employ classical molecular dynamics (MD) to explore whether the enzyme's conformation and solvent accessibility permit nucleophilic attack by the sulfur atom onto a disulfide sulfur. Such simulations provide spatial and statistical assessment of reactive-site accessibility, enabling identification of viable attack pathways for subsequent energetic evaluation. To further infer whether such reactions are thermodynamically and kinetically favorable, reaction barriers and energies can be computed from sampling

thermodynamic ensembles that represent all relevant molecular microstates. It becomes possible to compute free energy differences and thereby identify the most favorable reaction pathways connecting reactants and products. In hybrid quantum mechanics/molecular mechanics (QM/MM) simulations, in which the reactive center is treated quantum mechanically while the surrounding environment is modeled using classical force fields, higher accuracy can be achieved.[34] However, high activation barriers make transitions between states too infrequent to observe with adequate computational effort. In addition, the complex energy landscape of biomolecules, with many stable and intermediate conformations, restricts sampling efficiency and often causes the system to remain trapped in one state.

Efficient exploration of the conformational space can be achieved by employing semiempirical quantum methods that balance computational cost and accuracy, thereby enabling extensive sampling of complex free energy landscapes. Among these approaches, the semi-empirical density functional tight binding (DFTB) method. Derived from density functional theory (DFT) through systematic approximations, DFTB preserves the essential electronic structure description while achieving speedups of two to three orders of magnitude compared with conventional DFT calculations using medium-sized basis sets.[120,122,123] The accuracy of DFTB critically depends on the underlying parameterization. Parameters can be optimized for broad chemical applicability or tailored for a specific system. With a well-calibrated parameter set, DFTB typically outperforms other semiempirical quantum mechanical methods. For a wide range of organic molecules, it has demonstrated reliable performance for equilibrium geometries, vibrational frequencies, and reaction energies.[123,325]

Qualitative errors in DFTB arise mainly from its inherent approximations, including the use of a confined minimal basis set, two-center integral and monopole approximations.[93,115,300] Known deficiencies include inaccurate proton affinities of nitrogen-containing[123] compounds and errors in the description of P–O bonds,[124] as well as the general underestimation of non-covalent interactions.[32,115,300] Furthermore, the accuracy achievable with standard DFTB parameterizations is inherently limited because the repulsive energy term (Erep) accounts only for two-body interactions. As a consequence, equilibrium bond lengths can be described with reasonable precision, while angular and torsional angles, which depend on three- and four-body interactions, remain largely unaffected by Erep. Depending on the nature of the interactions present in a molecular system, the approximations inherent in DFTB can lead to qualitative errors that fundamentally alter the underlying energetics. Standard DFTB relies on precomputed integrals obtained from DFT using the PBE functional and therefore inherits the same limitations as this reference functional, most notably the delocalization error. A case in point for such qualitative errors is the TDE.[52] A benchmark study by Neves et al. showed that proper inclusion of electron correlation is required to obtain the correct energetics and transition state geometry, where the three sulfur atoms are linearly aligned with S–S bonds of about 2.4 Å. However, with DFTB the S–S bonds are too long (2.7 Å), and the activation energy has an error exceeding 6 kcal mol^{-1} due to deficiencies inherited from the PBE functional. The trisulfide intermediate is not linear (160°),

exhibits an excessively deep minimum in the gas phase (∼8 kcal mol^{-1}), and the water/protein trisulfide state displays an inadequate local minimum.[52]

The aforementioned deficiency of DFTB in describing TDE has been addressed using two distinct strategies. (1) One approach employs an ad hoc solution within the DFTB framework by reparametrizing the repulsive potential for the specific application scenario, called specific reaction parameterization (SRP). When performed carefully, the fitted repulsive interaction can partially compensate for errors introduced by the approximations inherent in the DFTB energy expression. The quality of the resulting repulsive potential can be optimized for a selected choice of systems and by selecting the physical properties considered during parameterization.[124,326] To overcome this limitation in TDE, a SRP of the repulsive S–S pair potentials was carried out, ensuring that the resulting energetics were consistent with higher-level quantum mechanical reference data from B3LYP and G3B3 calculations. This ad hoc adjustment provided an accurate description of the TDE, successfully reproducing the correct transition-state geometry and energy.[221] (2) Machine learning (ML) methods can improve the accuracy of calculations without altering the underlying DFTB framework, thereby offering greater flexibility in the type of corrections that can be applied. For instance, they can incorporate multi-body interactions that are not explicitly accounted for in SRP.[220] In the so-called Δ-ML approach, originally introduced by Ramakrishnan et al.[210], the key idea is to correct systematic errors of low-level quantum methods by learning the difference to high-level reference data, thus combining the computational efficiency of the former with the accuracy of the latter. This strategy has been successfully applied to improve quantum mechanics/molecular mechanics (QM/MM) calculations by compensating for discrepancies between different QM levels,[211] as well as for long-[218] and short-range[219] corrections of interaction energies between the QM and MM regions. In previous work, Gómez-Flores et al.[221] introduced the Δ-ML approach for describing the TDE. The model is based on the Behler–Parrinello artificial neural network (ANN),[205,206] which was trained to learn the energy difference between DFTB and higher-level quantum mechanical methods (B3LYP and CCSD(T)) for the TDE in the gas phase. The Δ-ML scheme reproduced the energetics and geometries of the TDE with *ab initio* accuracy at a computational cost comparable to standard DFTB calculations. Moreover, the ANN trained on gas-phase data could be directly applied to TDE in aqueous solution and in proteins without a significant loss of accuracy. Further information on the Behler–Parrinello ANN[205,206] is provided in Section 5.1 of the Theory section.

Building on the achievements of the previously developed ANN, this work employs the Δ-ML model[221] in enhanced sampling simulations to investigate the proposed catalytic reduction cycle of Hma by the monothiol Grx, with GSH serving as a co-substrate. Classical MD simulations of the different systems are carried out to analyze sulfur–sulfur distances and inter-sulfur angles, providing estimates of the regioselectivity and accessibility of the various thiol–disulfide exchange reactions. In addition, the corresponding multidimensional free-energy surfaces (FESs) are subsequently obtained from extensive QM/MM metadynamics (MTD) simulations using SRP and the Δ-ML approach to characterize the underlying reaction mechanism in detail.

7.2. Methods

7.2.1. Model

The structural model of Grx is based on a NMR solution structure of dithiol Grx in the fully reduced form (PDB ID: 1JHB).[323] To generate the monothiol model, the C-terminal cysteine (Cys26) in the active site was mutated to a serine. The sulfur atom of the enzymatically active Cys23 was prepared as an anion to enable the reaction with disulfide bonded sulfurs. For the protein substrate Hma, the NMR solution structure from Ref. [324] was used (PDB ID: 2KKH). The additional water molecules and the zinc ion in the structure were removed and a disulfide bond between Cys27 and Cys28 was formed by manually reducing the distances between the sulfur atoms. The sulfur atom in glutathione was prepared as an anion (GS^-) to enable reactions with disulfide bonded sulfurs. GS^- contains a γ-glutamyl residue that is not included in the standard parameterization of the AMBER99SB-ILDN force field[327] used in this work and was therefore explicitly parametrized. For the parameterization, the zwitterionic molecule of γ-glutamyl-(N-methyl)amide zwitterion was geometry optimized at the level B3LYP/6-31G* using the polarizable continuum model (PCM) at 300 K. The application of PCM was necessary to prevent an undesired proton transfer from the amino- to the carboxyl group, which had occurred in pilot optimizations of the molecule in the gas phase. Then, the electrostatic potential induced in the surroundings of the molecule was obtained at the level HF/6-31G*, and was determined on four layers of points surrounding the molecule, starting at a distance of 1.4 times the Merz–Kollman radius of the respective nearest atom and spaced by 0.2 times the radius, with the density of 1 point per $Å^2$. (The Merz–Kollman radii are 1.2, 1.5, 1.5 and 1.4 Å for H, C, N and O, respectively.) The quantum chemical calculations were performed with GAUSSIAN 09 A.02.[286] The atomic charges were obtained with the two-stage restrained electrostatic potential fit,[328] as implemented in the Antechamber tool in the AmberTools suite.[329] The charges of the peptide backbone atoms were constrained to their respective values occurring in the standard AMBER force field. Finally, the capping group NH–CH_3 was removed to yield the topology and parameter file for an N-terminal γ-glutamyl residue, termed GGL. The obtained parameters can be found in Ref. [223] as Gromacs topology.

7.2.2. Classical Simulations

All classical simulations were performed with GROMACS 2020.2[290] patched with PLUMED 2.6.1.[330,331] The AMBER99SB-ILDN[327] force field was used, periodic boundary conditions were set and electrostatics and Lennard-Jones (LJ) interactions were calculated using a cutoff of 1 nm. Long-range electrostatic interactions were calculated by particle-mesh Ewald summation,[165] the neighbour list was updated every 10 MD steps. The leap-frog integrator[96] was used with a time step of 2 fs. Initial velocities of the atoms were assigned from the Maxwell–Boltzmann distribution at 300 K. The temperature was maintained at 300 K by the Bussi thermostat[332] with $\tau_T = 0.1$ ps,

in the NVT- and NPT-ensemble. In NPT simulations, the pressure was kept constant with the Parrinello–Rahman barostat[173] at p = 1 bar and $\tau_p = 2.0$ ps.

For the fist catalytic **step 1** shown in Figure 7.1D, monothiol HsGrx1 and Hma were placed together in a cubic simulation box. The distance between the molecules and the box was about 2 nm, which corresponds to a box size of ca. $11 \times 11 \times 11$ nm^3. The box was solvated with 36436 TIP3P water molecules and electro-neutralized by adding four chloride atoms. The system was shortly equilibrated for 10 ns in a NVT ensemble and subsequently for 10 ns in a NPT ensemble, during which harmonic position restraints were applied to the heavy atoms with a force constant of 10 000 kJ mol^{-1} nm^{-2}. A 500 ns NPT simulation followed, from which two structures were selected that showed a large difference in their RMSD and radius of gyration. Each structure was then simulated for 500 ns after assigning new initial velocities from the Maxwell-Boltzmann distribution at 300 K. During the simulations the distances between the sulfur atom of HsGrx1 and the sulfur atoms of Hma were restrained to values smaller than 9 Å with a force constant of 10 000 kJ mol^{-1} nm^{-2} to reduce the conformational sampling. For the reaction **step 2**, a snapshot of the system containing the Grx-S-S-Hma intermediate was selected from a QM/MM metadynamics simulation of reaction (**1**). Due to the previous TDE, one of the sulfur atoms of Hma was deprotonated and thus carried a negative charge. To prepare the system for a nucleophilic attack by GS$^-$, the following equilibration scheme was applied. First, the system was equilibrated with the deprotonated sulfur atom for 100 ns. Next, the sulfur atom was protonated, one chloride ion added, and the system equilibrated for 100 ns. Then the GS$^-$ molecule was introduced and two chloride ions were introduced into the system which was simulated for another 100 ns. Two structures with high RMSD and radius of gyration difference were selected from the obtained trajectory and, analogously to the procedure described in the previous paragraph, used as starting structure for two additional 500 ns long simulations with new initial velocities. The distances between the sulfur atom of GS$^-$ and the sulfur atoms of the Grx-S-S-Hma intermediate were restrained to values smaller than 9 Å with a force constant of 50 000 kJ mol^{-1} nm^{-2}. For the third and final catalytic **step 3**, a structure of the HsGrx1-S-SG intermediate was taken from a QM/MM metadynamics simulation of reaction (**2**). The molecule was placed in a cubic box of ca. $6 \times 6 \times 6$ nm^3, solvated with 8126 TIP3P water molecules, electro-neutralized with one sodium ion and equilibrated for 100 ns. The nucleophile GS$^-$ was then introduced followed by another simulation of 100 ns, from which two starting structures were selected according to the same criteria described for the reactions (**1**) and (**2**). Analogously, two 500 ns long simulations were performed with new initial velocities of the atoms, keeping the S–S distances between GS$^-$ and HsGrx1–S–SG below 6 Å with a force constant of 10 000 kJ mol^{-1} nm^{-2}. For all simulated reaction step, the 2×500 ns long trajectories per system were analyzed to estimate the regioselectivity of the possible thiol-disulfide exchanges. 2D histograms of the distances between the nucleophilic sulfur atoms and the two respective target sulfur atoms were obtained with a bin size of 0.1 Å. Based on this analysis, an attack was considered possible if the the distance between the nucleophilic sulfur and the target was less than 5 Å and the attack angle greater than 130°, indicated by gray shaded ares.

7.2.3. QM/MM simulations

Δ-ML and SRP

All QM/MM simulation employ DFTB3 with a different set of parameters. When employing standalone DFTB3, the SRP developed in Ref. [221] was applied, which had been parametrized against B3LYP calculations. For Δ-ML augmented DFTB3, the standard 3ob-mod parameter set[124] was used. In this setup, the energies are first evaluated using DFTB3 and subsequently corrected by the Δ-ML component. The underlying concept is that the network is trained to learn the energy difference, $E_{\Delta\mathrm{ML}_{\mathrm{CC}}}$, between the DFTB3 baseline and the CCSD(T)/aug-cc-pVTZ reference. The corrected DFTB3/Δ-ML energy is then obtained by adding this correction to the baseline energy $E_{\mathrm{DFTB3/\Delta ML}} = E_{\mathrm{DFTB3}} + E_{\Delta\mathrm{ML}_{\mathrm{CC}}}$. The Δ-ML model is implemented in DFTB+ and is available on Github.[333] Theoretical details can be found in Section 5.1.1.

Unbiased Simulations

All QM/MM simulations were performed with a local GROMACS 2020[290] version patched with PLUMED 2.5.1[330,331] and interfaced with a modified DFTB+ 19.1[291] extended by the Δ-ML correction. Analogously to previous studies[221,334], the QM regions of the respective systems comprised the side chains of the three cysteines for which a thiol-disulfide exchange was investigated. The link atom approach was used to cap the QM region with hydrogen atoms that were placed along the Cα and Cβ bonds at a fixed distance. The QM regions consisted of 15 atoms described by the semiempirical density functional theory method DFTB3 and two different sets QM/MM simulations of the catalytic cycle were performed. The first set used the 3OB parameter set[124] with a reparamterized S–S repulsive potential based on B3LYP/def2-TZVPP data.[221] In the second set, the artificial neural network correction that learned the energy difference between DFTB with the unmodified 3OB parameter set and CCSD(T)/aug-cc-pVTZ level of theory was appplied.[221] The rest of the systems were described with the AMBER99SB-ILDN[327] force field and TIP3P water. For each system, a starting structure was taken from one of the two respective classical 500 ns MD simulations that met an accessibility criterion for a possible nucleophilic attack. An attack was considered possible if the distance between the nucleophilic sulfur and the targeted sulfur was less than 6 Å and the attack angle greater than 130°. The systems were equilibrated for 100 ps in an NPT ensemble with the same settings as for the classical simulations, with two changes. A time step of 0.5 fs was used and the electrostatic interactions between the QM region and the MM system were scaled down by a factor of 0.75 to compensate for the missing polarization of the MM environment.[303,304]

Metadynamics Simulations

The free energy profiles of the TDE using the SRP and the Δ-ML approach were obtained with QM/MM well-tempered multiple walker metadynamics.[177,181,182,184] A 2D setup was used, where the S–S distances between the respective nucleophilic sulfur atoms S_{nuc} and the attacked sulfur atoms S_{ctr} were used as first reaction coordinate and the S–S distances between the attacked

sulfur atoms S_{ctr} and the leaving sulfur atoms S_{lg} as second reaction coordinate. Depending on the system, the S–S distances were restrained to values smaller than or 10 Å with a force constant of $10\,000\,kJ\,mol^{-1}\,nm^{-2}$ to reduce conformational sampling. Moreover, the S_{nuc}–S_{ctr}–S_{lg} angles were restrained to values larger than 130° with a force constant of $100\,000\,kJ\,mol^{-1}\,rad^{-1}$. Either 16 or 24 walkers were used with a simulation time of at least 1.8 ns or 1.4 ns per Walker, respectively. This resulted in a total simulation time of at least 28.8 ns for each system. Gaussian potentials with a width of 0.2 Å and an initial height of $0.5\,kJ\,mol^{-1}$ were deposited and read every 500 fs. A bias factor of $\gamma = 20$ was used. Following the setup in Ref. [221] and Ref. [334], the sum of switching functions depending on the three S–S distances was restrained to prevent bond breaking of the disulfide bond while the sulfur anion S_{nuc} is too far away. Restraints were also applied to the coordination numbers of the Cβ atoms with their bonded hydrogen atoms to prevent deprotonation by the sulfur anion at short distances.

7.3. Results and Discussion

7.3.1. Regioselectivity

The proposed monothiol reduction cycle of Grx involves three catalytic steps, see Figure 7.1D.[62] In each step, the respective nucleophilic sulfur anion S_{nuc} can attack one of the disulfide bonded sulfurs, resulting in two possible thiol-disulfide exchanges per step. In **step 1** the catalytic cycles is initiated by the sulfur anion S^{23}_{Grx} either attacking the sulfur atom S^{27}_{Hma} or S^{28}_{Hma} of the protein substrate Hma. In order to proceed, **step 2** requires an attack of the glutathione thiolate GS_1^- on the disulfide bonded S^{23}_{Grx}. However, the disulfide bonded sulfur atom of Hma (S^{27}_{Hma} or S^{28}_{Hma}) could also be attacked which would then lead to a different pathway. In the final **step 3**, a second glutathione anion GS_2^- must attack the disulfide bonded glutathione GS_1 to form GSSG, but an attack on S^{23}_{Grx} is a also conceivable although this would regenerate the same mixed disulfide molecule (HsGrx1-S–SG).

To estimate the regioselectivity, 2D histograms has been calculated for distances between the respective nucleophilic sulfur atoms S_{nuc} and the potential targets S_{ctr} from classical molecular dynamics simulations, compare Figures 7.2-7.4. The number of approaches of S_{nuc} onto the target sulfur atoms such that an attack complex can be formed were counted. Only geometries where the S_{nuc}–S_{ctr} distances were less than 5 Å and the angle between the three sulfur atoms $\angle(S_{nuc}S_{ctr}S_{lg}) \geq 130°$ were considered. For each system, the accessibility for each attack was calculated, expressed as the percentage of the structures that met the criterion, see Table 7.1.

It was found in **step 1** (Figure 7.2) that S^{27}_{Hma} is attacked more often by S^{23}_{Grx} than S^{28}_{Hma}. The estimated accessibilities are 0.54% and 0.04%, respectively. However, QM/MM metadynamics of this attack showed a very large barrier of more than 23 kcal/mol (Figure B.1 in the Appx.) whereas the barrier height for an attack on S^{28}_{Hma} is much smaller with ca. 12 kcal/mol (Figure 7.5A and D). Therefore, S^{28}_{Hma} is considered as the main nucleophilic target.

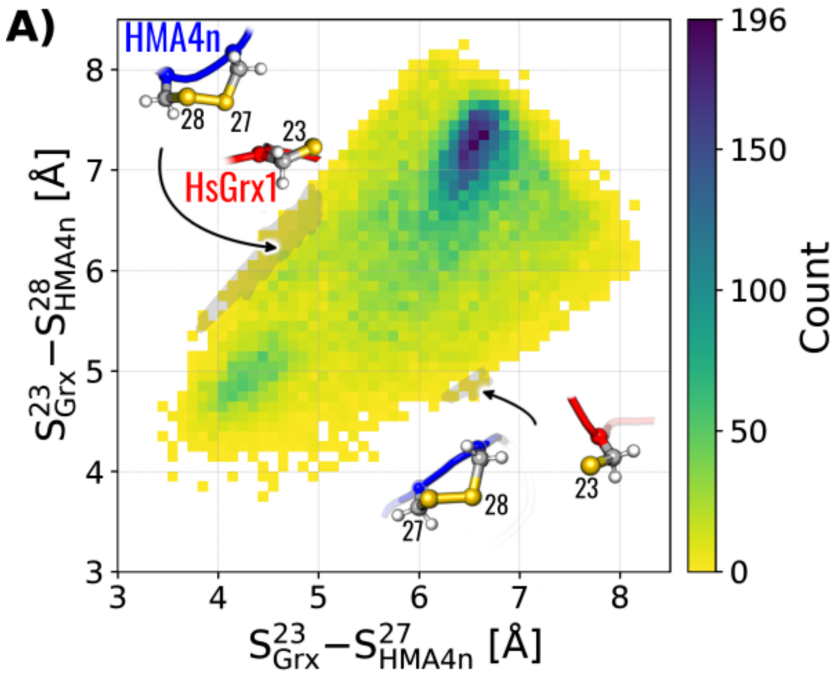

Figure 7.2.: Evaluation of accessibility for the nucleophilic attack based on the histogram of the sulfur–sulfur distances calculated from classical MD simulations of the reaction **step 1** including both regioisomers S^{23}_{Grx}–S^{27}_{Hma} and S^{23}_{Grx}–S^{28}_{Hma}. The gray shaded areas correspond to structures that meet the accessibility criterion.

In **step 2**, the mixed disulfide bond S^{23}_{Grx}–S^{28}_{Hma} between the enzyme and the protein substrate is then attacked by GS_1^-, see Figure 7.3. In the classical simulations, GS_1^- can easily attack S^{23}_{Grx} with an accessibility of 1.30% compared to 0.39% for an attack on S^{28}_{Hma}. The analysis for the alternative regioisomer from step 1, S^{23}_{Grx}–S^{27}_{Hma} is shown in Figure B.2 in the Appx. This observation suggests the possible formation of glutathionylated HMA and the reduced form of Grx as a competing side reaction, warranting further consideration.

step	attack	accessibility [%]
1	Grx-S23$^-$ → S27-Hma	0.54
	Grx-S23$^-$ → S28-Hma	0.04
2	GS_1^- → S23-Grx	1.30
	GS_1^- → S28-Hma	0.39
3	GS_2^- → GS_1	28.04
	GS_2^- → S23-Grx	0.04

Table 7.1.: Estimated accessibility of the different possible nucleophilic attacks in the catalytic reduction cycle of HsGrx1 based on the histograms shown in Figure 7.2-7.4. An attack was considered feasible if the distance between the nucleophilic and the attacked sulfur atom (S_{nuc}–S_{ctr}) was less than 5 Å and the attack angle between the sulfurs $\angle(S_{nuc}S_{ctr}S_{lg}) \geq 130°$. The accessibility is expressed as the sum of structures that met the criterion divided by the total number of counts.

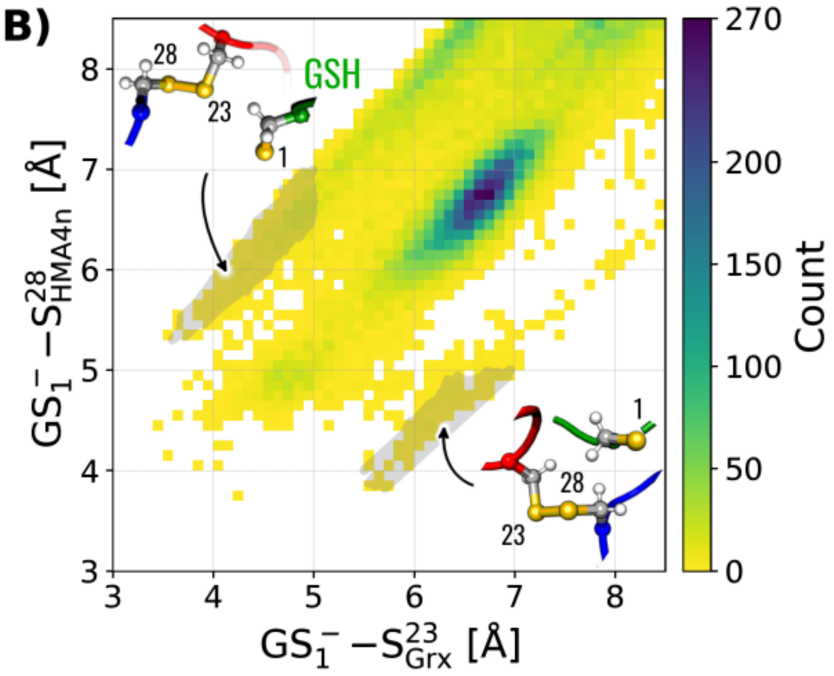

Figure 7.3.: Evaluation of accessibility for the nucleophilic attack based on the histogram of the sulfur–sulfur distances calculated from classical MD simulations of the reaction **step 2** including both regioisomers GS_1^-–S^{23}_{Grx} and GS_1^-–S^{28}_{Hma}. The gray shaded areas correspond to structures that meet the accessibility criterion.

In **step 3**, another GS_2^- molecule attacks one sulfur atom of the newly formed disulfide bond GS_1^-–S^{23}_{Grx}, compare Figure 7.4. An attack on GS_1^- is more likely to occur with an accessibility of 28.04% compared to an attack on S^{23}_{Grx} with 0.04%. The regioselectivity of **step 1** is not known from experiments but the estimated regiospecificities for **step 2** and **step 3** are the same as those experimentally observed by Ukuwela et al.[62] They find only small traces of the glutathionylated Hma, the product for the less likely attack for step **2** in this study. In addition, small traces of the glutathionylated HsGrx1 enzyme were found, the product of **step 2** and the less likely attack for **step 3** found in this work. To further investigate the possible reaction pathways, free energy profiles of the three regioselective attacks were computed with QM/MM metadynamics simulations.

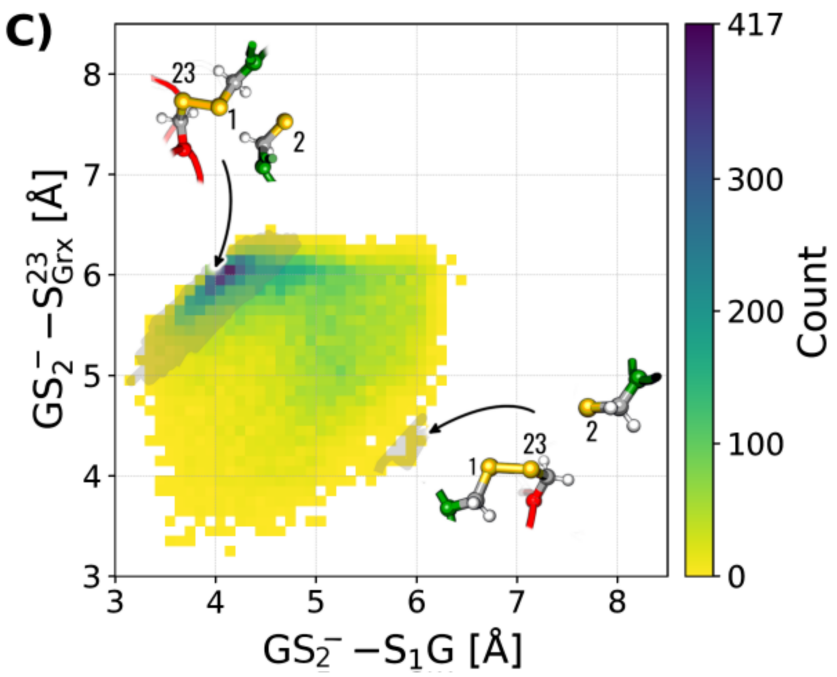

Figure 7.4.: Evaluation of accessibility for the nucleophilic attack based on the histogram of the sulfur–sulfur distances calculated from classical MD simulations of the reaction **step 3** including both regioisomers GS_2^-–S_1G and GS_2^-–S^{23}_{Grx}. The gray shaded areas correspond to structures that meet the accessibility criterion.

7.3.2. Free Energy Surfaces

Each attack was simulated twice, using either the SRP or the Δ-ML energy correction. The obtained FESs are shown in Figure 7.5 and the reaction barriers in Table 7.2. The barrier heights and reaction energies determined by the two methods agree very well, with differences ranging from 0.2 to 1.2 kcal/mol.

In **step 1**, the initial disulfide bond S^{27}Hma–S^{28}Hma represents the global minimum on the FES. The reduction product S^{23}Grx–S^{28}Hma corresponds to a local minimum, in which S^{27}_{Hma} remains in its deprotonated form, since protonation steps are not included in the present QM/MM setup. Using DFTB/SRP and DFTB/Δ-ML as the QM methods, the computed activation barriers for the reduction step are $\Delta G^{\ddagger}$red = 11.3 and 12.5 kcal mol^{-1}, respectively. The corresponding reaction free energies are ΔG = +5.0 and +5.8 kcal mol^{-1}, which implies barrier heights for the reverse oxidation reaction of $\Delta G^{\ddagger}$ox = 6.3 and 6.7 kcal mol^{-1}.

In the catalytic step 2, the global minimum corresponds to the disulfide bond S^{23}Grx–S^{28}Hma, with S^{27}Hma being protonated in the present setup. A nucleophilic attack of a glutathione anion on the sulfur atom of HsGrx1 forms the disulfide GS^1–S^{23}Grx, which represents a local minimum on the free energy surface. The reaction free energies are ΔG = +6.5 and +7.2 kcal mol^{-1} for DFTB/SRP and DFTB/Δ-ML, respectively. The corresponding activation barriers are $\Delta G^{\ddagger}$red = 18.6 and 20.1 kcal mol^{-1} for the reduction, and $\Delta G^{\ddagger}_{ox}$ = 12.1 and 12.1 kcal mol^{-1} for the reverse

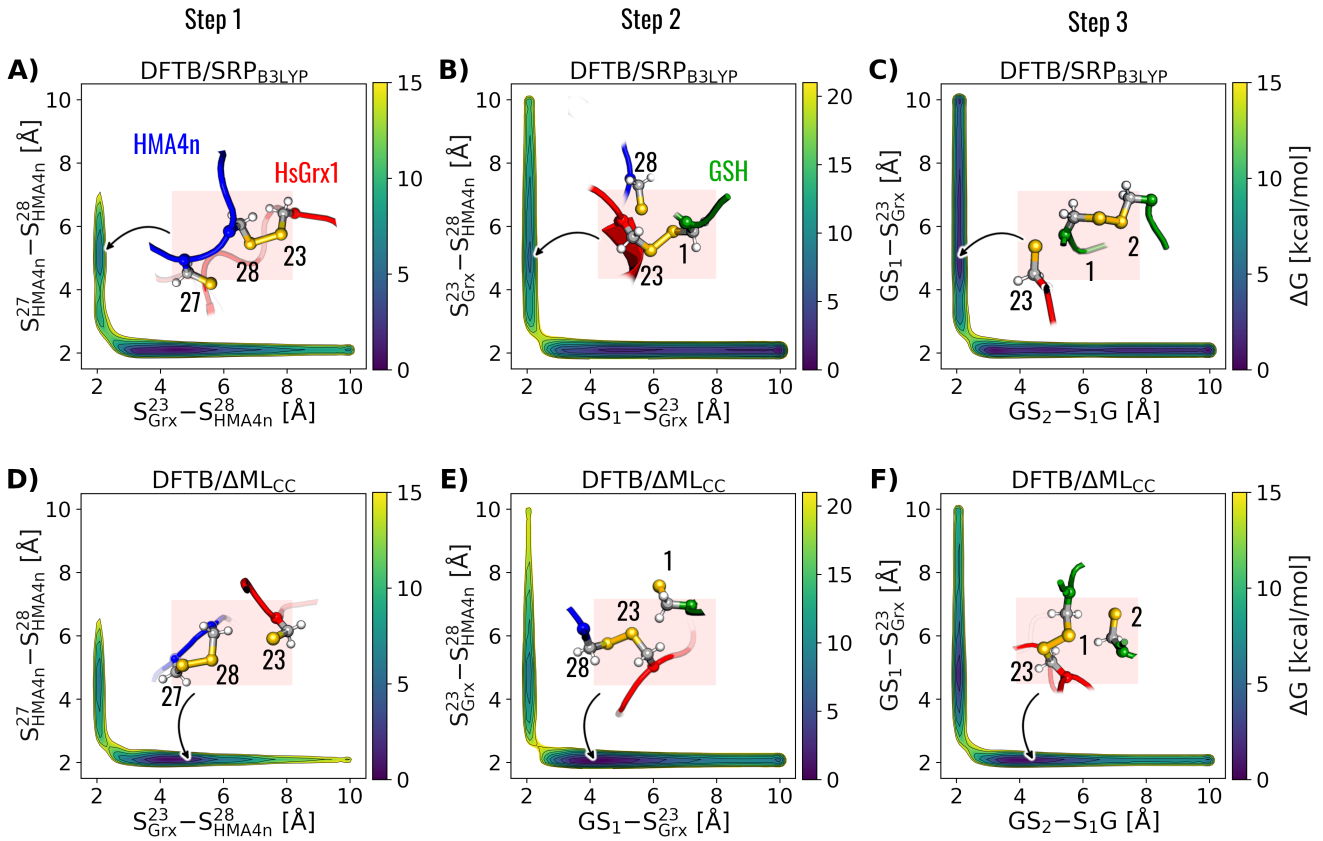

Figure 7.5.: Free-energy surfaces (FESs) of the three consecutive thiol-disulfide exchanges in the monothiol route of HsGrx1 with Hma as substrate and GSH as co-substrate. FESs of **step 1 to 3** (left to right) obtained with DFTB using the SRP (A-C) and with DFTB using the Δ-ML correction (D-F). Contour lines are drawn every 2.5 kcal/mol.

oxidation reaction. In the final step 3, a second glutathione anion attacks the first glutathione moiety disulfide-bonded to HsGrx1, yielding oxidized glutathione (GSSG) as a local minimum on the free energy surface. Using either DFTB/SRP or DFTB/Δ-ML, the reaction free energy is $\Delta G = 1.0$ kcal mol^{-1} in both cases. The corresponding activation barriers are $\Delta G^{\ddagger}\text{red} = 12.1$ and 12.4 kcal mol^{-1} for the reduction, and $\Delta G^{\ddagger}\text{ox} = 11.1$ and 11.4 kcal mol^{-1} for the reverse oxidation reaction.

Table 7.2.: Reaction barriers of the catalytic reactions between HsGrx1 (Grx), the protein substrate Hma (P), and GSH. The barriers were obtained with DFTB using the 3OB-mod parameter set or the Δ-ML model. All values in kcal/mol.

Method	Grx-S$^-$ + P-(S)$_2$ ⇌ Grx-S-S-P(S$^-$)	Grx-S-S-P(SH) + GS$^-$ ⇌ Grx-S-SG + P-(SH)(S$^-$)	Grx1-S-SG + GS$^-$ ⇌ Grx-S$^-$ + GSSG
DFTB/SRP	11.3 / 6.3	18.6 / 12.1	12.1 / 11.1
DFTB/Δ-ML	12.5 / 6.7	20.1 / 12.1	12.4 / 11.4

The FESs obtained with the two correction schemes differ markedly in both their energetics and overall topology. In the DFTB/Δ-ML calculations, the minima appear narrower and the energy rises more steeply than in the DFTB/SRP results. For instance, in **step 3**, the global minimum associated with the disulfide bond GS1–S^{23}Grx spans GS^{2}–S^{1}Grx distances of 3.5–5.5 Å with DFTB/Δ-ML (horizontal minimum in Figure 7.5F), whereas the corresponding minimum obtained with DFTB/SRP extends over a broader range from 3.5 to nearly 10 Å (Figure 7.5C). This discrepancy originates from the different treatment of many-body effects. The SRP approach modifies only the two-body repulsive potential Erep, while the Δ-ML correction explicitly incorporates many-body interactions. These effects become particularly significant when the sulfur atoms deviate from linear alignment, as the S–S–S angles in the present setup vary between 130° and 180°.

7.3.3. Model Evaluation

For completeness, the following section provides a brief summary of the comparative performance of DFTB/Δ-ML and DFTB/SRP. A detailed analysis is available in the previous study in Ref. [221], and the full discussion in the context of the present work is given in Ref. [223].

The evaluation was performed by comparing free-energy surfaces (FESs) and relative energies for a model system consisting of a methyl thiolate and dimethyl disulfide in the gas phase. Structures from the corresponding data set were analyzed using CCSD(T) and B3LYP as reference methods. The geometric analysis focused on the torsion angle spanning the disulfide bridge, identified as the main contributor to the observed errors. The data set comprised two subsets: (1) a linear scan of S–S distances ranging from 2.0 to 3.2 Å, and (2) a non-linear set obtained from QM/MM metadynamics simulations covering S–S separations up to 7.0 Å and variable S–S–S angles. For the linear subset, DFTB/SRP reproduced the B3LYP reference energies within ±2 kcal mol^{-1}, whereas DFTB/Δ-ML matched CCSD(T) results with deviations below 0.5 kcal mol^{-1} across the entire potential energy surface (PES). In the more flexible non-linear subset, DFTB/SRP and B3LYP PESs were qualitatively similar but exhibited quantitative deviations of up to 10 kcal mol^{-1}, particularly for short and non-linear S–S arrangements. These discrepancies originate from the two-body nature of the SRP correction and its limited ability to describe torsional and many-body effects. By contrast, DFTB/Δ-ML reproduced the CCSD(T) PES with high fidelity, typically maintaining deviations within ±3 kcal mol^{-1}. To further assess torsional behavior, potential energy scans of the C–S–S–C dihedral in dimethyl disulfide were performed in the gas phase. DFTB/SRP and DFTB/Δ-ML energies agreed closely near the staggered conformation, differing by less than 1 kcal mol^{-1}. However, for other torsional configurations, particularly the eclipsed conformation, SRP exhibited significant deviations of up to 5.5 kcal mol^{-1}, confirming its tendency to underestimate rotational barriers due to the neglect of three- and four-center interactions.[220,335] The Δ-ML correction alleviates this limitation by incorporating many-body effects and thereby provides a more accurate torsional energy profile.

7.4. Conclusion

The mechanism of enzymatic disulfide bond reduction by glutaredoxins is still under debate and several models have been proposed. In this work, classical and QM/MM simulations were used to investigate the reduction pathway proposed by Ukuwela et al.[62] Based on their experiments, the reduction cycle should proceed over three consecutive, regiospecific thiol-disulfide exchanges between the monothiol enzyme HsGrx1, the protein substrate Hma and the co-substrate GSH. In classical MD simulations, similar regioselectivity by means of an accessibility criterion from histograms of the S–S distances between the respective nucleophilic and the two target sulfur atoms was found. Feasibility of individual enzymatic reaction steps were assessed by the reaction barriers present in the free-energy surface (FES) obtained via QM/MM metadynamics.

This approach requires extensive phase space sampling, which poses a challenge for *ab initio* and DFT methods due to their high computational cost. As an alternative, minimum energy pathway algorithms can be employed or relaxed geometry optimization calculations at stationary points along a reaction coordinate performed.[336] However, such approaches usually neglect motions of the environment, which can lead to errors. In addition, approximations for the entropy have to be used to obtain the Gibbs free energy. In contrast, adequate sampling accounts for all important configurational changes, and the Gibbs free energy is directly obtained. This was achieved by using the semiempirical DFTB method as a QM method, which is about 3 orders of magnitude faster than DFT-GGA using moderately sized basis sets. However, DFTB fails to accurately describe the thiol-disulfide exchange reaction, as do most DFT-GGA functionals due to correlation effects.[222] As a workaround, specific reaction parameters (SRP) and a machine-learned energy correction (Δ-ML) were developed in previous work[221] and are employed here for the free energy calculations. The computational cost of the Δ-ML correction is comparable to a DFTB calculation. With both corrections, the obtained barriers heights are about 12 kcal/mol for **step 1** and **3** and about 20 kcal/mol for **step 2**, which lies in the order of magnitude of typical enzymatic reactions. Therefore, the calculation indicate that disulfide bond reduction by HsGrx1 most likely occurs via the mechanism proposed by Ukuwela et al.

However, there are some differences in the obtained free energy profiles. The Δ-ML correction yields barriers that are up to 1.5 kcal/mol larger than those obtained with the SRP, and the minima are narrower than with the SRP. Comparing the corrections with their respective reference methods, B3LYP for the SRP and CCSD(T) for the Δ-ML correction, showed that the SRP reproduces the reference energies at short S–S distances very well, but exhibits large errors at larger S-S distances. In addition, the SRP underestimates the torsional energy of the C-S-S-C dihedral angle between disulfide bonded molecules. The machine-learned energy correction, on the other hand, reproduces the reference energies for all given structures with high accuracy. Hence, the PMFs obtained with the Δ-ML correction are considered more accurate.

Nevertheless, all investigated reactions are uphill, which is unexpected for an enzymatic reactions. This behavior likely arises from the QM/MM setup, in which the subsequent protonation of the

cysteinyl thiols S28 and S27 in the protein substrate HMA was omitted for technical reasons. The protonated Hma species are most likely lower in energy than the deprotonated ones, since most cysteinyl thiols are considered to have a pK_a of 8 or higher. In contrast, the enzymatically active cysteinylthiols of glutaredoxins typically have a $pK_a < 5$ and are therefore usually deprotonated and readily available to initiate a nucleophilic attack. Moreover, the direction of the catalytic cycle is controlled by the concentration of GSH. An excess of GSH leads to the reduction of the disulfide bond of the substrate and an excess of GSSG to oxidation. Considering all these findings, it can be concluded that disulfide bond reduction by HsGrx1 most likely follows the mechanism proposed by Ukuwela et al. The present work represents the first application of the DFTB/Δ-ML approach since its introduction, demonstrating its potential for accurate free energy simulations at moderate computational cost. This framework can be readily applied in future studies to achieve extensive sampling with improved accuracy. Further investigations may explore alternative mechanistic models, comparing their regioselectivities and barrier heights with the results reported here.

8. Transferring Collective Variables from Molecular Dynamics Simulations to QM/MM Simulations for Reactivity Exploration in Dynamic Systems

8.1. Introduction

Proteins exhibit a hierarchical organization spanning multiple spatial and temporal scales, encompassing local chemical reactivity, non-covalent interactions, and large-scale conformational motions. Together as outlined in Chapter 1, these layers define the fundamental framework from which biomolecular structure and function emerge. However, inquiring into biomolecular processes requires more than methods that merely span a spectrum of spatial and temporal scales. Different timescales can be coupled in nonlinear ways, forming hierarchical dynamics between levels.[337]

Reactions in proteins occur at specific sites, where substrates bind, undergo sequential transformations, and are released as products. These chemical steps are often coupled to slower conformational motions that gate access to the active site, reshape binding sites, and reorganize local environments, thereby modulating reactivity.[243,338,339] For instance, human glucokinase exhibits distinct conformers whose relative populations determine catalytic rates.[340] Importantly, the coupling can occur bidirectionally. Fast, local fluctuations and reactive events can feed back onto slower processes, biasing or even triggering larger-scale rearrangements.[341] In dihydrofolate reductase, ligand binding, while local and comparatively rapid, can reorganize the µs–ms conformational dynamics of the enzyme.[342]

Hierarchical coupling between fast and slow motions has also been observed in T4 lysozyme, where long molecular dynamics (MD) simulations combined with dimensionality reduction and targeted perturbations revealed that rapid hinge opening–closing is linked to a slower locking step.[240] Reciprocal interactions between reactivity and conformational dynamics are further evident in the formation of a mature fibrin clot from fibrinogen precursors in blood coagulation.[343] Fast thiol–disulfide exchange (TDE) reactions (see Section 1.1.1) occur at specific cysteine pairs and alter local protein topology.[14–16] Observations of TDE in protein systems suggest that these reactions redistribute strain and reorganize hydrogen bonding and electrostatics.[334,344,345] Accordingly, these local changes propagate across the molecule on slower timescales, producing domain movements and interface repacking that reshape access to reactive cysteines and modify their microenvironments. The slow-motion cycle can be reset when a subsequent TDE, now primed by the preceding global rearrangement, occurs.[17–19] Thus, for the reaction network it can be expected

that rapid reactive steps gate slow structural transitions and that the resulting conformational state, in turn, gates the next reaction, perpetuating a reaction–dynamics cycle.

To elucidate the mechanistic coupling between chemical reactivity and conformational dynamics in such systems, methods are needed that can resolve individual reaction events and relate them to slower, large-scale structural transitions. A pragmatic approach is to generate conformational ensembles with MD and then probe the reactivity at selected conformations.[346,347] This manual selection of states is only feasible for systems with few accessible states and clear timescale separation. For macromolecules that undergo conformational cycles or exhibit promiscuous interactions, this approach quickly becomes intractable because of the number of states to be considered. This shifts the focus toward approaches that also account for transitions between states, thereby providing a more complete picture of how molecular processes unfold.

In response, suitable methods should avoid bias towards predefined states and instead enable a more continuous exploration of states. Various methodological advances aim to capture such dynamics more effectively. The combination of kinetic Monte Carlo with MD extends the timescales that can be accessed within a classical framework and allows for reactivity.[348,349] Gräter et al. applied this strategy to investigate how local bond scission[350] and hydrogen atom transfer[351] can trigger large-scale structural rearrangements in collagen. However, such approaches remain constrained by the approximations inherent to the underlying force field and the assumption of strict timescale separation.[350]

On the other hand, quantum mechanics/molecular mechanics (QM/MM) simulations allow sampling of protein conformations while retaining reactivity at active sites, reducing computational cost and extending timescales. However, the computational cost of the QM region still limits extensive conformational exploration.[127,339] In their 2021 review,[127] Cui et al. discuss the improvement of sampling efficiency in QM/MM simulations as one of the major "burning issues" in the field. In principle, adaptive QM/MM schemes[147–156] could be used to apply quantum mechanics only when reactions occur and revert to more efficient models when conformational sampling dominates. However, these approaches are still under development and not yet ready for simulations of macromolecules. They are methodologically sophisticated and can lead to temporal and spatial artifacts and additional uncertainty in calculations.[147,151,153] An alternative avenue is a static QM/MM partitioning combined with enhanced sampling to accelerate the exploration of protein conformations directly in the QM/MM framework. Starting from a typical QM/MM setup that employs a set of collective variables (CVs) to sample the reaction within the QM region, one can extend this set to also accelerate sampling of the MM environment, such as conformational changes in proteins. Efficient sampling of the environment reduces simulation time needed to reveal potential couplings between chemical reactions and conformational dynamics.[127] Despite its promise, the explicit use of a second set of CVs to characterize the environment has rarely been applied in QM/MM simulations, and its capacity to uncover mechanistic couplings remains largely unexplored. Reported applications have been restricted to additional CVs targeting local

motions of single residues,[133,352] or to less specific descriptors of protein structures such as solvent accessible surface area[353] or root-mean-square deviations.[354] A notable gap remains in the systematic developments and applications.

This limited progress underscores a critical challenge: suitable CVs for complex macromolecular motions remain difficult to define, and the computational expense of QM/MM restricts the statistical robustness needed to learn effective collective variables (CVs) via machine learning (ML) algorithms.[191,192,195,197,355,356] To address this challenge, the present exploratory study transfers machine-learned CVs obtained from long classical MD to QM/MM simulations in order to improve conformational sampling efficiency. The learning procedure employs two classical linear dimensionality-reduction algorithms, principal component analysis (PCA) and time lagged independent component analysis (tICA). As a pilot system, TDE in a simplified model of fibrinogen is considered, which exemplifies the coupling of disulfide exchange with protein conformational dynamics. The dimensionality-reduction task compresses the feature space defined by five dihedral angles that characterize the conformational dynamics of a single disulfide bond into a 1-dimensional CV.[357,358] The choice of these dihedral descriptors is motivated by the established observation that distinct disulfide conformations are associated with specific structural and functional roles in proteins.[357,358] Although developed in this specific context, the strategy relies on classical ML to reduce complexity, preserve interpretability, and facilitate evaluation and transferability, providing a foundation for broader applications in QM/MM simulations.

8.2. Methods

The computational workflow of this study integrates classical MD and QM/MM simulations in a sequential manner to address the challenge of sampling conformational changes coupled to chemical reactivity. (1) Classical MD simulations were carried out to generate statistically robust training data and ensure adequate sampling of rare conformational events. (2) Linear dimensionality reduction methods, namely principal component analysis (PCA) and time-lagged independent component analysis (tICA), were applied to the trajectory data to extract low-dimensional CVs that encode essential dynamical modes. PCA[238,359] and tICA[360,361] have been successfully applied to derive CVs for protein dynamics in classical MD simulations. The aforementioned approaches were chosen because they are computationally inexpensive and data efficient, and they produce interpretable variables with fewer parameters than deep learning methods, thereby improving validation, reproducibility, and transferability across systems.[190,203,231] (3) The learned CVs were applied in QM/MM metadynamics (MTD) simulations, combined with a second CV describing the TDE to construct a 2-dimensional enhanced sampling setup. Finally, the resulting simulations were analyzed to characterize transition events, probe the coupling between protein conformational changes and chemical reactivity, and assess the structural heterogeneity of the space sampled.

Model

A simplified system for studying reaction dynamics in fibrinogen aggregates was constructed from two small protein models linked by a disulfide bridge. *Homo sapiens* glutaredoxin (Grx) (PDB ID: 1JHB) and HMA4n (Hma) (PDB ID: 2KKH) were covalently linked by a disulfide bridge between Cys23 of Grx and Cys27 of Hma. Cys26 of Grx is deprotonated and can approach the disulfide bridge to initiate a TDE. This pilot system allows the probing of domain movements and interface repacking, since the minimal structural unit consists of a central disulfide and the surrounding interfaces (Figure 8.1C). The prospective application of dimensionality reduction aims to reduce the 10-dimensional feature space describing the torsional dynamics of the critical disulfide bond to a single CV (see *Machine Learning* below). The choice of these dihedral descriptors is motivated by the well-established observation that distinct disulfide conformations are associated with specific structural and functional roles in proteins.[357,358] By capturing these fundamental processes in a reduced system, the dynamics of the larger macromolecular complex can be repetitively reconstructed by extending the number of considered disulfide moieties.

Classical MD Simulation

All simulations were performed with periodic boundary conditions using GROMACS 2020.2[362] and the AMBER99SB-ILDN force field.[327] Short-range electrostatic and Lennard-Jones interactions were calculated with a cutoff of 10 Å, while long-range electrostatics were treated with particle-mesh Ewald summation.[165] The neighbor list was updated every 10 MD steps. The leap-frog integrator[163] was used with a 2 fs integration time step. Initial atomic velocities were drawn from a Maxwell–Boltzmann distribution at 300 K and controlled by the Bussi thermostat[332] with a relaxation time constant of 0.1 ps. Pressure was maintained at 1 bar using the Parrinello–Rahman barostat[173] with a coupling constant of 2.0 ps, isotropic coupling, and a compressibility of 4.5×10^{-5} bar^{-1} in all directions. The prepared systems were equilibrated in two stages, beginning with a 10 ns isothermal-isochoric ensemble (NVT) run followed by a 10 ns isothermal-isobaric ensemble (NPT) run. During equilibration, harmonic position restraints with a force constant of 1000 kJ mol^{-1} nm^{-2} were applied. After equilibration, unrestrained production simulations of 1 μs in length were performed under the same conditions, and snapshots of the trajectories were saved every 80 ps, resulting in a dataset of 12500 configurations.

Machine Learning

Features. The new CV was learned from 12500 configurations generated by classical MD simulations. The five dihedral angles spanning the disulfide bond were chosen as input features (Figure 8.2). The choice of these dihedral descriptors is motivated by the well-established observation that distinct disulfide conformations are associated with specific structural and functional roles in proteins.[357,358] Because dihedral angles are periodic, they cannot be directly employed in

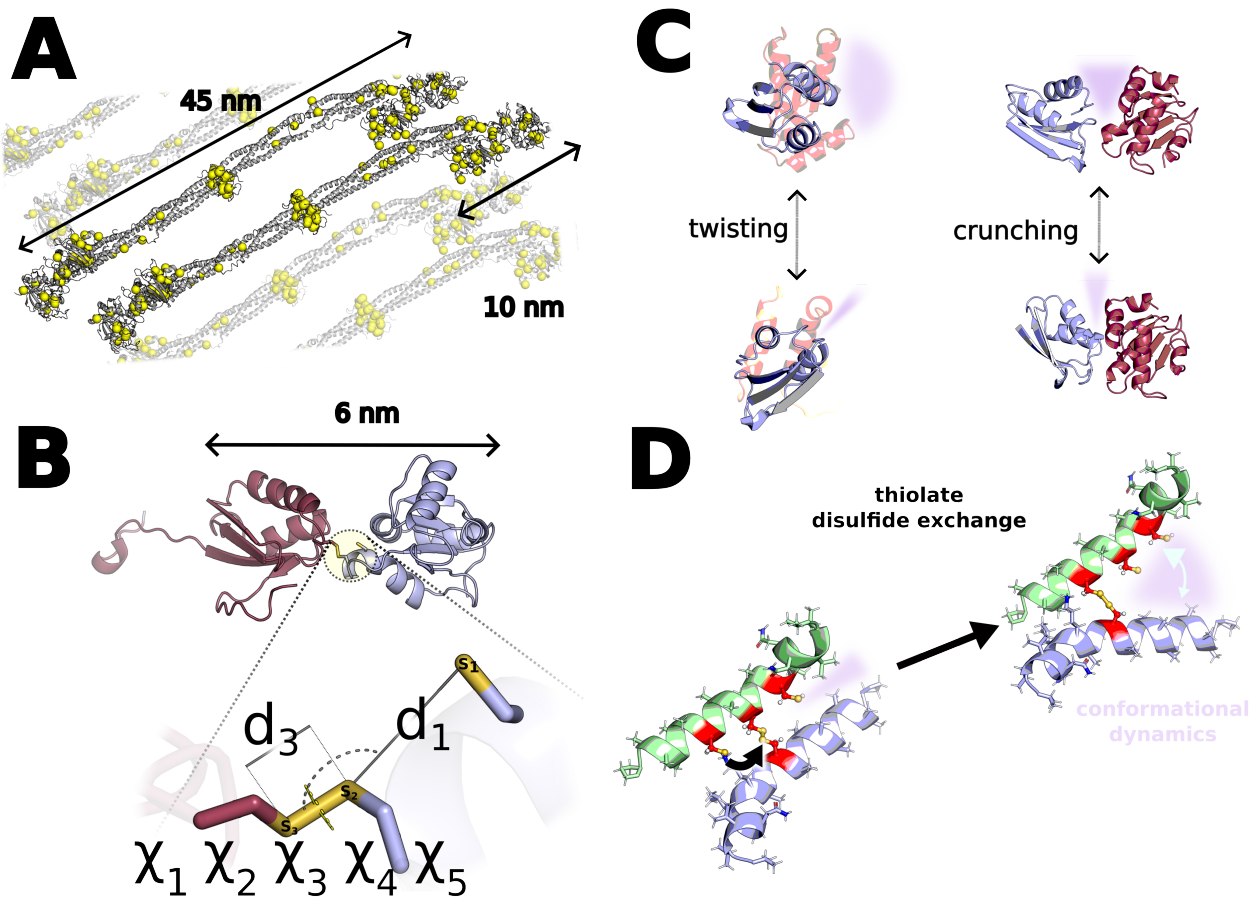

Figure 8.1.: Hierarchical organization and model system of disulfide-coupled dynamics in fibrinogen aggregates. (A) Structural model of fibrinogen aggregates showing the spatial distribution of disulfide bonds (yellow spheres) along the longitudinal axis. (B) Simplified model composed of Grx (blue) and Hma (red) covalently linked by a central disulfide bridge. The system size is reduced to an approximate diameter of 6 nm. The five torsional angles (χ_1–χ_5) across the disulfide linkage define the structural features used for machine learning, while the distances d_1 and d_3 define the CV describing the TDE. (C) Representative twisting and compressive motions at the protein–protein interface, constrained by the central disulfide bond, are shown as plausible modes of flexibility implied by general structural considerations. (D) Illustration of conformational changes following thiolate–disulfide exchange. The structural rearrangement is depicted as a hinge motion between two α-helices, representing a local conformational response within a larger framework.

ML due to numerical discontinuities. To ensure continuity, each dihedral was embedded in Euclidean space by transforming it into its sine and cosine components, thereby mapping the torsion onto the unit circle. Formally, a torsion angle χ is represented as the pair $(\cos\chi, \sin\chi)$.[357,358] This transformation expands the feature set from five torsional angles to ten sine–cosine components, yielding a smooth and Euclidean representation well suited for ML applications.

Principal Component Analysis. PCA was carried out using the Python package scikit-learn (version 1.6.1). The exact full singular value decomposition algorithm was applied, and the data were centered prior to transformation. All components of the resulting space are listed in Table C.1, and the corresponding explained variances are shown in Figure 8.3 (left). Further details on PCA can be found in Section 5.2.1.

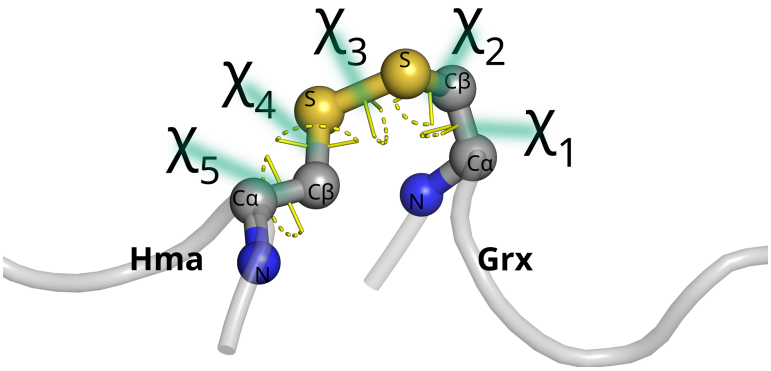

Figure 8.2.: Definition of the five torsional angles in a disulfide bond. The torsions χ_1, χ_2, χ_3, χ_4, χ_5 are defined by consecutive dihedral angles along the N–C–C–S–S–C–C–N linkage. In the present construct, the sequence of torsions is oriented from the Grx side of the disulfide bridge toward Hma. Together, these five dihedral angles describe the conformational flexibility of the disulfide bridge.[363]

Time-Lagged Independent Component Analysis. tICA was performed using the Python package PyEMMA (version 2.5.12) without kinetic mapping and with a lag time of 0.8 ns. VAMP2 scores for different lag times are presented in Figure C.1. All components of the resulting space are listed in Table C.2, and the corresponding implied timescales are shown in Figure 8.3 (right). Additional details on tICA are provided in Section 5.2.2.

QM/MM Simulations and Enhanced Sampling.

QM/MM Simulations. If not otherwise stated, simulation options were retained from the preceding classical MD setup. The QM region comprised the side chains of the three cysteine residues directly involved in the thiol–disulfide exchange (Cys23 and Cys26 of Grx and Cys27 of Hma). The truncation was applied at the C_β atom, with the bond between C_α and C_β capped by hydrogen link atoms placed at a fixed position along the bond vector. In total, the QM region consisted of 12 residue atoms and 3 link atoms. The QM/MM partitioning followed the setup previously reported in Ref. [334]. The QM region was treated using DFTB3,[120,122,288] using the 3ob[123,124] parameter set and a reparameterized S–S repulsive potential as presented in Ref. [221]. Electrostatic interactions between the charged QM region and the MM environment were scaled by a factor of 0.75. This scaling corresponds to the inverse square root of the optical dielectric constant and compensates for the absence of explicit electronic polarization in the MM environment.[303,304,334] To allow the system to adapt to the QM/MM Hamiltonian, an initial equilibration was carried out via a 100 ps NPT QM/MM simulation with a 0.5 fs integration step. The equilibrated structures were then used as start structures for MTD simulations, which were performed with a 1 fs integration step. All simulations were performed with a local implementation of QM/MM in GROMACS 2020.2[290] and DFTB+,[291] which is available from a public repository,[292,293] patched with PLUMED[330,331] (version 2.5.1).

Enhanced Sampling. One-dimensional (1D) and two-dimensional (2D) multiple-walker MTD [181,364,365] simulations were performed using 24 walkers with 2 ns simulation time each, resulting in

a total of 48 ns of trajectory data. In the 1D setup, the first collective variable CV_1 described the TDE by measuring the distances (d_1, d_3) of the lateral sulfur atoms (S1 and S3) from the central sulfur atom (S2) within the disulfide bond, as shown in Figure 8.1 panel B. S1 is located in Cys26 of Grx, which is deprotonated and can initiate TDE; S3 is located in Cys27 of Hma. CV_1 was defined as the antisymmetric distance coordinate difference $d_1 - d_3$. In the 2D setup, CV_1 was retained and a machine-learned CV was included as CV_2 to explore the conformational space. CV_2 was defined by the PCVARS directive in PLUMED. The Gaussian height was set to 0.5 kJ mol^{-1} and deposited every 0.5 ps. The deposited biases of all walkers were exchanged at the same interval. The Gaussian width was set to 0.01 for CV_1 and 0.05 for CV_2. Additional restraints were introduced to restrict the conformational space and prevent undesired side reactions within the QM region. The general setup followed the protocol in Ref. [334], where details on the switching functions and restrained coordination numbers can be found. Restraints were applied to confine the disulfide system within a physically meaningful region of conformational space by limiting sulfur–sulfur separations to below 10 Å, excluding bond-breaking events without a proximal thiolate through coordination-number restraints between the three sulfurs, and preventing C_β deprotonation by restraining the coordination between each sulfur and its C_β–H atoms.

Analysis

Additional analyses were carried out to assess sampling efficiency, structural heterogeneity, and protein–protein interactions. The attacking angle was defined by atoms S_1–S_2–S_3 (angle between Cys26,Cys23 and Cys27). The radius of gyration was computed with PLUMED, excluding the highly flexible C-terminal tail of Hma (residues 108–120) to avoid spurious fluctuations. Protein–protein interactions near the disulfide bridge were quantified with PLUMED by calculating coordination numbers (P_c) between atoms of both protein partners within a 6 Å cutoff. The solvent-accessible surface area (SASA) was calculated for the cysteines forming the disulfide bridge via the Hasel[366] approximation implemented in PLUMED. Conformational diversity was visualized using nonlinear dimensionality reduction via t-distributed Stochastic Neighbor Embedding (t-SNE), implemented in scikit-learn (version 1.6.1) with a perplexity of 40 and a learning rate of 200. The t-SNE algorithm projects high-dimensional data into a 2D map that preserves local structural relationships, enabling intuitive visualization of distinct conformational states.[367] Data from all simulations were labeled and combined to calculate the t-SNE projections used for comparing the sampled configurations. All 10 sine–cosine components of the torsion angles were used as input. For an additional input set, the input was extended by the radius of gyration and the coordination numbers (P_c). To further delineate discrete interaction states, a 2D Gaussian Mixture Model (GMM) was fitted to the results of prior analyses using scikit-learn (version 1.6.1). The attacking angle and the solvent-accessible surface area (SASA) disulfide were used as local descriptor and the radius of gyration and the coordination numbers (P_c) were used as global descriptions. Models with one to six components were trained with full covariance matrices, five

initializations, and a covariance regularization of 10^{-6}, and the optimal model was chosen by minimizing the Bayesian information criterion.[368] For the analysis of structural heterogeneity based on the 2D free-energy surface (FES), representative structural clusters were extracted from specific regions ("landmarks"). These landmarks were defined by rectangular windows in the respective 2D CV spaces. In the 2D PC1 QM/MM simulations, four regions were assigned according to their x- and y-coordinate ranges: Landmark 1 (x: 0.23–0.47, y: –1.40 to –0.14), Landmark 2 (x: 0.11–0.24, y: 0.88–1.26), Landmark 3 (x: –0.29 to –0.07, y: 0.88–1.26), and Landmark 4 (x: –0.30 to –0.15, y: –1.00 to –0.47). Similarly, in the 2D IC1 QM/MM simulations, four corresponding regions were defined as Landmark 1 (x: 0.20–0.30, y: –1.80 to –1.40), Landmark 2 (x: 0.20–0.30, y: 0.20–0.40), Landmark 3 (x: –0.30 to –0.10, y: 0.20–0.40), and Landmark 4 (x: –0.30 to –0.10, y: –1.90 to –1.50). The free-energy surface (FES) for component two (PC2 and tIC2) are shown in Figure C.6.

8.3. Results and Discussion

This study investigates how machine-learned CVs derived from classical MD simulations can enhance conformational sampling in QM/MM simulations of TDE as a pilot system for coupling between chemical reactions and conformational changes in protein systems. A detailed description of the computational workflow is provided in Section 8.2, and a description of the model system is given in Figure 8.1 to establish the context. The results are presented in three parts: (1) The machine-learned CVs optimized for classical MD trajectories are analyzed to verify that they capture physically meaningful dynamical modes and are suitable for application in QM/MM. (2) The 2D QM/MM MTD simulations are run and evaluated by comparing sampling efficiency, configurational coverage, and convergence with classical MD and 1D QM/MM simulations. This analysis shows how the learned CV affects reactivity and conformational sampling. (3) Based on the combined structural and energetic data, a mechanistic hypothesis for the thiol–disulfide exchange reaction is formulated.

8.3.1. Evaluating CVs

The PCA and tICA were run on 12500 configurations generated by classical MD simulations and used sine–cosine components of the five torsion angles in the disulfide bridge as features. Before employing the learned CVs in QM/MM simulations, it is essential to evaluate them to ensure their validity. This assessment can be conducted directly on the classical MD data. A new embedding is only meaningful if it provides a reduced representation that preserves the targeted metric of the original feature space within a low-dimensional space. This property is typically reflected by a spectral gap between successive components.[236,240] For PCA, the targeted metric is the explained variance, shown in Figure 8.3 (left), which exhibits a distinct gap between the first and second components. The first principal component alone already captures 85% of the total variance, demonstrating that the dimensionality can be effectively reduced from ten to one without

substantial information loss. For tICA, the targeted metric is the implied timescale derived from the eigenvalue spectrum (Figure 8.3, right). The first component captures the slowest dynamical mode with an implied timescale of 184.1 ps, while for the second component it decreases sharply to 4.8 ps, again revealing a significant spectral gap. This confirms that both PCA and tICA efficiently compress the torsional feature space into a single dominant CV that retains the essential dynamical information of the original data.

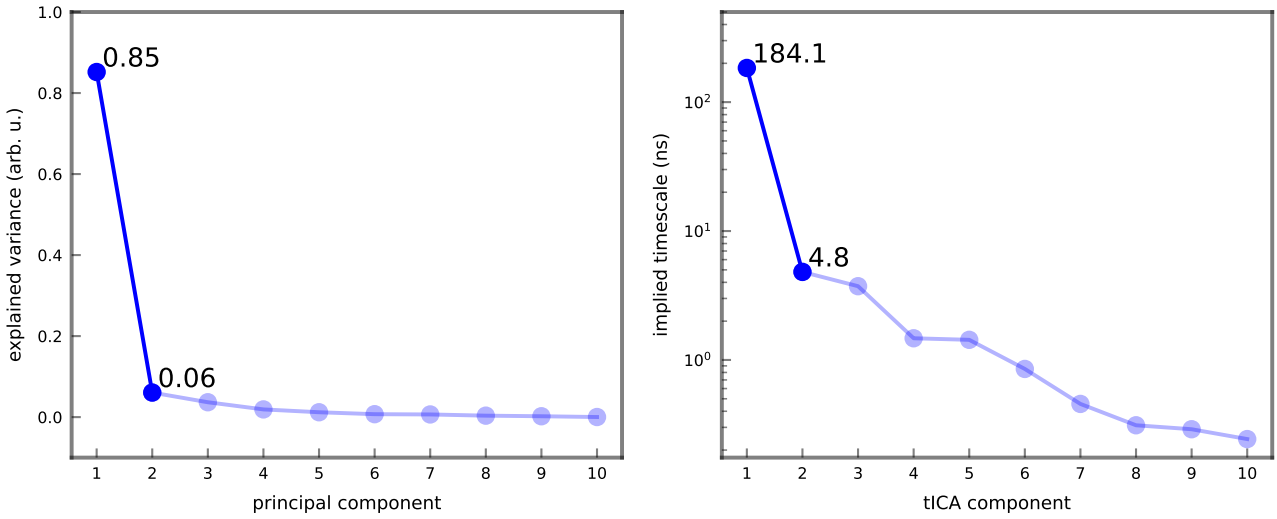

Figure 8.3.: Spectral properties of the PCA and tICA models trained on the torsional feature set (five $(\cos\chi, \sin\chi)$ pairs). The left panel shows the explained variance of the first ten principal components obtained from the PCA model, and the right panel displays the eigenvalue spectrum and corresponding implied timescales of the tICA model. Both reveal a clear spectral gap, indicating that a single dominant component captures the essential slow dynamics of the system.

The presence of a characteristic spectral gap confirms that both PCA and tICA perform effective dimensionality reduction. However, this criterion alone is not sufficient to ensure that the resulting components represent physically meaningful motions of the molecular system. To verify their relevance, the MD trajectory was projected onto the first components obtained from PCA and tICA. Both time series exhibit a closely matching temporal evolution, characterized by a sharp fluctuation at approximately 110 ns, a major transition around 650 ns, and a smaller rearrangement near 900 ns, as shown in Figure 8.4. In contrast, projections onto higher components (Figures C.2 and C.3) display only minor fluctuations without distinct switching behavior, reinforcing the interpretation of a spectral gap and indicating that only the first component describes a collective transition between two dominant states.

This conclusion is further supported by the pairwise scatter plots of the first five components obtained by dimensionality reduction (Figures C.4 and C.5 for PCA and tICA, respectively), where only combinations including the first component separate into two distinct clusters, while all others form diffuse, spherical distributions. The exploration of the 10-dimensional feature space sampled during the MD trajectory can be visualized by reducing it to two dimensions using t-SNE for illustrative purposes. Figure 8.5 shows four color-coded clusters that correspond to distinct

regions of the original feature space. These clusters indicate that specific time intervals of MD trajectories occupy separate regions in the high-dimensional torsion space and reveal underlying dynamical transitions between them. Overall, the leading components (PC1 and IC1) thus provide a compact, low-dimensional representation that distinguish two dominant conformational states, supporting their suitability as collective variables CVs for subsequent QM/MM simulations.

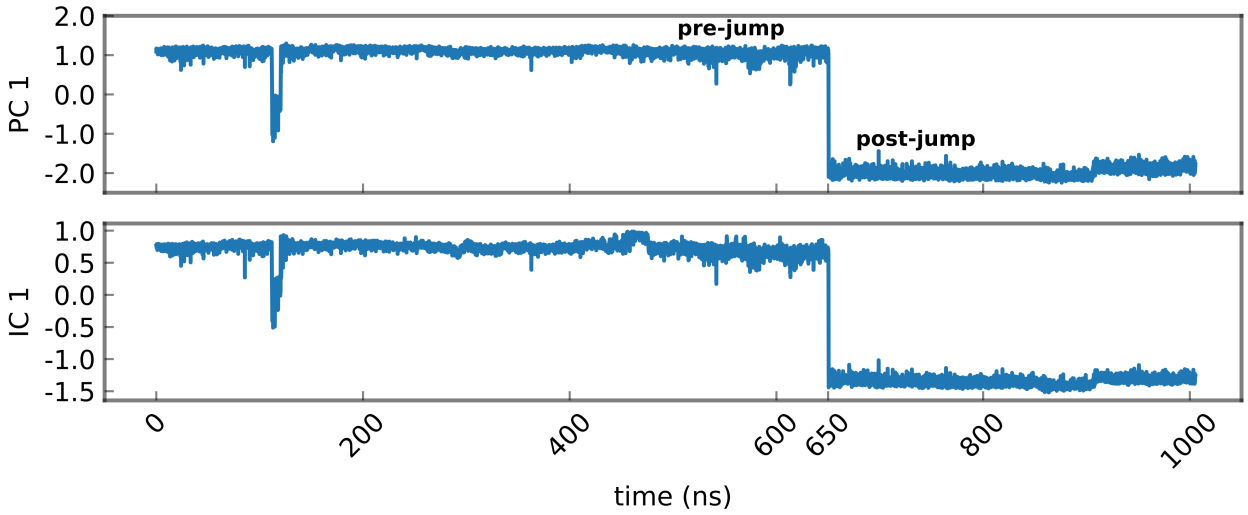

Figure 8.4.: Projection of the molecular dynamics trajectory onto the first component obtained from PCA (upper panel) and tICA (lower panel). Both projections reveal a comparable temporal evolution, illustrating that the leading component in each method captures a dominant mode of the system.

To resolve which structural motions underlie the state transition captured by the first principal component (PC1) and the first independent component (IC1), the torsional features were examined directly. Figure 8.6 (upper panel) shows the time series of the ten input features, represented as five sine–cosine pairs, in a window centered on the transition at 650 ns. The largest, concerted changes occur for χ_1, χ_2, and χ_5. Figure 8.6 (middle panel) reports the corresponding χ torsion angles over the full trajectory. Notably, the transition at 650 ns coincides with step-like shifts in χ_1, χ_2 and χ_5 that occur only once and persist thereafter. The corresponding structural change is shown in the lower panel. Changes in χ_2 and χ_5 mark the event and indicate a concerted reorientation of the cysteine side chains around the disulfide bond. For reference, χ_2 belongs to the Grx side of the bridge, whereas χ_5 belongs to the Hma side. This reorganization primes the system for the global rearrangement and also modulates local dynamics of the disulfide bridge.

Both the first principal component (PC1) and the first independent component (IC1) capture the same transition events, despite being optimized for distinct criteria, maximal variance and maximal autocorrelation, respectively. This agreement indicates that the targeted transition is characterized by both high variance and slow dynamics, consistent with a free energy surface composed of two narrow basins separated by a broad barrier, where intrastate fluctuations are small compared to those associated with the transition. Previous studies have emphasized that tICA may occasionally detect statistically insignificant[191] or random modes[369] due to its bias toward

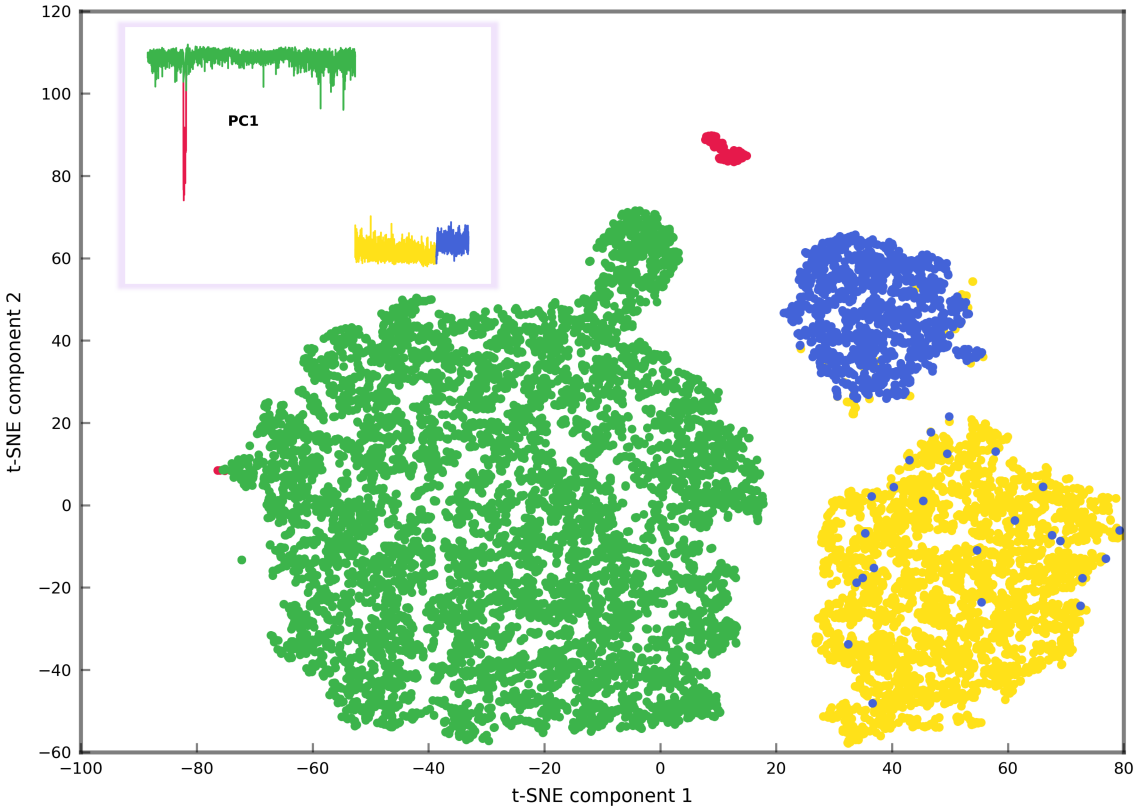

Figure 8.5.: Two-dimensional t-SNE projection of the 10-dimensional torsional feature space sampled during the MD trajectory. Four color-coded clusters (red, green, blue, yellow) correspond to distinct regions of the high-dimensional space, indicating that specific segments of the PC1 trajectory populate separate regions associated with characteristic dynamical states. The insets show the corresponding PC1 time series, highlighting the intervals that map onto each cluster.

rare events. However, no such artifacts are observed here, confirming that both methods identify physically meaningful collective motions. The individual components for all construced CVs are shown in Table C.3, with cosine similarity and correlation coefficients around 0.9, indicating high correspondence.

A noticeable similarity is observed in the temporal evolution of the component weights $c_{i,\mathrm{PC1}}$ (left) and $c_{i,\mathrm{IC1}}$ (right), as shown in Figure 8.7. The variance of these weights is higher for the features corresponding to the Hma side of the disulfide bridge (χ_3–χ_5), which could be attributed to the flexible loop from which the cysteine residue extends toward Grx. The weights of the PC1 components respond most clearly to the major transition at 650 ns and subsequently converge to stable values. The IC1 weights exhibit stronger initial fluctuations but gradually stabilize toward the end of the trajectory, indicating a slower convergence of the independent component.

A final aspect to consider is whether the observed conformational changes at the disulfide bridge couple to structural rearrangements spanning a lager part of the protein complex. Figure 8.8 compares the time evolution of PC1 (panel A) with the torsion angles χ_1–χ_5 (panel B), the radius of gyration R_g (panel C), and the coordination number P_c between the protein interfaces (panel D). The selected quantities provide measures of the protein environment: the χ_i angles capture local

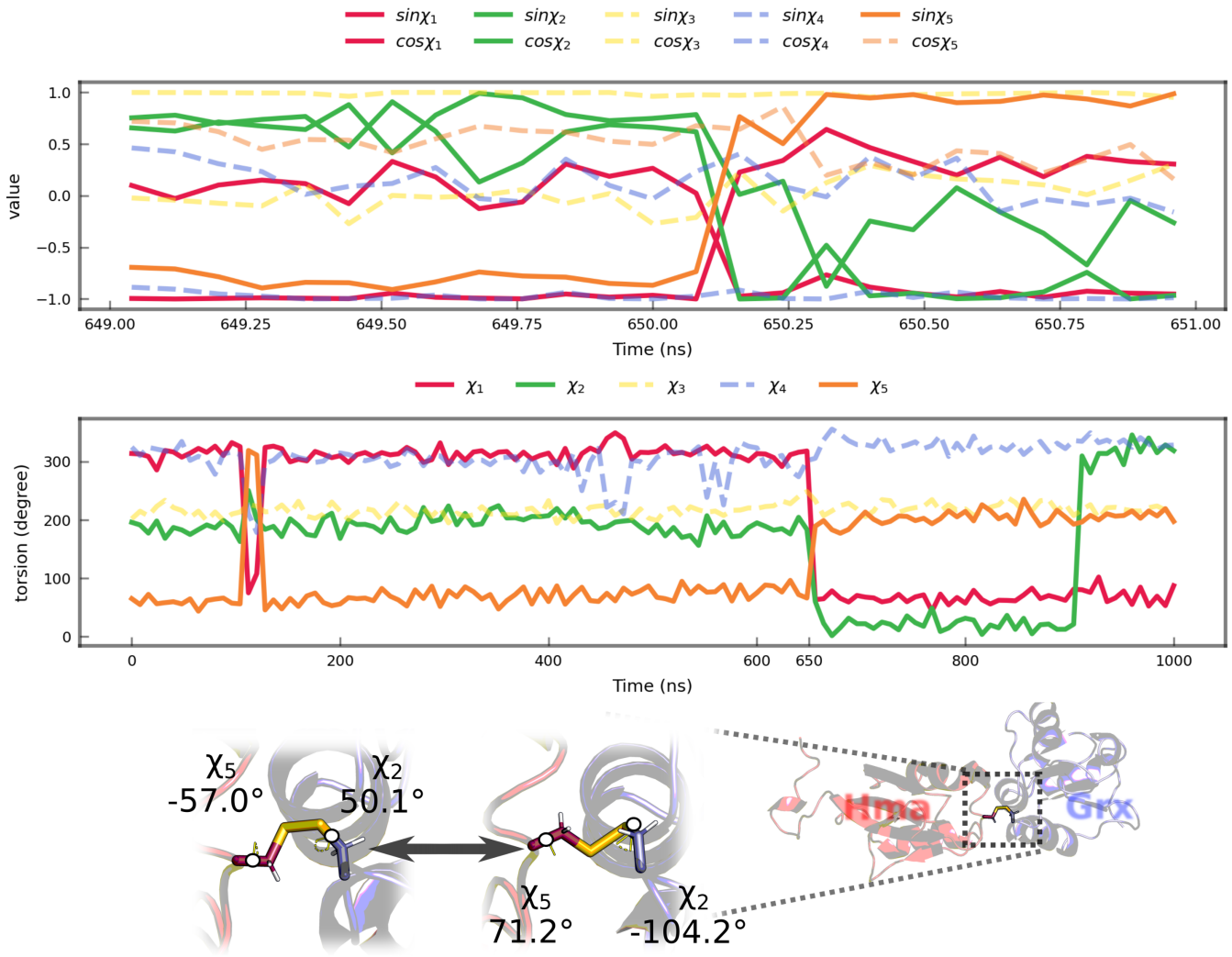

Figure 8.6.: Upper panel: sine–cosine representations of χ_1 to χ_5 in a window around 650 ns, showing concerted sign changes most prominently for χ_1, χ_2, and χ_5. Middle panel: χ_1 to χ_5 torsion angles over the full trajectory; the 650 ns event corresponds to step-like, persistent shifts in χ_1, χ_2 and χ_5, with smaller adjustments in the remaining torsions. In both panels, solid lines denote features with the largest changes, whereas dashed lines denote features with comparatively minor variations. Lower panel: corresponding concerted reorientation of the cysteine side chains around the disulfide bond.

conformational changes directly linked to the disulfide geometry, R_g reflects global changes in molecular compactness and overall shape, and P_c quantifies interfacial contacts that report on packing and interaction strength between the two protein domains. In contrast to the step-like transitions observed for the disulfide torsions, both R_g and P_c vary more gradually over time, with their extrema around 350 ns. Minor but discernible shifts also occur near 110 ns and 650 ns, coinciding with transitions detected in PC1. These trends indicate that variations in the disulfide geometry are accompanied by subtle adjustments of protein packing and overall compactness.

Overall, the analysis shows that the machine-learned CVs derived from classical MD are suited for use in QM/MM simulations. Both PCA and tICA reveal a clear spectral gap and capture a distinct transition involving a concerted reorientation of the cysteine side chains. The corresponding mode links local disulfide dynamics with broader structural rearrangements, indicating that changes in

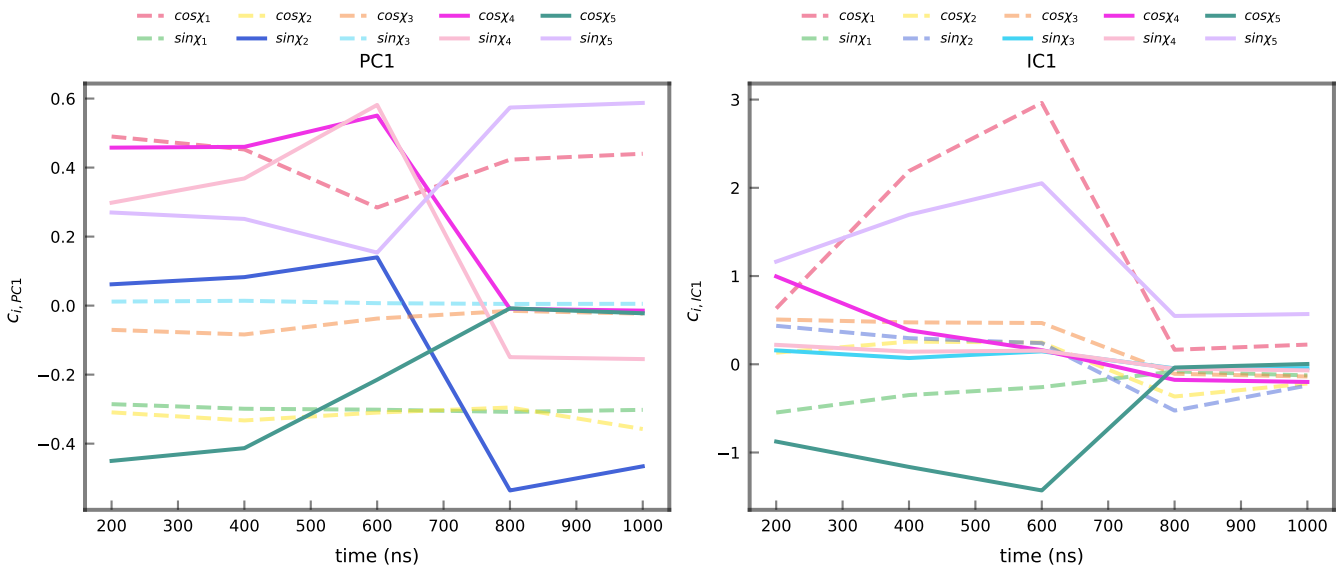

Figure 8.7.: Time evolution of the component weights $c_{i,\mathrm{PC1}}$ (left) and $c_{i,\mathrm{IC1}}$ (right) derived from the sine–cosine representations of χ_1–χ_5. The PC1 weights converge steadily after the transition, while IC1 shows stronger initial fluctuations and slower stabilization.

the bridge geometry coincide with subtle adjustments in protein packing and compactness. Further 2D QM/MM simulations will supplement the current view of whether these motions are correlated. They may also provide greater capacity to explore how this relationship is relevant for describing or controlling the coupling between reactivity and conformational change in QM/MM simulations.

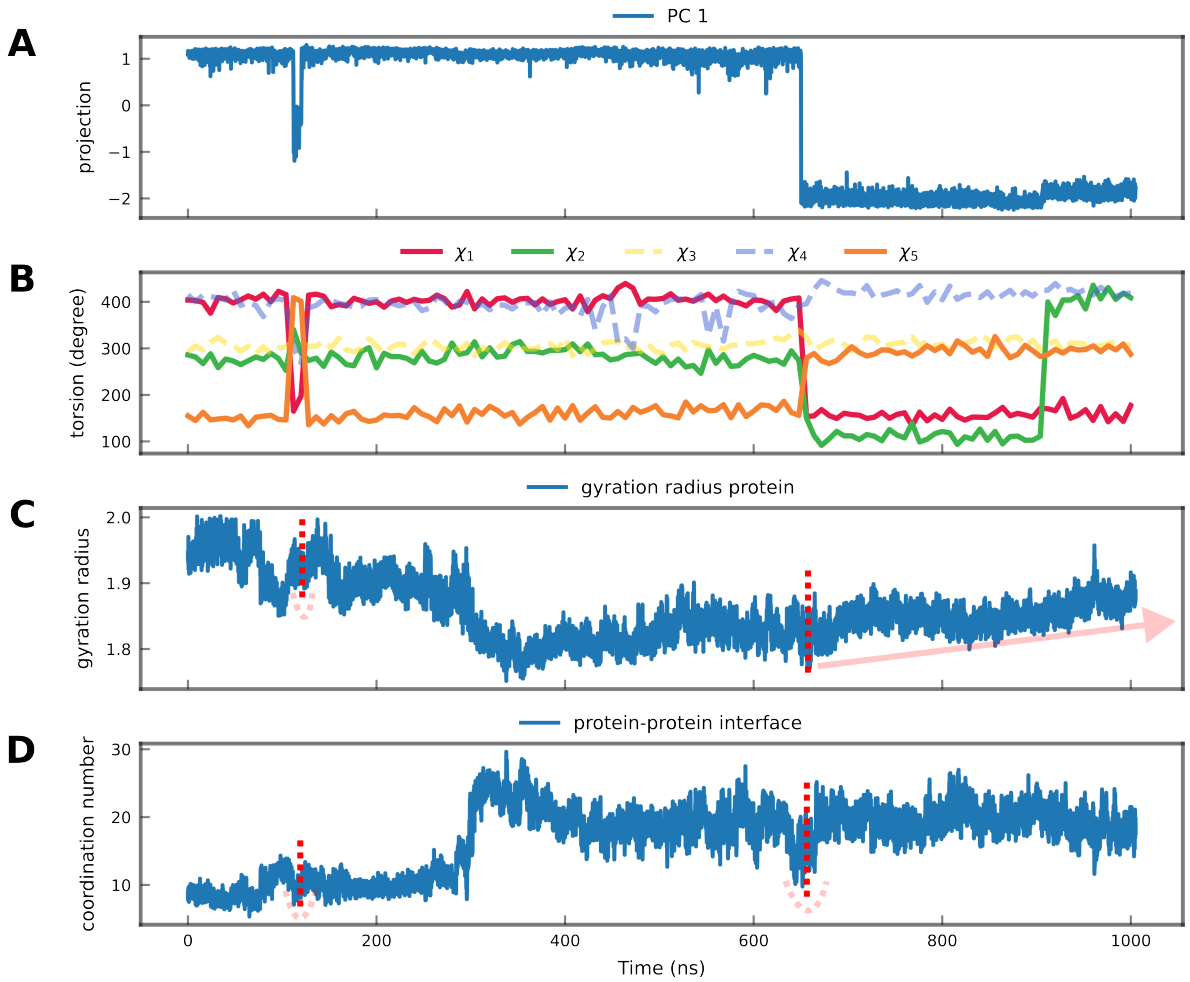

Figure 8.8.: Time evolution of local and global structural descriptors compared to the projection onto PC1. (A) Projection of the MD trajectory onto PC1, identifying major conformational transitions at approximately 110 ns and 650 ns. (B) Time series of the torsional angles χ_1–χ_5 describing the local geometry of the disulfide bridge; step-like changes in χ_2, χ_2 and χ_5 mark the transition. (C) Radius of gyration R_g of the protein, reporting on overall compactness and global shape; gradual changes are observed over time, with minor perturbations coinciding with the main transition events. (D) Coordination number P_c between the protein interfaces, reflecting interdomain packing and contact formation; local minima at 110 ns and 650 ns indicate transient loosening of the interface. Wells or transition points that coincide with the events observed in PC1 are indicated by red dashed lines; where gradual trends are detected, their direction is highlighted by red arrows.

8.3.2. Applying CVs in QM/MM

The newly derived and validated CVs were subsequently employed in QM/MM enhanced sampling simulations. 1D and 2D QM/MM multiple-walker metadynamic simulations were performed with a total simulation time of 48 ns each. The first collective variable, CV_1, described the TDE. In the 2D setup, CV_1 was retained and a machine-learned CV was included as CV_2 to explore the conformational space. The 1D setup serves as a reference to judge the influence of additional CVs on sampling. Central to this evaluation are the sampling efficiency within the CV space, the 10-dimensional torsional feature space, and the influence of global conformational changes.

The underlying idea is to transfer the machine-learned CV from classical MD simulations to the QM/MM framework in order to enhance sampling of the relevant conformational space. These CVs were trained to capture a dominant transition that is accessible on the MD timescale. The states associated with these transitions are referred to as the pre-jump and post-jump states, as illustrated in Figure 8.4. Consequently, improved sampling in the QM/MM simulations is achieved when these states are visited and interconverted more frequently.

Figure 8.9 illustrates the exploration of the CV space during the QM/MM metadynamics simulations. Each column corresponds to a distinct setup: the first two employ 2D simulations using either the first principal component (PC1) or the first time-lagged independent component (IC1) as the second CV, while the third column represents the 1D reference simulation along the reactive CV_1. The rows display projections onto the PC1 and IC1 components, respectively, enabling a direct comparison of the conformational space sampled in each setup. The machine-learned CVs were derived from classical MD trajectories in which the disulfide bridge remained intact and therefore capture the dynamics of the covalently connected cysteine pair. In contrast, the QM/MM simulations explicitly sample the TDE, involving bond rupture and reformation, which introduces distinct dynamical regimes. Accordingly, configurations corresponding to the broken disulfide bond are shown in pale colors. These regions lie outside the domain where the learned CVs are well-defined. The dashed lines indicate the values of the CV that define the pre-jump and post-jump states observed in the MD trajectory (Figure 8.4). Sampling efficiency can be assessed according to three criteria: the frequency of transitions between both states, the residence times within each state, and the relative populations of the broken and intact disulfide forms.

The sampling behavior differs markedly between the setups (Figure 8.9). Both 2D simulations employing PC1 and IC1 as the second CV reach the post-jump state consistently. In contrast, the 1D simulation visits this state only briefly, as indicated by sharp transient spikes, suggesting short-lived fluctuations rather than stable configurations. The 2D simulations, however, not only reach but also maintain the post-jump state for extended periods, demonstrating improved stability and more extensive sampling of the relevant conformational space. Moreover, in the 1D simulation, the system rapidly proceeds to the broken disulfide state and remains there for most of the trajectory. In the 2D setups, by contrast, the reduced population of the broken disulfide form

indicates that inclusion of the additional CV facilitates broader and more efficient exploration of the conformational landscape.

In both 2D setups, PC1 and IC1 exhibit stable sampling of the post-jump state. However, the sampling is generally more efficient within the space defined by the employed CV. For example, the simulation using PC1 as the second CV shows a higher transition frequency and greater state stability along PC1, while IC1 in this setup is still sampled more effectively than in the 1D reference. Conversely, in the 2D simulation employing IC1, this component is sampled more extensively than PC1, although the difference is less pronounced. Notably, the broken disulfide state is reached more readily and explored more frequently in the IC1 setup, suggesting that PC1 favors conformations less conducive to bond cleavage. This offers a more nuanced view compared to the analysis based on the classical MD results, in which the CVs exhibited nearly identical projections.

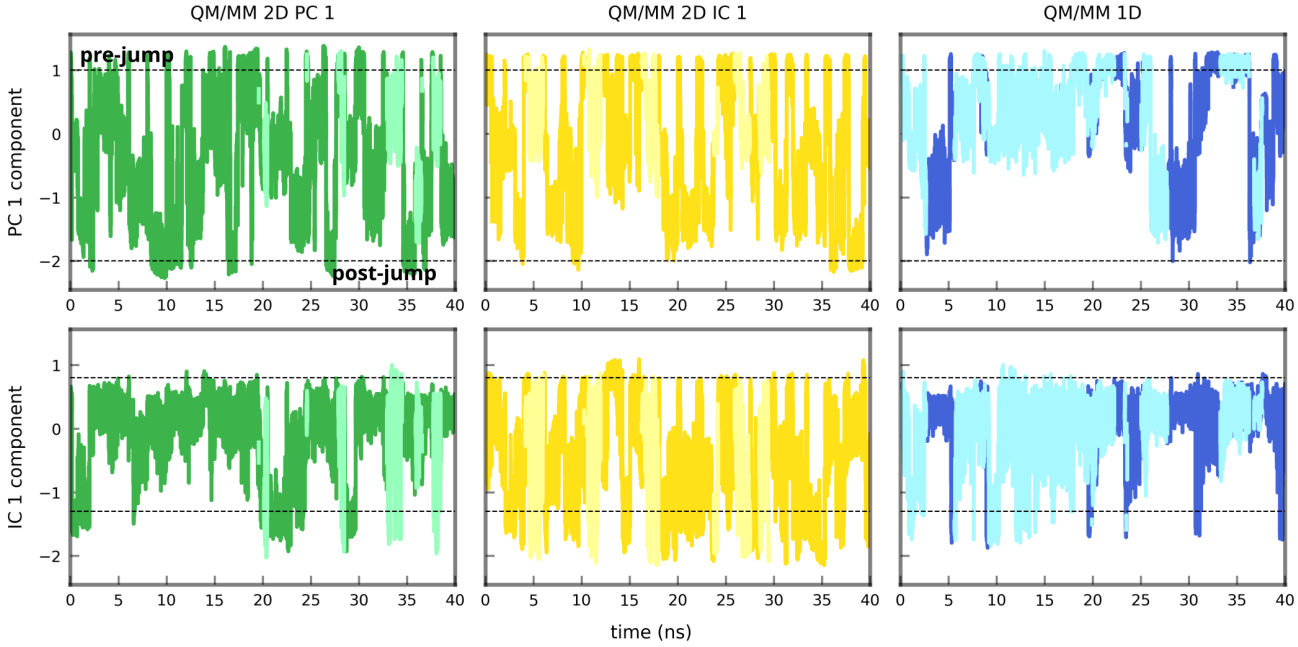

Figure 8.9.: Time evolution of the first principal (PC1, top row) and time-lagged independent (IC1, bottom row) components during the QM/MM metadynamics simulations. Columns correspond to different simulation setups: 2D simulations using PC1 (left) or IC1 (middle) as the second collective variable, and the 1D reference simulation (right). Dashed lines indicate the CV values defining the pre- and post-jump states observed in the classical MD trajectory. Pale colors denote configurations associated with the broken disulfide bond, where the machine-learned CVs lose their intended definition. Total simulation time for each setup was 48 ns.

The 2D QM/MM metadynamics setups achieved better sampling of the IC1 and PC1 spaces than the one-dimensional setup. A more comprehensive assessment, however, is obtained by examining the full 10-dimensional torsional space, which provides a detailed view of how the underlying conformational space is explored. Figure 8.10, panel (A), presents the t-SNE projection of this 10-dimensional torsional space onto two dimensions. The first column shows the conformational space sampled in the classical MD simulation, with color coding distinguishing the pre-jump and

post-jump states. The subsequent columns show the corresponding projections for the QM/MM metadynamics simulations, where the post-jump states from the classical trajectory are retained as a reference. A comparison based on the projected area of sampled configurations indicates that sampling efficiency increases in the order: 1D < 2D (IC1) < 2D (PC1). Overall, the 2D simulations achieve a more heterogeneous and extensive exploration of the conformational landscape. Remarkably, in contrast to the observations made in the reduced CV spaces (Figure 8.9), the post-jump states are not sampled by the QM/MM simulations in the 10-dimensional torsional space. Instead, all three simulations predominantly explore conformational clusters located between the regions corresponding to the post-jump states form the classical MD, with the 2D setups showing notably denser coverage of these intermediate regions.

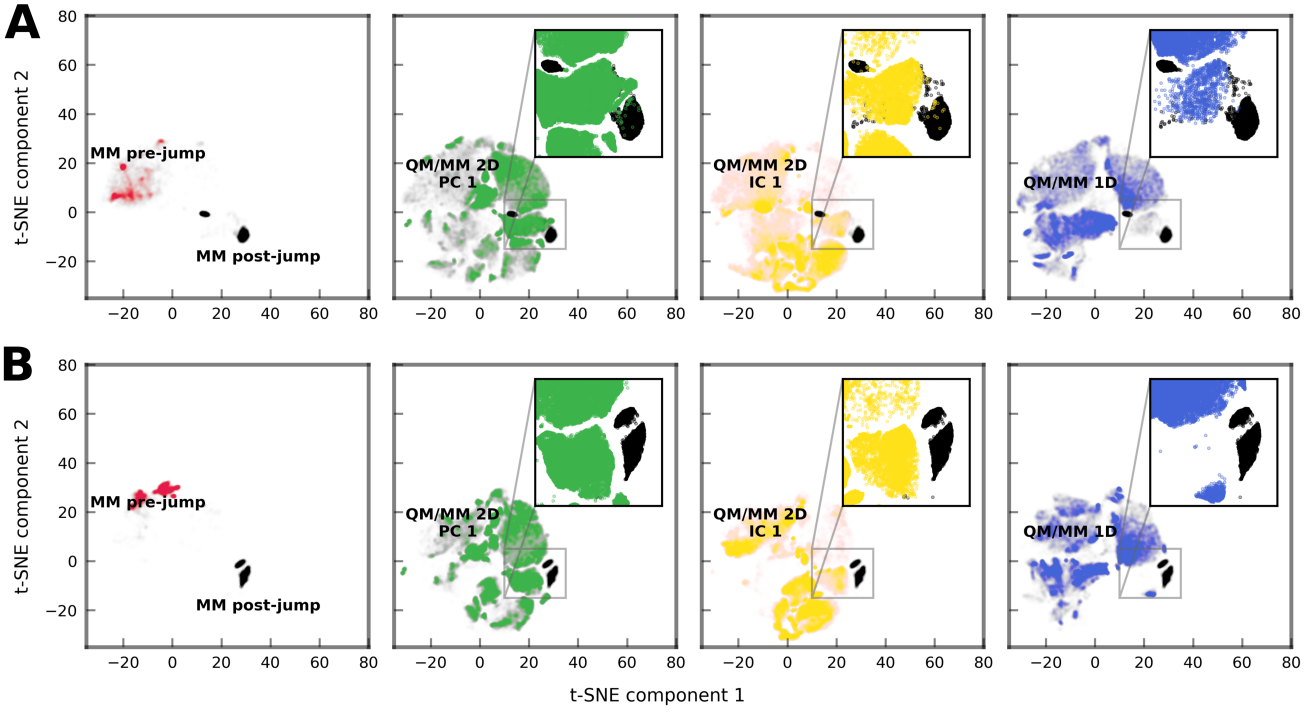

Figure 8.10.: t-SNE projections of the sampled conformational space based on torsional and global structural descriptors. Panel (A) shows the 10-dimensional torsional feature set, while panel (B) includes the extended twelve-dimensional set incorporating the radius of gyration and coordination number of interfacial residues. Each column corresponds to one simulation setup: classical MD (left), 2D QM/MM MTD using PC1 and IC1 as collective variables (middle), and 1D QM/MM MTD (right). Insets highlight regions near the classical post-jump basin. The inclusion of global descriptors in the 12D projection refines the separation between pre- and post-jump ensembles and reveals distinct sampling behavior among the different setups.

A possible explanation for the absence of stabilized pre- and post-jump states involves global protein conformational changes. As discussed in the analysis of the CVs, Figure 8.8 illustrates how the global protein structure can undergo continuous drift, which remains unaccounted for by the learned CV. To test this hypothesis, the same t-SNE clustering analysis was repeated using an extended feature set comprising twelve dimensions. The additional features included the radius of gyration and the coordination number characterizing the interacting protein surfaces. The results,

shown in Figure 8.10, panel (B), follow the same structural layout as panel (A). Incorporating these global descriptors resulted in a clearer separation of the conformational clusters, suggesting that the pre- and post-jump states differ from the conformations sampled in the 2D QM/MM simulations, due to changes in the overall protein structure. Furthermore, the analysis reveals that the 1D simulation fails to capture a cluster near the reference post-jump state, which is sampled in the 2D setups. This observation suggests that the machine-learned CV is not fully orthogonal to global protein conformational dynamics and may implicitly facilitate sampling of the corresponding conformational space.

These results confirm that the overall sampling of the genuine 10D torsion space is more wide-ranginge in the 2D setup than in the 1D case. However, enforced exploration of previously observed states in the classical MD simulations is hindered in the QM/MM simulations for two main reasons. (1) The construction of the machine-learned CV introduces a higher degree of degeneracy. Even when the CV values appear similar, the corresponding conformational ensembles can differ substantially. (2) Continuous drift of the global protein structure can stabilize distinct conformational states, preventing their recurrence when PC1 and IC1 are applied as CVs in the QM/MM simulations.

8.3.3. Mechanism Hypotheses

The 2D setup establishes a framework for systematically modeling the underlying reaction mechanism. By mapping the reaction pathway on the FES, this approach integrates both conformational and reactivity information. The improved sampling captures a broader range of relevant structures, offering a more reliable basis for identifying the conformational changes that drive the reaction. Once the critical regions and transition states on this surface are identified, a detailed analysis of structural heterogeneity can be conducted to characterize the ensemble that dominates each segment of the reaction path.

Panel B and E in Figure 8.11 show the 2D FESs obtained using the PC1 and IC1 setups, respectively. Each FES exhibits a similar topology characterized by two broad basins along the PC1/IC1 direction, connected by a transition region at high CV values that forms a corridor. Local minima were defined as landmarks, as indicated by the numbers in the FESs. The presence of this restricted pathway indicates that the simulations sample conformations of differing reactivity. The basin lowest in free energy in both setups is located at positive values of d1–d3, representing the reactant disulfide (initial state). The second basin, corresponding to the product disulfide, is shallow and lies 12 kcal mol^{-1} higher in energy than the former. This destabilization likely arises from the Grx to Hma binding, which is unfavorable and imposes strain on the newly formed disulfide bond. The FES based on PC1 shows a transition state at approximately 20 kcal mol^{-1}, about 2 kcal mol^{-1} lower than that obtained with IC1. However, the barrier between landmarks 2 and 3 is similar for both surfaces, around 17.5 kcal mol^{-1}. In the PC1 FES, the transition state is not elevated relative to landmark 2, but landmark 1 is lowered in energy, resulting in a deeper

basin with a relative barrier of about 5 kcal mol^{-1}. This feature is absent in the IC1 FES, where the corresponding basin is shallower with a relative barrier of about 2.5 kcal mol^{-1}. Thus, PC1 was able to identify lower-energy conformations in the landmark 1 region.

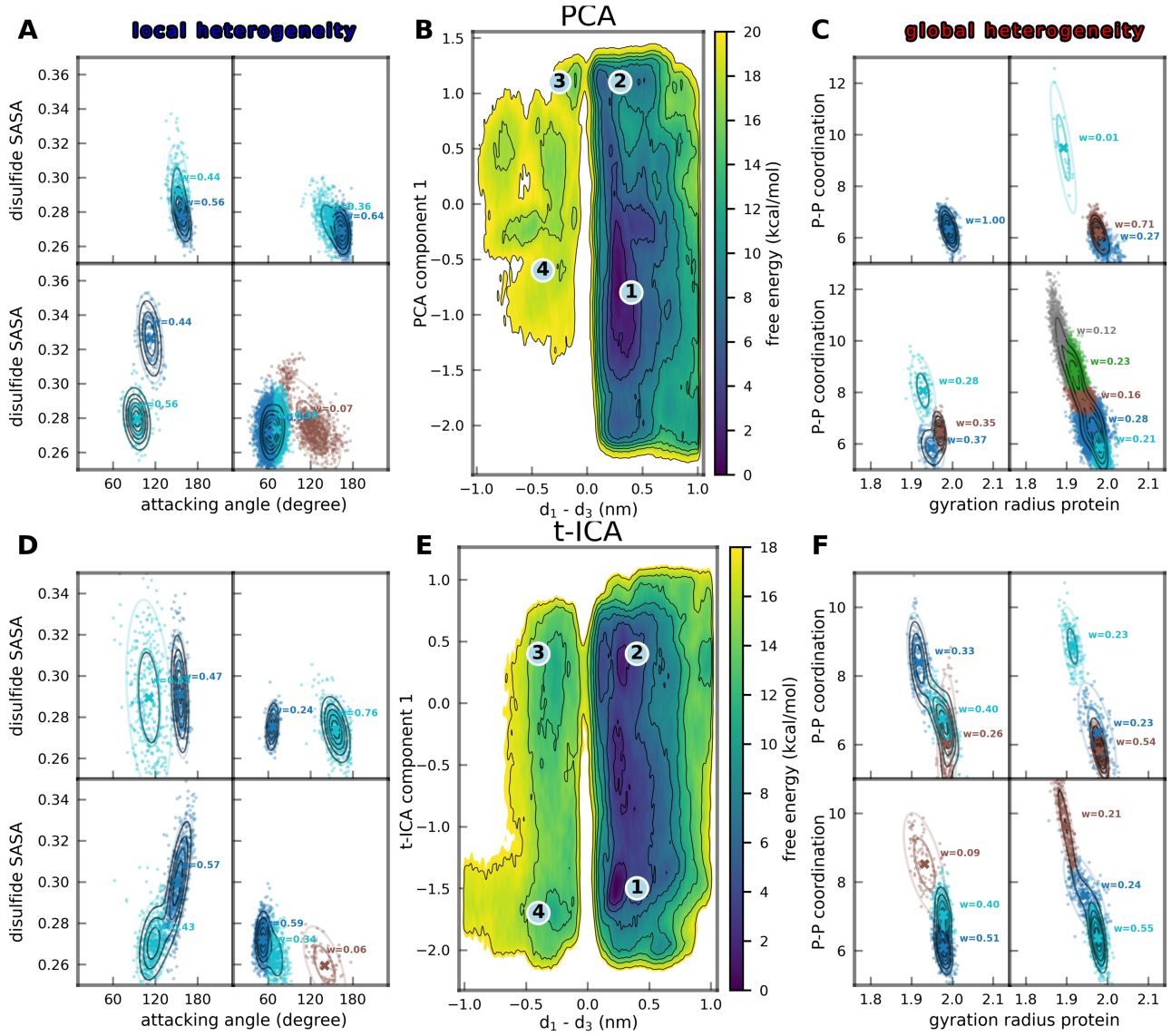

Figure 8.11.: Local and global structural heterogeneity along the 2D QM/MM MTD simulations performed using PC1 (top row) and IC1 (bottom row) as collective variables. (A,D) Local features capture structural variability around the disulfide bridge based on the disulfide SASA and the nucleophilic attack angle between the nucleophilic and electrophilic sulfur atoms. (B,E) Free energy surfaces (FESs) obtained from the 2D projections using PC1 and IC1, respectively, showing four main regions (1–4) corresponding local minima along the reaction coordinate. Contours are drawn in 2.5 kcal mol^{-1} increments. (C,F) Global descriptors represent large-scale conformational changes based on the protein radius of gyration and the interdomain coordination number, reporting on molecular compactness and interfacial packing. Clustering was performed using a Gaussian Mixture Model (GMM) to identify distinct structural ensembles associated with local and global heterogeneity along the reaction pathway. The grid sectors in the left and right panels correspond to the four regions indicated in the central panels, illustrating the characteristic structural features within each basin. The GMM weights (w) are indicated for each cluster, and the ellipsoids represent one standard deviation of the corresponding Gaussian components.

Having identified the landmarks, the structural analysis was further refined by clustering local and global descriptors. Clustering is widely used to identify reaction intermediates, trace transition pathways, and distinguish kinetically distinct conformational ensembles.[231,370,371] The clustering was performed using a Gaussian Mixture Model (GMM), which models the observed density as a superposition of Gaussian distributions and thus helps to delineate underlying processes and their relative contributions. The local descriptors capture structural changes occurring at the disulfide bridge and in its immediate vicinity. This analysis was based on the solvent-accessible surface area (SASA) of the disulfide and on the nucleophilic attack angle between the nucleophilic and electrophilic sulfur atoms. Alterations in the local environment or in the disulfide conformation modulate its solvent exposure, which is quantified by the SASA.[372] The attack angle provides a complementary measure, as the transition state (TS) of the TDE reaction follows a prototypical S_N2 mechanism, for which a near-linear geometry is optimal.[50,64–66] Given the coexistence of multiple structural ensembles that preorganize the system to varying degrees toward the TS, the attack angle serves as a sensitive descriptor of this preorganization.[372] Panel A and D of Figure 8.11 show the local clustering results for the 2D QM/MM MTD simulations using PC1 and IC1, respectively. The global clustering was based on the radius of gyration (R_g) and the coordination number of interfacial interactions (P_c). R_g reflects global changes in molecular compactness and overall shape, whereas P_c quantifies interfacial contacts that report on the packing and interaction strength between the two protein domains. Panel C and F show the clustering results obtained from the global descriptors.

Focusing first on the local clustering, both setups reveal that the structures associated with landmark 1 can be distinguished by their attack angle. The structures are dominated an ensemble that exhibits smaller attack angles, indicating a preorganization that disfavors formation of an optimal transition-state geometry and explaining the absence of reactive configurations in this region of the FES. Conversely, landmark 2 is dominated by structures that support a nearly linear sulfur geometry, consistent with a lower transition-state barrier. In the PC1 setup, all structures display attack angles between 120° and 180°, whereas in the IC1 setup a subpopulation of approximately 24% adopts smaller angles near 60°. The ensemble corresponding to landmark 3 closely resembles that of landmark 2 but exhibits higher solvent accessibility of the disulfide. In contrast, for landmark 4, the disulfide SASA becomes the distinguishing feature, revealing that these structures expand in a way that increases solvent exposure. However, despite the enhanced accessibility, reactivity does not increase, as the entering solvent molecules displace the attacking sulfur from its coordination shell.

Turning to the global clustering, the IC1 setup reveals three clusters for each landmark, all located within similar ranges of the global descriptors. This heterogeneity reflects the sampling of distinct protein conformations and torsional states, as discussed in Section 8.3.2, which can influence the system's reactivity. In contrast, the PC1 setup exhibits pronounced heterogeneity in landmark 1, where five distinct clusters are observed. These clusters correspond to multiple global conformations and binding poses that restrict the accessible torsional configuration space. Upon progressing from landmark 1 to landmark 2, the ensemble converges into two closely spaced clusters, indicating

a reduction in global heterogeneity as the system approaches the near-transition-state ensemble. This suggests that landmark 1 functions as a conformational reservoir from which only a subset of structures, those preorganized for reactivity, proceed toward the transition region. The accompanying decrease in the number of clusters from landmark 1 to 2 thus reflects a conformational filtering process that selects reactive configurations. Consistent with this interpretation, the PC1 setup exhibits greater heterogeneity in landmark 1, which coincides with the identification of lower-energy conformations in this landmark region compared to IC1. Landmarks 2 and 3, representing the reactive ensemble, display comparable local and global heterogeneity within each setup. However, the IC1 simulations retain a higher degree of structural diversity, as seen in Panels D and F, compared to PC1 in Panels A and C. This observation suggests that local and global motions are not decoupled and highlights the importance of their coupling to achieve thorough sampling. Overall, these findings demonstrate that global protein–protein interactions strongly influence the binding pose and, consequently, the local reactivity at the disulfide bridge. While the 2D sampling enhances exploration of the disulfide torsional space, differences in binding geometry impose constraints on the extent to which this torsional space can be effectively sampled.

8.4. Conclusion

In a novel approach, this study investigated the coupling between chemical reactivity and conformational change in protein systems by enhanced conformational sampling in QM/MM simulations through the use of machine-learned CVs. By applying principal component analysis (PCA) and time lagged independent component analysis (tICA) for dimensionality reduction to generate CVs from classical MD data, it establishes a framework that not only improves configurational sampling in QM/MM but also facilitates its analysis. The resulting 2D MTD simulations revealed a complex but interpretable interplay between local and global structural heterogeneity, in which reactive and conformational transitions are dynamically linked. The development was tested for thiol–disulfide exchange (TDE) in a protein system coupled to dynamics of a central disulfide bridge. However, its simple and broadly applicable design ensures general transferability to other proteins.

The collective variables PC1 and IC1, learned from PCA and tICA, respectively, were identified as suitable low-dimensional representations that effectively reduce the original 10D torsional feature space of a disulfide bridge to a single dimension. Both components capture the dominant conformational events observed in the classical MD trajectory, indicating a partial overlap in the configurational subspaces spanned by these modes. When extending 1D QM/MM MTD simulations of the thiol–disulfide exchange (TDE) to 2D setups by adding PC1 or IC1 as second CV, the sampling of the conformational space was markedly improved. However, the conformational space during the QM/MM simulations does not fully overlap with that represented in the original MD training data. The learned CVs exhibit a higher degree of degeneracy, leading to the exploration of structures that are indistinguishable by the new CVs but differ substantially in

the genuine 10D space. This effect becomes particularly relevant when global protein geometry varies, as protein–protein interactions constrain the accessible disulfide torsional space and limit the extent to which it can be effectively sampled. Consequently, an inherent asymmetry arises between the analytical and exploratory properties of PC1 and IC1: during analysis, the structural context is fixed by the reference data, whereas during exploration, this context can shift dynamically, altering the relation between the CVs and the underlying conformational landscape. The findings further emphasize that local and global motions are not fully decoupled. More efficient sampling of the conformational space of the disulfide torsion angles also alters global dynamics, leading to a slow shift in binding poses and interface repacking. Conversely, protein–protein interactions modulate both the accessibility and the reactivity of the disulfide center. Differences in binding geometry impose constraints on the extent to which the torsional space can be effectively sampled, explaining the non-overlapping configurations observed between the 10D torsional space of the MD data and the QM/MM simulations.

Reaction modeling based on structural clustering suggests that ensembles are more reactive if they exhibit local compression of the disulfide bond, resulting in a more compact active site, and in preorganized geometries that support a near-linear S_N2 transition state. The observed reduction in cluster diversity indicates a conformational filtering process in which only preorganized states proceed toward the transition region. The IC1 setup explores a larger fraction of reactive configurations, whereas PC1 achieves broader sampling of protein conformations and binding poses, leading to the identification of lower-energy states. Moreover, PC1 demonstrates the ability to transition from a heterogeneous, non-reactive ensemble to a more homogeneous, reactive ensemble, reflecting higher specificity. From this perspective, PC1 represents a more suitable choice for conformational sampling in this setup.

MTD inherently introduces flexibility and heterogeneity into the system, allowing less interdependent ensembles to emerge as individual walkers explore distinct regions of the FES. This behavior, while expected, highlights an opportunity to exploit the coupling between local reactivity and global conformational dynamics as a design element for controlling sampling behavior. For instance, uncontrolled fluctuations between binding poses interfere with both convergence and reproducibility of the simulation. The observed degeneracy of the machine-learned CVs can be constrained by the protein binding interface, which provides a structural anchor. Variations in binding poses may introduce ambiguities and emphasize the need for explicit control over the global context during enhanced sampling. Future work could aim to investigate the extent to which the coupling between local reactivity and global conformational dynamics can be exploited as a controllable design feature in enhanced sampling. By constructing tailored simulation setups and CVs specifically designed to represent the coupling between local reactivity and global conformational change, it may be possible to stabilize binding orientations and reduce ambiguities arising from multiple binding poses. Moreover, refining the machine-learned CVs to incorporate global structural information or to adapt dynamically to the conformational context could help mitigate degeneracy and improve sampling consistency. Such developments would enhance the

reproducibility and interpretability of QM/MM simulations and would ultimately enable more precise exploration of complex reactive landscapes.

Part IV.

Summary and Outlook

9. Summary and Outlook

The challenge of computational studies of proteins stems from a complex hierarchy spanning spatial and temporal scales, as introduced in Chapter 1. It is complex in a recursive sense, as localized chemical reactions can initiate global conformational changes, which in turn feed back to modulate the reactivity of that reactive site. A case in point is thiol–disulfide exchange (TDE). Here, the reaction between sulfur atoms in cysteine residues can break a disulfide bridge and prime the conformational ensemble to undergo a larger-scale conformational rearrangement, which subsequently modulates localized reactivity by relieving or imposing strain or by altering the electrostatic environment. Such coupling between local chemical reactivity and global conformational dynamics calls for methods that combine chemical accuracy with sampling efficiency to access timescales relevant to protein function. Hybrid quantum mechanics/molecular mechanics (QM/MM) methods tackle this issue in a conceptually elegant way to balance chemical accuracy and computational efficiency. They mirror the system's inherent hierarchy by treating the reactive site quantum chemically (QM) while representing the surrounding protein environment classically (MM). The choice of QM method is central to this balance, as it must provide sufficient accuracy at the reactive site without imposing a computational cost that would hinder the overall sampling required to describe biologically relevant motions. Equally important is the embedding of the QM region within the MM environment, since inaccuracies at the interface can introduce significant artifacts that compromise the reliability of the entire calculation. Even when these aspects are carefully controlled, conformational sampling can remain a bottleneck, which necessitates additional strategies.

The work presented in this thesis addressed the computational study of protein systems by integrating QM/MM simulation, enhanced sampling, and machine learning within a multiscale framework. It investigated three central questions. (1) Does the electrostatic embedding of the QM region within the MM environment introduce significant errors by truncating nonbonded interactions? If so, how severe are these errors, and can they be mitigated? (2) For elucidating the TDE mechanism catalyzed by *Homo sapiens* glutaredoxin (Grx), can QM/MM simulations augmented with a artificial neural network (ANN) based Δ-ML correction enhance the accuracy of the QM region? What specific improvements does this correction provide for the QM region, and how do these advances enable a more reliable mechanistic characterization in a system of realistic biological complexity? (3) Can simple machine-learned collective variables (CVs) derived from classical trajectories be transferred into QM/MM enhanced-sampling simulations to improve conformational sampling?

Summary. (1) Chapter 6, Non-covalent Interactions at the QM-MM Interface in the Semi-Empirical and Density-Functional Limit, investigated how the QM–MM interface limits the accuracy of QM/MM simulations, with a particular focus on hydrogen bonding in neutral and ionic dimers. The QM region was treated using two representative methods: the density functional theory (DFT) functional ωB97X-V and the semiempirical density functional tight binding (DFTB) model, while the General Amber Force Field (GAFF) was used for the MM region. Prior to this analysis, the magnitude and origin of interface-induced errors had only been quantitatively characterized, leaving open how strongly interaction energies are perturbed when key polarization or charge transfer (CT) interactions cross the QM–MM boundary. This limitation is consequential because even localized energetic errors can propagate across larger spatial and temporal scales in multiscale simulations. The results demonstrated that, even when reliable density functionals are used in the QM region, substantial errors arise from mismatches in polarity, polarizability, and CT description across the interface, with particularly pronounced inaccuracies for ionic hydrogen bonds. The study further showed that unoptimized Lennard–Jones parameters and missing short-range polarization introduce additional errors that cannot be resolved by simple measures such as scaling the QM–MM interactions. Strikingly, these deficiencies persist despite the widespread use of QM/MM approaches. By analysing these effects systematically, the chapter established practical guidelines for QM region construction, showing that key donors, acceptors, and CT partners must lie fully within the QM region. These findings provide a concrete step toward improving the reliability of QM/MM simulations in protein settings.

(2) Chapter 7, Reduction Pathway of Glutaredoxin 1 Investigated with QM/MM Molecular Dynamics Using a Neural Network correction, demonstrated the effectiveness of applying a recently introduced DFTB-based Δ-ML correction, an ANN correction, to enzymatic sulfur chemistry. This model addresses the qualitative deficiencies of the standard DFTB description of the TDE reaction, which arise from its limited treatment of electronic correlation and omission of many-body interactions. As a result, uncorrected DFTB overestimates S–S bond distances and yields inadequate transition states, leading to errors of up to 5 kcal mol^{-1}, an unacceptable magnitude for investigating enzymatic mechanisms. Grx, the enzyme studied here, catalyzes TDE and plays a central role in maintaining cellular redox homeostasis. When applied to the Grx system, QM/MM metadynamics (MTD) at the DFTB/Δ-ML level reproduced the experimentally inferred regioselectivity of the three successive TDE steps and yielded more reliable barrier heights by recovering the missing correlation and many-body effects. Remarkably, these improvements in the accuracy of the QM region come with only minimal computational overhead without a substantial loss of sampling efficiency. Consequently, analyses based on ensemble averages, such as the regioselectivity assessed in this study, become both feasible and reliable. These results confirmed the plausibility of the proposed reaction pathway and highlight both the effectiveness of the method and the broader appeal of machine-learned corrections for accurate, computationally efficient multiscale simulations of enzymatic reactivity.

(3) Chapter 8, Transferring Collective Variables from Molecular Dynamics Simulations to QM/MM Simulations for Reactivity Exploration in Dynamic Systems, introduced a novel scheme in which

collective variables (CVs) learned from long classical molecular dynamics (MD) simulations accelerate conformational sampling in QM/MM MTD simulations of TDE. Linear dimensionality-reduction methods were used to identify key torsional modes of a disulfide bridge, yielding transferable low-dimensional descriptors of protein dynamics. Incorporated as additional coordinates in two-dimensional QM/MM MTD, these machine-learned CVs improved sampling and revealed coupling between local disulfide rearrangements and global protein geometry. The principal component analysis (PCA)-derived CV provided more efficient sampling than the time lagged independent component analysis (tICA)-based descriptor, especially in the binding regime. The new CV also facilitates analysis. Only a subset of conformations preorganized the active site for a near-linear S_N2 attack, indicating a conformational filtering mechanism that governs reactivity. The results also highlight that learned CVs perform more reliably in analysis than in biasing. When used to bias phase-space exploration, the CVs can exhibit significant degeneracy, which can be constrained by uncontrolled motions such as protein binding. Using enhanced sampling in QM/MM to improve conformational sampling of the environment represents a previously less emphasized direction.[127] QM/MM developments have typically focused on accuracy rather than dynamics. The introduced strategy establishes the CV as a central design element. Machine learning enables CV construction from the system's own dynamics rather than from dynamics-agnostic assumptions. This provides a direct route to capture environment/reactivity coupling within enhanced sampling in QM/MM simulations, an essential feature that a multiscale model should include.

Limitations. At the same time, each line of investigation revealed limitations. (1) For the hydrogen-bonding benchmark, the analysis was restricted to gas-phase dimers and a small number of cluster-type microenvironments, all described with fixed-charge models and a limited set of QM methods. This design restricted the systematic evaluation of cooperative effects and explicit MM polarization. As a result, the findings on QM region partitioning are most reliable for neutral or weakly polar hydrogen bond (H-bond) motifs. They are less likely to transfer quantitatively to solvated or highly charged systems where many-body polarization and CT play a more prominent role. The sharp increase in QM/MM errors for ionic complexes, together with the strong correlation between error magnitude and CT, underscores this limitation and points to the need for embedding schemes that capture polarization and charge redistribution.

(2) In the Grx application, the simulated reaction path omits upstream and downstream proton–transfer steps of the cysteine residues. This omission alters the underlying free energy landscape and likely contributes to the endergonic reaction profiles observed. Uncertainties in the binding poses present an additional limitation because their reliable optimization requires specialized strategies that were not applied here. As a result, the MTD bias accelerates exploration along the chosen CVs but may not allow the global structure sufficient time to relax into a more favorable binding pose. Further limitations arise from the treatment of electrostatics. The charged nature of the QM region and the high polarizability of sulfur imply that the thermodynamics of disulfide exchange are highly sensitive to the local electrostatic environment. Fixed protonation states near

the active site can therefore introduce systematic bias because protonation–deprotonation equilibria influence both charge distribution and local polarization. Finally, the current Δ-ML correction adjusts only the intrinsic QM energetics relative to the target method. It does not capture changes in the polarization of the QM region induced by the MM environment. This constraint may be significant for accurately describing TDE in heterogeneous protein environments.

(3) The machine-learned CVs were derived from 10-dimensional input data. Because these CVs are constructed as linear combinations of the underlying torsional coordinates, they retain an inherent degree of degeneracy. The structural configurations present in the training data generated by MD simulation can impose local and global constraints that can partially lift the degeneracy by limiting accessible conformations and shaping the exploration of phase space. For example, a specific binding pose may immobilize a torsion that would otherwise remain flexible. When the same CVs are transferred to a QM/MM simulation, the structural context can change and thereby alter the relationship between the CV values and the set of actual molecular configurations indistinguishable by the CV. As a result, identical CV values may correspond to distinct global structures such as different binding poses, and slow drift in global protein structure can further distort the mapping between the reduced representation and the underlying conformational landscape. The corresponding free-energy surface (FES) should therefore be interpreted as qualitative rather than quantitatively converged. A detailed analysis of CV degeneracy lies beyond the scope of this work, but it remains a central consideration in CV design. Incorporating more global descriptors represents a reasonable direction for reducing ambiguity in future applications.

Future Prospects. These limitations point toward several avenues for future development. (1) For noncovalent interactions at QM–MM interfaces, expanding the set of systems to include larger clusters, explicit solvent, and polarizable force fields would better capture condensed-phase many-body responses and help separate interface artifacts from errors intrinsic to the underlying methods. Rather than relying solely on geometric heuristics, QM region selection algorithms could be employed to make a pertinent choice of QM region that reduces interface effects. The data set created can facilitate the development. Recent extensions of DFTB based on chemical-potential equalization and multipolar expansions offer promising ways to improve charge redistribution and polarization. Evaluating these models using the data generated here is a natural next step for understanding how the QM–MM interface affects embedding. Assessing their robustness across different interface types will be important for advancing model accuracy and transferability. Focusing on free energies rather than binding energies as the central metric incorporates entropic effects and may provide a more relevant objective function for optimization. Such efforts would require free energy perturbation or reweighting schemes to probe the effects of the QM–MM interface. Developing such approaches represents a compelling direction for future work.

(2) The application of the Δ-ML model to TDE in the Grx demonstrates its usefulness for resolving the energetics of disulfide exchange, motivating its application to other biologically and pharmaceutically relevant systems. Antibodies, for instance, contain multiple disulfide bridges that are essential for structural stability and function, making them high-value targets where

accurate modeling of redox chemistry would be particularly important. Looking ahead, incorporating environmental electrostatics into the Δ-ML framework represents a natural progression. This could be achieved by expanding the correction to account not only for intrinsic QM energetics but also for the influence of the protein's electrostatic landscape on the QM region. An additional advance would be the integration of QM/MM simulations with constant-pH simulations, enabling exploration of different protonation states in the MM environment and computation of free energy surfaces that more closely reflect physiological conditions. To clarify the origin of the endergonic reaction profiles, several steps can be taken. The proton-transfer steps of the cysteine residues could be modeled using QM/MM MTD with an additional proton-transfer CV, which would provide a more complete representation of the reaction mechanism. However, the optimization of the binding pose is likely the more significant omission. The present results indicate that resolving this issue should be a higher priority, even though it has not yet been addressed systematically in the field of QM/MM simulations. Structures generated by AlphaFold or docking protocols offer reasonable starting points, and the introduction of additional CVs to guide binding-pose relaxation appears appealing.

(3) As this contribution highlights the value of enhanced sampling within QM/MM for improving conformational sampling of the environment, it also underscores the need to adapt and evaluate these strategies across different systems and applications. Future developments may incorporate nonlinear dimensionality-reduction techniques, global structural descriptors during training, or iterative refinement of CVs within the QM/MM environment. Constructing composite CVs that explicitly capture the coupling between local reactivity and global conformational dynamics could reduce degeneracy, stabilize sampling, and enhance the convergence and interpretability of enhanced-sampling simulations.

Conclusion. More broadly, this thesis offers an encouraging outlook for advancing the calculability of protein systems across multiple scales. It demonstrates that progress requires not only improved electronic-structure accuracy but also a deeper understanding of how errors propagate across QM–MM interfaces, how approximate potentials can be corrected and reused, and how machine learning can enhance sampling without compromising interpretability. The results extend well beyond the specific systems investigated. The QM-region selection principles derived from hydrogen-bonding analysis are suitable to inform QM/MM partitioning in both enzymatic and materials contexts. The use of a Δ-ML-enhanced semiempirical model in a realistic enzyme system demonstrates that targeted corrections toward higher QM reference methods can yield chemically meaningful free energy profiles at a fraction of the computational cost. The transfer of machine-learned CVs from classical to QM/MM simulations is practical for integrating long-timescale classical dynamics with accurate reactive modeling. Future efforts that consolidate these advances by combining improved interface descriptions, ML-corrected QM methods, and data-driven enhanced sampling into a unified workflow hold substantial promise for narrowing the gap between biological complexity and computational tractability.

Part V.

Appendix

A. Non-covalent Interactions at the QM-MM Interface in the Semi-Empirical and Density-Functional Limit

Analysis

$$\mathrm{RMSE}(X) = \sqrt{\frac{1}{N}\sum_{i=1}^{N}\left(\Delta E_{\mathrm{int}}^{(i)}(X) - \Delta E_{\mathrm{int}}^{(i)}(\mathrm{ref})\right)^2} \tag{A.1}$$

$$\mathrm{MSE}(X) = \frac{1}{N}\sum_{i=1}^{N}\left(\Delta E_{\mathrm{int}}^{(i)}(X) - \Delta E_{\mathrm{int}}^{(i)}(\mathrm{ref})\right) \tag{A.2}$$

$$\mathrm{RMSE}/\mu = \frac{\mathrm{RMSE}(X)}{\frac{1}{N}\sum_{i=1}^{N}\Delta E_{\mathrm{int}}^{(i)}(\mathrm{ref})} \tag{A.3}$$

$$\mathrm{MSE}/\mu = \frac{\mathrm{MSE}(X)}{\frac{1}{N}\sum_{i=1}^{N}\Delta E_{\mathrm{int}}^{(i)}(\mathrm{ref})} \tag{A.4}$$

DFTB/GAFF Interaction Energies

Neutral Hydrogen Bonds

Table A.1.: Composition of HB375x10 and IHB100x10 datasets; groups by interaction type, their size, and average interaction energy ΔE_{int} (kcal/mol) in each group.

	HB375			IHB100		
No.	Type	Size	ΔE_{int}	Type	Size	ΔE_{int}
1	OH · · · O	60	-8.1	$OH^+ \cdots O$	1	-22.4
2	NH · · · O	65	-5.6	$NH^+ \cdots O$	15	-23.0
3	OH · · · N	45	-9.0	$NH^+ \cdots N$	15	-22.7
4	NH · · · N	53	-5.8	$NH^+ \cdots C$	4	-23.9
5	CH · · · O	20	-4.4	$OH \cdots O^-$	15	-26.2
6	CH · · · N	19	-4.5	$OH \cdots N^-$	3	-25.5
7	noHB	113	-3.3	$OH \cdots C^-$	2	-17.8
8				$NH \cdots O^-$	15	-19.4
9				$NH \cdots N^-$	6	-16.1
10				$NH \cdots C^-$	5	-14.5
11				$CH \cdots O^-$	15	-9.3
12				$CH \cdots N^-$	3	-8.3
13				$CH \cdots C^-$	1	-2.6
all		375	-5.6		100	-19.0

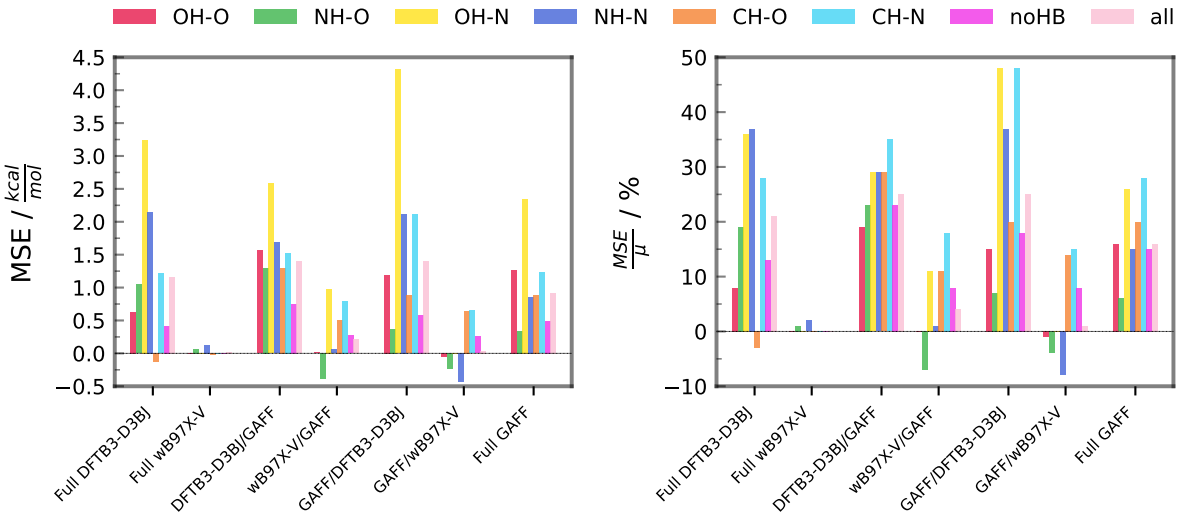

Figure A.1.: MSE errors per bond type for HB375. DFTB/3ob and ωB97X-V/ma-def2-TZVPP as QM for comparison, GAFF as MM, CCSD(T)/CBS as reference.

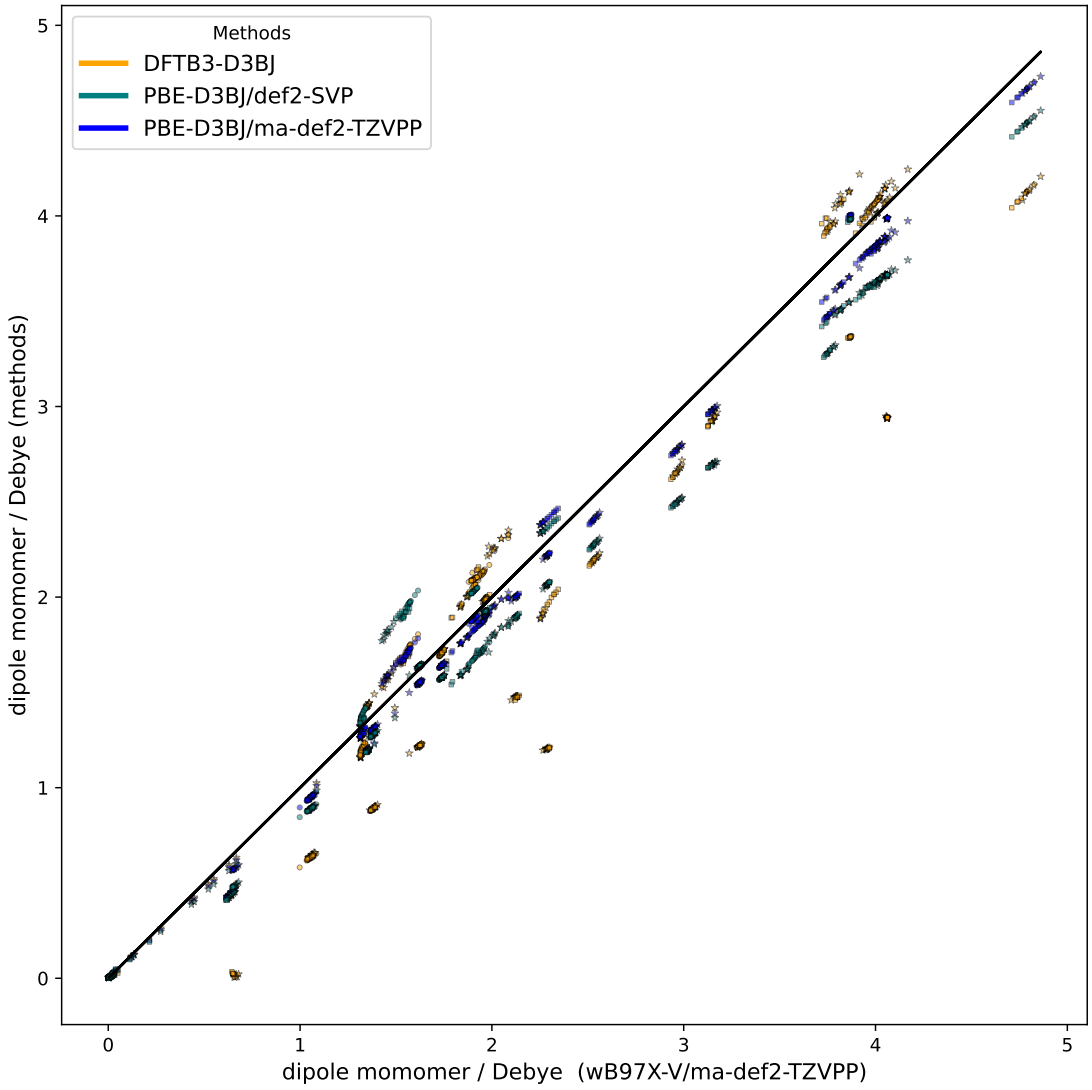

Figure A.2.: Reference calculations for dipole moments of monomers in vacuum for HB375, ωB97X-V/ma-def2-TZVPP as reference method.

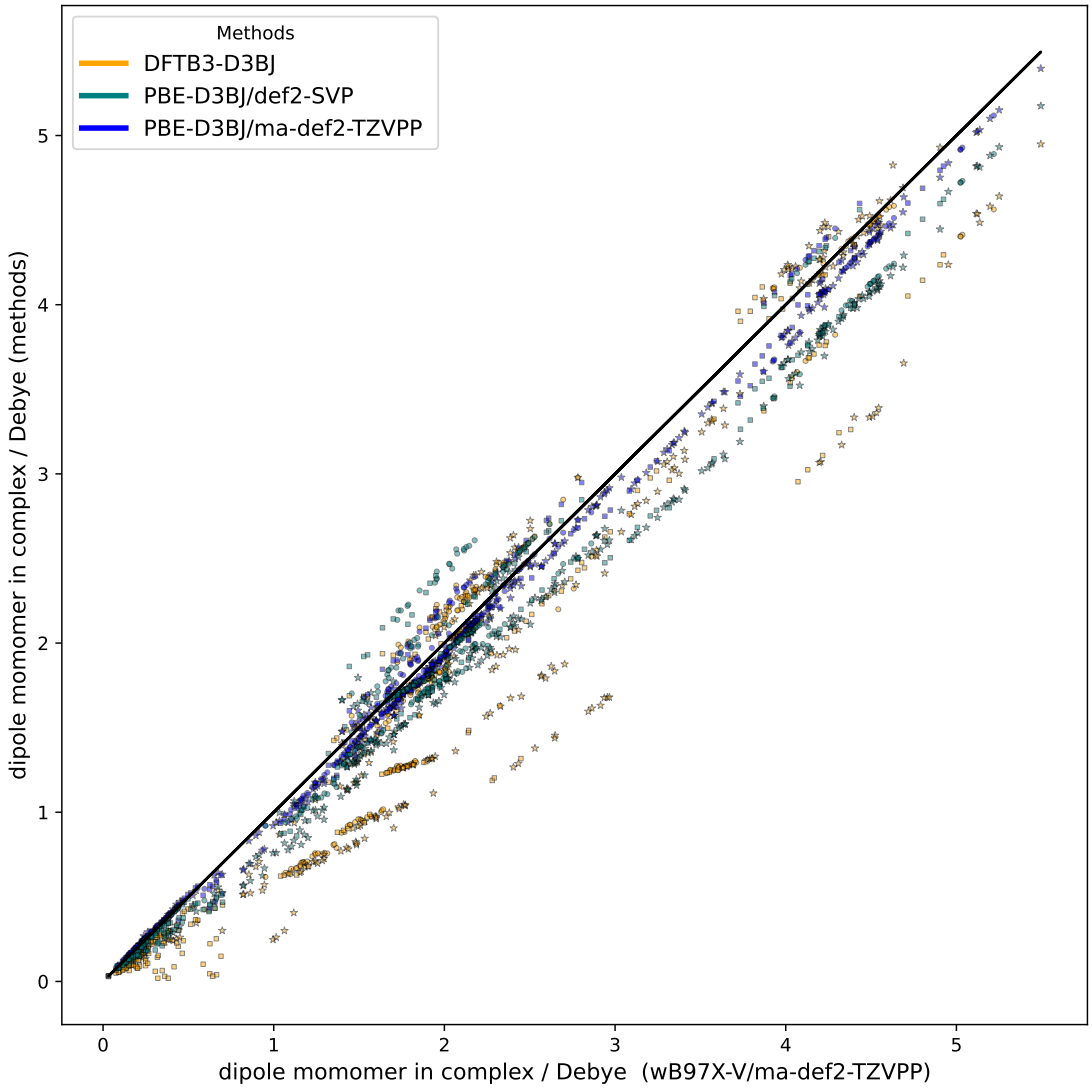

Figure A.3.: Reference calculations for dipole moments of monomers in the complex for HB375, ωB97X-V/ma-def2-TZVPP as reference method.

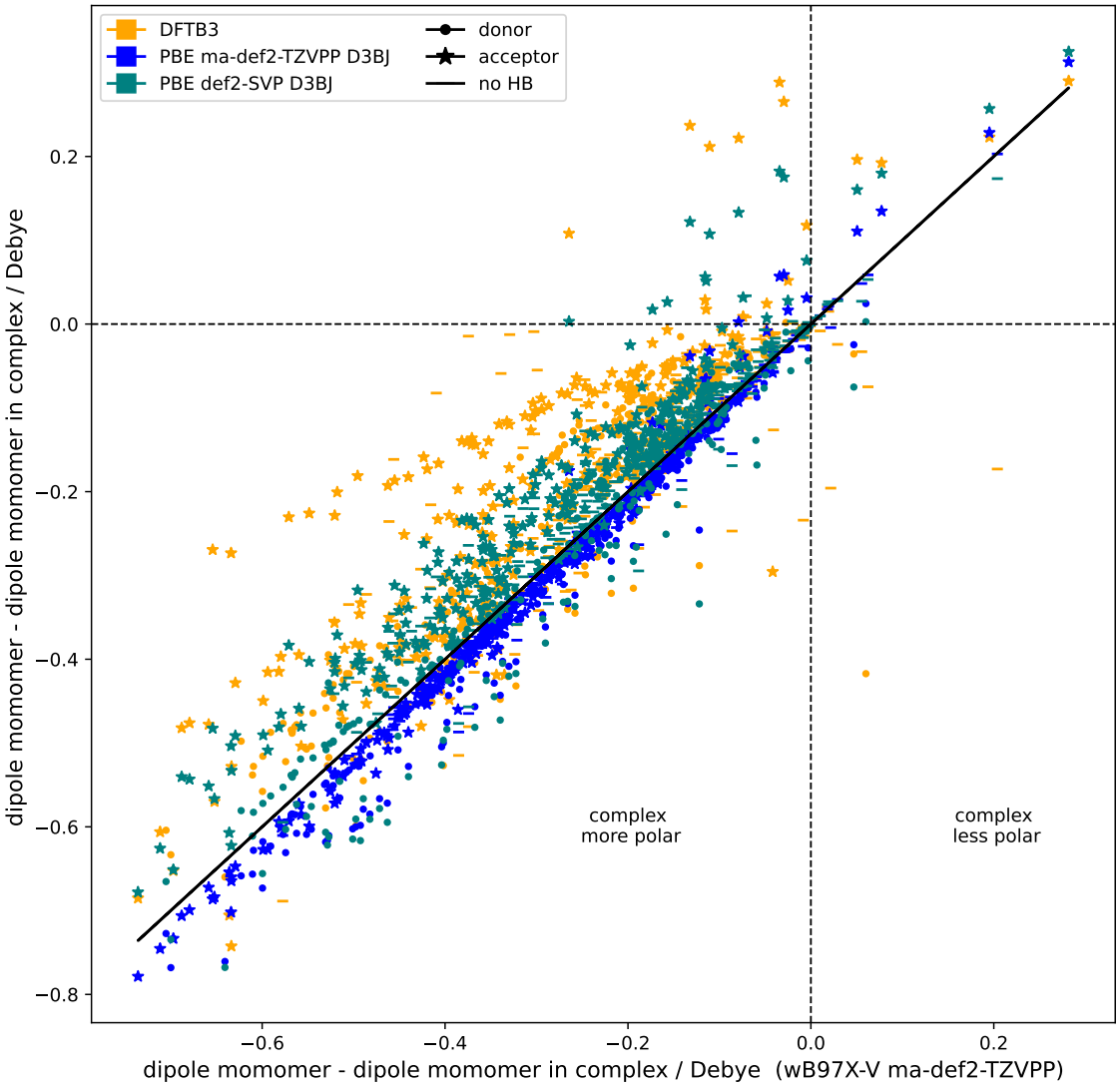

Figure A.4.: Reference calculations for the polarization response of the monomers in the QM/GAFF models in HB375, ωB97X-V/ma-def2-TZVPP as reference method.

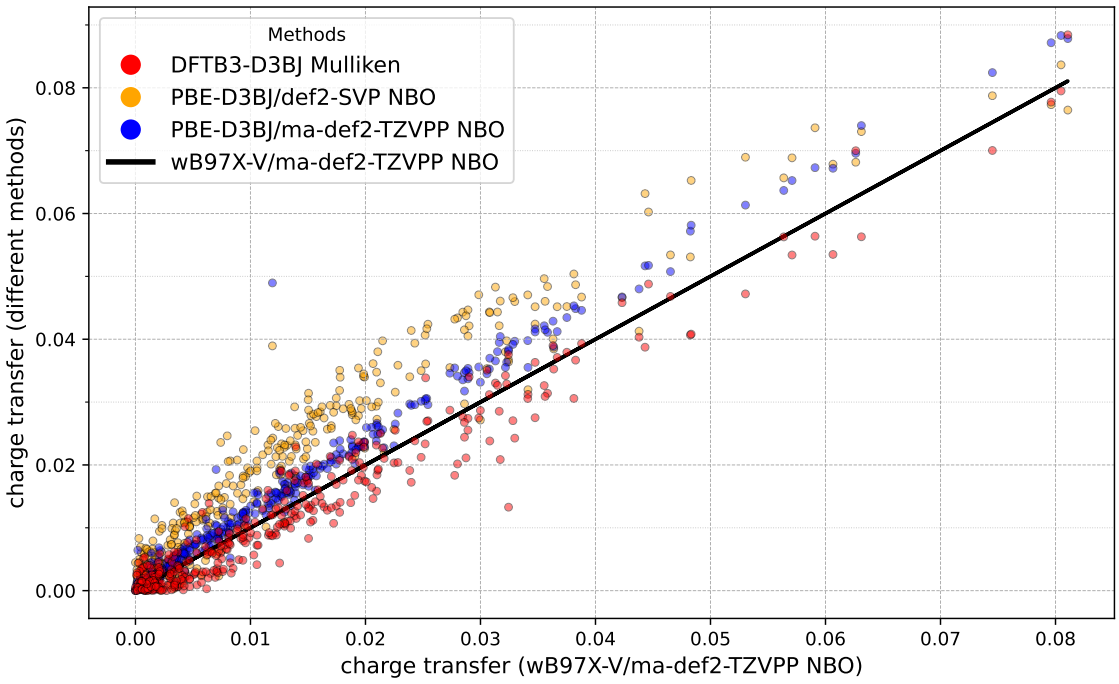

Figure A.5.: Reference calculations for charge transfer in HB375 estimated by DFTB, ωB97X-V/ma-def2-TZVPP NBO as reference method.

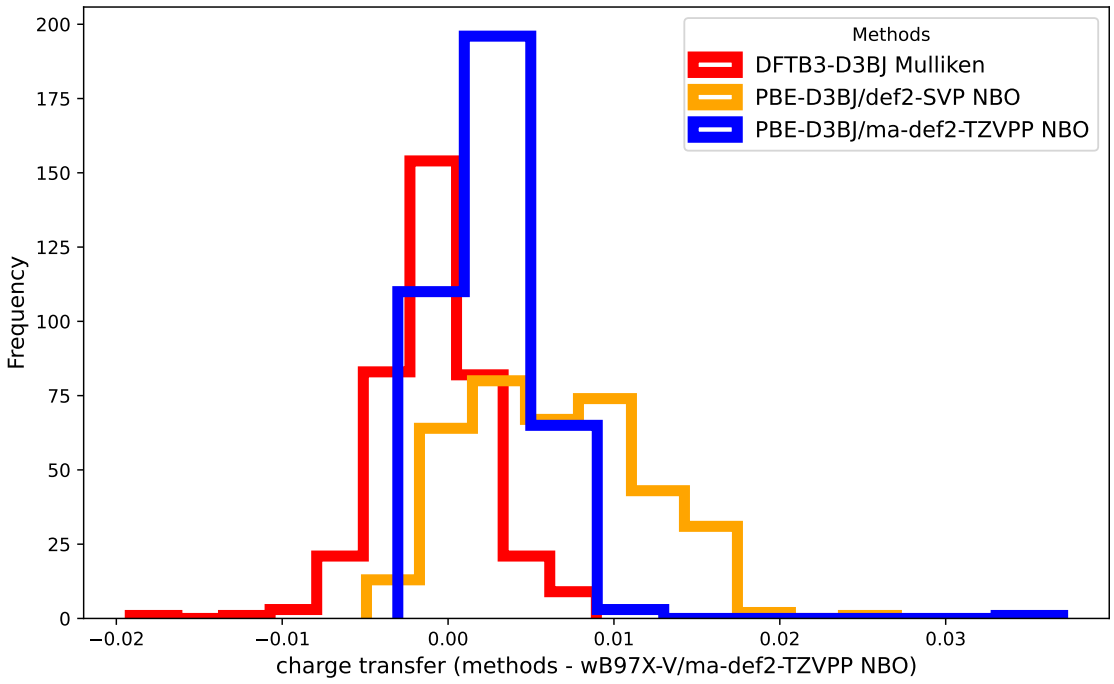

Figure A.6.: Error distribution for charge transfer estimations in HB375, ωB97X-V/ma-def2-TZVPP NBO as reference method.

Ionic Hydrogen Bonds

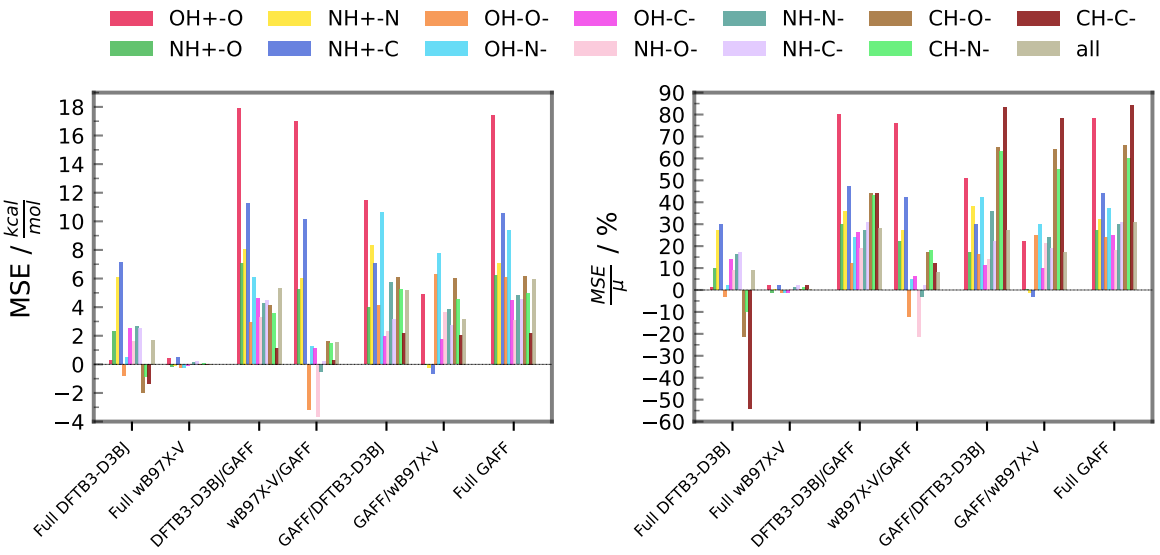

Figure A.7.: MSE errors per bond type for IHB100, DFTB/3ob and ωB97X-V as QM, GAFF as MM, CCSD(T)/CBS as reference.

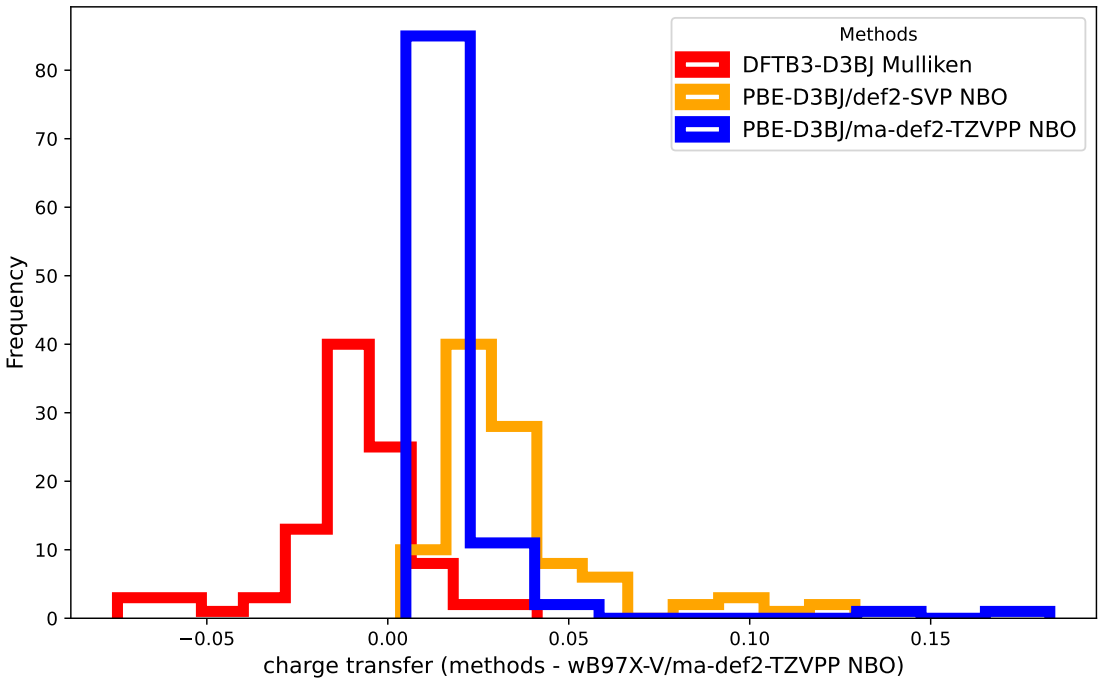

Figure A.8.: Error distribution for charge transfer estimations in IHB100, ωB97X-V/ma-def2-TZVPP NBO as reference method.

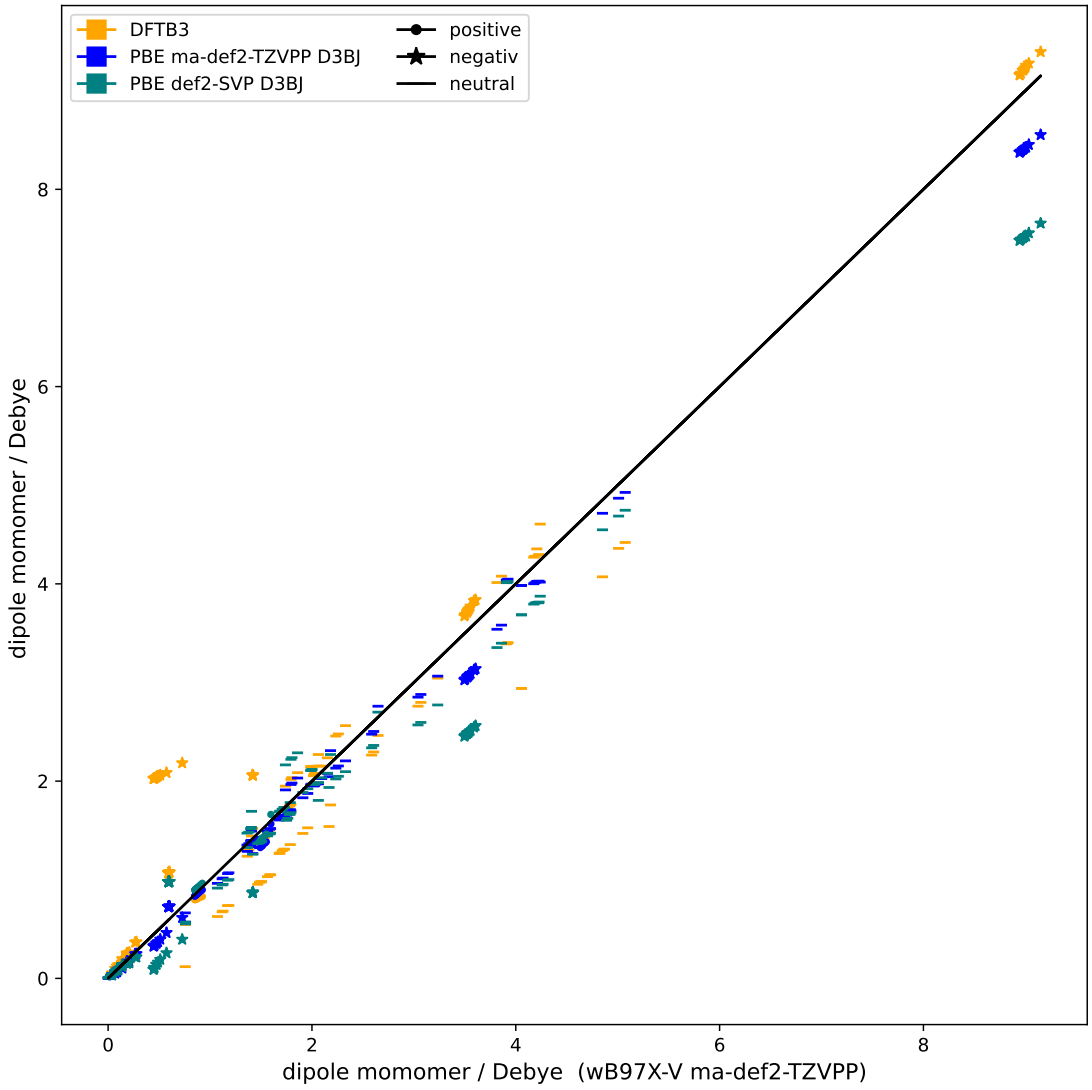

Figure A.9.: Reference calculations for dipole moments of monomers in vacuum for IHB100, ωB97X-V/ma-def2-TZVPP as reference method.

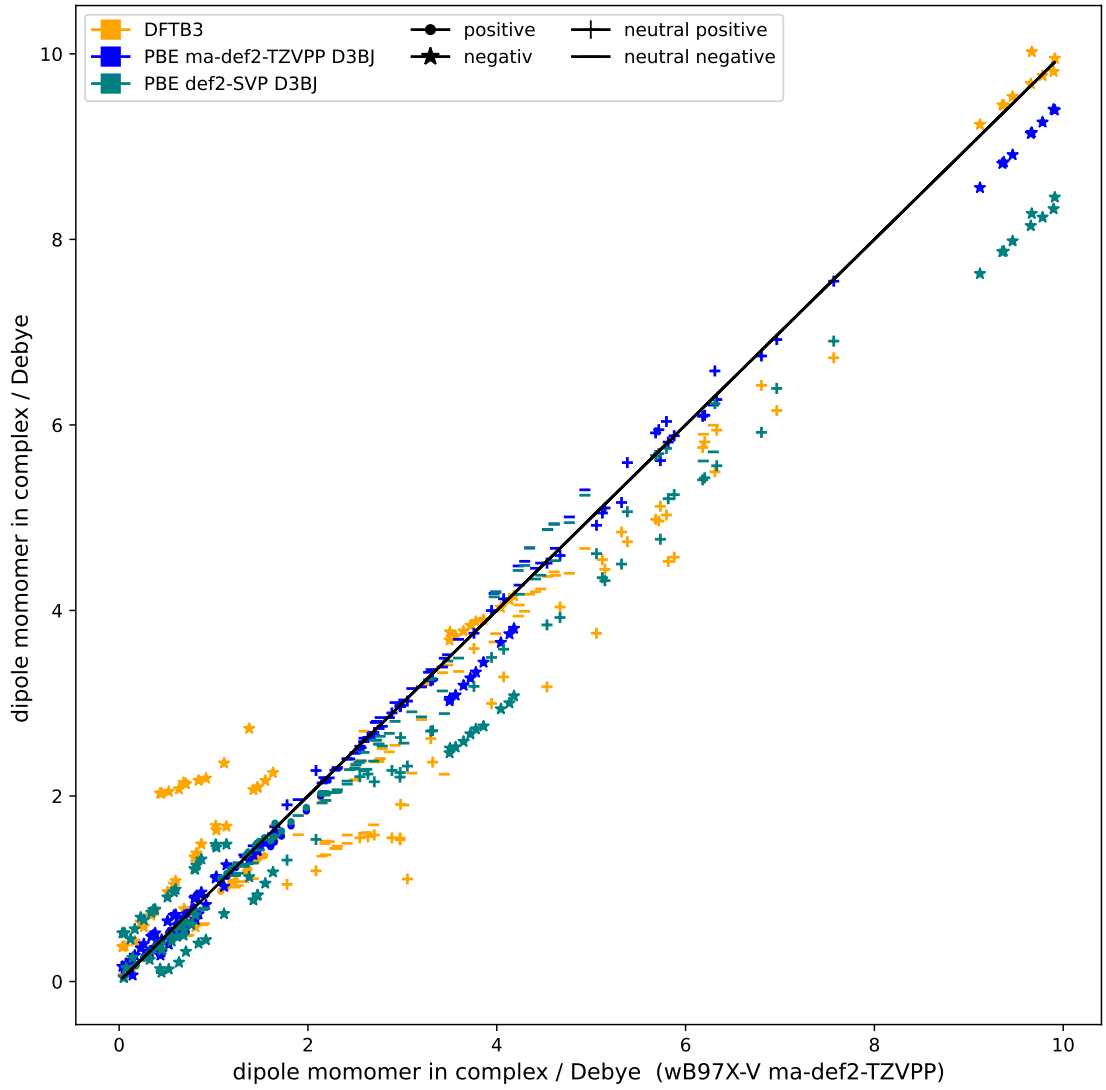

Figure A.10.: Reference calculations for dipole moments of monomers in the complex for IHB100, ωB97X-V/ma-def2-TZVPP as reference method.

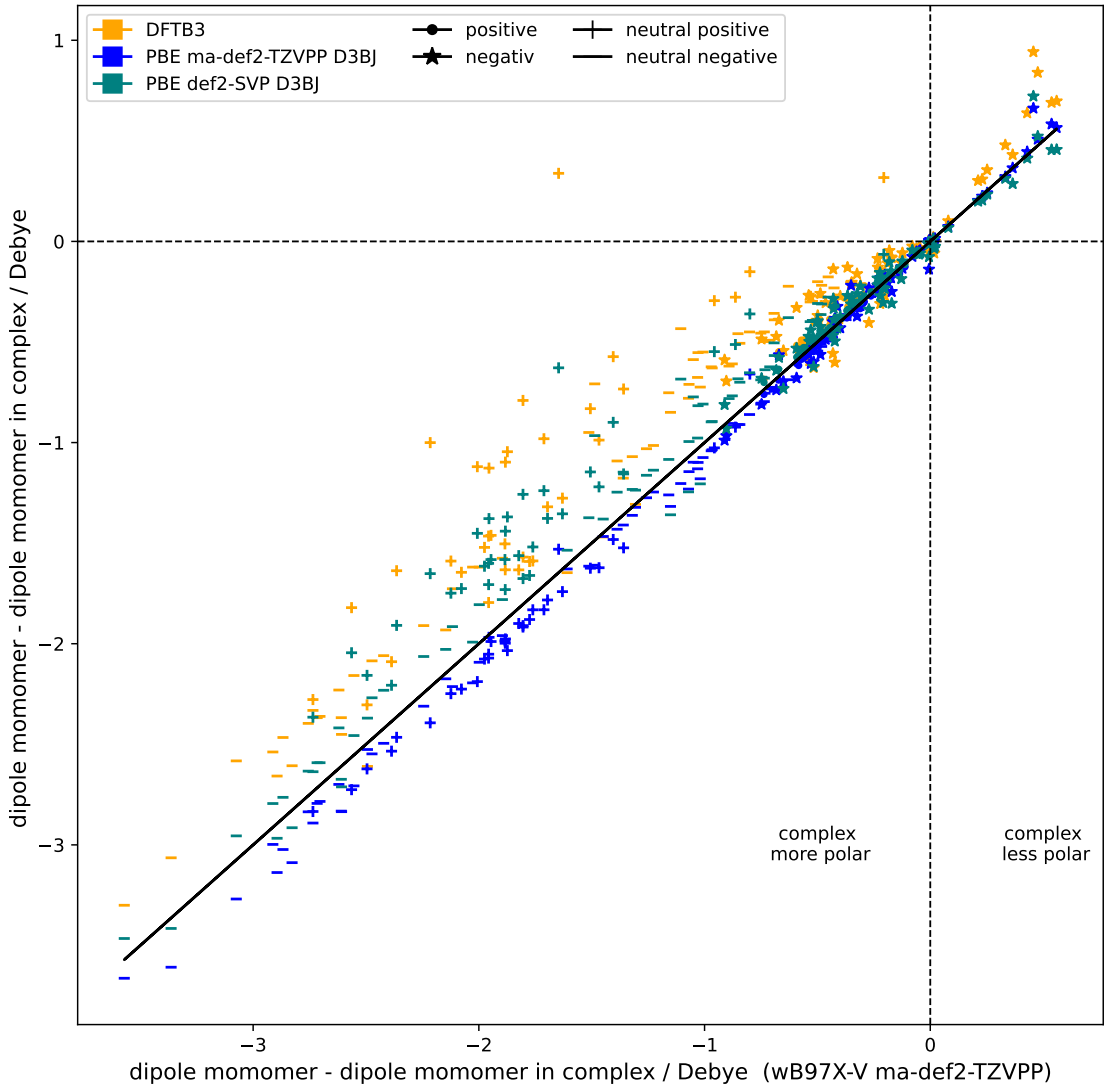

Figure A.11.: Reference calculations for the polarization response of the monomers in the QM/GAFF models in IHB100, ωB97X-V/ma-def2-TZVPP as reference method.

DFTB-CPE applied to HB375x10 and IHB100x10

Table A.2.: RMSE in kcal/mol for HB375 using DFTB/3ob or DFTB-CPE as QM and CCSD(T)/CBS as reference.

	DFTB	DFTB/GAFF	DFTB-CPE/GAFF	GAFF/DFTB	GAFF/DFTB-CPE	GAFF
OH-O	1.00	1.85	1.81	1.76	1.73	1.76
NH-O	1.16	1.43	1.39	0.76	0.76	0.66
OH-N	3.52	3.23	3.21	4.80	4.75	3.12
NH-N	2.33	1.89	1.85	2.35	2.31	1.29
CH-O	0.49	1.37	1.36	0.96	0.92	0.96
CH-N	1.34	1.63	1.62	2.16	2.15	1.30
noHB	0.66	0.93	0.92	0.76	0.74	0.70

Table A.3.: MSE in kcal/mol for IHB100 using DFTB/3ob or DFTB-CPE as QM and CCSD(T)/CBS as reference.

	DFTB	DFTB/GAFF	DFTB-CPE/GAFF	GAFF/DFTB	GAFF/DFTB-CPE	GAFF
OH+-O	0.26	17.89	17.89	11.46	11.54	17.41
NH+-O	2.35	7.11	7.07	3.98	3.68	6.23
NH+-N	6.13	8.04	7.98	8.37	8.14	7.10
NH+-C	7.16	11.26	11.23	7.08	6.79	10.59
OH-O-	-0.80	2.98	2.86	4.13	3.98	6.12
OH-N-	0.52	6.08	5.95	10.62	10.62	9.38
OH-C-	2.55	4.64	4.60	1.99	1.99	4.50
NH-O-	1.62	3.33	3.16	2.35	2.28	3.07
NH-N-	2.65	4.31	4.09	5.74	5.74	4.82
NH-C-	2.54	4.46	4.27	3.18	3.17	4.53
CH-O-	-1.96	4.16	4.10	6.11	6.10	6.20
CH-N-	-0.85	3.60	3.54	5.25	5.24	4.96
CH-C-	-1.39	1.14	1.14	2.15	2.16	2.19

Dissociation Curve for HB375x10 and IHB100x10

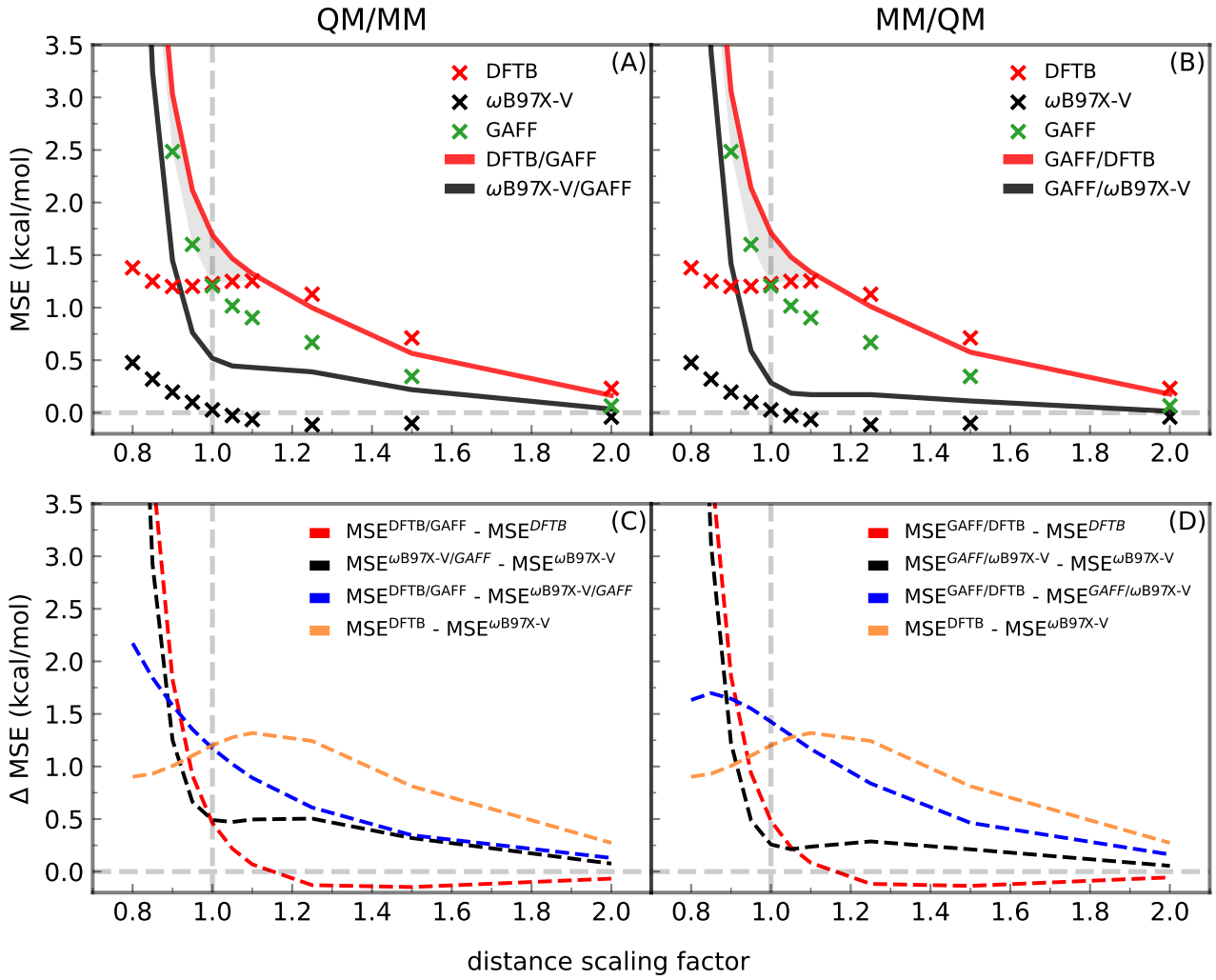

Figure A.12.: MSE values along the entire dissociation curves in HB375x10. Results are shown for both compartmentalization schemes: QM/GAFF (left) and GAFF/QM (right), using CCSD(T)/CBS as the reference. The upper row shows the RMSEs for the respective QM (QM/MM) methods relative to the reference. Gray-shaded regions indicate areas where the DFTB/GAFF (or GAFF/DFTB) hybrid model introduces additional error compared to isolated DFTB and GAFF components. The lower row displays the differences between the curves shown in the upper row.

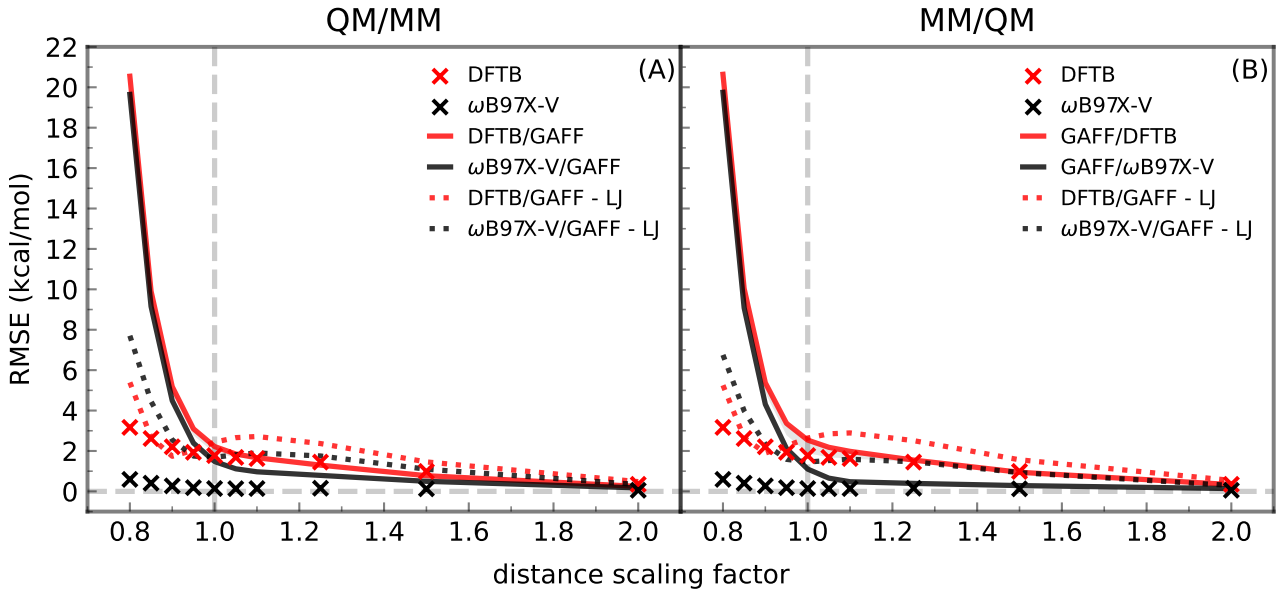

Figure A.13.: RMSE of ΔE_{int} along the full dissociation curves in HB375x10 for both partitioning schemes, QM/GAFF (left) and GAFF/QM (right). Solid lines include the Lennard-Jones contribution, while dotted lines exclude it. At short distances, removing the LJ contribution markedly reduces the RMSE, indicating that the LJ parameters dominate the short-range error. The remaining error after LJ removal suggests additional contributions from the QM–MM interface.

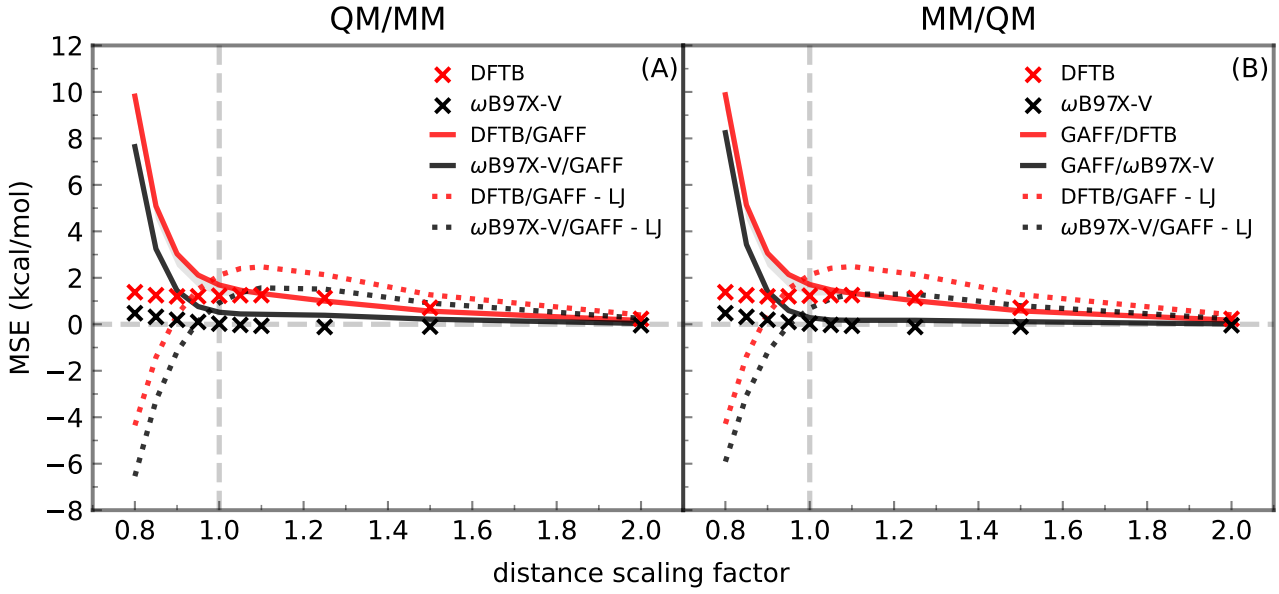

Figure A.14.: MSE of ΔE_{int} along the full dissociation curves in HB375x10 for both partitioning schemes, QM/-GAFF (left) and GAFF/QM (right). Solid lines include the Lennard-Jones contribution, while dotted lines exclude it. At short distances, removing the LJ contribution markedly reduces the MSE, indicating that the LJ parameters dominate the short-range error. The remaining error after LJ removal suggests additional contributions from the QM–MM interface.

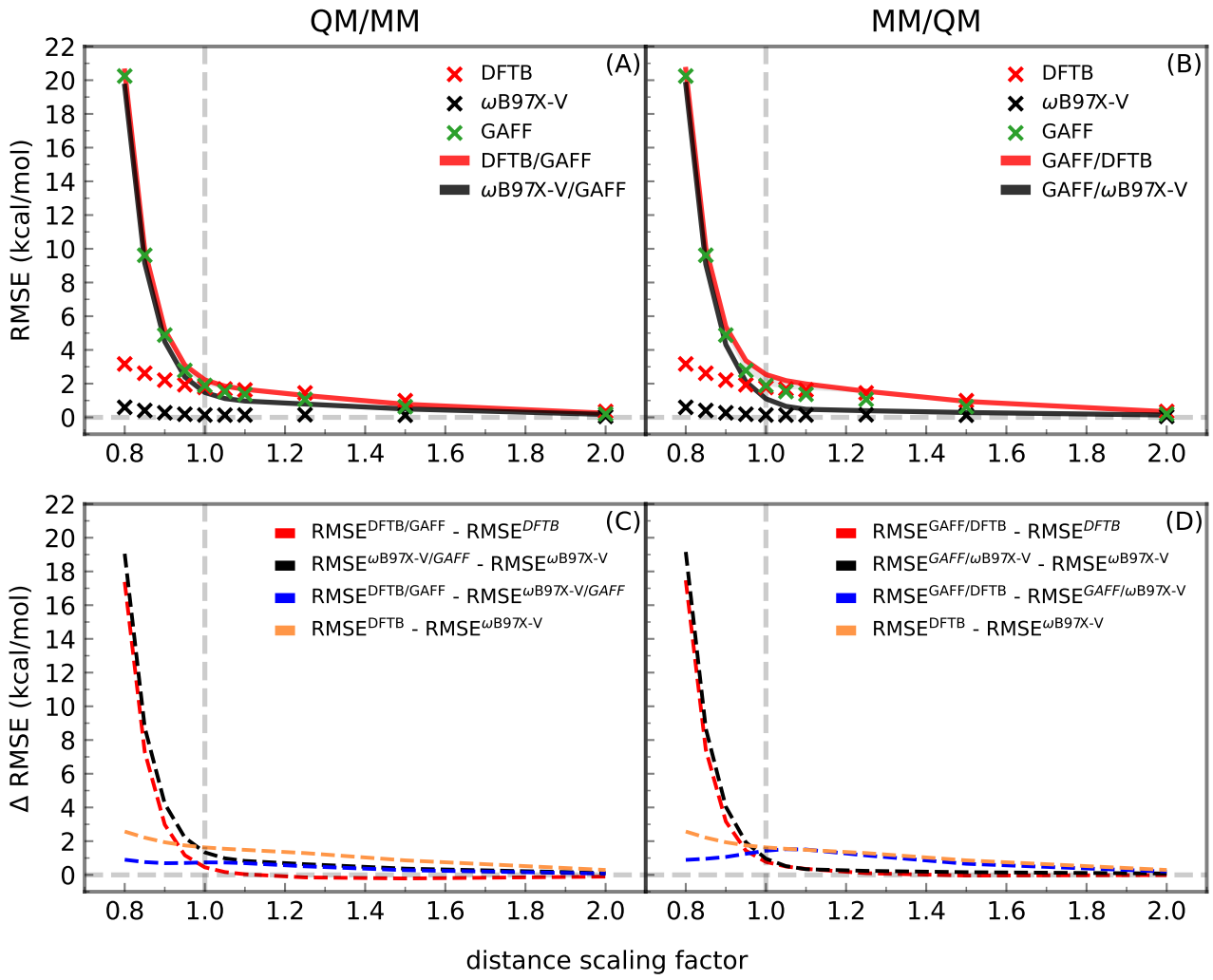

Figure A.15.: Full range RMSE values at identical distance scaling factor along the entire dissociation curves in HB375x10. The figure provides a complete view of the RMSE trends for both QM/GAFF and GAFF/QM models for HB375x10.

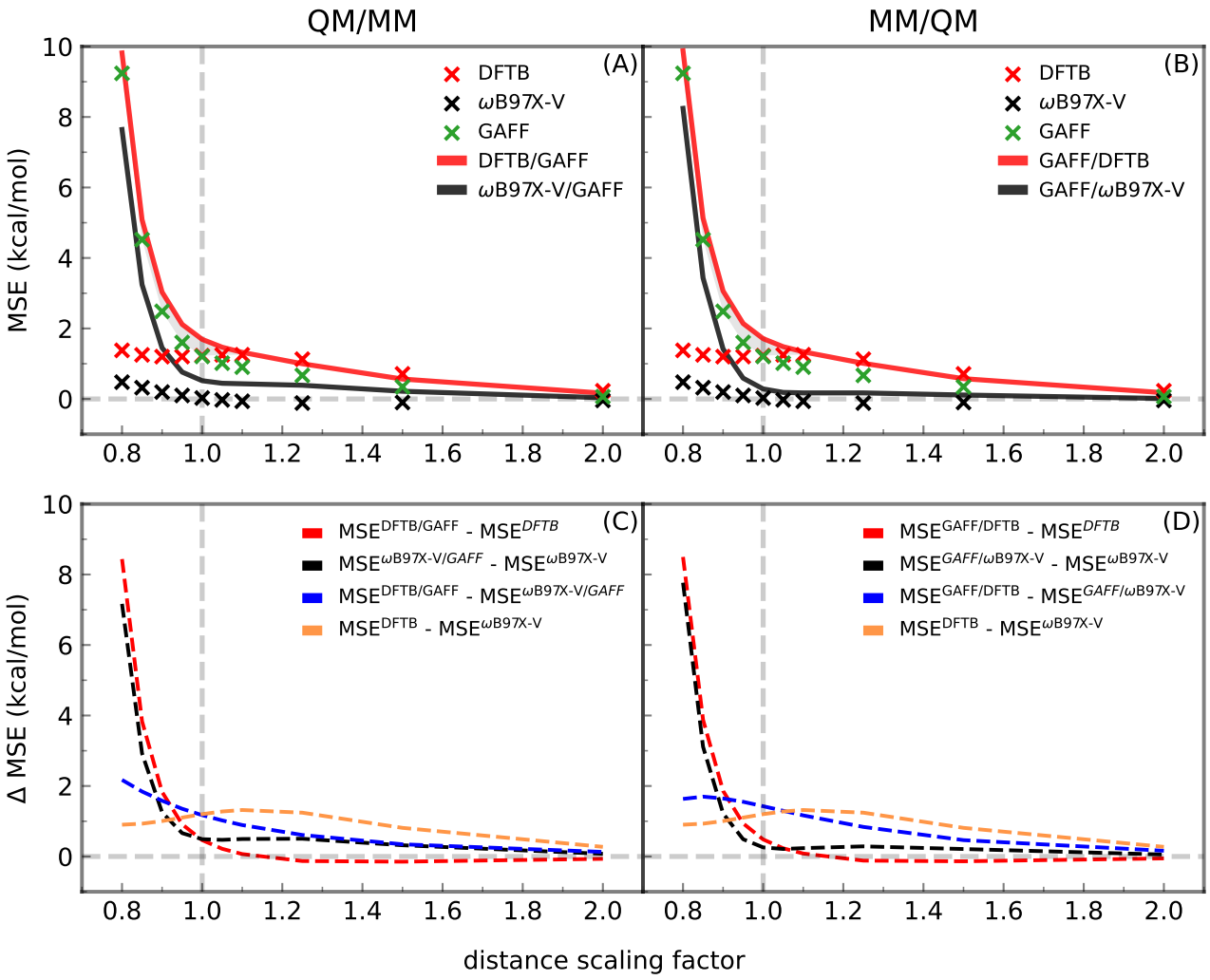

Figure A.16.: Full range MSE values at identical distance scaling factor along the entire dissociation curves in HB375x10. The figure provides a complete view of the MSE trends for both QM/GAFF and GAFF/QM models for HB375x10.

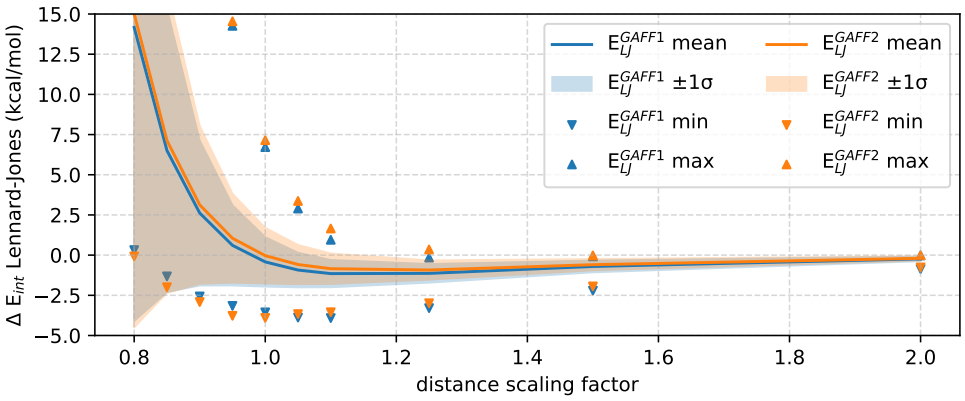

Figure A.17.: Range of mean, minimum, and maximum Lennard–Jones (LJ) energy contributions in the HB735×10 dataset as a function of the distance scaling factor. Shaded areas represent the standard deviation (±1σ) around the mean for GAFF1 and GAFF2 parameters. The steep increase in LJ energy below a scaling factor of 1.0 indicates excessive short-range repulsion.

Table A.4.: Systems in HB375x10 that show the largest Lennard-Jones interaction energies in kcal/mol at f_{dscaling} of 0.8 and 1.0. $(\mu+\sigma)$ is shown for reference. Energies were calculated from the GAFF parameters.

ID	f_{dscaling}=0.8	f_{dscaling}=1.0	ID	f_{dscaling}=0.8	f_{dscaling}=1.0
6.01	128.94	6.72	5.013	59.44	2.32
6.004	120.14	6.43	1.013	24.90	2.32
6.008	119.49	6.02	1.002	28.46	2.28
5.008	101.30	5.42	5.007	60.08	2.25
6.009	98.75	5.13	3.002	18.56	2.25
5.012	100.32	4.94	3.006	21.16	2.24
6.006	91.46	4.83	3.004	22.04	2.18
5.002	91.58	4.40	3.011	25.94	2.14
5.014	71.61	3.84	6.003	56.18	2.13
5.006	78.87	3.70	5.001	51.63	1.99
6.002	64.91	3.45	1.003	26.79	1.93
1.059	31.30	3.12	6.007	49.26	1.93
1.014	19.37	2.89	1.009	23.57	1.71
5.009	68.12	2.76	3.106	21.08	1.71
5.005	68.13	2.74	3.012	23.07	1.48
1.008	20.62	2.68	3.008	24.91	1.42
6.003	59.22	2.64	1.001	20.31	1.25
6.001	51.28	2.37			
					$\mu + \sigma = 1.11$

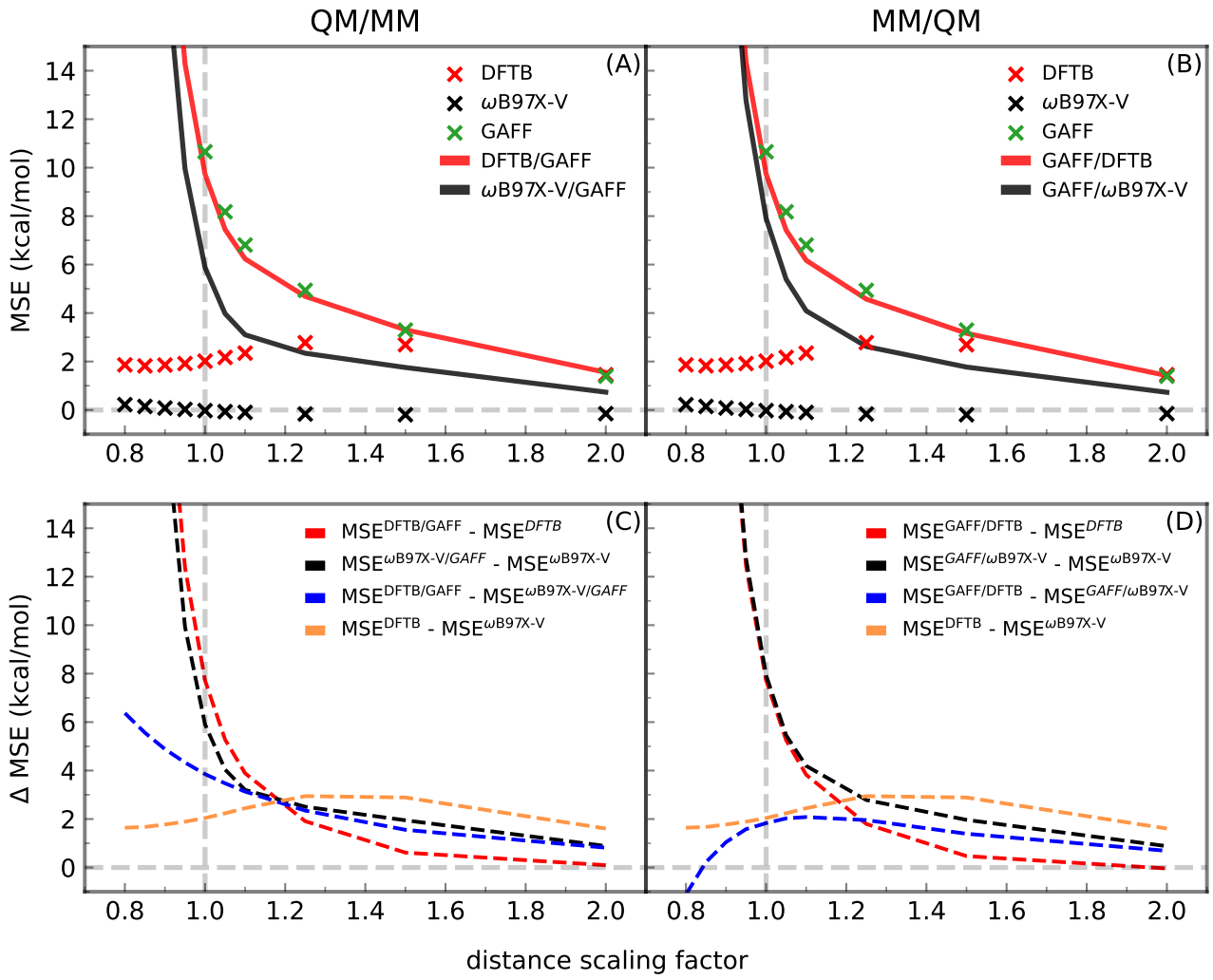

Figure A.18.: MSE values at identical distance scaling factor along the entire dissociation curves in IHB100x10. Results are shown for both compartmentalization schemes: QM/GAFF (left) and GAFF/QM (right), using CCSD(T)/CBS as the reference. The upper row shows MSEs between the respective QM (QM/MM) methods and the reference. The lower row shows the differences between the curve in the upper row.

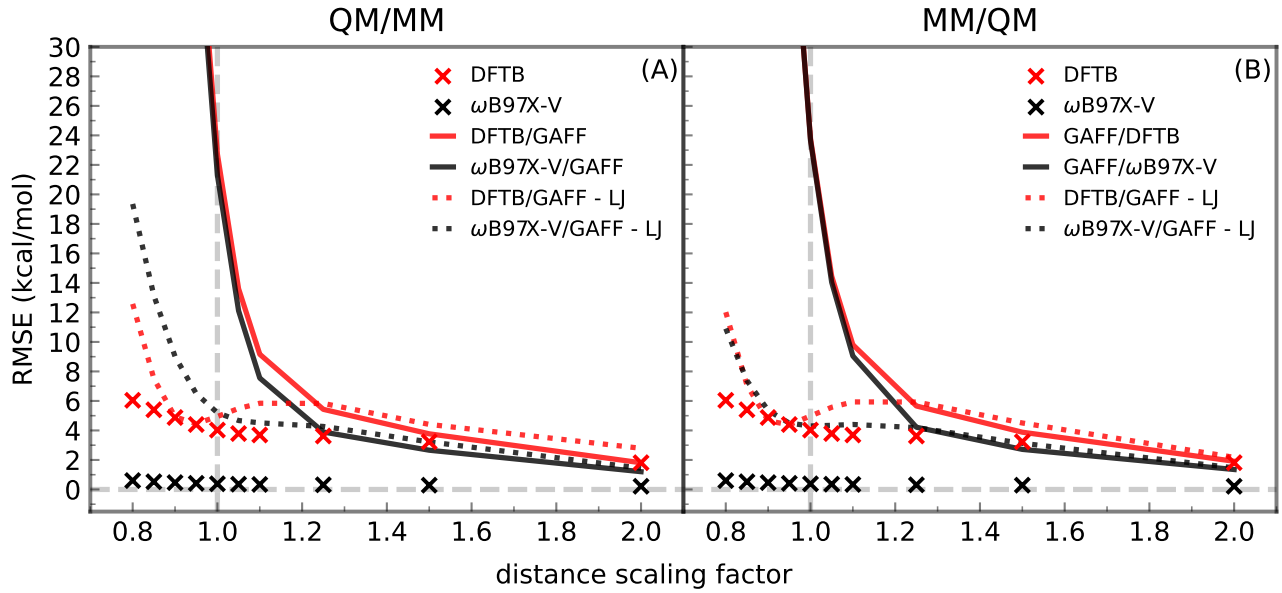

Figure A.19.: RMSE of ΔE_{int} and subtracted LJ contribution along the full dissociation curves in IHB100x10 for both partitioning schemes, QM/GAFF (left) and GAFF/QM (right). Solid lines include the Lennard–Jones contribution, while dotted lines exclude it. At short distances, removing the LJ contribution markedly reduces the RMSE, indicating that the LJ parameters dominate the short-range error. The remaining error after LJ removal suggests additional contributions from the QM–MM interface.

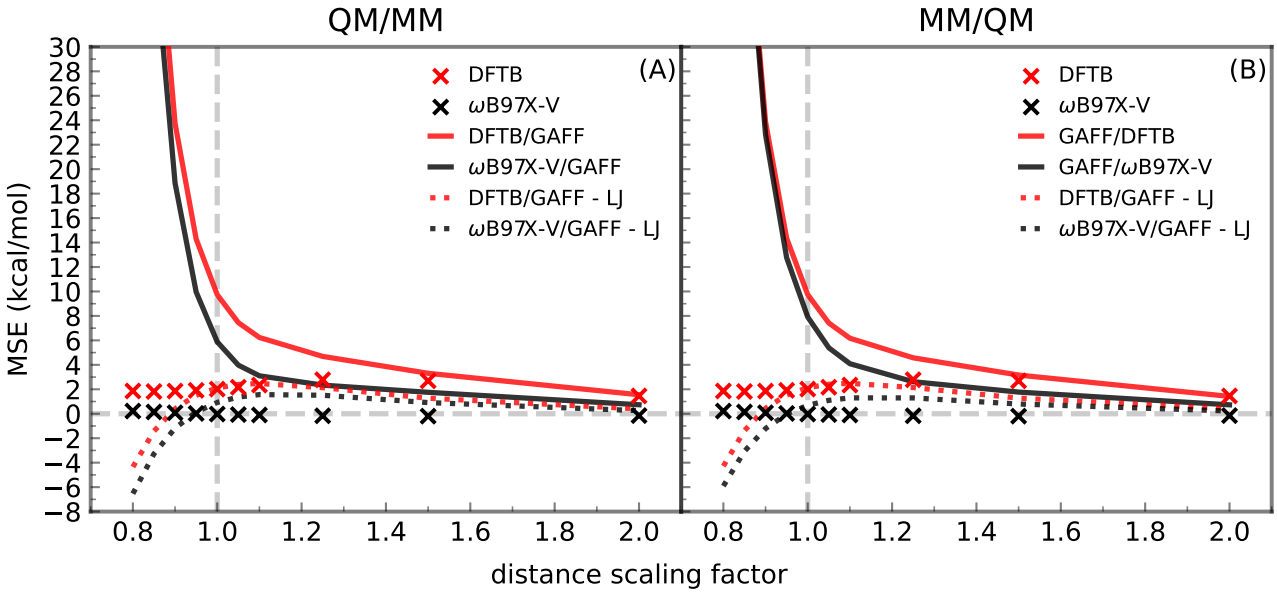

Figure A.20.: MSE of ΔE_{int} and subtracted LJ contribution along the full dissociation curves in IHB100x10 for both partitioning schemes, QM/GAFF (left) and GAFF/QM (right). Solid lines include the Lennard–Jones contribution, while dotted lines exclude it. At short distances, removing the LJ contribution markedly reduces the MSE, indicating that the LJ parameters dominate the short-range error. The remaining error after LJ removal suggests additional contributions from the QM–MM interface.

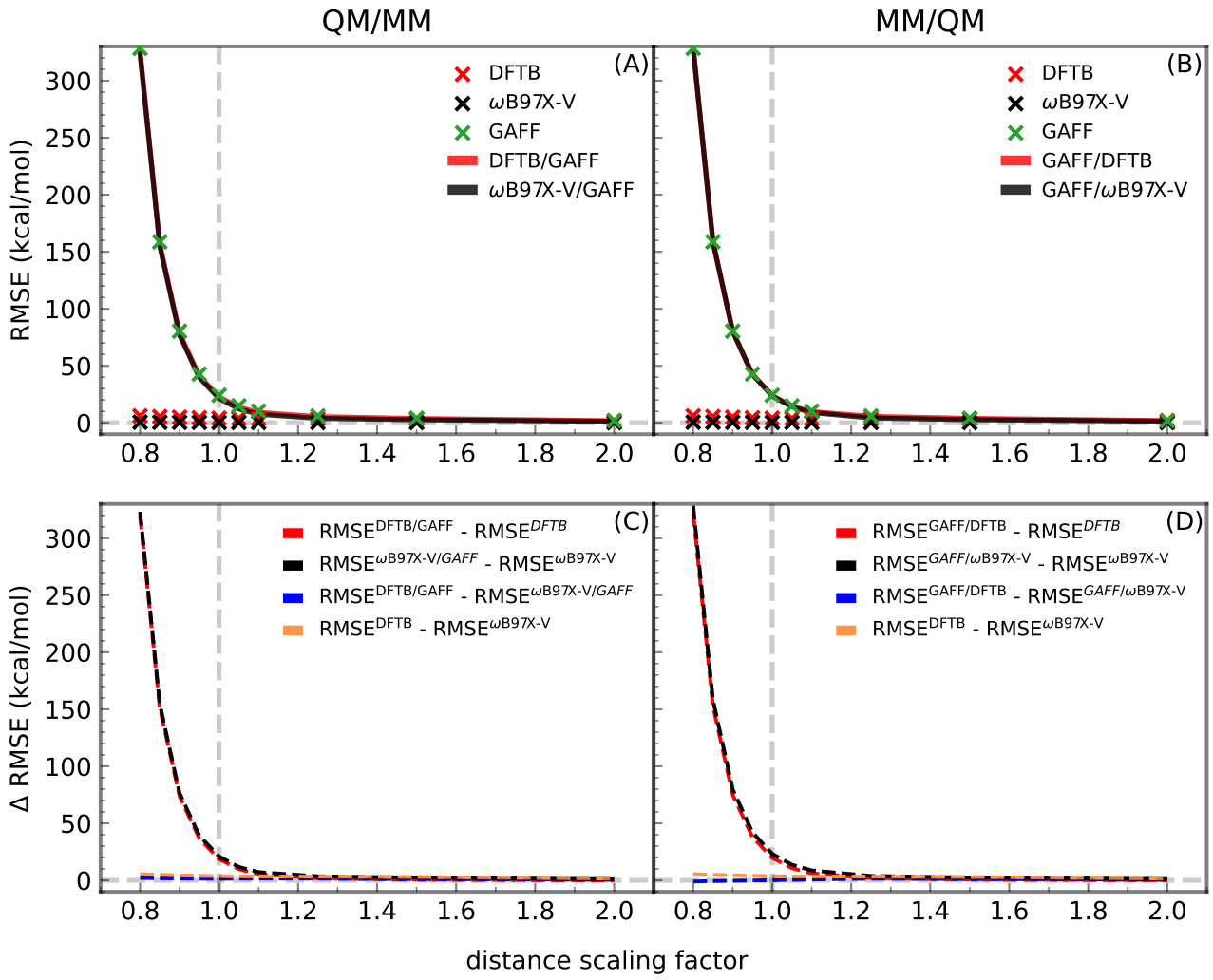

Figure A.21.: Full range RMSE values at identical distance scaling factor along the entire dissociation curves in IHB100x10. The figure provides a complete view of the RMSE trends for both QM/GAFF and GAFF/QM models for IHB100x10.

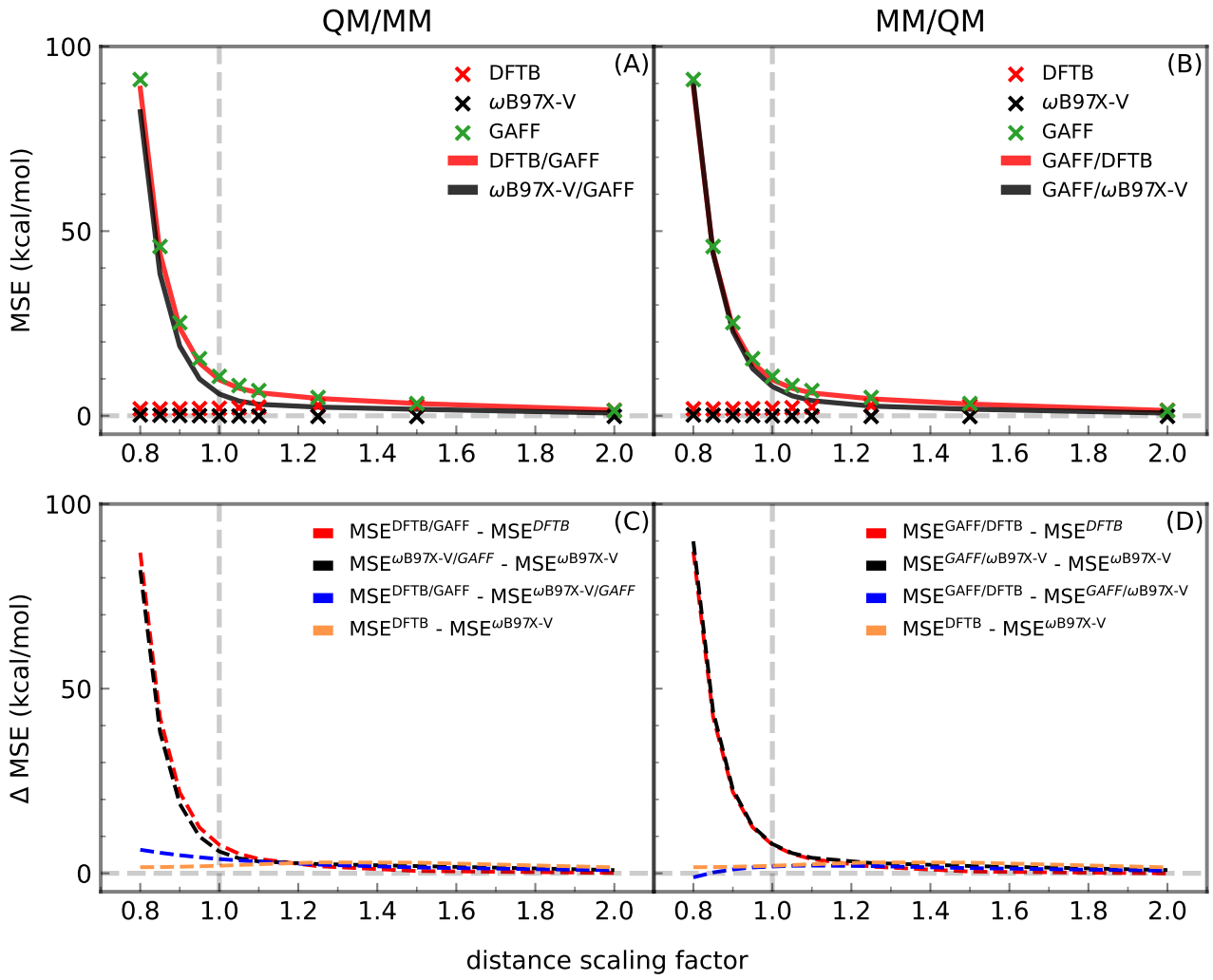

Figure A.22.: Full range MSE values at identical distance scaling factor along the entire dissociation curves in IHB100x10. The figure provides a complete view of the MSE trends for both QM/GAFF and GAFF/QM models for IHB100x10.

We analyzed the distribution of LJ energy contributions across the dataset, as shown in Figures A.23 and A.24. At $f_{\text{dscaling}} = 1.0$, the mean of LJ energy is ∼6 kcal/mol, but five systems stand out as extreme outliers with LJ energies reaching ∼196 kcal/mol. Table A.5 shows the systems with the highest LJ energies at short distances in IHB100x10. A similar trend is observed for neutral H-bonding, as shown in Figure A.17, but with a smaller magnitude of the deviation. We further tested whether these outliers obscure the overall performance trends. For instance, ethyne was a recurrent component in these outliers. For IHB100x10, excluding systems comprising ethyne (4 systems), the error at f_{dscaling} of 1.0 changes from 24 to 12 kcal/mol and at f_{dscaling} of 0.8 from 328 to 139 kcal/mol. Consistent with this, only 6 out of 100 systems in IHB100x10 show overbinding at $f_{\text{dscaling}} = 1.0$ for GAFF. In HB375x10, the effect persists but is smaller in magnitude. When excluding systems comprising ethyne (26 systems), the RMSE at f_{dscaling} of 1.0 changes from 1.8 to 1.6 kcal/mol and from 20.3 to 8.5 kcal/mol at f_{dscaling} of 0.8. Only 48 out of 375 systems show overbinding at f_{dscaling} of 1.0 in the GAFF calculations. These results show that systematic exclusion of outliers, such as ethyne-containing systems, remarkably reduces the RMSE but does not alter the qualitative conclusion. The remaining deviations indicate that the issue extends beyond these outliers and originates from generally over-repulsive LJ parameters in GAFF at short distances.

In GAFF, the LJ parameters are identical for ionic and neutral systems. For example, the oxygen atom type 'o' is uniformly assigned to hydrogen-bond acceptors in both ionic species, such as oxalate, nitrite, acetate, and hydroxide, and in neutral molecules, such as acetamide or dimethylcarbonate. This lack of differentiation becomes particularly problematic for ionic complexes, where equilibrium donor–acceptor distances can be shorter. While the R_{min} donor–acceptor distance defined in GAFF is 3.5 Å, the equilibrium distances observed in the dataset are notably shorter. For example, the value is 2.6 Å for the ammonium · · · dimethylcarbonate complex and 3.1 Å for the ammonia · · · acetone complex. In addition, some systems exhibit unusually short equilibrium distances relative to other systems of the same H-bond type, such as 2.9 Å in benzene · · · hydroxide versus 3.2 Å in benzene · · · acetate. These findings highlight a fundamental limitation of QM/MM calculations using LJ parameters from FF, as their transferability to diverse short-range interactions is limited.

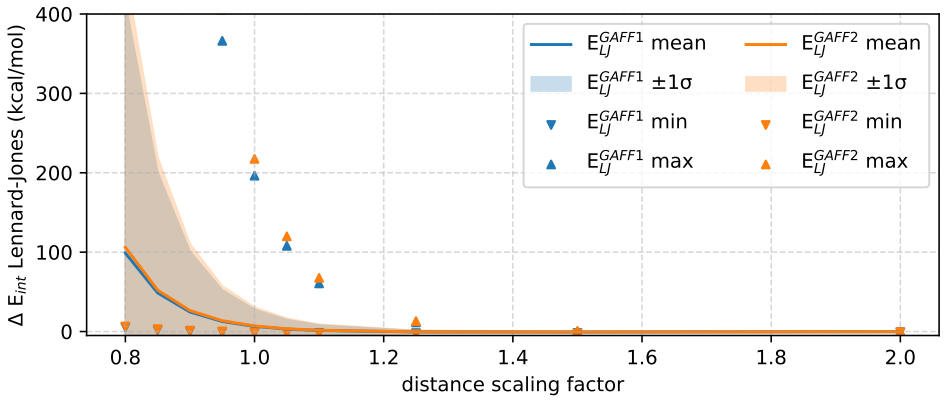

Figure A.23.: Broader range of mean, minimum, and maximum Lennard–Jones (LJ) energy contributions in the IHB100×10 dataset as a function of the distance scaling factor. Shaded areas represent the standard deviation (±1σ) around the mean for GAFF1 and GAFF2 parameters. The steep increase in LJ energy below a scaling factor of 1.0 indicates excessive short-range repulsion.

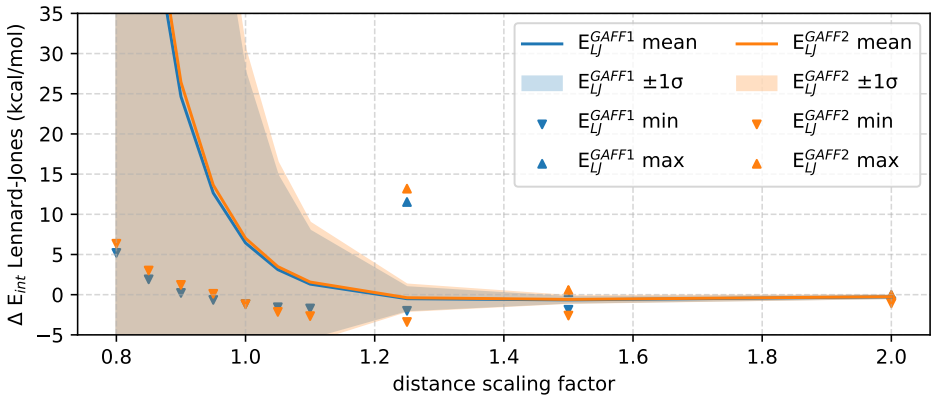

Figure A.24.: Zoomed-in view of mean Lennard–Jones (LJ) energy contributions in the IHB100×10 dataset as a function of the distance scaling factor. Shaded areas represent the standard deviation (±1σ) around the mean for GAFF1 and GAFF2 parameters. The steep increase in LJ energy below a scaling factor of 1.0 indicates excessive short-range repulsion.

Table A.5.: Systems in IHB100x10 that show the largest Lennard–Jones interaction energies in kcal/mol at f_{dscaling} of 0.8 and 1.0. (μ) and ($\mu+\sigma$) are shown for reference. Energies were calculated from the GAFF parameters.

ID	f_{dscaling}=0.8	f_{dscaling}=1.0
11.001	2906.90	196.36
11.003	1026.70	67.71
11.005	727.86	47.67
11.007	560.90	36.25
12.003	429.18	27.69
11.010	305.49	19.25
11.008	240.02	14.50
2.002	141.18	10.88
2.003	139.70	10.78
3.005	115.48	9.31
2.007	106.89	7.84
5.003	36.07	7.11
3.017	122.25	7.02
2.001	86.29	6.97
6.001	38.83	6.82
5.012	30.65	6.52
11.002	130.84	6.48
		$\mu = 6.43$
		$\mu + \sigma = 27.69$

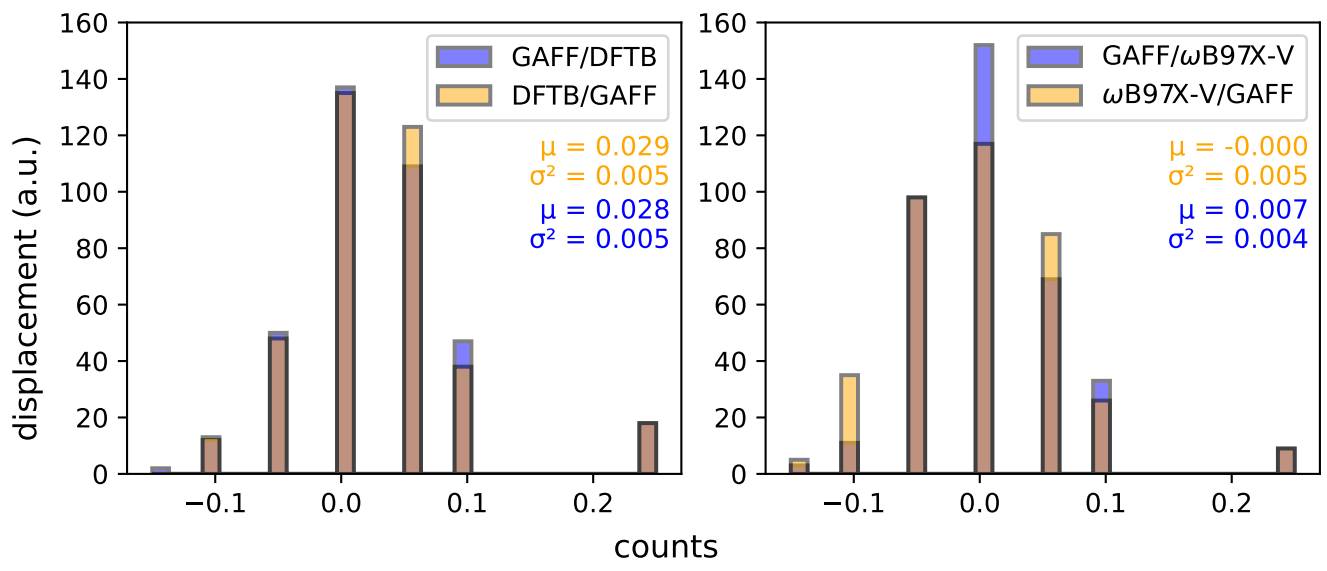

Figure A.25.: Deviations of the equilibrium position of the dissociation curve between the QM/GAFF models and the CCSD(T)/CBS reference in HB375.

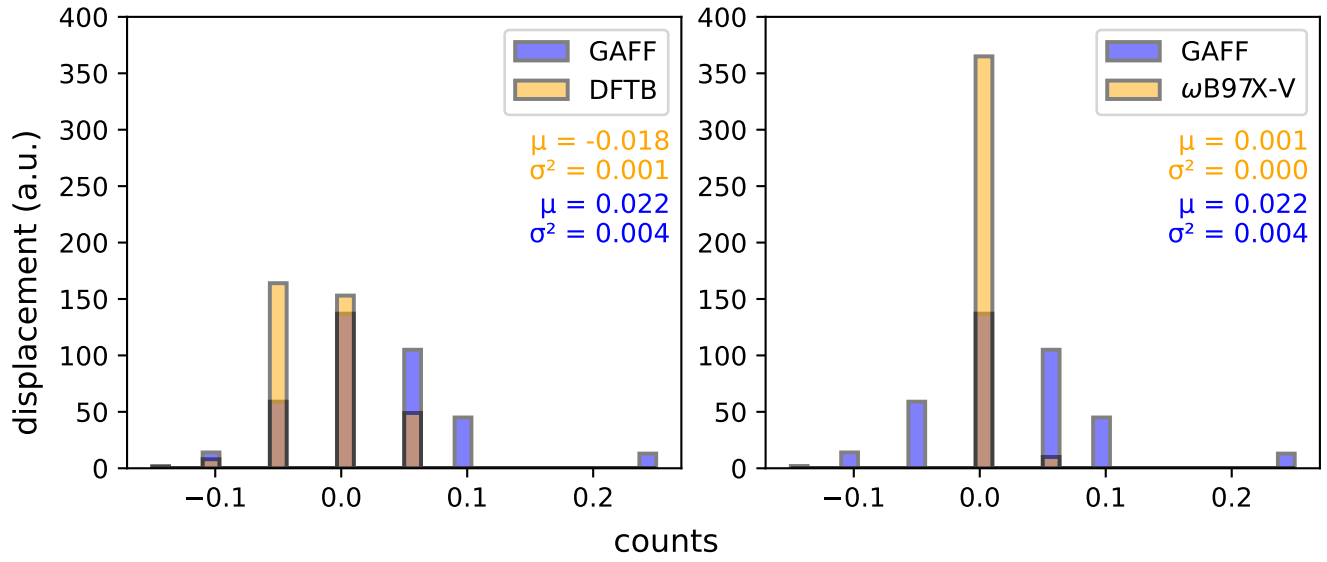

Figure A.26.: Deviations of the equilibrium position of the dissociation curve between the QM models or the GAFF model and the CCSD(T)/CBS reference in HB375.

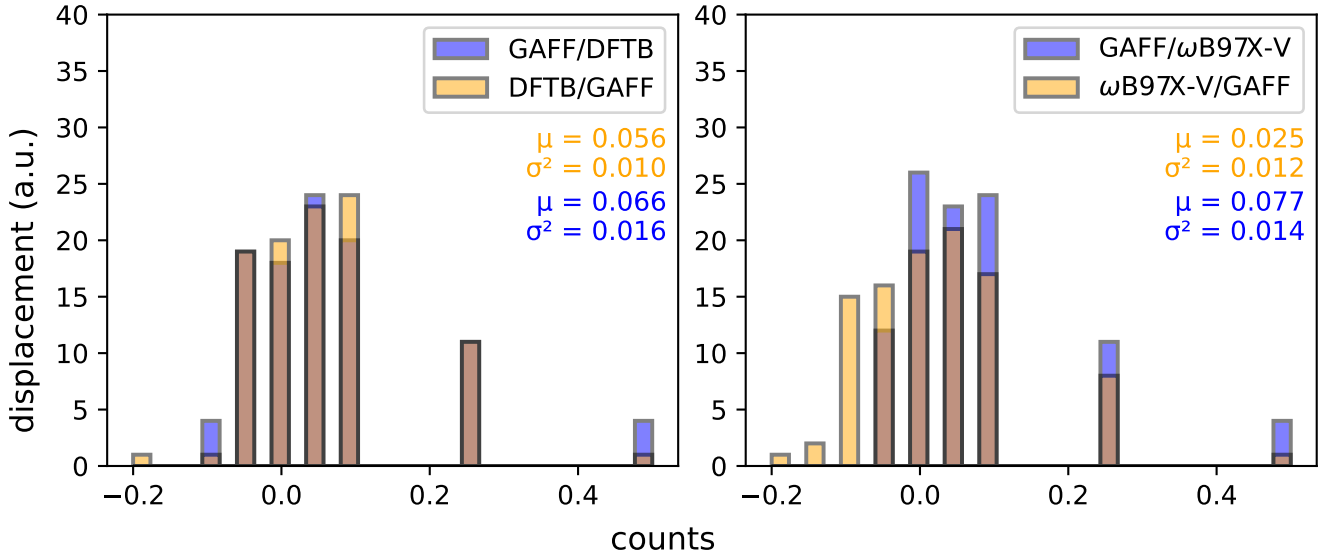

Figure A.27.: Deviations of the equilibrium position of the dissociation curve between the QM/GAFF models and the CCSD(T)/CBS reference in IHB100.

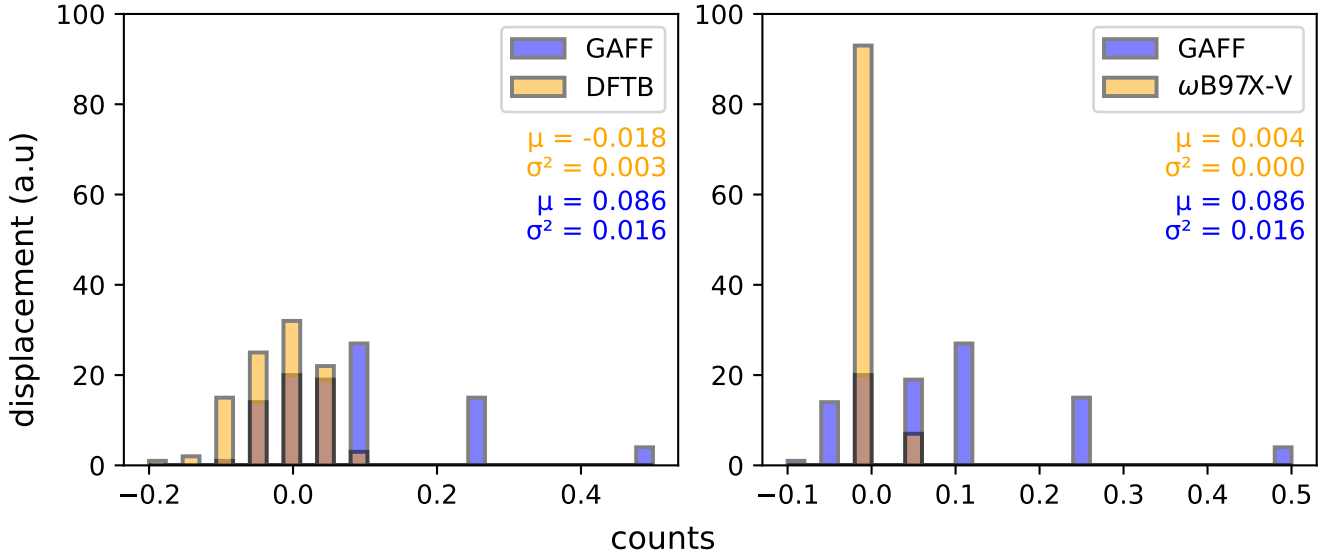

Figure A.28.: Deviations of the equilibrium position of the dissociation curve between the QM models or the GAFF model and the CCSD(T)/CBS reference in IHB100.

Table A.6.: Summary of differences between optimized values of f_{dscaling} (corresponding to the structure with the lowest energy for each method) and the reference value of f_{dscaling}=1.0 taken from the datasets HB375x10 and IHB100x10.

	System	μ	σ^2
HB375x10	GAFF	0.022	0.004
	DFTB	-0.0018	0.001
	DFTB/GAFF	0.029	0.005
	AMBER/DFTB	0.028	0.005
	ωB97X-V	0.001	0.000
	ωB97X-V/GAFF	0.000	0.005
	GAFF/ωB97X-V	0.007	0.004
IHB100x10	GAFF	0.086	0.003
	DFTB	-0.018	0.003
	DFTB/GAFF	0.056	0.010
	AMBER/DFTB	0.066	0.016
	ωB97X-V	0.004	0.000
	ωB97X-V/GAFF	0.025	0.012
	GAFF/ωB97X-V	0.077	0.014

PL-REX dataset - microenvironment models

Result for PL-REX

Table A.7.: Identity and number of ligands in the selected subsets of receptor–ligand systems from the PL-REX dataset.

No. Target	Protein	Lig.
01-CA2	Hum. carbonic anhydrase II	10
02-HIV-PR	HIV-1 protease	22
03-CK2	Zea mays casein kinase 2	16
05-Cath-D	Hum. cathepsin D	10
06-BACE1	Hum. beta-secretase 1	16
07-JAK1	Hum. Janus kinase 1	12
09-CDK2	Hum. cyclin-dependent kinase 2	31
10-MMP12	Hum. matrix metallopeptdase 12	18

Table A.8.: Mean number of H-bonds that involve donor or acceptor atoms of the ligand and are located within a radius of 3.2 Å to the complementing atom of the receptor in PL-REX. Only nitrogen and oxygen species were considered and reported separately as donors (D. N and D. O) and acceptors (A. N and A. O) for the ligand. *H*over and *H*under count the mean number of ionic H-bonds types that showed overestimation (CH or OH donor to ASP or GLU carboxylate acceptor) or underestimation (NH donor to ASP or GLU carboxylate acceptor; N or O acceptor to LYS or ARG ammonium donor) in IHB100x10. Also reported are the mean contributions from LJ and electrostatic interactions (el.) of the DFTB/MM models, energy in kcal/mol.

System	D. N	D. O	A. N	A. O	*H*total	*H*over	*H*under	$\Delta E_{\text{int}}^{\text{el.}}$		$\Delta E_{\text{int}}^{\text{LJ}}$
								DFTB/GAFF	AMBER/DFTB	
02-HIV-PR	1.86	2.50	0.05	3.86	8.27	2.95	0.32	-82.95	-84.97	-70.67
05-Cath-D	2.90	1.80	0.10	3.90	8.70	0.9	0.0	-84.54	-53.17	-53.17
06-BACE1	2.81	1.50	0.00	2.00	6.31	1.06	0.0	-3.56	-6.16	-63.43
03-CK2	0.06	0.25	0.00	0.31	0.62	0.19	0.06	-11.00	-10.44	-36.91
07-JAK1	1.33	0.33	1.00	0.67	3.33	0.42	1.42	-52.05	-48.70	-46.41
09-CDK2	2.61	0.00	0.16	0.65	3.42	0.0	1.48	-48.30	-42.09	-41.18

Scaling

Effects of Charge Scaling in HB375/IHB100

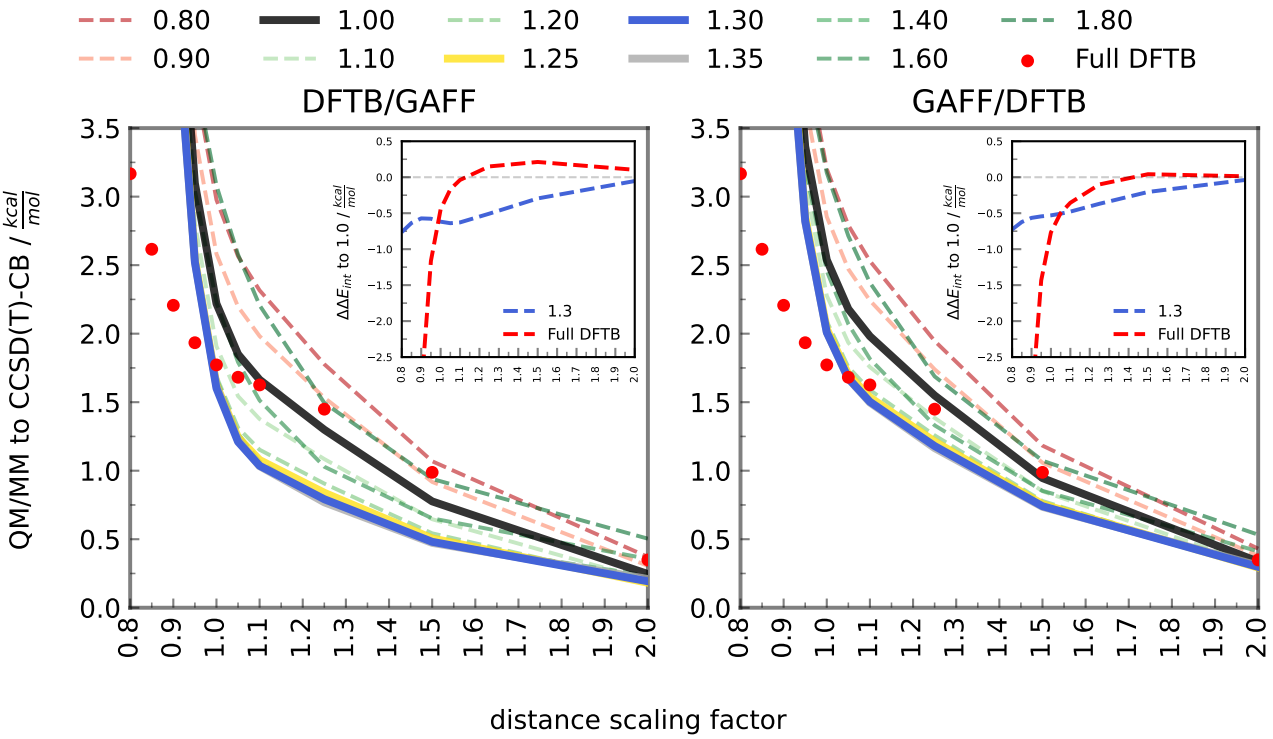

Figure A.29.: Effects of QM–MM scaling factors on the RMSE along the dissociation curves in HB375x10. Results are shown for both partitioning schemes: QM/GAFF (left) and GAFF/QM (right), using CCSD(T)/CBS as the reference.

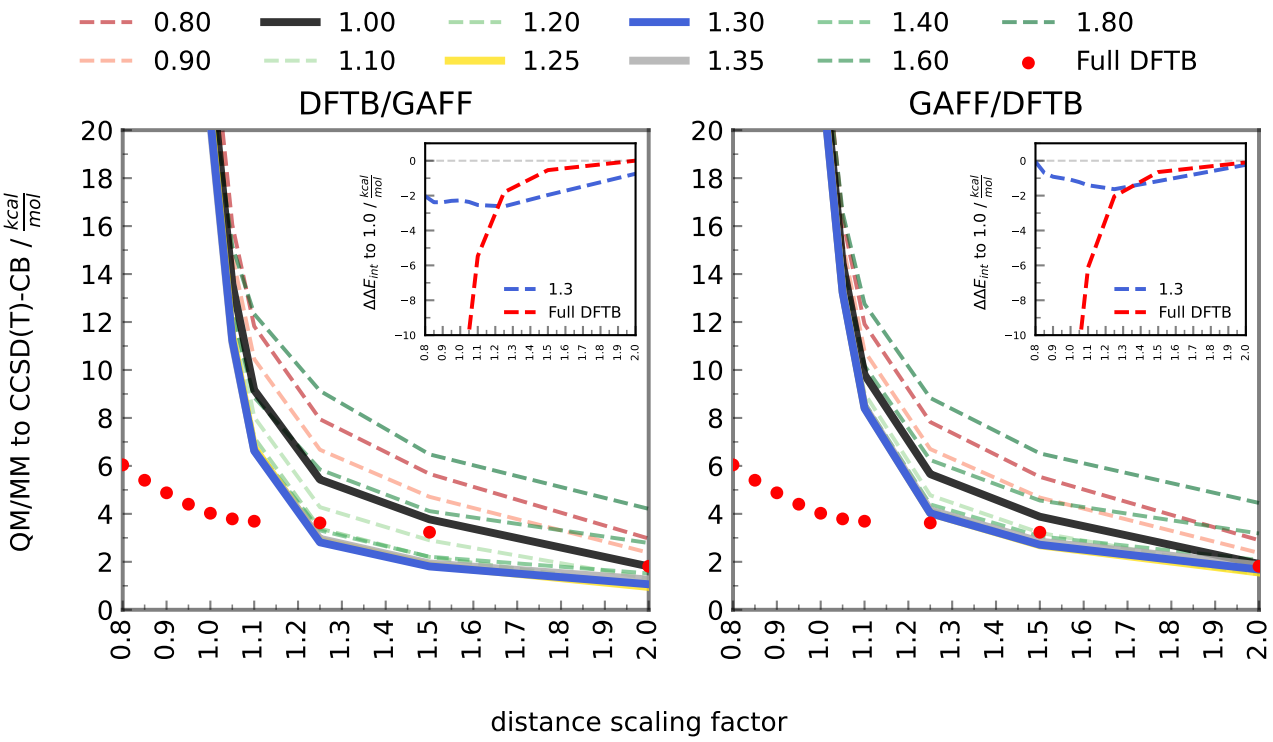

Figure A.30.: Effects of QM–MM scaling factors on the RMSE along the dissociation curves in IHB100x10. Results are shown for both partitioning schemes: QM/GAFF (left) and GAFF/QM (right), using CCSD(T)/CBS as the reference.

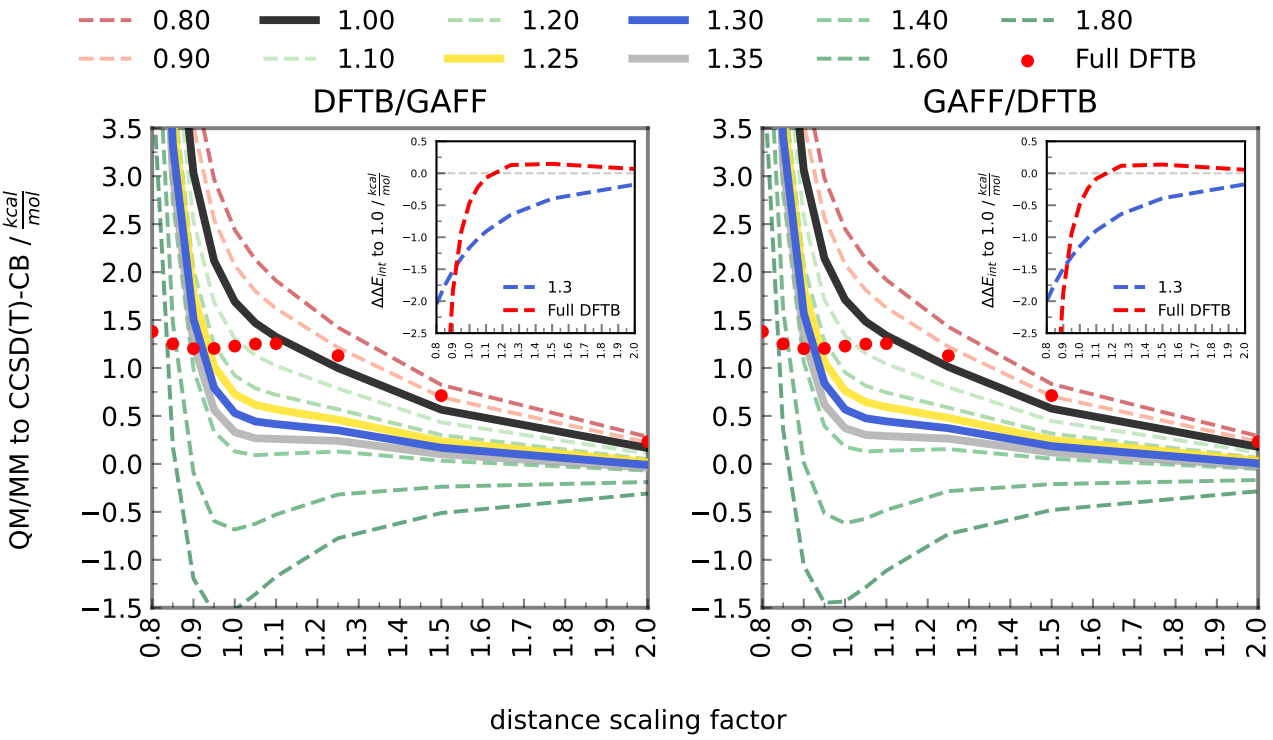

Figure A.31.: Effects of QM–MM scaling factors on the MSE along the dissociation curves in HB375x10. Results are shown for both partitioning schemes: QM/GAFF (left) and GAFF/QM (right), using CCSD(T)/CBS as the reference.

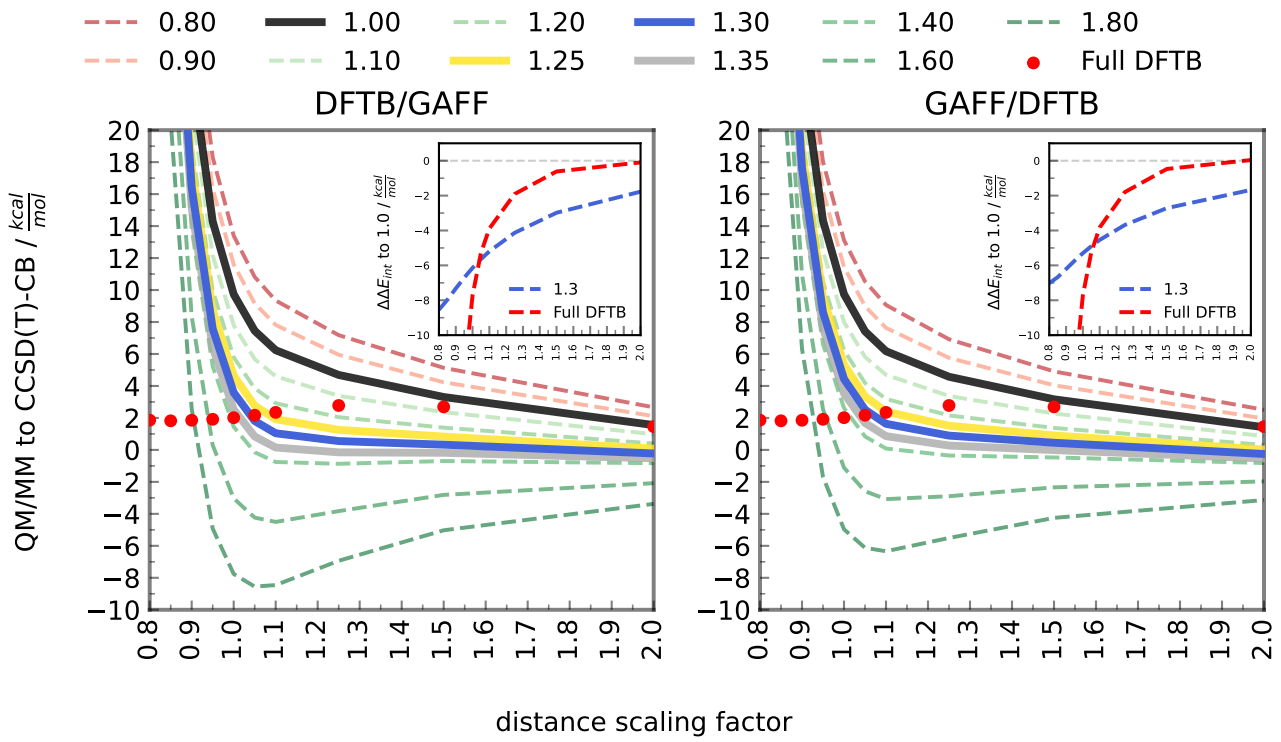

Figure A.32.: Effects of QM–MM scaling factors on the MSE along the dissociation curves in IHB100x10. Results are shown for both partitioning schemes: QM/GAFF (left) and GAFF/QM (right), using CCSD(T)/CBS as the reference.

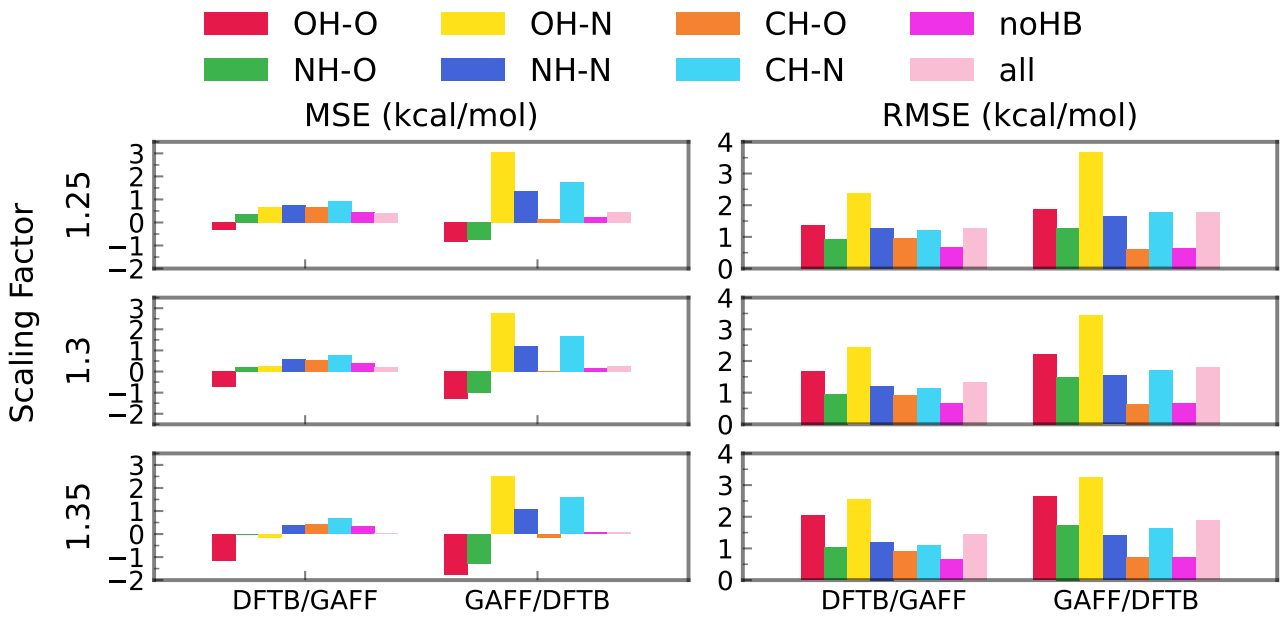

Figure A.33.: Effects of QM–MM scaling factors on the individual compound classes for HB375.

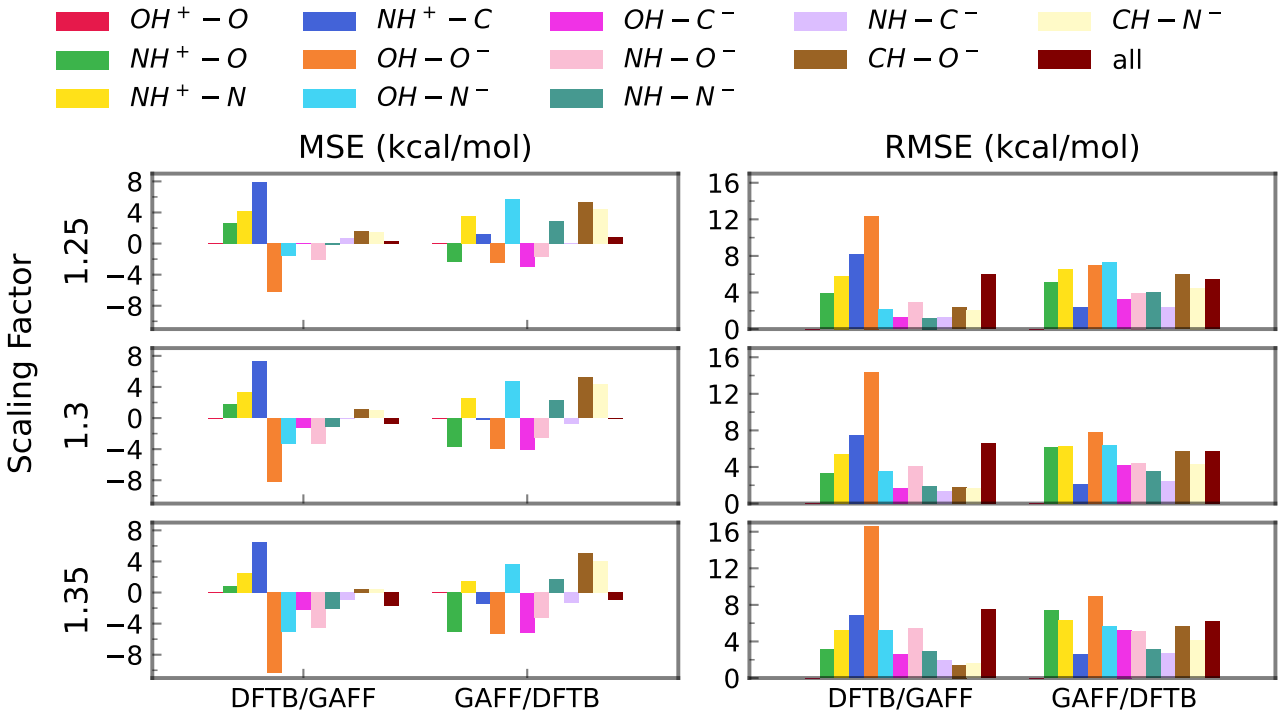

Figure A.34.: Effects of QM–MM scaling factors on the individual compounds classes for IHB100.

Table A.9.: Effects of QM–MM scaling factors on the RMSEs for ωB97X-V/GAFF models applied to HB375x10.

	Full QM	QM/MM	MM/QM	MM/MM
1.00	0.14	1.20	0.68	1.50
1.10	0.14	1.43	1.03	1.50
1.20	0.14	1.96	1.67	1.50
1.30	0.14	2.65	2.42	1.50

Table A.10.: Effects of QM–MM scaling factors on the MSEs for ωB97X-V/GAFF models applied to HB375x10.

	Full QM	QM/MM	MM/QM	MM/MM
1.00	0.03	0.21	0.03	0.92
1.10	0.03	-0.35	-0.54	0.92
1.20	0.03	-0.95	-1.14	0.92
1.30	0.03	-1.57	-1.76	0.92

Table A.11.: Effects of QM–MM scaling factors on the RMSEs for ωB97X-V/GAFF models applied to IHB100x10.

	Full QM	QM/MM	MM/QM	MM/MM
1.00	0.38	6.00	5.28	7.35
1.10	0.38	7.00	4.95	7.35
1.20	0.38	9.05	5.61	7.35
1.30	0.38	11.72	7.26	7.35

Table A.12.: Effects of QM–MM scaling factors on the MSEs for ωB97X-V/GAFF models applied to HB375x10.

	Full QM	QM/MM	MM/QM	MM/MM
1.00	-0.03	1.57	3.18	5.96
1.10	-0.03	-0.87	1.20	5.96
1.20	-0.03	-3.46	-0.86	5.96
1.30	-0.03	-6.16	-3.01	5.96

Effects of Charge Scaling in PL-REX

Table A.13.: Errors for best QM–MM scaling factors (λ). Content of the rows in descending order for each model: error for optimal λ, corresponding optimal λ, improvements for optimal λ compared to the unscaled model.

	System	1	2	3	5	6	7	9	10
RMSE	**DFTB/GAFF**	5.54	3.40	4.28	2.31	1.76	3.87	3.44	7.46
	λ	1.15	1.0	1.1	1.0	0.9	1.0	1.0	1.1
	Δ	-20.88	0.0	-1.09	0.0	-1.76	0.0	0.0	6.26
	AMBER/DFTB	4.71	3.92	4.29	2.11	3.50	4.25	4.10	4.62
	λ	0.65	1.0	1.2	1.0	0.85	1.05	1.1	0.7
	Δ	119.09	0.0	-2.12	0.0	-3.73	0.09	-2.75	51.52
MSE	**DFTB/GAFF**	-4.93	0.79	-0.07	-1.54	0.10	-1.34	-0.83	-1.86
	λ	1.1	1.0	1.3	1.0	0.9	1.0	1.0	1.15
	Δ	-31.28	0.0	-3.97	0.0	-1.57	0.0	0.0	-9.96
	AMBER/DFTB	4.35	-1.26	0.23	0.30	-0.03	-0.78	0.33	2.09
	λ	0.65	1.0	1.35	1.0	0.8	1.05	1.1	0.7
	Δ	119.43	0.0	-4,21	0.0	4,05	0.56	0.49	54.37

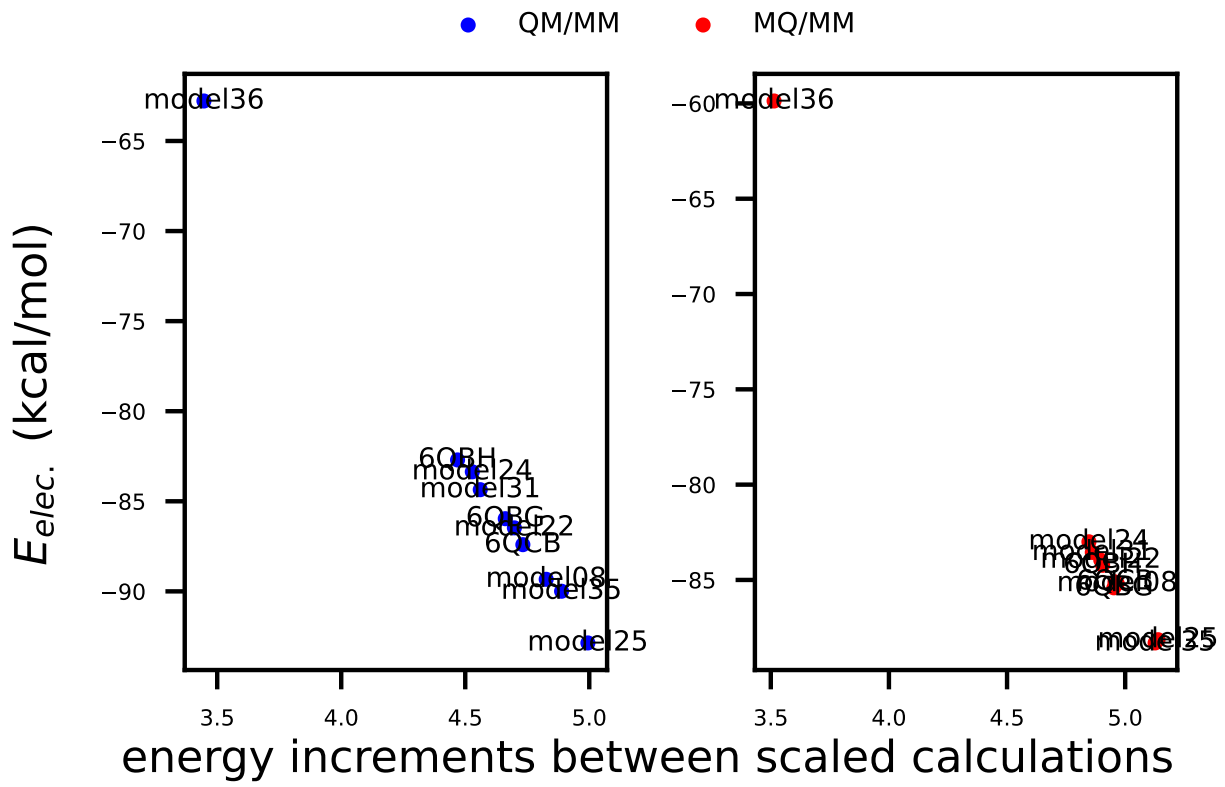

Figure A.35.: Correlation ΔE_{int} between increment QM–MM scaling factors and the electrostatic contribution in the QM/MM models for system 005Cath.

B. Reduction Pathway of Glutaredoxin 1 Investigated with QM/MM Molecular Dynamics Using a Neural Network correction

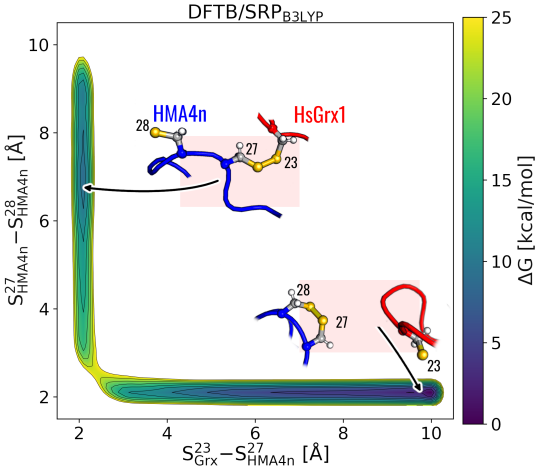

Figure B.1.: FES for alternative regioselectivity of TDE in the monothiol pathway of Grx reacting with Hma as substrate and GSH as co-substrate in step 1, calculated using the specific reaction parameterization (SRP) method. Contour lines are drawn every 2.5 kcal/mol.

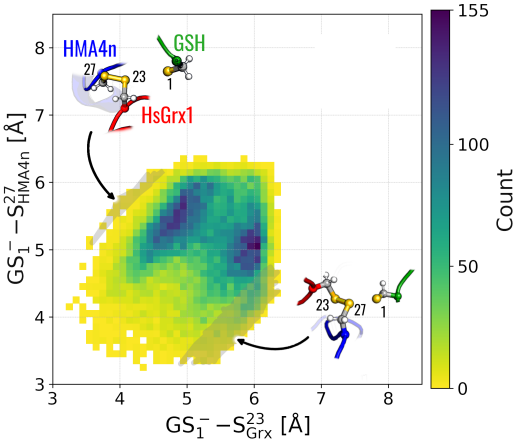

Figure B.2.: Evaluation of accessibility for the nucleophilic attack based on the histogram of the sulfur–sulfur distances calculated from classical MD simulations of the alternative reaction **step 2** including both regioisomers S^{23}_{Grx}–S^{27}_{Hma} and S^{23}_{Grx}–S^{28}_{Hma}. The gray shaded areas correspond to structures that meet the accessibility criterion.

C. Machine Learned Collective Variables for Augmented QM/MM Sampling

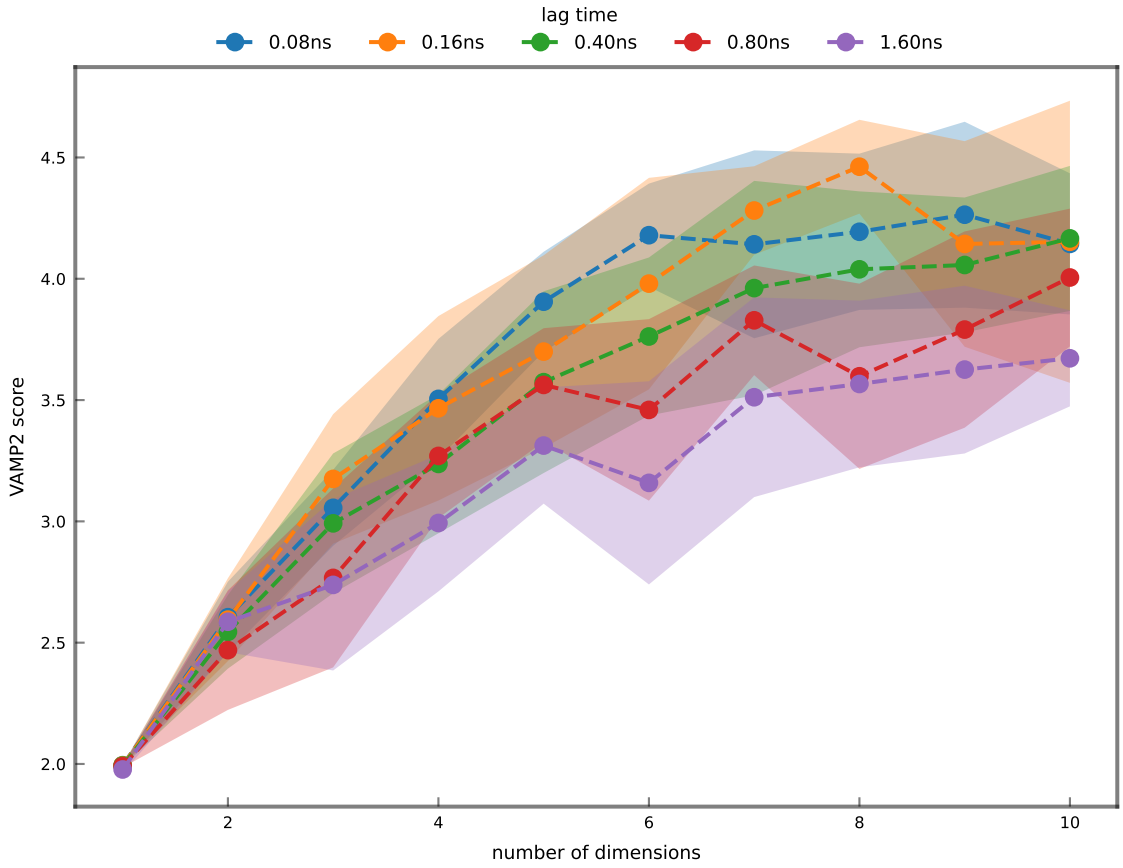

Figure C.1.: VAMP2 scores are shown for different lag times using 10 sine–cosine pairs derived from the five disulfide torsion angles.

Table C.1.: Cosine and sine components of the disulfide torsion angles (χ_i) defining the principal component obtained by PCA.

	PC1	PC2	PC3	PC4	PC5	PC6	PC7	PC8	PC9	PC10
$\cos(\chi_1)$	-0.44	-0.19	-0.01	0.16	-0.16	-0.44	-0.39	0.23	0.56	0.01
$\sin(\chi_1)$	0.30	0.06	0.30	-0.10	-0.02	-0.06	-0.83	-0.21	-0.26	-0.01
$\cos(\chi_2)$	0.36	0.60	-0.30	0.20	-0.10	-0.35	-0.02	0.48	-0.11	-0.01
$\sin(\chi_2)$	0.47	-0.64	0.27	-0.08	-0.02	-0.26	0.17	0.44	-0.09	-0.01
$\cos(\chi_3)$	0.02	0.00	0.04	-0.08	-0.96	0.21	0.05	-0.01	-0.02	-0.13
$\sin(\chi_3)$	-0.01	-0.00	-0.01	0.02	0.13	-0.03	-0.00	-0.01	0.03	-0.99
$\cos(\chi_4)$	0.01	-0.27	-0.50	0.08	-0.13	-0.54	0.07	-0.50	-0.32	-0.00
$\sin(\chi_4)$	0.15	-0.27	-0.71	-0.24	0.06	0.42	-0.32	0.22	0.12	-0.00
$\cos(\chi_5)$	0.02	0.21	0.02	-0.89	0.01	-0.31	0.11	-0.06	0.21	0.00
$\sin(\chi_5)$	-0.59	-0.04	0.00	-0.21	0.01	-0.02	-0.09	0.41	-0.66	-0.02

Table C.2.: Cosine and sine components of the disulfide torsion angles (χ_i) defining the principal component obtained by tICA.

	IC1	IC2	IC3	IC4	IC5	IC6	IC7	IC8	IC9	IC10
$\cos(\chi_1)$	-0.22	0.41	0.73	-1.62	-1.96	2.38	-2.59	7.59	-0.31	-2.80
$\sin(\chi_1)$	0.13	-1.54	0.29	2.75	-2.96	2.80	2.65	-2.48	3.50	-2.77
$\cos(\chi_2)$	0.22	0.10	0.31	-1.03	-4.45	-1.75	-3.51	-0.11	0.83	1.47
$\sin(\chi_2)$	0.24	3.28	-1.53	-0.62	-2.58	-1.54	-2.71	-0.24	0.35	1.21
$\cos(\chi_3)$	0.14	-0.13	0.42	-1.90	3.25	-1.04	-1.32	-0.18	6.72	0.59
$\sin(\chi_3)$	0.04	0.35	-1.65	2.78	4.58	-3.16	7.37	12.22	30.94	22.77
$\cos(\chi_4)$	0.20	0.54	3.74	2.53	-0.54	-4.11	4.30	-2.30	1.02	-2.02
$\sin(\chi_4)$	0.07	-0.39	0.53	1.11	0.64	4.14	-3.15	0.35	0.18	1.17
$\cos(\chi_5)$	-0.00	-0.24	-1.36	2.69	1.30	-1.90	-1.23	3.45	-0.59	-1.72
$\sin(\chi_5)$	-0.57	1.46	-1.16	1.86	-4.50	-1.74	-1.88	-7.17	2.87	2.53

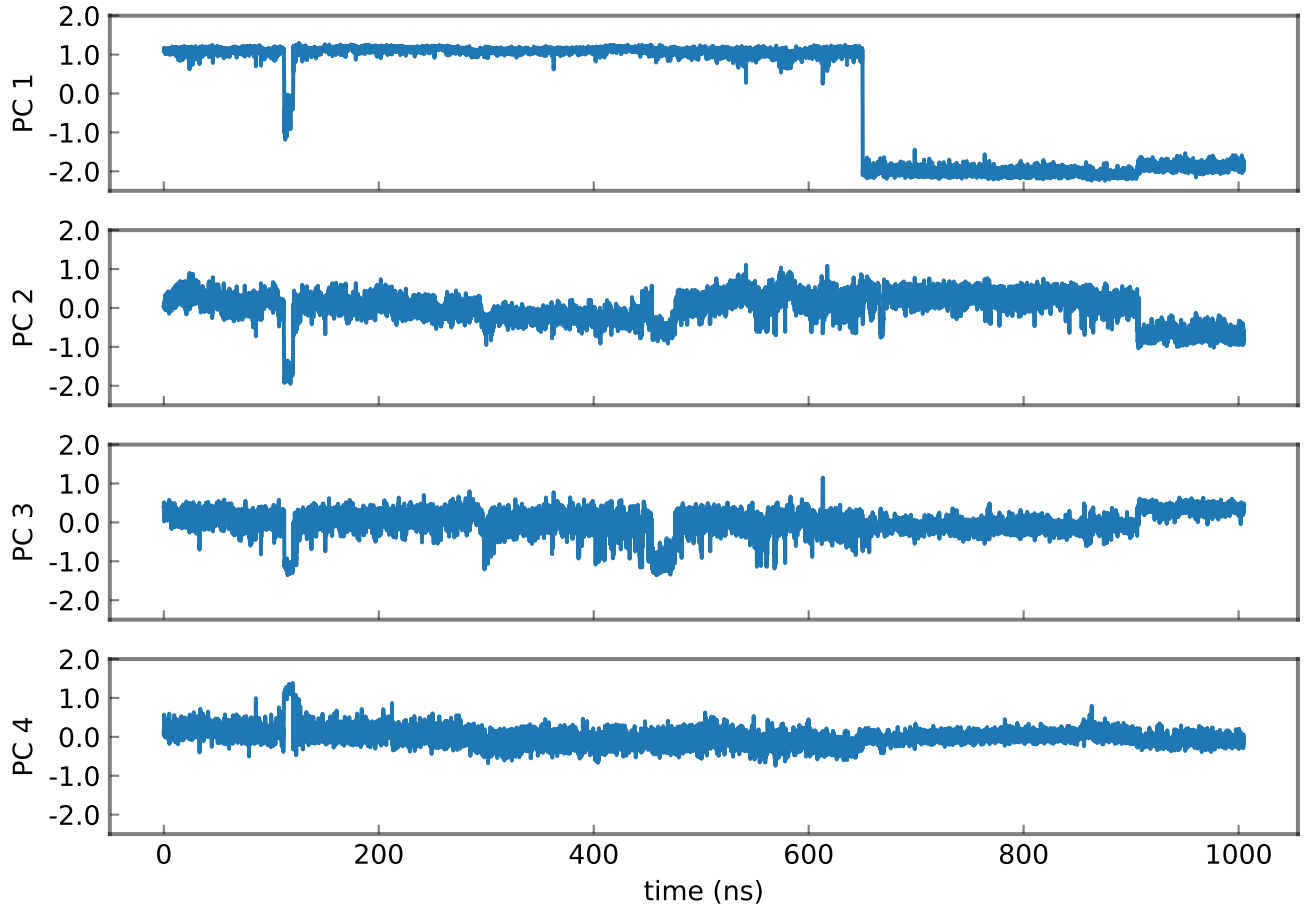

Figure C.2.: Projections of the MD trajectory onto the first four principal components (PC1–PC4) obtained from the PCA. Compared to the first component, higher components display moderate fluctuations and several smaller transitions over the course of the simulation, indicating that these components represent higher-frequency or less collective motions of the system.

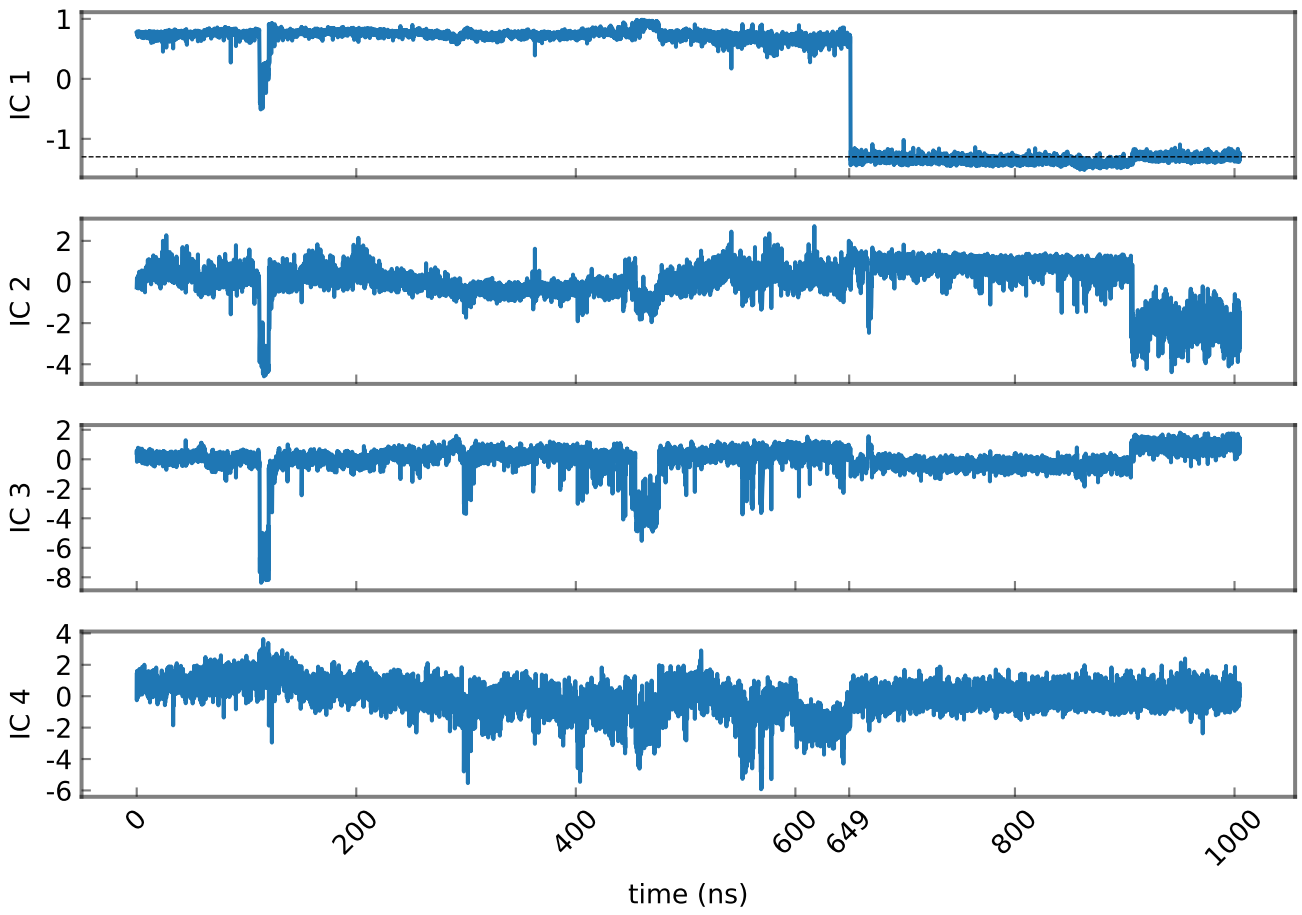

Figure C.3.: Projections of the molecular dynamics trajectory onto the first four independent components (IC1–IC4) obtained from the tICA. The first component shows a clear two-state transition, while the higher components display smaller fluctuations and intermittent transitions, corresponding to faster or less dominant dynamical processes in the system.

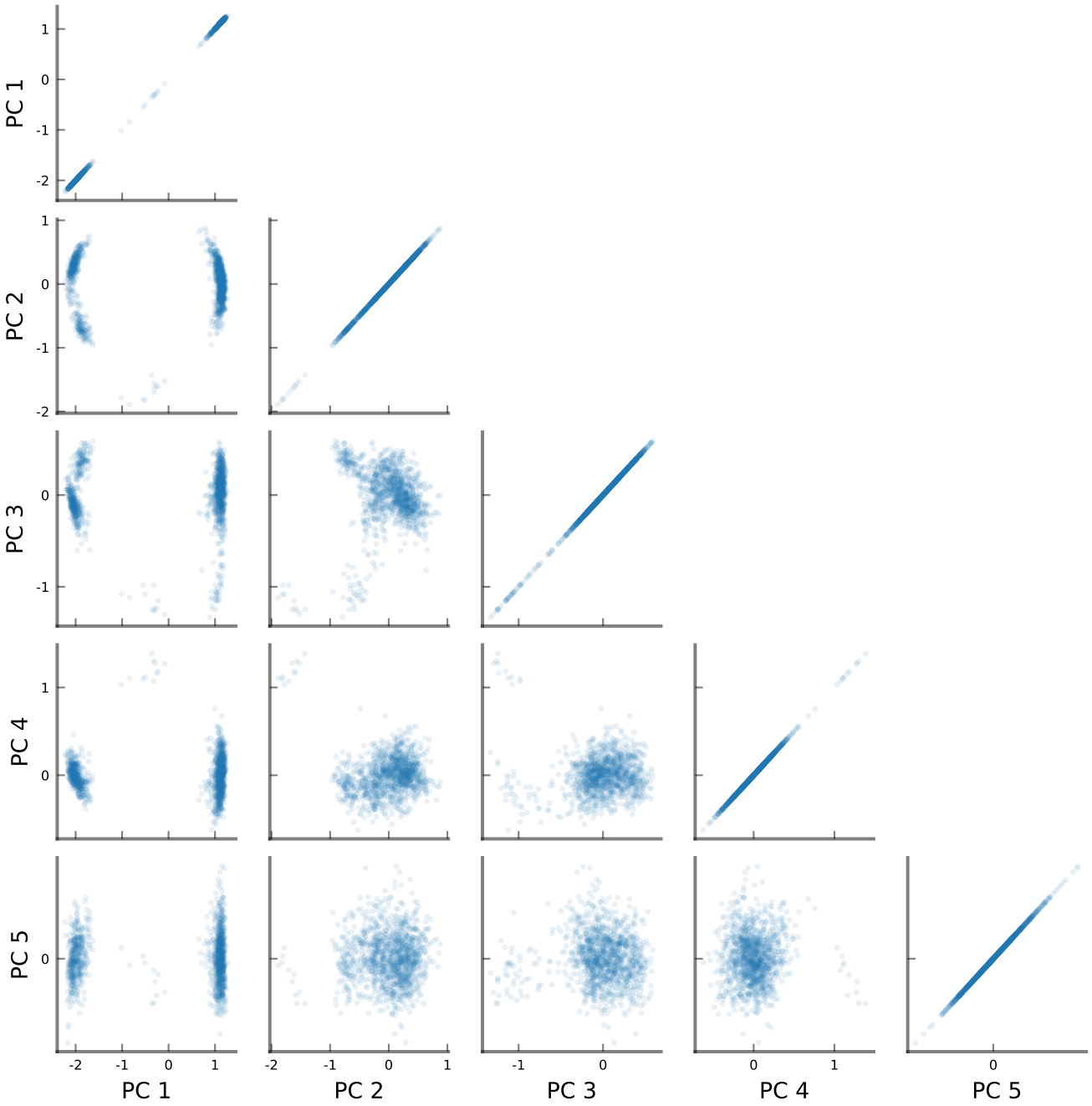

Figure C.4.: Pairwise scatter plots of the first five principal components obtained from the PCA. Distinct separation is observed only for projections involving PC1, while the remaining component pairs form diffuse, isotropic distributions, indicating that most structural variance is captured by the first principal component.

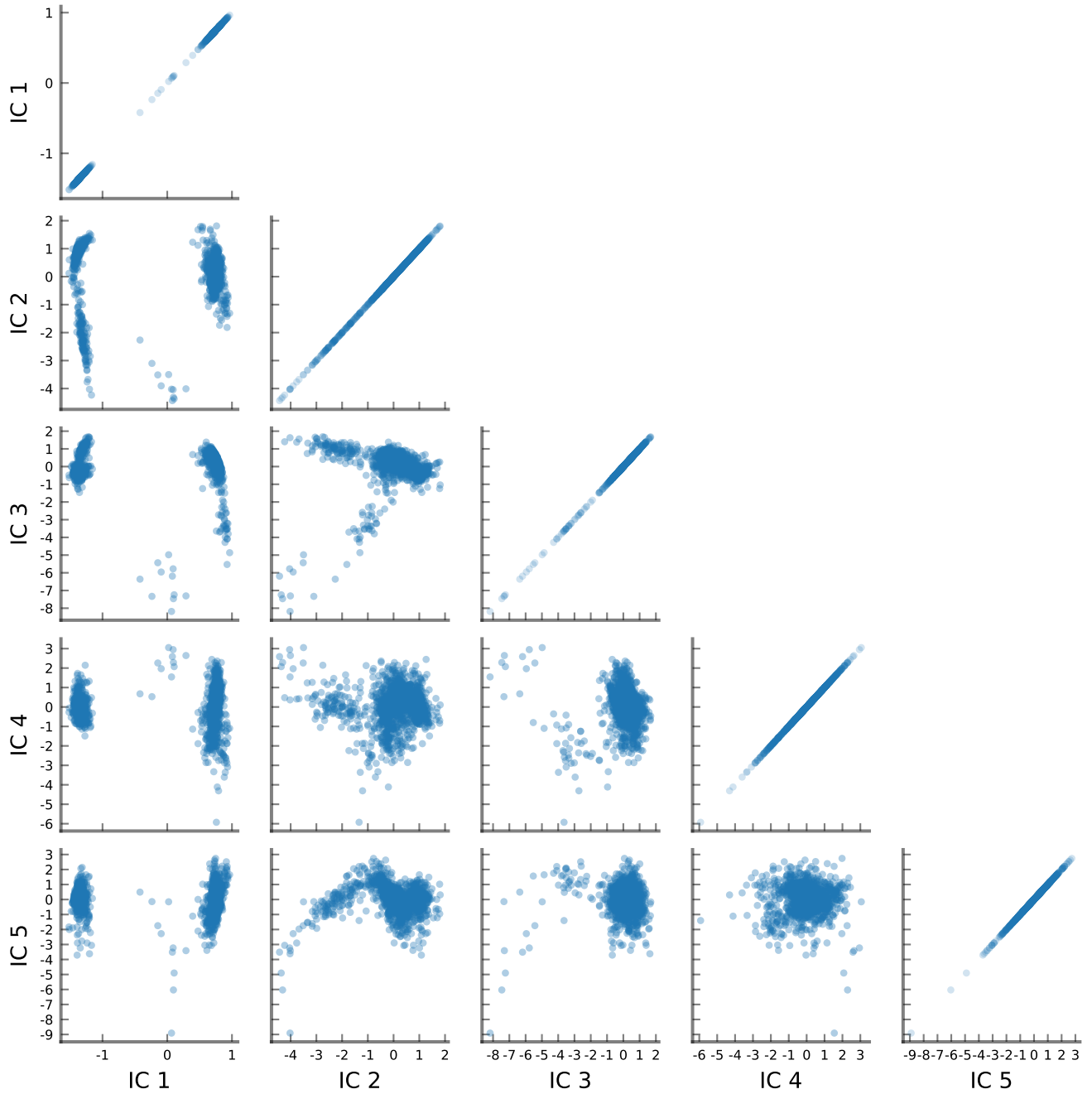

Figure C.5.: Pairwise scatter plots of the first five independent components obtained from the tICA. Clear separation between two states is observed in plots involving IC1, while the remaining component pairs form diffuse or overlapping distributions, indicating that the dominant slow process is primarily captured by the first independent component.

	IC1	normal	PC1	mean
$\cos(\chi_1)$	-0.22	-0.30	-0.44	-0.49
$\sin(\chi_1)$	0.13	0.17	0.30	-0.32
$\cos(\chi_2)$	0.22	0.29	0.36	0.16
$\sin(\chi_2)$	0.24	0.32	0.47	0.28
$\cos(\chi_3)$	0.14	0.19	0.02	0.15
$\sin(\chi_3)$	0.04	0.05	-0.01	0.97
$\cos(\chi_4)$	0.20	0.27	0.01	-0.91
$\sin(\chi_4)$	0.07	0.09	0.15	0.07
$\cos(\chi_5)$	0.00	-0.01	0.02	0.37
$\sin(\chi_5)$	-0.57	-0.76	-0.59	-0.24

Table C.3.: Comparison of the feature weights for the IC1 from tICA and the PC1 from PCA. Note that IC1 values were normalized, as the independent component does not have unit norm by default. The listed coefficients correspond to the trigonometric components of the dihedral angles χ_i ($i = 1$–5). Both vectors have a high cosine similarity and correlation values (approximately 0.9).

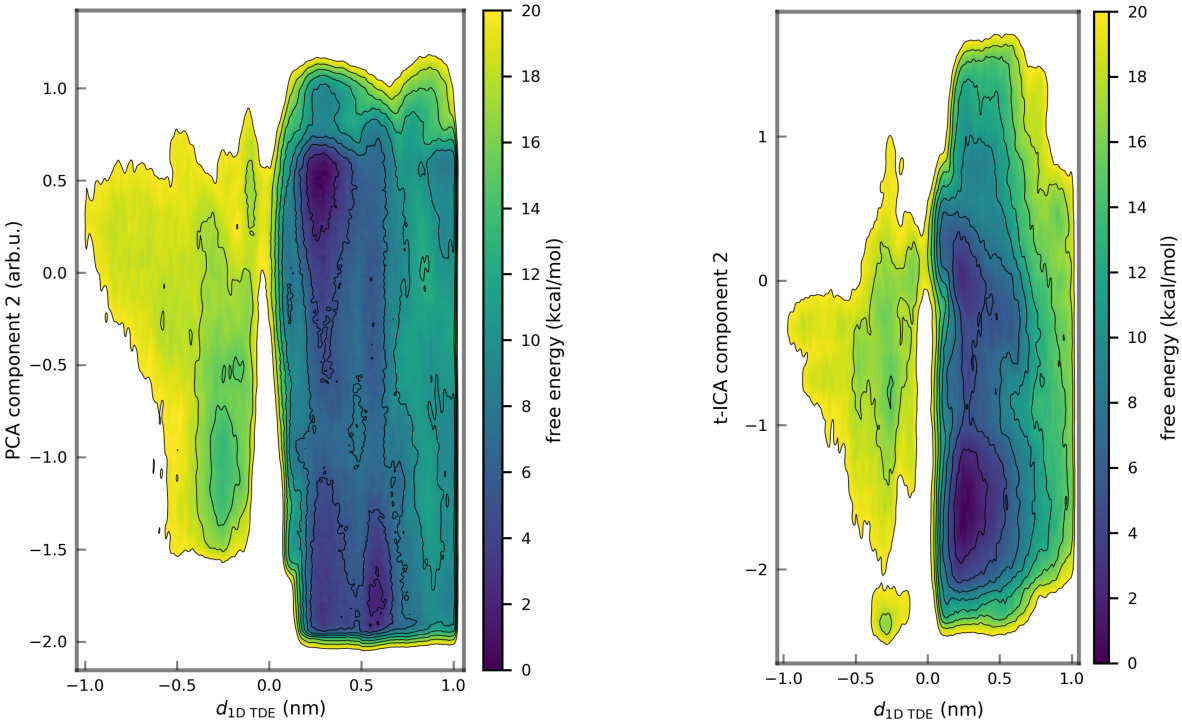

Figure C.6.: FES obtained from MTD simulations using PC2 (left) and IC2 (right) as the second CV.

Bibliography

[1] G. S. Adair, A. V. Bock, and H. Field. “THE HEMOGLOBIN SYSTEM: VI. THE OXYGEN DISSOCIATION CURVE OF HEMOGLOBIN”. In: *Journal of Biological Chemistry* 63.2 (Mar. 1925), pp. 529–545.

[2] Igor A. Lavrinenko, Gennady A. Vashanov, and Yury D. Nechipurenko. “Study of hemoglobin by G. S. Adair and his oxygenation equation: background, history, and significance—on the 100th anniversary of Adair’s equation”. In: *Biophysical Reviews* (Aug. 2025).

[3] J. C. Kendrew et al. “A Three-Dimensional Model of the Myoglobin Molecule Obtained by X-Ray Analysis”. In: *Nature* 181.4610 (Mar. 1958), pp. 662–666.

[4] Peter Y. Chou and Gerald D. Fasman. “Prediction of protein conformation”. In: *Biochemistry* 13.2 (Jan. 1974), pp. 222–245.

[5] B. J. Alder and T. E. Wainwright. “Phase Transition for a Hard Sphere System”. In: *The Journal of Chemical Physics* 27.5 (Nov. 1957), pp. 1208–1209.

[6] Scott A. Hollingsworth and Ron O. Dror. “Molecular Dynamics Simulation for All”. In: *Neuron* 99.6 (Sept. 2018), pp. 1129–1143.

[7] Alexandre Ambrogelly, Sotiria Palioura, and Dieter Söll. “Natural expansion of the genetic code”. In: *Nature Chemical Biology* 3.1 (Jan. 2007), pp. 29–35.

[8] Roman A. Laskowski, James D. Watson, and Janet M. Thornton. “From protein structure to biochemical function?” In: *Journal of Structural and Functional Genomics* 4.2 (June 2003), pp. 167–177.

[9] David Lee, Oliver Redfern, and Christine Orengo. “Predicting protein function from sequence and structure”. In: *Nature Reviews Molecular Cell Biology* 8.12 (Dec. 2007), pp. 995–1005.

[10] Nikolaos Louros, Joost Schymkowitz, and Frederic Rousseau. “Mechanisms and pathology of protein misfolding and aggregation”. In: *Nature Reviews Molecular Cell Biology* 24.12 (Dec. 2023), pp. 912–933.

[11] Nigel Goldenfeld and Leo P. Kadanoff. “Simple Lessons from Complexity”. In: *Science* 284.5411 (Apr. 1999), pp. 87–89.

[12] Gregory C. Finnigan et al. “Evolution of increased complexity in a molecular machine”. In: *Nature* 481.7381 (Jan. 2012), pp. 360–364.

[13] Richard N. McLaughlin Jr et al. “The spatial architecture of protein function and adaptation”. In: *Nature* 491.7422 (Nov. 2012), pp. 138–142.

[14] P. J. Hogg. “Contribution of allosteric disulfide bonds to regulation of hemostasis”. In: *Journal of Thrombosis and Haemostasis* 7.s1 (2009), pp. 13–16.

[15] Kyungho Kim et al. “Platelet protein disulfide isomerase is required for thrombus formation but not for hemostasis in mice”. In: *Blood* 122.6 (Aug. 2013), pp. 1052–1061.

[16] Diego Butera and Philip J. Hogg. “Fibrinogen function achieved through multiple covalent states”. In: *Nature Communications* 11.1 (Oct. 2020), p. 5468.

[17] Chuanliu Wu et al. “Interplay of Chemical Microenvironment and Redox Environment on Thiol–Disulfide Exchange Kinetics”. In: *Chemistry – A European Journal* 17.36 (2011), pp. 10064–10070.

[18] Wenbo Zhang et al. “Intra- and inter-protein couplings of backbone motions underlie protein thiol-disulfide exchange cascade”. In: *Scientific Reports* 8.1 (Oct. 2018), p. 15448.

[19] Mathivanan Chinnaraj, Robert Flaumenhaft, and Nicola Pozzi. “Reduction of protein disulfide isomerase results in open conformations and stimulates dynamic exchange between structural ensembles”. In: *Journal of Biological Chemistry* 298.8 (Aug. 2022).

[20] Vishal Annasaheb Adhav and Kayarat Saikrishnan. “The Realm of Unconventional Noncovalent Interactions in Proteins: Their Significance in Structure and Function”. In: *ACS Omega* 8.25 (June 2023), pp. 22268–22284.

[21] Ana-Nicoleta Bondar. “Graphs of Hydrogen-Bond Networks to Dissect Protein Conformational Dynamics”. In: *The Journal of Physical Chemistry B* 126.22 (June 2022), pp. 3973–3984.

[22] Eleanor Campbell et al. “The role of protein dynamics in the evolution of new enzyme function”. In: *Nature Chemical Biology* 12.11 (Nov. 2016), pp. 944–950.

[23] Daniele Sonaglioni et al. “Dynamic Personality of Proteins and Effect of the Molecular Environment”. In: *The Journal of Physical Chemistry Letters* 15.20 (May 2024), pp. 5543–5548.

[24] Werner Kühlbrandt. “Structure and Mechanisms of F-Type ATP Synthases”. In: *Annual Review of Biochemistry* 88 (June 2019), pp. 515–549.

[25] Hui Guo and John L. Rubinstein. “Structure of ATP synthase under strain during catalysis”. In: *Nature Communications* 13.1 (Apr. 2022), p. 2232.

[26] Gregory A. Petsko and Dagmar Ringe. *Protein Structure and Function*. Oxford: Oxford University Press, 2004.

[27] Peter J. Bickel et al. “Finding important sites in protein sequences”. In: *Proceedings of the National Academy of Sciences* 99.23 (Nov. 2002), pp. 14764–14771.

[28] Alexandra Shulman-Peleg, Ruth Nussinov, and Haim J. Wolfson. “Recognition of Functional Sites in Protein Structures”. In: *Journal of Molecular Biology* 339.3 (June 2004), pp. 607–633.

[29] Matthew C Zwier and Lillian T Chong. “Reaching biological timescales with all-atom molecular dynamics simulations”. In: *Current Opinion in Pharmacology*. Endocrine and metabolic diseases/New technologies - the importance of protein dynamics 10.6 (Dec. 2010), pp. 745–752.

[30] Andreas Kukol, ed. *Molecular Modeling of Proteins*. Vol. 1215. Methods in Molecular Biology. New York, NY: Springer New York, 2015.

[31] Trygve Helgaker, Poul Jørgensen, and Jeppe Olsen. *Molecular Electronic-Structure Theory*. Chichester: Wiley, 2000.

[32] Anders S. Christensen et al. “Semiempirical Quantum Mechanical Methods for Noncovalent Interactions for Chemical and Biochemical Applications”. In: *Chemical Reviews* 116.9 (May 2016), pp. 5301–5337.

[33] W. G. Noid. “Perspective: Coarse-grained models for biomolecular systems”. In: *The Journal of Chemical Physics* 139.9 (Sept. 2013), p. 090901.

[34] A. Warshel and M. Levitt. “Theoretical studies of enzymic reactions: Dielectric, electrostatic and steric stabilization of the carbonium ion in the reaction of lysozyme”. In: *Journal of Molecular Biology* 103.2 (May 1976), pp. 227–249.

[35] Hans Martin Senn and Walter Thiel. “QM/MM Methods for Biomolecular Systems”. In: *Angewandte Chemie International Edition* 48.7 (2009), pp. 1198–1229.

[36] Marc W. van der Kamp and Adrian J. Mulholland. “Combined Quantum Mechanics/Molecular Mechanics (QM/MM) Methods in Computational Enzymology”. In: *Biochemistry* 52.16 (Apr. 2013), pp. 2708–2728.

[37] Xiya Lu et al. “QM/MM free energy simulations: recent progress and challenges”. In: *Molecular Simulation* 42.13 (Sept. 2016), pp. 1056–1078.

[38] Katja-Sophia Csizi and Markus Reiher. “Universal QM/MM approaches for general nanoscale applications”. In: *WIREs Computational Molecular Science* 13.4 (2023), e1656.

[39] Yonathan Lissanu Deribe, Tony Pawson, and Ivan Dikic. “Post-Translational Modifications in Signal Integration”. In: *Nat Struct Mol Biol* 17.6 (6 2010), pp. 666–672.

[40] Shahin Ramazi and Javad Zahiri. “Post-Translational Modifications in Proteins: Resources, Tools and Prediction Methods”. In: *Database* 2021 (2021), baab012.

[41] Deborah Fass and Colin Thorpe. “Chemistry and Enzymology of Disulfide Cross-Linking in Proteins”. In: *Chem. Rev.* 118.3 (2018), pp. 1169–1198.

[42] William J. Wedemeyer et al. “Disulfide Bonds and Protein Folding”. In: *Biochemistry* 39.15 (2000), pp. 4207–4216.

[43] Yu. M. Torchinskii. *Sulfhydryl and Disulfide Groups of Proteins*. Boston, MA: Springer US, 1974.

[44] Keith Brocklehurst and Marek P. J. Kierstan. “Propapain and Its Conversion to Papain: A New Type of Zymogen Activation Mechanism Involving Intramolecular Thiol-Disulphide Interchange”. In: *Nature New Biology* 242.119 (119 1973), pp. 167–170.

[45] Mitsuhiro Okamoto and Yoshimasa Morino. “Affinity Labeling of Aspartate Aminotransferase Isozymes by Bromopyruvate”. In: *Journal of Biological Chemistry* 248.1 (1973-01-10), pp. 82–90.

[46] Philip Hogg. *Functional Disulphide Bonds: Methods and Protocols*. Humana New York, NY, 2019.

[47] Hiram F. Gilbert. “[2] Thiol/Disulfide Exchange Equilibria and Disulfidebond Stability”. In: *Methods in Enzymology*. Vol. 251. Biothiols Part A Monothiols and Dithiols, Protein Thiols, and Thiyl Radicals. Academic Press, 1995, pp. 8–28.

[48] Robert B. Freedman. “How Many Distinct Enzymes Are Responsible for the Several Cellular Processes Involving Thiol:Protein-Disulphide Interchange?” In: *FEBS Letters* 97.2 (1979), pp. 201–210.

[49] Glenn Dranoff. “Targets of Protective Tumor Immunity”. In: *Annals of the New York Academy of Sciences* 1174.1 (2009), pp. 74–80.

[50] Pedro Alexandrino Fernandes and Maria João Ramos. “Theoretical Insights into the Mechanism for Thiol/Disulfide Exchange”. In: *Chemistry – A European Journal* 10.1 (2004), pp. 257–266.

[51] Péter Nagy. “Kinetics and Mechanisms of Thiol–Disulfide Exchange Covering Direct Substitution and Thiol Oxidation-Mediated Pathways”. In: *Antioxidants & Redox Signaling* 18.13 (2013-05), pp. 1623–1641.

[52] Marina Putzu et al. “On the Mechanism of Spontaneous Thiol–Disulfide Exchange in Proteins”. In: *Phys. Chem. Chem. Phys.* 20.23 (2018), pp. 16222–16230.

[53] Zhiyong Cheng et al. “Reactivity of Thioredoxin as a Protein Thiol-Disulfide Oxidoreductase”. In: *Chem. Rev.* 111.9 (2011-09-14), pp. 5768–5783.

[54] Marcel Deponte. “Glutathione Catalysis and the Reaction Mechanisms of Glutathione-Dependent Enzymes”. In: *Biochimica et Biophysica Acta (BBA) - General Subjects*. Cellular Functions of Glutathione 1830.5 (2013), pp. 3217–3266.

[55] Yuan Qi and Nick V. Grishin. “Structural Classification of Thioredoxin-like Fold Proteins”. In: *Proteins: Structure, Function, and Bioinformatics* 58.2 (2005), pp. 376–388.

[56] Jonathan D. Gough et al. “Folding Disulfide-Containing Proteins Faster with an Aromatic Thiol”. In: *J. Am. Chem. Soc.* 124.15 (2002-04-01), pp. 3885–3892.

[57] Luis Eduardo S. Netto et al. “Conferring Specificity in Redox Pathways by Enzymatic Thiol/Disulfide Exchange Reactions”. In: *Free Radic. Res.* 50.2 (2016), pp. 206–245.

[58] Fredrik Åslund et al. “Glutaredoxin-3 from Escherichia Coli: AMINO ACID SEQUENCE, 1H AND 15N NMR ASSIGNMENTS, AND STRUCTURAL ANALYSIS”. In: *Journal of Biological Chemistry* 271.12 (1996-03-22), pp. 6736–6745.

[59] Jennifer L Martin. “Thioredoxin —a Fold for All Reasons”. In: *Structure* 3.3 (1995-03-01), pp. 245–250.

[60] A. Holmgren. “Thioredoxin and Glutaredoxin Systems”. In: *J Biol Chem* 264.24 (1989-08-25), pp. 13963–13966.

[61] Hideaki Kamata and Hajime Hirata. “Redox Regulation of Cellular Signalling”. In: *Cellular Signalling* 11.1 (1999-01-01), pp. 1–14.

[62] Ashwinie A. Ukuwela et al. “Glutaredoxins Employ Parallel Monothiol–Dithiol Mechanisms to Catalyze Thiol–Disulfide Exchanges with Protein Disulfides”. In: *Chem. Sci.* 9.5 (2018), pp. 1173–1183.

[63] Fernando T. Ogata et al. “Glutaredoxin: Discovery, Redox Defense and Much More”. In: *Redox Biology* 43 (2021), p. 101975.

[64] Robert D. Bach, Olga Dmitrenko, and Colin Thorpe. “Mechanism of thiolate-disulfide interchange reactions in biochemistry”. In: *The Journal of Organic Chemistry* 73.1 (Jan. 2008), pp. 12–21.

[65] Steven M. Bachrach and Debbie C. Mulhearn. “Nucleophilic Substitution at Sulfur: SN2 or Addition-Elimination”. In: *The Journal of Physical Chemistry* 100.9 (Jan. 1996), pp. 3535–3540.

[66] Manikandan Paranjothy et al. “Mechanism of Thiolate-Disulfide Exchange: Addition–Elimination or Effectively SN2? Effect of a Shallow Intermediate in Gas-Phase Direct Dynamics Simulations”. In: *The Journal of Physical Chemistry A* 116.47 (Nov. 2012), pp. 11492–11499.

[67] Marco Bortoli et al. “Addition–Elimination or Nucleophilic Substitution? Understanding the Energy Profiles for the Reaction of Chalcogenolates with Dichalcogenides”. In: *J. Chem. Theory Comput.* 12.6 (2016), pp. 2752–2761.

[68] Martina Wunderlich, Rainer Jaenicke, and Rudi Glockshuber. “The Redox Properties of Protein Disulfide Isomerase (DsbA) of Escherichia Coli Result from a Tense Conformation of Its Oxidized Form”. In: *Journal of Molecular Biology* 233.4 (1993), pp. 559–566.

[69] N. Srinivasan et al. “Conformations of Disulfide Bridges in Proteins”. In: *International Journal of Peptide and Protein Research* 36.2 (1990), pp. 147–155.

[70] Maurice L. Huggins. “The Structure of Fibrous Proteins.” In: *Chemical Reviews* 32.2 (Apr. 1943), pp. 195–218.

[71] Linus Pauling, Robert B. Corey, and H. R. Branson. “The structure of proteins: Two hydrogen-bonded helical configurations of the polypeptide chain”. In: *Proceedings of the National Academy of Sciences* 37.4 (Apr. 1951), pp. 205–211.

[72] Alan R. Fersht et al. “Hydrogen bonding and biological specificity analysed by protein engineering”. In: *Nature* 314.6008 (Mar. 1985), pp. 235–238.

[73] George A. Jeffrey. *An Introduction to Hydrogen Bonding*. Oxford, U.K.: Oxford University Press, 1997.

[74] Hideaki Umeyama and Keiji Morokuma. “The origin of hydrogen bonding. An energy decomposition study”. In: *Journal of the American Chemical Society* 99.5 (Mar. 1977), pp. 1316–1332.

[75] Stephanie C. C. van der Lubbe and Célia Fonseca Guerra. “The Nature of Hydrogen Bonds: A Delineation of the Role of Different Energy Components on Hydrogen Bond Strengths and Lengths”. In: *Chemistry – An Asian Journal* 14.16 (2019), pp. 2760–2769.

[76] George N. Pairas and Petros G. Tsoungas. “H-Bond: The Chemistry-Biology H-Bridge”. In: *ChemistrySelect* 1.15 (2016), pp. 4520–4532.

[77] Tamar Schlick. *Molecular Modeling and Simulation: An Interdisciplinary Guide*. 2nd ed. New York: Springer, 2010.

[78] N. S. Punekar. *Enzymes: Catalysis, Kinetics and Mechanisms*. Singapore: Springer Nature Singapore, 2018.

[79] Gordon G. Hammes, Stephen J. Benkovic, and Sharon Hammes-Schiffer. "Flexibility, Diversity, and Cooperativity: Pillars of Enzyme Catalysis". In: *Biochemistry* 50.48 (Dec. 2011), pp. 10422–10430.

[80] Daniel Herschlag and Aditya Natarajan. "Fundamental Challenges in Mechanistic Enzymology: Progress toward Understanding the Rate Enhancements of Enzymes". In: *Biochemistry* 52.12 (Mar. 2013), pp. 2050–2067.

[81] N. S. Golubev et al. "The role of short hydrogen bonds in mechanisms of enzymatic action". In: *Journal of Molecular Structure*. HORIZONS IN HYDROGEN BOND RESEARCH 1993 Proceedings of the Xth Workshop \ldHorizons in Hydrogen Bond Research\rd, 322 (June 1994), pp. 83–91.

[82] Daniel Herschlag and Margaux M. Pinney. "Hydrogen Bonds: Simple after All?" In: *Biochemistry* 57.24 (June 2018), pp. 3338–3352.

[83] Kumari Soniya and Amalendu Chandra. "Free energy landscapes of prototropic tautomerism in pyridoxal 5'-phosphate schiff bases at the active site of an enzyme in aqueous medium". In: *Journal of Computational Chemistry* 39.21 (2018), pp. 1629–1638.

[84] Philip Hanoian et al. "Perspectives on Electrostatics and Conformational Motions in Enzyme Catalysis". In: *Accounts of Chemical Research* 48.2 (Feb. 2015), pp. 482–489.

[85] Elinor Erez, Deborah Fass, and Eitan Bibi. "How intramembrane proteases bury hydrolytic reactions in the membrane". In: *Nature* 459.7245 (May 2009), pp. 371–378.

[86] Ofer Rahat et al. "Understanding hydrogen-bond patterns in proteins using network motifs". In: *Bioinformatics* 25.22 (Nov. 2009), pp. 2921–2928.

[87] Lydia Nisius and Stephan Grzesiek. "Key stabilizing elements of protein structure identified through pressure and temperature perturbation of its hydrogen bond network". In: *Nature Chemistry* 4.9 (Sept. 2012), pp. 711–717.

[88] Hiroshi Ishikita and Keisuke Saito. "Proton transfer reactions and hydrogen-bond networks in protein environments". In: *Journal of The Royal Society Interface* 11.91 (Feb. 2014), p. 20130518.

[89] Malte Siemers et al. "Bridge: A Graph-Based Algorithm to Analyze Dynamic H-Bond Networks in Membrane Proteins". In: *Journal of Chemical Theory and Computation* 15.12 (Dec. 2019), pp. 6781–6798.

[90] Michalis Lazaratos, Konstantina Karathanou, and Ana-Nicoleta Bondar. "Graphs of dynamic H-bond networks: from model proteins to protein complexes in cell signaling". In: *Current Opinion in Structural Biology*. Biophysical and Computational Methods Cryo EM 64 (Oct. 2020), pp. 79–87.

[91] Masayoshi Nakasako. "Network of Hydrogen Bonds Around Proteins". In: *Hydration Structures of Proteins*. Ed. by Masayoshi Nakasako. Soft and Biological Matter. Springer, 2021, pp. 163–182.

[92] Jiří Černý and Pavel Hobza. "Non-covalent interactions in biomacromolecules". en. In: *Physical Chemistry Chemical Physics* 9.39 (2007), pp. 5291–5303.

[93] Anders S. Christensen et al. "Intermolecular interactions in the condensed phase: Evaluation of semiempirical quantum mechanical methods". In: *The Journal of Chemical Physics* 147.16 (Oct. 2017).

[94] Ruben Santamaria. *Molecular Dynamics*. Cham, Switzerland: Springer Nature Switzerland AG, 2023.

[95] Andrew R. Leach. *Molecular Modelling: Principles and Applications*. 2nd ed. Harlow, England: Prentice Hall, 2001.

[96] Frank Jensen. *Introduction to Computational Chemistry*. Third edition. Chichester, UK ; Hoboken, NJ: John Wiley & Sons, 2017. 638 pp.

[97] Harold C. Urey and Charles A. Bradley. “The Vibrations of Pentatonic Tetrahedral Molecules”. In: *Phys. Rev.* 38 (11 Dec. 1931), pp. 1969–1978.

[98] Matthias Buck et al. “Importance of the CMAP Correction to the CHARMM22 Protein Force Field: Dynamics of Hen Lysozyme”. In: *Biophysical Journal* 90.4 (Feb. 2006), pp. L36–L38.

[99] Wei Kang, Fan Jiang, and Yun-Dong Wu. “Universal Implementation of a Residue-Specific Force Field Based on CMAP Potentials and Free Energy Decomposition”. In: *Journal of Chemical Theory and Computation* 14.8 (Aug. 2018), pp. 4474–4486.

[100] Wendy D. Cornell et al. “A Second Generation Force Field for the Simulation of Proteins, Nucleic Acids, and Organic Molecules”. In: *Journal of the American Chemical Society* 117.19 (May 1995), pp. 5179–5197.

[101] Alexander D. MacKerell et al. “All-Atom Empirical Potential for Molecular Modeling and Dynamics Studies of Proteins”. In: *Journal of Physical Chemistry B* 102 (1998), pp. 3586–3616.

[102] Jay W. Ponder et al. “Current Status of the AMOEBA Polarizable Force Field”. In: *The Journal of Physical Chemistry B* 114.8 (Mar. 2010), pp. 2549–2564.

[103] Adri C. T. van Duin et al. “ReaxFF: A Reactive Force Field for Hydrocarbons”. In: *Journal of Physical Chemistry A* 105 (2001), pp. 9396–9409.

[104] Siewert J. Marrink et al. “The MARTINI Force Field: Coarse Grained Model for Biomolecular Simulations”. In: *Journal of Physical Chemistry B* 111 (2007), pp. 7812–7824.

[105] Petra Florová et al. “Explicit Water Models Affect the Specific Solvation and Dynamics of Unfolded Peptides While the Conformational Behavior and Flexibility of Folded Peptides Remain Intact”. In: *Journal of Chemical Theory and Computation* 6.11 (Nov. 2010), pp. 3569–3579.

[106] Saeed Izadi, Ramu Anandakrishnan, and Alexey V. Onufriev. “Building Water Models: A Different Approach”. In: *The Journal of Physical Chemistry Letters* 5.21 (Nov. 2014), pp. 3863–3871.

[107] Alexey V. Onufriev and Saeed Izadi. “Water models for biomolecular simulations”. In: *WIREs Computational Molecular Science* 8.2 (2018), e1347.

[108] Sachini P. Kadaoluwa Pathirannahalage et al. “Systematic Comparison of the Structural and Dynamic Properties of Commonly Used Water Models for Molecular Dynamics Simulations”. In: *Journal of Chemical Information and Modeling* 61.9 (Sept. 2021), pp. 4521–4536.

[109] Chulwoo Park, Ferlin Robinson, and Daejoong Kim. “On the Choice of Different Water Model in Molecular Dynamics Simulations of Nanopore Transport Phenomena”. In: *Membranes* 12.11 (Nov. 2022), p. 1109.

[110] Chuan Tian et al. “ff19SB: Amino-Acid-Specific Protein Backbone Parameters Trained against Quantum Mechanics Energy Surfaces in Solution”. In: *Journal of Chemical Theory and Computation* 16.1 (Jan. 2020), pp. 528–552.

[111] P. Hohenberg and W. Kohn. “Inhomogeneous Electron Gas”. In: *Phys. Rev.* 136 (3B 1964-11-09), B864–B871.

[112] Wolfram Koch and Max C. Holthausen. *A Chemist’s Guide to Density Functional Theory*. 2nd ed. Weinheim: Wiley-VCH, 2001.

[113] John P. Perdew and Karla Schmidt. “Jacob’s Ladder of Density Functional Approximations for the Exchange–Correlation Energy”. In: *AIP Conference Proceedings*. Vol. 577. 1. AIP, 2001, pp. 1–20.

[114] Markus Bursch et al. “Best-Practice DFT Protocols for Basic Molecular Computational Chemistry**”. In: *Angewandte Chemie International Edition* 61.42 (2022), e202205735.

[115] Van-Quan Vuong and Qiang Cui. “Reparameterization of the chemical-potential equalization model with DFTB3: A practical balance between accuracy and transferability”. In: *The Journal of Chemical Physics* 158.6 (Feb. 2023), p. 064111.

[116] Michael Gaus, Qiang Cui, and Marcus Elstner. “Density Functional Tight Binding: Application to Organic and Biological Molecules”. In: *WIREs Comput Mol Sci* 4.1 (2014), pp. 49–61.

[117] G Seifert, H Eschrig, and W Bieger. “An Approximation Variant of LCAO-X-ALPHA Methods”. In: *Zeitschrift Fur Physikalische Chemie-Leipzig* 267.3 (1986), pp. 529–539.

[118] Gotthard Seifert and Jan-Ole Joswig. “Density-Functional Tight Binding—an Approximate Density-Functional Theory Method”. In: *WIREs Computational Molecular Science* 2.3 (2012), pp. 456–465.

[119] D. Porezag et al. “Construction of tight-binding-like potentials on the basis of density-functional theory: Application to carbon”. In: *Physical Review B* 51.19 (May 1995), pp. 12947–12957.

[120] M. Elstner et al. “Self-Consistent-Charge Density-Functional Tight-Binding Method for Simulations of Complex Materials Properties”. In: *Phys. Rev. B* 58.11 (1998), pp. 7260–7268.

[121] Marcus Elstner and Gotthard Seifert. “Density Functional Tight Binding”. In: *Philosophical Transactions of the Royal Society A: Mathematical, Physical and Engineering Sciences* 372.2011 (2014-03-13), p. 20120483.

[122] Michael Gaus, Qiang Cui, and Marcus Elstner. “DFTB3: Extension of the Self-Consistent-Charge Density-Functional Tight-Binding Method (SCC-DFTB)”. In: *Journal of Chemical Theory and Computation* 7.4 (Apr. 2011), pp. 931–948.

[123] Michael Gaus, Albrecht Goez, and Marcus Elstner. “Parametrization and Benchmark of DFTB3 for Organic Molecules”. In: *Journal of Chemical Theory and Computation* 9.1 (Jan. 2013), pp. 338–354.

[124] Michael Gaus et al. “Parameterization of DFTB3/3OB for Sulfur and Phosphorus for Chemical and Biological Applications”. In: *Journal of Chemical Theory and Computation* 10.4 (Apr. 2014), pp. 1518–1537.

[125] Xiya Lu et al. “Parametrization of DFTB3/3OB for Magnesium and Zinc for Chemical and Biological Applications”. In: *The Journal of Physical Chemistry B* 119.3 (Jan. 2015), pp. 1062–1082.

[126] Maximilian Kubillus et al. “Parameterization of the DFTB3 Method for Br, Ca, Cl, F, I, K, and Na in Organic and Biological Systems”. In: *Journal of Chemical Theory and Computation* 11.1 (Jan. 2015), pp. 332–342.

[127] Qiang Cui, Tanmoy Pal, and Luke Xie. “Biomolecular QM/MM Simulations: What Are Some of the “Burning Issues”?” In: *The Journal of Physical Chemistry B* 125.3 (Jan. 2021), pp. 689–702.

[128] Jan Řezáč and Pavel Hobza. “Advanced Corrections of Hydrogen Bonding and Dispersion for Semiempirical Quantum Mechanical Methods”. In: *Journal of Chemical Theory and Computation* 8.1 (Jan. 2012), pp. 141–151.

[129] Qiang Cui et al. “A QM/MM Implementation of the Self-Consistent Charge Density Functional Tight Binding (SCC-DFTB) Method”. In: *The Journal of Physical Chemistry B* 105.2 (Jan. 2001), pp. 569–585.

[130] Xiya Lu et al. “Regulation and Plasticity of Catalysis in Enzymes: Insights from Analysis of Mechanochemical Coupling in Myosin”. In: *Biochemistry* 56.10 (Mar. 2017), pp. 1482–1497.

[131] Daniel Roston, Darren Demapan, and Qiang Cui. “Extensive free-energy simulations identify water as the base in nucleotide addition by DNA polymerase”. In: *Proceedings of the National Academy of Sciences* 116.50 (Dec. 2019), pp. 25048–25056.

[132] Beatrix M. Bold et al. “Benchmark and performance of long-range corrected time-dependent density functional tight binding (LC-TD-DFTB) on rhodopsins and light-harvesting complexes”. In: *Physical chemistry chemical physics* 22.19 (May 2020), pp. 10500–10518.

[133] Denis Maag et al. “O to bR transition in bacteriorhodopsin occurs through a proton hole mechanism”. In: *Proceedings of the National Academy of Sciences* 118.39 (Sept. 2021), e2024803118.

[134] Junichi Ono, Chika Okada, and Hiromi Nakai. “Hydroxide Ion Mechanism for Long-Range Proton Pumping in the Third Proton Transfer of Bacteriorhodopsin”. In: *ChemPhysChem* 23.22 (2022), e202200109.

[135] Rui Lai, Guohui Li, and Qiang Cui. “Flexibility of Binding Site is Essential to the Ca^{2+} Selectivity in EF-Hand Calcium-Binding Proteins”. In: *Journal of the American Chemical Society* 146.11 (Mar. 2024), pp. 7628–7639.

[136] “Mixed Quantum Mechanical/Molecular Mechanical Molecular Dynamics Simulations of Biological Systems in Ground and Electronically Excited States”. In: *Chemical Reviews* (2015). Ed. by Elizabeth Brunk and Ursula Rothlisberger.

[137] John R. Sabin, Erkki Brändas, and Sylvio Canuto. *Combining Quantum Mechanics and Molecular Mechanics: Some Recent Progresses in QM-MM Methods*. Advances in Quantum Chemistry 59. Amsterdam Boston: Elsevier Academic Press, 2010.

[138] Gérald Monard et al. “Determination of enzymatic reaction pathways using QM/MM methods”. In: *International Journal of Quantum Chemistry* 93.3 (2003), pp. 229–244.

[139] Gerrit Groenhof. “Introduction to QM/MM Simulations”. In: *Biomolecular Simulations*. Ed. by Luca Monticelli and Emppu Salonen. Vol. 924. Methods in Molecular Biology. Totowa, NJ: Humana Press, 2013, pp. 43–66.

[140] Hai Lin and Donald G. Truhlar. “Redistributed Charge and Dipole Schemes for Combined Quantum Mechanical and Molecular Mechanical Calculations”. In: *The Journal of Physical Chemistry A* 109.17 (May 2005), pp. 3991–4004.

[141] Guanhua Hou et al. “A Modified QM/MM Hamiltonian with the Self-Consistent-Charge Density-Functional-Tight-Binding Theory for Highly Charged QM Regions”. In: *Journal of Chemical Theory and Computation* 8.11 (Nov. 2012), pp. 4293–4304.

[142] Patricia Amara and Martin J. Field. “Evaluation of an ab initio quantum mechanical/molecular mechanical hybrid-potential link-atom method”. In: *Theoretical Chemistry Accounts* 109.1 (Feb. 2003), pp. 43–52.

[143] Bo Wang and Donald G. Truhlar. “Including Charge Penetration Effects in Molecular Modeling”. In: *Journal of Chemical Theory and Computation* 6.11 (Nov. 2010), pp. 3330–3342.

[144] G. Andrés Cisneros, Jean-Philip Piquemal, and Thomas A. Darden. “Quantum Mechanics/Molecular Mechanics Electrostatic Embedding with Continuous and Discrete Functions”. In: *The Journal of Physical Chemistry B* 110.28 (July 2006), pp. 13682–13684.

[145] Tomáš Kubař, Kai Welke, and Gerrit Groenhof. “New QM/MM Implementation of the DFTB3 Method in the Gromacs Package”. In: *Journal of Computational Chemistry* 36.26 (2015), pp. 1978–1989.

[146] Mattia Bondanza et al. “Polarizable embedding QM/MM: the future gold standard for complex (bio)systems?” In: *Physical Chemistry Chemical Physics* 22.26 (July 2020), pp. 14433–14448.

[147] Rosa E. Bulo et al. “Toward a Practical Method for Adaptive QM/MM Simulations”. In: *Journal of Chemical Theory and Computation* 5.9 (Sept. 2009), pp. 2212–2221.

[148] Soroosh Pezeshki and Hai Lin. “Recent developments in QM/MM methods towards open-boundary multi-scale simulations”. In: *Molecular Simulation* 41.1-3 (Feb. 2015), pp. 168–189.

[149] Min Zheng and Mark P. Waller. “Adaptive quantum mechanics/molecular mechanics methods”. In: *WIREs Computational Molecular Science* 6.4 (2016), pp. 369–385.

[150] Adam W. Duster et al. “Adaptive quantum/molecular mechanics: what have we learned, where are we, and where do we go from here?” In: *WIREs Computational Molecular Science* 7.5 (2017), e1310.

[151] Hiroshi C. Watanabe and Qiang Cui. “Quantitative Analysis of QM/MM Boundary Artifacts and Correction in Adaptive QM/MM Simulations”. In: *Journal of Chemical Theory and Computation* (May 2019).

[152] Zeng-hui Yang. “On-the-fly determination of active region centers in adaptive-partitioning QM/MM”. In: *Physical Chemistry Chemical Physics* 22.34 (Sept. 2020), pp. 19307–19317.

[153] Jia-Ning Wang et al. “Accelerated Computation of Free Energy Profile at Ab Initio Quantum Mechanical/Molecular Mechanics Accuracy via a Semiempirical Reference Potential. 4. Adaptive QM/MM”. In: *Journal of Chemical Theory and Computation* 17.3 (Mar. 2021), pp. 1318–1325.

[154] Joani Mato et al. “Adaptive-Partitioning Multilayer Dynamics Simulations: 1. On-the-Fly Switch between Two Quantum Levels of Theory”. In: *Journal of chemical theory and computation* 17.9 (Sept. 2021), pp. 5456–5465.

[155] Shengheng Yan, Binju Wang, and Hai Lin. “Reshaping the QM Region On-the-Fly: Adaptive-Shape QM/MM Dynamic Simulations of a Hydrated Proton in Bulk Water”. In: *Journal of Chemical Theory and Computation* 20.9 (May 2024), pp. 3462–3472.

[156] Holden Paz et al. “The Effects of Conformational Sampling and QM Region Size in QM/MM Simulations: An Adaptive QM/MM Study With Model Systems”. In: *Journal of Computational Chemistry* 46.11 (Apr. 2025), p. 70109.

[157] Mark E. Tuckerman. *Statistical Mechanics: Theory and Molecular Simulation*. Oxford Graduate Texts. Oxford: Oxford University Press, 2010.

[158] Herman J. C. Berendsen. *Simulating the Physical World: Hierarchical Modeling from Quantum Mechanics to Fluid Dynamics*. Cambridge: Cambridge University Press, 2007.

[159] George David Birkhoff. “Proof of the ergodic theorem”. In: *Proceedings of the National Academy of Sciences* 17.12 (1931), pp. 656–660.

[160] Daan Frenkel and Berend Smit. *Understanding Molecular Simulation: From Algorithms to Applications*. Computational Science Series. San Diego: Academic Press, 2002.

[161] Efrem Braun et al. “Best Practices for Foundations in Molecular Simulations [Article v1.0]”. In: *Living journal of computational molecular science* 1.1 (2019), p. 5957.

[162] Benedict J. Leimkuhler, Sebastian Reich, and Robert D. Skeel. “Integration Methods for Molecular Dynamics”. In: *Mathematical Approaches to Biomolecular Structure and Dynamics*. Ed. by Jill P. Mesirov, Klaus Schulten, and De Witt Sumners. New York, NY: Springer New York, 1996, pp. 161–185.

[163] Michael P. Allen and Dominic J. Tildesley. *Computer Simulation of Liquids*. Oxford University Press, June 2017.

[164] Loup Verlet. “Computer "Experiments" on Classical Fluids. I. Thermodynamical Properties of Lennard-Jones Molecules”. In: *Phys. Rev.* 159.1 (1967-07-05), pp. 98–103.

[165] Tom Darden, Darrin York, and Lee Pedersen. “Particle mesh Ewald: An N log(N) method for Ewald sums in large systems”. In: *The Journal of Chemical Physics* 98.12 (June 1993), pp. 10089–10092.

[166] GROMACS Development Team. *GROMACS User Manual*. accessed 2025-11-23. GROMACS. 2025.

[167] Shuichi Miyamoto and Peter A. Kollman. “Settle: An analytical version of the SHAKE and RATTLE algorithm for rigid water models”. In: *Journal of Computational Chemistry* 13.8 (1992), pp. 952–962.

[168] Jean-Paul Ryckaert, Giovanni Ciccotti, and Herman J. C Berendsen. “Numerical Integration of the Cartesian Equations of Motion of a System with Constraints: Molecular Dynamics of n-Alkanes”. In: *Journal of Computational Physics* 23.3 (1977-03-01), pp. 327–341.

[169] Berk Hess et al. “LINCS: A Linear Constraint Solver for Molecular Simulations”. In: *Journal of Computational Chemistry* 18.12 (1997), pp. 1463–1472.

[170] Lorién López-Villellas et al. “ILVES: Accurate and Efficient Bond Length and Angle Constraints in Molecular Dynamics”. In: *Journal of Chemical Theory and Computation* 21.18 (Sept. 2025), pp. 8711–8719.

[171] H. J. C. Berendsen et al. “Molecular dynamics with coupling to an external bath”. In: *The Journal of Chemical Physics* 81.8 (Oct. 1984), pp. 3684–3690.

[172] D. J. Evans and B. L. Holian. “The Nose–Hoover Thermostat”. In: *J. Chem. Phys.* 83.8 (1985), pp. 4069–4074.

[173] M. Parrinello and A. Rahman. “Polymorphic transitions in single crystals: A new molecular dynamics method”. In: *Journal of Applied Physics* 52.12 (Dec. 1981), pp. 7182–7190.

[174] Herbert Solomon. *Geometric Probability*. CBMS-NSF Regional Conference Series in Applied Mathematics 28. Philadelphia: Society for Industrial and Applied Mathematics (SIAM), 1978.

[175] Raosaheb Latpate et al. *Advanced Sampling Methods*. Singapore: Springer, 2021.

[176] Clara D. Christ, Alan E. Mark, and Wilfred F. van Gunsteren. “Basic ingredients of free energy calculations: A review”. In: *Journal of Computational Chemistry* 31.8 (2010), pp. 1569–1582.

[177] Alessandro Barducci, Massimiliano Bonomi, and Michele Parrinello. “Metadynamics”. In: *WIREs Computational Molecular Science* 1.5 (2011), pp. 826–843.

[178] Leslie L. Chavez, José N. Onuchic, and Cecilia Clementi. “Quantifying the Roughness on the Free Energy Landscape: Entropic Bottlenecks and Protein Folding Rates”. In: *J. Am. Chem. Soc.* 126.27 (2004-07-14), pp. 8426–8432.

[179] Vojtech Spiwok, Zoran Sucur, and Petr Hosek. “Enhanced sampling techniques in biomolecular simulations”. In: *Biotechnology Advances*. BioTech 2014 and 6th Czech-Swiss Biotechnology Symposium 33.6, Part 2 (Nov. 2015), pp. 1130–1140.

[180] Wenhui Shen, Tong Zhou, and Xinghua Shi. “Enhanced sampling in molecular dynamics simulations and their latest applications—A review”. In: *Nano Research* 16.12 (Dec. 2023), pp. 13474–13497.

[181] A. Laio and M. Parrinello. “Escaping free-energy minima”. In: *Proceedings of the National Academy of Sciences* 99.20 (Oct. 2002), pp. 12562–12566.

[182] Alessandro Laio and Francesco L Gervasio. “Metadynamics: A Method to Simulate Rare Events and Reconstruct the Free Energy in Biophysics, Chemistry and Material Science”. In: *Rep. Prog. Phys.* 71.12 (2008), p. 126601.

[183] Alessandro Barducci, Giovanni Bussi, and Michele Parrinello. “Well-Tempered Metadynamics: A Smoothly Converging and Tunable Free-Energy Method”. In: *Phys. Rev. Lett.* 100.2 (2008), p. 020603.

[184] Paolo Raiteri et al. “Efficient Reconstruction of Complex Free Energy Landscapes by Multiple Walkers Metadynamics”. In: *J. Phys. Chem. B* 110.8 (2006), pp. 3533–3539.

[185] G. M. Torrie and J. P. Valleau. “Nonphysical sampling distributions in Monte Carlo free-energy estimation: Umbrella sampling”. In: *Journal of Computational Physics* 23.2 (Feb. 1977), pp. 187–199.

[186] Mihaly Mezei. “Adaptive umbrella sampling: Self-consistent determination of the non-Boltzmann bias”. In: *Journal of Computational Physics* 68.1 (Jan. 1987), pp. 237–248.

[187] Johannes Kästner. “Umbrella sampling”. In: *WIREs Computational Molecular Science* 1.6 (2011), pp. 932–942.

[188] Eric Darve, David Rodríguez-Gómez, and Andrew Pohorille. “Adaptive biasing force method for scalar and vector free energy calculations”. In: *The Journal of Chemical Physics* 128.14 (Apr. 2008), p. 144120.

[189] Omar Valsson and Michele Parrinello. “Variational Approach to Enhanced Sampling and Free Energy Calculations”. In: *Physical Review Letters* 113.9 (Aug. 2014), p. 090601.

[190] Soumendranath Bhakat. “Collective variable discovery in the age of machine learning: reality, hype and everything in between”. In: *RSC Advances* 12.38 (2022), pp. 25010–25024.

[191] Florian Sittel and Gerhard Stock. “Perspective: Identification of collective variables and metastable states of protein dynamics”. In: *The Journal of Chemical Physics* 149.15 (Oct. 2018), p. 150901.

[192] Robert T. McGibbon, Brooke E. Husic, and Vijay S. Pande. “Identification of simple reaction coordinates from complex dynamics”. In: *The Journal of Chemical Physics* 146.4 (Jan. 2017), p. 044109.

[193] Alexandros Altis et al. “Construction of the free energy landscape of biomolecules via dihedral angle principal component analysis”. In: *The Journal of Chemical Physics* 128.24 (June 2008), p. 245102.

[194] Rafael C. Bernardi, Marcelo C.R. Melo, and Klaus Schulten. “Enhanced Sampling Techniques in Molecular Dynamics Simulations of Biological Systems”. In: *Biochimica et Biophysica Acta (BBA) - General Subjects* 1850.5 (2015-05), pp. 872–877.

[195] Hythem Sidky, Wei Chen, and Andrew L. Ferguson. “Machine learning for collective variable discovery and enhanced sampling in biomolecular simulation”. In: *Molecular Physics* 118.5 (Mar. 2020), e1737742.

[196] Jakub Rydzewski, Ming Chen, and Omar Valsson. “Manifold learning in atomistic simulations: a conceptual review”. In: *Machine Learning: Science and Technology* 4.3 (Sept. 2023), p. 031001.

[197] Shams Mehdi et al. “Enhanced Sampling with Machine Learning: A Review”. In: *Annual review of physical chemistry* 75.1 (June 2024), pp. 347–370.

[198] Paraskevi Gkeka et al. “Machine Learning Force Fields and Coarse-Grained Variables in Molecular Dynamics: Application to Materials and Biological Systems”. In: *Journal of Chemical Theory and Computation* 16.8 (Aug. 2020), pp. 4757–4775.

[199] Raul P. Pelaez et al. “TorchMD-Net 2.0: Fast Neural Network Potentials for Molecular Simulations”. In: *Journal of Chemical Theory and Computation* 20.10 (May 2024), pp. 4076–4087.

[200] Kobchikova P. P. et al. “Machine learning interatomic potentials in biomolecular modeling: principles, architectures, and applications”. In: *Biophysical Reviews* (Aug. 2025).

[201] Yuanqing Wang et al. “On the design space between molecular mechanics and machine learning force fields”. In: *Applied Physics Reviews* 12.2 (Apr. 2025), p. 021304.

[202] Ian Goodfellow, Yoshua Bengio, and Aaron Courville. *Deep Learning*. Adaptive Computation and Machine Learning. Cambridge, MA: MIT Press, 2016.

[203] Trevor Hastie, Robert Tibshirani, and Jerome Friedman. *The Elements of Statistical Learning: Data Mining, Inference, and Prediction*. 2nd. Springer Series in Statistics. New York, NY: Springer, 2017.

[204] Yinuo Yang et al. “Machine Learning of Reactive Potentials”. In: *Annual Review of Physical Chemistry* 75 (June 2024), pp. 371–395.

[205] Jörg Behler and Michele Parrinello. “Generalized Neural-Network Representation of High-Dimensional Potential-Energy Surfaces”. In: *Phys. Rev. Lett.* 98.14 (Apr. 2007), p. 146401.

[206] Jörg Behler. “Four Generations of High-Dimensional Neural Network Potentials”. In: *Chem. Rev.* 121.16 (2021), pp. 10037–10072.

[207] K. T. Schütt et al. “SchNet – A deep learning architecture for molecules and materials”. In: *The Journal of Chemical Physics* 148.24 (Mar. 2018), p. 241722.

[208] Michael Gastegger, Kristof T. Schütt, and Klaus-Robert Müller. “Machine learning of solvent effects on molecular spectra and reactions”. In: *Chemical Science* 12.34 (Sept. 2021), pp. 11473–11483.

[209] Philipp Thölke and Gianni De Fabritiis. *TorchMD-NET: Equivariant Transformers for Neural Network based Molecular Potentials*. arXiv:2202.02541 [physics] version: 2. Apr. 2022.

[210] Raghunathan Ramakrishnan et al. “Big Data Meets Quantum Chemistry Approximations: The Δ-Machine Learning Approach”. In: *J. Chem. Theory Comput.* 11.5 (May 2015), pp. 2087–2096.

[211] Lin Shen and Weitao Yang. “Molecular Dynamics Simulations with Quantum Mechanics/Molecular Mechanics and Adaptive Neural Networks”. In: *J. Chem. Theory Comput.* 14.3 (Mar. 2018), pp. 1442–1455.

[212] Raidel Martin-Barrios et al. “An overview about neural networks potentials in molecular dynamics simulation”. In: *International Journal of Quantum Chemistry* 124.11 (2024), e27389.

[213] Martin Nováček and Jan Řezáč. “PM6-ML: The Synergy of Semiempirical Quantum Chemistry and Machine Learning Transformed into a Practical Computational Method”. In: *Journal of Chemical Theory and Computation* (Jan. 2025).

[214] Jinzhe Zeng et al. “Development of Range-Corrected Deep Learning Potentials for Fast, Accurate Quantum Mechanical/Molecular Mechanical Simulations of Chemical Reactions in Solution”. In: *Journal of Chemical Theory and Computation* 17.11 (Nov. 2021), pp. 6993–7009.

[215] Grégoire Ferré, Terry Haut, and Kipton Barros. “Learning molecular energies using localized graph kernels”. In: *The Journal of Chemical Physics* 146.11 (Mar. 2017), p. 114107.

[216] Frank Noé et al. “Machine Learning for Molecular Simulation”. In: *Annual Review of Physical Chemistry* 71 (Apr. 2020), pp. 361–390.

[217] Lifeng Xu and Jian Jiang. “Synergistic Integration of Physical Embedding and Machine Learning Enabling Precise and Reliable Force Field”. In: *Journal of Chemical Theory and Computation* 20.18 (Sept. 2024), pp. 7785–7795.

[218] Lennard Böselt, Moritz Thürlemann, and Sereina Riniker. “Machine Learning in QM/MM Molecular Dynamics Simulations of Condensed-Phase Systems”. In: *Journal of Chemical Theory and Computation* 17.5 (May 2021), pp. 2641–2658.

[219] Timothy J. Giese et al. “Combined QM/MM, machine learning path integral approach to compute free energy profiles and kinetic isotope effects in RNA cleavage reactions”. In: *Journal of Chemical Theory and Computation* 18.7 (July 2022), pp. 4304–4317.

[220] Junmian Zhu et al. “Artificial neural network correction for density-functional tight-binding molecular dynamics simulations”. In: *MRS Communications* 9.3 (Sept. 2019), pp. 867–873.

[221] Claudia L. Gómez-Flores et al. “Accurate Free Energies for Complex Condensed-Phase Reactions Using an Artificial Neural Network Corrected DFTB/MM Methodology”. In: *Journal of Chemical Theory and Computation* 18.2 (Feb. 2022), pp. 1213–1226.

[222] Rui P. P. Neves et al. “Benchmarking of Density Functionals for the Accurate Description of Thiol–Disulfide Exchange”. In: *J. Chem. Theory Comput.* 10.11 (Nov. 2014), pp. 4842–4856.

[223] Julian Böser et al. “Reduction pathway of glutaredoxin 1 investigated with QM/MM molecular dynamics using a neural network correction”. In: *The Journal of Chemical Physics* (2022), p. 154104.

[224] Thom H. Dunning Jr. “Gaussian basis sets for use in correlated molecular calculations. I. The atoms boron through neon and hydrogen”. In: *The Journal of Chemical Physics* 90.2 (Jan. 1989), pp. 1007–1023.

[225] Krishnan Raghavachari et al. “A fifth-order perturbation comparison of electron correlation theories”. In: *Chemical Physics Letters* 157.6 (May 1989), pp. 479–483.

[226] Giulio Imbalzano et al. “Automatic selection of atomic fingerprints and reference configurations for machine-learning potentials”. In: *The Journal of Chemical Physics* 148.24 (Apr. 2018), p. 241730.

[227] Bastien Casier et al. “Using principal component analysis for neural network high-dimensional potential energy surface”. In: *The Journal of Chemical Physics* 152.23 (June 2020), p. 234103.

[228] Kun Yao et al. “The TensorMol-0.1 model chemistry: a neural network augmented with long-range physics”. In: *Chemical Science* 9.8 (Feb. 2018), pp. 2261–2269.

[229] M. Gastegger et al. “wACSF—Weighted atom-centered symmetry functions as descriptors in machine learning potentials”. In: *The Journal of Chemical Physics* 148.24 (Mar. 2018), p. 241709.

[230] Haohao Fu et al. “Collective Variable-Based Enhanced Sampling: From Human Learning to Machine Learning”. In: *The Journal of Physical Chemistry Letters* 15.6 (Feb. 2024), pp. 1774–1783.

[231] Aldo Glielmo et al. “Unsupervised Learning Methods for Molecular Simulation Data”. In: *Chemical Reviews* 121.16 (Aug. 2021), pp. 9722–9758.

[232] Andrea Amadei, Antonius B. M. Linssen, and Herman J. C. Berendsen. “Essential dynamics of proteins”. In: *Proteins: Structure, Function, and Genetics* 17.4 (Dec. 1993), pp. 412–425.

[233] Gia G. Maisuradze, Adam Liwo, and Harold A. Scheraga. “Principal component analysis for protein folding dynamics”. In: *Journal of molecular biology* 385.1 (Jan. 2009), pp. 312–329.

[234] Charles C. David and Donald J. Jacobs. “Principal Component Analysis: A Method for Determining the Essential Dynamics of Proteins”. In: *Methods in molecular biology (Clifton, N.J.)* 1084 (2014), pp. 193–226.

[235] Guillermo Pérez-Hernández et al. “Identification of slow molecular order parameters for Markov model construction”. In: *The Journal of Chemical Physics* 139.1 (July 2013), p. 015102.

[236] Pratyush Tiwary and B. J. Berne. “Spectral gap optimization of order parameters for sampling complex molecular systems”. In: *Proceedings of the National Academy of Sciences* 113.11 (Mar. 2016), pp. 2839–2844.

[237] Alessandro Giuliani. “The application of principal component analysis to drug discovery and biomedical data”. In: *Drug Discovery Today* 22.7 (July 2017), pp. 1069–1076.

[238] Vojtěch Spiwok, Petra Lipovová, and Blanka Králová. “Metadynamics in Essential Coordinates: Free Energy Simulation of Conformational Changes”. In: *The Journal of Physical Chemistry B* 111.12 (Mar. 2007), pp. 3073–3076.

[239] Florian Sittel, Thomas Filk, and Gerhard Stock. “Principal component analysis on a torus: Theory and application to protein dynamics”. In: *The Journal of Chemical Physics* 147.24 (Dec. 2017), p. 244101.

[240] Matthias Ernst, Steffen Wolf, and Gerhard Stock. “Identification and Validation of Reaction Coordinates Describing Protein Functional Motion: Hierarchical Dynamics of T4 Lysozyme”. In: *Journal of Chemical Theory and Computation* 13.10 (Oct. 2017), pp. 5076–5088.

[241] I. T. Jolliffe. *Principal Component Analysis*. Second. New York: Springer, 2002.

[242] Christian R. Schwantes and Vijay S. Pande. “Improvements in Markov State Model Construction Reveal Many Non-Native Interactions in the Folding of NTL9”. In: *Journal of Chemical Theory and Computation* 9.4 (Apr. 2013), pp. 2000–2009.

[243] Shingo Ito et al. “Toward understanding whole enzymatic reaction cycles using multi-scale molecular simulations”. In: *Current Opinion in Structural Biology* 95 (Dec. 2025), p. 103153.

[244] Iván Solt et al. “Evaluating Boundary Dependent Errors in QM/MM Simulations”. In: *The Journal of Physical Chemistry B* 113.17 (Apr. 2009), pp. 5728–5735.

[245] Rimsha Mehmood and Heather J. Kulik. “Both Configuration and QM Region Size Matter: Zinc Stability in QM/MM Models of DNA Methyltransferase”. In: *Journal of Chemical Theory and Computation* 16.5 (May 2020), pp. 3121–3134.

[246] Álvaro Pérez-Barcia et al. “Effect of the QM Size, Basis Set, and Polarization on QM/MM Interaction Energy Decomposition Analysis”. In: *Journal of Chemical Information and Modeling* 63.3 (Feb. 2023), pp. 882–897.

[247] Goran Giudetti et al. “How Reproducible Are QM/MM Simulations? Lessons from Computational Studies of the Covalent Inhibition of the SARS-CoV-2 Main Protease by Carmofur”. In: *Journal of Chemical Theory and Computation* 18.8 (Aug. 2022), pp. 5056–5067.

[248] Camila M. Clemente, Luciana Capece, and Marcelo A. Martí. “Best Practices on QM/MM Simulations of Biological Systems”. In: *Journal of Chemical Information and Modeling* 63.9 (May 2023), pp. 2609–2627.

[249] Junming Ho et al. “How Accurate Are QM/MM Models?” In: *The Journal of Physical Chemistry A* (Dec. 2024).

[250] Carles Curutchet et al. “Electronic Energy Transfer in Condensed Phase Studied by a Polarizable QM/MM Model”. In: *Journal of Chemical Theory and Computation* 5.7 (July 2009), pp. 1838–1848.

[251] Albert DeFusco et al. “Modeling Solvent Effects on Electronic Excited States”. In: *The Journal of Physical Chemistry Letters* 2.17 (Sept. 2011), pp. 2184–2192.

[252] Filippo Lipparini, Chiara Cappelli, and Vincenzo Barone. “Linear Response Theory and Electronic Transition Energies for a Fully Polarizable QM/Classical Hamiltonian”. In: *Journal of Chemical Theory and Computation* 8.11 (Nov. 2012), pp. 4153–4165.

[253] Nanna Holmgaard List, Jógvan Magnus Haugaard Olsen, and Jacob Kongsted. “Excited states in large molecular systems through polarizable embedding”. In: *Physical Chemistry Chemical Physics* 18.30 (July 2016), pp. 20234–20250.

[254] Daniele Loco et al. “A QM/MM Approach Using the AMOEBA Polarizable Embedding: From Ground State Energies to Electronic Excitations”. In: *Journal of Chemical Theory and Computation* 12.8 (Aug. 2016), pp. 3654–3661.

[255] Christopher J. R. Illingworth et al. “Classical Polarization in Hybrid QM/MM Methods”. In: *The Journal of Physical Chemistry A* 110.20 (May 2006), pp. 6487–6497.

[256] Abir Ganguly, Eliot Boulanger, and Walter Thiel. “Importance of MM Polarization in QM/MM Studies of Enzymatic Reactions: Assessment of the QM/MM Drude Oscillator Model”. In: *Journal of Chemical Theory and Computation* 13.6 (June 2017), pp. 2954–2961.

[257] Gerhard König et al. “A Comparison of QM/MM Simulations with and without the Drude Oscillator Model Based on Hydration Free Energies of Simple Solutes”. In: *Molecules* 23.10 (Oct. 2018), p. 2695.

[258] Heather J. Kulik et al. “How Large Should the QM Region Be in QM/MM Calculations? The Case of Catechol O-Methyltransferase”. In: *The Journal of Physical Chemistry B* 120.44 (Nov. 2016), pp. 11381–11394.

[259] Klaus Müller-Dethlefs and Pavel Hobza. “Noncovalent Interactions: A Challenge for Experiment and Theory”. In: *Chemical Reviews* 100.1 (Jan. 2000), pp. 143–168.

[260] Kevin E. Riley and Pavel Hobza. “Noncovalent interactions in biochemistry”. In: *WIREs Computational Molecular Science* 1.1 (2011), pp. 3–17.

[261] Carles Curutchet et al. “Energy decomposition in molecular complexes: Implications for the treatment of polarization in molecular simulations”. In: *Journal of Computational Chemistry* 24.10 (2003), pp. 1263–1275.

[262] Kittusamy Senthilkumar et al. “Analysis of polarization in QM/MM modelling of biologically relevant hydrogen bonds”. In: *Journal of The Royal Society Interface* 5.suppl_3 (Sept. 2008), pp. 207–216.

[263] Peng Zhou et al. “Fluorine Bonding — How Does It Work In Protein–Ligand Interactions?” In: *Journal of Chemical Information and Modeling* 49.10 (Oct. 2009), pp. 2344–2355.

[264] Sadhana Kumbhar, Frank D. Fischer, and Mark P. Waller. “Assessment of Weak Intermolecular Interactions Across QM/MM Noncovalent Boundaries”. In: *Journal of Chemical Information and Modeling* 52.1 (Jan. 2012), pp. 93–98.

[265] Xinchun Guo et al. “Use of QM/MM scheme to reproduce macromolecule–small molecule noncovalent binding energy”. In: *Computational and Theoretical Chemistry* 991 (July 2012), pp. 134–140.

[266] Rong-Zhen Liao and Walter Thiel. “Comparison of QM-Only and QM/MM Models for the Mechanism of Tungsten-Dependent Acetylene Hydratase”. In: *Journal of Chemical Theory and Computation* 8.10 (Oct. 2012), pp. 3793–3803.

[267] Jakub Kollar and Vladimir Frecer. “How accurate is the description of ligand–protein interactions by a hybrid QM/MM approach?” In: *Journal of Molecular Modeling* 24.1 (Dec. 2017), p. 11.

[268] Nedjoua Drici. “Analysis of polarization in hydrogen bonded complexes: An asymptotic projection approach”. In: *Chemical Physics Letters* 696 (Mar. 2018), pp. 1–7.

[269] Shani Zev et al. “A Benchmark Study of Quantum Mechanics and Quantum Mechanics-Molecular Mechanics Methods for Carbocation Chemistry”. In: *Journal of Chemical Theory and Computation* 18.1 (Jan. 2022), pp. 167–178.

[270] Roberto López et al. “QM/MM Energy Decomposition Using the Interacting Quantum Atoms Approach”. In: *Journal of Chemical Information and Modeling* 62.6 (Mar. 2022), pp. 1510–1524.

[271] Elahe K. Astani et al. “DFT QM/MM MD Calculations to Identify Intermolecular Interactions within the Active Sites of MraYAA Bound to Antibiotics Capuramycin, Carbacaprazamycin, and 3ˊHydroxymureidomycin A”. In: *ChemistrySelect* 8.46 (2023), e202302657.

[272] Xuewei Xiong et al. “QM/MM-Based Energy Decomposition Analysis Method for Large Systems”. In: *The Journal of Physical Chemistry A* 128.18 (May 2024), pp. 3529–3538.

[273] Jan Řezáč. “Non-Covalent Interactions Atlas Benchmark Data Sets: Hydrogen Bonding”. In: *J. Chem. Theory Comput.* 16.4 (Apr. 2020), pp. 2355–2368.

[274] José A. Fernández. “Exploring Hydrogen Bond in Biological Molecules”. In: *Journal of the Indian Institute of Science* 100.1 (Jan. 2020), pp. 135–154.

[275] Martin B. Peters et al. “Structural Survey of Zinc-Containing Proteins and Development of the Zinc AMBER Force Field (ZAFF)”. In: *Journal of Chemical Theory and Computation* 6.9 (Sept. 2010), pp. 2935–2947.

[276] John A. Gerlt et al. “Understanding enzymic catalysis: the importance of short, strong hydrogen bonds”. In: *Chemistry & Biology* 4.4 (Apr. 1997), pp. 259–267.

[277] Abigail G. Doyle and Eric N. Jacobsen. “Small-Molecule H-Bond Donors in Asymmetric Catalysis”. In: *Chemical Reviews* 107.12 (Dec. 2007), pp. 5713–5743.

[278] Li L. Duan et al. “Intra-protein hydrogen bonding is dynamically stabilized by electronic polarization”. In: *The Journal of Chemical Physics* 130.11 (Mar. 2009), p. 115102.

[279] Yang Li et al. “Electrostatic Polarization Effect on Cooperative Aggregation of Full Length Human Islet Amyloid”. In: *Journal of Chemical Information and Modeling* 58.8 (Aug. 2018), pp. 1587–1595.

[280] Adam Pecina et al. “SQM2.20: Semiempirical quantum-mechanical scoring function yields DFT-quality protein–ligand binding affinity predictions in minutes”. In: *Nature Communications* 15.1 (Feb. 2024), p. 1127.

[281] Marek Freindorf and Jiali Gao. “Optimization of the Lennard-Jones parameters for a combined ab initio quantum mechanical and molecular mechanical potential using the 3-21G basis set”. In: *Journal of Computational Chemistry* 17.4 (1996), pp. 386–395.

[282] Demian Riccardi, Guohui Li, and Qiang Cui. “Importance of van der Waals Interactions in QM/MM Simulations”. In: *The Journal of Physical Chemistry B* 108.20 (May 2004), pp. 6467–6478.

[283] Junmei Wang et al. “Development and testing of a general amber force field”. In: *Journal of Computational Chemistry* 25.9 (July 2004), pp. 1157–1174.

[284] Romelia Salomon-Ferrer, David A. Case, and Ross C. Walker. “An overview of the Amber biomolecular simulation package”. In: *WIREs Computational Molecular Science* 3.2 (2013), pp. 198–210.

[285] David A. Case et al. “AmberTools”. In: *Journal of Chemical Information and Modeling* 63.20 (Oct. 2023), pp. 6183–6191.

[286] M. J. Frisch et al. *Gaussian 09, Revision A.02*. Gaussian, Inc. Wallingford CT, 2016.

[287] Narbe Mardirossian and Martin Head-Gordon. “ωB97M-V: A combinatorially optimized, range-separated hybrid, meta-GGA density functional with VV10 nonlocal correlation”. In: *The Journal of Chemical Physics* 144.21 (June 2016), p. 214110.

[288] Qiang Cui and Marcus Elstner. “Density functional tight binding: values of semi-empirical methods in an ab initio era”. In: *Physical Chemistry Chemical Physics* 16.28 (June 2014), pp. 14368–14377.

[289] Jan Řezáč. “Empirical Self-Consistent Correction for the Description of Hydrogen Bonds in DFTB3”. In: *Journal of Chemical Theory and Computation* 13.10 (Oct. 2017), pp. 4804–4817.

[290] Mark James Abraham et al. “GROMACS: High performance molecular simulations through multi-level parallelism from laptops to supercomputers”. In: *SoftwareX* 1-2 (2015), pp. 19–25.

[291] B. Hourahine et al. “DFTB+, a software package for efficient approximate density functional theory based atomistic simulations”. In: *The Journal of Chemical Physics* 152.12 (2020), p. 124101.

[292] Tomáš Kubař. https://github.com/tomaskubar/dftbplus. last accessed 2025-02-17.

[293] Tomáš Kubař. `https://github.com/tomaskubar/gromacs-dftbplus`. last accessed 2025-02-17.

[294] Darrin M. York and Weitao Yang. “A chemical potential equalization method for molecular simulations”. In: *The Journal of Chemical Physics* 104.1 (Jan. 1996), pp. 159–172.

[295] Timothy J. Giese and Darrin M. York. “Density-functional expansion methods: grand challenges”. en. In: *Theoretical Chemistry Accounts* 131.3 (Feb. 2012), p. 1145.

[296] Steve Kaminski et al. “Extended Polarization in Third-Order SCC-DFTB from Chemical-Potential Equalization”. In: *The Journal of Physical Chemistry A* 116.36 (Sept. 2012), pp. 9131–9141.

[297] Anders Steen Christensen. https://github.com/andersx/cpe-source. last accessed 2025-02-17.

[298] F. Neese. “Software update: the ORCA program system, version 5.0”. In: *WIRES Comput. Molec. Sci.* 12.1 (2022), e1606.

[299] Eric D. Glendening, Clark R. Landis, and Frank Weinhold. “NBO 6.0: Natural bond orbital analysis program”. In: *Journal of Computational Chemistry* 34.16 (2013), pp. 1429–1437.

[300] Van-Quan Vuong et al. “Multipole Expansion of Atomic Electron Density Fluctuation Interactions in the Density-Functional Tight-Binding Method”. In: *Journal of Chemical Theory and Computation* 19.21 (Nov. 2023), pp. 7592–7605.

[301] Jaroslaw A. Kalinowski et al. “Class IV Charge Model for the Self-Consistent Charge Density-Functional Tight-Binding Method”. In: *The Journal of Physical Chemistry A* 108.13 (Apr. 2004), pp. 2545–2549.

[302] Omar Demerdash, Eng-Hui Yap, and Teresa Head-Gordon. “Advanced Potential Energy Surfaces for Condensed Phase Simulation”. In: *Annual Review of Physical Chemistry* 65.Volume 65, 2014 (Apr. 2014), pp. 149–174.

[303] Igor Leontyev and Alexei Stuchebrukhov. “Accounting for electronic polarization in non-polarizable force fields”. In: *Physical Chemistry Chemical Physics* 13.7 (Feb. 2011), pp. 2613–2626.

[304] Brian J. Kirby and Pavel Jungwirth. “Charge Scaling Manifesto: A Way of Reconciling the Inherently Macroscopic and Microscopic Natures of Molecular Simulations”. In: *The Journal of Physical Chemistry Letters* 10.23 (Dec. 2019), pp. 7531–7536.

[305] Timothy J. Giese and Darrin M. York. “Many-body force field models based solely on pairwise Coulomb screening do not simultaneously reproduce correct gas-phase and condensed-phase polarizability limits”. In: *The Journal of Chemical Physics* 120.21 (June 2004), pp. 9903–9906.

[306] Riccardo Chelli, Vincenzo Schettino, and Piero Procacci. “Comparing polarizable force fields to ab initio calculations reveals nonclassical effects in condensed phases”. In: *The Journal of Chemical Physics* 122.23 (June 2005).

[307] John D. Chodera and David L. Mobley. “Entropy-Enthalpy Compensation: Role and Ramifications in Biomolecular Ligand Recognition and Design”. In: *Annual Review of Biophysics* 42.Volume 42, 2013 (May 2013), pp. 121–142.

[308] Eliot Boulanger and Walter Thiel. “Toward QM/MM Simulation of Enzymatic Reactions with the Drude Oscillator Polarizable Force Field”. In: *Journal of Chemical Theory and Computation* 10.4 (Apr. 2014), pp. 1795–1809.

[309] Qiang Zhu et al. “Treating Polarization Effects in Charged and Polar Bio-Molecules Through Variable Electrostatic Parameters”. In: *Journal of Chemical Theory and Computation* 19.2 (Jan. 2023), pp. 396–411.

[310] Maria Karelina and Heather J. Kulik. “Systematic Quantum Mechanical Region Determination in QM/MM Simulation”. In: *Journal of Chemical Theory and Computation* 13.2 (Feb. 2017), pp. 563–576.

[311] Timothy J. Giese, Jinzhe Zeng, and Darrin M. York. “Transferability of MACE Graph Neural Network for Range Corrected Δ-Machine Learning Potential QM/MM Applications”. In: *The Journal of Physical Chemistry B* 129.22 (June 2025), pp. 5477–5490.

[312] Xiaoliang Pan et al. “Machine-Learning-Assisted Free Energy Simulation of Solution-Phase and Enzyme Reactions”. In: *Journal of Chemical Theory and Computation* 17.9 (Sept. 2021), pp. 5745–5758.

[313] Jonathan A. Semelak et al. *Advancing Multiscale Molecular Modeling with Machine Learning-Derived Electrostatics*. en. Feb. 2025.

[314] Ge Song and Weitao Yang. “NepoIP/MM: Toward Accurate Biomolecular Simulation with a Machine Learning/Molecular Mechanics Model Incorporating Polarization Effects”. In: *Journal of Chemical Theory and Computation* 21.11 (June 2025), pp. 5588–5598.

[315] Marcel Baer et al. “Spectral Signatures of the Pentagonal Water Cluster in Bacteriorhodopsin”. In: *ChemPhysChem* 9.18 (2008), pp. 2703–2707.

[316] Darren Demapan et al. “Factors That Determine the Variation of Equilibrium and Kinetic Properties of QM/MM Enzyme Simulations: QM Region, Conformation, and Boundary Condition”. In: *Journal of Chemical Theory and Computation* 18.4 (Apr. 2022), pp. 2530–2542.

[317] Julian Böser. “QM/MM Molecular Dynamics Simulation of Thiol-Disulfide Exchange by Glutaredoxin”. Master’s Thesis. Karlsruhe, Germany: Karlsruhe Institute of Technology, 2022.

[318] Yanwu Yang et al. “Reactivity of the Human Thioltransferase (Glutaredoxin) C7S, C25S, C78S, C82S Mutant and NMR Solution Structure of Its Glutathionyl Mixed Disulfide Intermediate Reflect Catalytic Specificity,” in: *Biochemistry* 37.49 (1998), pp. 17145–17156.

[319] Ashwinie A. Ukuwela et al. “Reduction Potentials of Protein Disulfides and Catalysis of Glutathionylation and Deglutathionylation by Glutaredoxin Enzymes”. In: *Biochem. J.* 474.22 (2017), pp. 3799–3815.

[320] Jannik Zimmermann et al. “One Cysteine Is Enough: A Monothiol Grx Can Functionally Replace All Cytosolic Trx and Dithiol Grx”. In: *Redox Biology* 36 (2020), p. 101598.

[321] Molly M. Gallogly, David W. Starke, and John J. Mieyal. “Mechanistic and Kinetic Details of Catalysis of Thiol-Disulfide Exchange by Glutaredoxins and Potential Mechanisms of Regulation”. In: *Antioxid. Redox Signal.* 11.5 (2009), pp. 1059–1081.

[322] Christopher Horst Lillig and Carsten Berndt. “Glutaredoxins in Thiol/Disulfide Exchange”. In: *Antioxidants & Redox Signaling* 18.13 (2013), pp. 1654–1665.

[323] Chaohong Sun, Marcelo J Berardi, and John H Bushweller. “The NMR solution structure of human glutaredoxin in the fully reduced form”. In: *J. Mol. Biol.* 280.4 (1998), pp. 687–701.

[324] Matthias Zimmermann et al. “Metal Binding Affinities of Arabidopsis Zinc and Copper Transporters: Selectivities Match the Relative, but Not the Absolute, Affinities of Their Amino-Terminal Domains”. In: *Biochemistry* (2009), pp. 11640–11654.

[325] Maja Gruden et al. “Benchmarking Density Functional Tight Binding Models for Barrier Heights and Reaction Energetics of Organic Molecules”. In: *J. Comput. Chem.* 38.25 (Sept. 2017), pp. 2171–2185.

[326] Zoltán Bodrog, Bálint Aradi, and Thomas Frauenheim. “Automated Repulsive Parametrization for the DFTB Method”. In: *Journal of Chemical Theory and Computation* 7.8 (Aug. 2011), pp. 2654–2664.

[327] Kresten Lindorff-Larsen et al. “Improved side-chain torsion potentials for the Amber ff99SB protein force field”. In: *Proteins: Structure, Function, and Bioinformatics* 78.8 (2010), pp. 1950–1958.

[328] Christopher I. Bayly et al. “A well-behaved electrostatic potential based method using charge restraints for deriving atomic charges: the RESP model”. In: *J. Phys. Chem.* 97.40 (1993), pp. 10269–10280.

[329] Junmei Wang et al. “Automatic Atom Type and Bond Type Perception in Molecular Mechanical Calculations”. In: *J. Mol. Graph. Model.* 25.2 (2006), pp. 247–260.

[330] Massimiliano Bonomi et al. “Promoting transparency and reproducibility in enhanced molecular simulations”. In: *Nature Methods* 16.8 (Aug. 2019), pp. 670–673.

[331] Gareth A. Tribello et al. “PLUMED 2: New feathers for an old bird”. In: *Computer Physics Communications* 185.2 (Feb. 2014). arXiv: 1310.0980, pp. 604–613.

[332] Giovanni Bussi, Davide Donadio, and Michele Parrinello. “Canonical sampling through velocity rescaling”. In: *The Journal of Chemical Physics* 126.1 (Jan. 2007), p. 014101.

[333] T. Kubař. `https://github.com/tomaskubar/dftbplus/tree/machine-learning`. last accessed on 27 July 2022. 2021.

[334] Denis Maag et al. “Electrostatic interactions contribute to the control of intramolecular thiol–disulfide isomerization in a protein”. In: *Physical Chemistry Chemical Physics* 23.46 (Dec. 2021), pp. 26366–26375.

[335] Ka Hung Lee et al. “Performance of Density-Functional Tight-Binding in Comparison to Ab Initio and First-Principles Methods for Isomer Geometries and Energies of Glucose Epimers in Vacuo and Solution”. In: *ACS Omega* 3.12 (2018), pp. 16899–16915.

[336] Rui P. P. Neves, Pedro Alexandrino Fernandes, and Maria João Ramos. “Mechanistic Insights on the Reduction of Glutathione Disulfide by Protein Disulfide Isomerase”. In: *Proc. Natl. Acad. Sci. U.S.A.* 114.24 (June 2017), E4724–E4733.

[337] Sebastian Buchenberg, Norbert Schaudinnus, and Gerhard Stock. “Hierarchical Biomolecular Dynamics: Picosecond Hydrogen Bonding Regulates Microsecond Conformational Transitions”. In: *Journal of Chemical Theory and Computation* 11.3 (Mar. 2015), pp. 1330–1336.

[338] Steven D. Schwartz. “Protein dynamics and the enzymatic reaction coordinate”. In: *Topics in current chemistry* 337 (2013), pp. 189–208.

[339] T. Kubař, M. Elstner, and Q. Cui. “Hybrid Quantum Mechanical/Molecular Mechanical Methods For Studying Energy Transduction in Biomolecular Machines”. In: *Annual Review of Biophysics* 52.Volume 52, 2023 (May 2023), pp. 525–551.

[340] Yasmin Abu Aqel et al. “Glucokinase (GCK) in diabetes: from molecular mechanisms to disease pathogenesis”. In: *Cellular & Molecular Biology Letters* 29.1 (Sept. 2024), p. 120.

[341] Ville R. I. Kaila. “Resolving Chemical Dynamics in Biological Energy Conversion: Long-Range Proton-Coupled Electron Transfer in Respiratory Complex I”. In: *Accounts of Chemical Research* 54.24 (Dec. 2021), pp. 4462–4473.

[342] Randall V. Mauldin, Mary J. Carroll, and Andrew L. Lee. “Dynamic Dysfunction in Dihydrofolate Reductase Results from Antifolate Drug Binding: Modulation of Dynamics within a Structural State”. In: *Structure* 17.3 (Mar. 2009), pp. 386–394.

[343] Anna C. Nelson et al. “Mathematical models of fibrin polymerization: past, present, and future”. In: *Current Opinion in Biomedical Engineering* 20 (Dec. 2021), p. 100350.

[344] Arun P. Wiita et al. “Force-dependent chemical kinetics of disulfide bond reduction observed with single-molecule techniques”. In: *Proceedings of the National Academy of Sciences* 103.19 (May 2006), pp. 7222–7227.

[345] Fabian Kutzki et al. “Disulfide bond reduction and exchange in C4 domain of von Willebrand factor undermines platelet binding”. In: *Journal of Thrombosis and Haemostasis* 21.8 (Aug. 2023), pp. 2089–2100.

[346] Yang Yang, Haibo Yu, and Qiang Cui. “Extensive Conformational Transitions Are Required to Turn On ATP Hydrolysis in Myosin”. In: *Journal of Molecular Biology* 381.5 (Sept. 2008), pp. 1407–1420.

[347] Anil R. Mhashal et al. “The role of the Met20 loop in the hydride transfer in *Escherichia coli* dihydrofolate reductase”. In: *Journal of Biological Chemistry* 292.34 (Aug. 2017), pp. 14229–14239.

[348] Daniel T Gillespie. “A general method for numerically simulating the stochastic time evolution of coupled chemical reactions”. In: *Journal of Computational Physics* 22.4 (Dec. 1976), pp. 403–434.

[349] Emanuel K. Peter, Igor V. Pivkin, and Joan-Emma Shea. “A kMC-MD method with generalized move-sets for the simulation of folding of α-helical and β-stranded peptides”. In: *The Journal of Chemical Physics* 142.14 (Apr. 2015), p. 144903.

[350] Benedikt Rennekamp et al. “Hybrid Kinetic Monte Carlo/Molecular Dynamics Simulations of Bond Scissions in Proteins”. In: *Journal of Chemical Theory and Computation* 16.1 (Jan. 2020), pp. 553–563.

[351] Kai Riedmiller et al. “Substituting density functional theory in reaction barrier calculations for hydrogen atom transfer in proteins”. In: *Chemical Science* 15.7 (Feb. 2024), pp. 2518–2527.

[352] Marko Hanzevacki et al. “All Roads Lead to Carbinolamine: QM/MM Study of Enzymatic C–N Bond Cleavage in Anaerobic Glycyl Radical Enzyme Choline Trimethylamine-Lyase (CutC)”. In: *The Journal of Physical Chemistry B* 129.37 (Sept. 2025), pp. 9322–9332.

[353] Sani Idris Alhassan et al. “Multiscale Computational Workflow to Determine Stability of Disulfide Bridges in Proteins-Application to IgG Antibodies”. In: *Journal of Chemical Information and Modeling* (Oct. 2025), pp. 11187–11202.

[354] Rui P. P. Neves, Pedro A. Fernandes, and Maria J. Ramos. “Role of Enzyme and Active Site Conformational Dynamics in the Catalysis by α-Amylase Explored with QM/MM Molecular Dynamics”. In: *Journal of Chemical Information and Modeling* 62.15 (Aug. 2022), pp. 3638–3650.

[355] Dahlia R. Weiss and Michael Levitt. “Can Morphing Methods Predict Intermediate Structures?” In: *Journal of Molecular Biology* 385.2 (Jan. 2009), pp. 665–674.

[356] Laura Orellana. “Large-Scale Conformational Changes and Protein Function: Breaking the in silico Barrier”. In: *Frontiers in Molecular Biosciences* 6 (Nov. 2019).

[357] Yuguang Mu, Phuong H. Nguyen, and Gerhard Stock. “Energy landscape of a small peptide revealed by dihedral angle principal component analysis”. In: *Proteins: Structure, Function, and Bioinformatics* 58.1 (Jan. 2005), pp. 45–52.

[358] Alexandros Altis et al. “Dihedral angle principal component analysis of molecular dynamics simulations”. In: *The Journal of Chemical Physics* 126.24 (June 2007), p. 244111.

[359] François Sicard and Patrick Senet. “Reconstructing the free-energy landscape of Met-enkephalin using dihedral principal component analysis and well-tempered metadynamics”. In: *The Journal of Chemical Physics* 138.23 (June 2013), p. 235101.

[360] James McCarty and Michele Parrinello. “A variational conformational dynamics approach to the selection of collective variables in metadynamics”. In: *The Journal of Chemical Physics* 147.20 (Nov. 2017), p. 204109.

[361] Mohammad M. Sultan and Vijay S. Pande. “tICA-Metadynamics: Accelerating Metadynamics by Using Kinetically Selected Collective Variables”. In: *Journal of Chemical Theory and Computation* 13.6 (June 2017), pp. 2440–2447.

[362] Mark J. Abraham et al. *GROMACS 2020 User Manual*. Accessed: 2 October 2025. GROMACS development team. 2020.

[363] Joyce Chiu and Philip J. Hogg. “Allosteric disulfides: Sophisticated molecular structures enabling flexible protein regulation”. In: *Journal of Biological Chemistry* 294.8 (Feb. 2019), pp. 2949–2960.

[364] M. Bonomi and M. Parrinello. “Enhanced Sampling in the Well-Tempered Ensemble”. In: *Physical Review Letters* 104.19 (May 2010), p. 190601.

[365] Giovanni Bussi and Alessandro Laio. “Using metadynamics to explore complex free-energy landscapes”. In: *Nature Reviews Physics* 2.4 (Mar. 2020), pp. 200–212.

[366] Winnfried Hasel, Thomas F. Hendrickson, and W. Clark Still. “A rapid approximation to the solvent accessible surface areas of atoms”. In: *Tetrahedron Computer Methodology* 1.2 (Jan. 1988), pp. 103–116.

[367] Vojtěch Spiwok and Pavel Kříž. “Time-Lagged t-Distributed Stochastic Neighbor Embedding (t-SNE) of Molecular Simulation Trajectories”. In: *Frontiers in Molecular Biosciences* 7 (2020).

[368] Geoffrey J. McLachlan and Suren Rathnayake. “On the number of components in a Gaussian mixture model”. In: *WIREs Data Mining and Knowledge Discovery* 4.5 (2014), pp. 341–355.

[369] Steffen Schultze and Helmut Grubmüller. “Time-Lagged Independent Component Analysis of Random Walks and Protein Dynamics”. In: *Journal of Chemical Theory and Computation* 17.9 (Sept. 2021), pp. 5766–5776.

[370] Jun-hui Peng et al. “Clustering algorithms to analyze molecular dynamics simulation trajectories for complex chemical and biological systems†”. In: *Chinese Journal of Chemical Physics* 31.4 (Aug. 2018), pp. 404–420.

[371] Sayari Bhattacharya and Suman Chakrabarty. “Mapping conformational landscape in protein folding: Benchmarking dimensionality reduction and clustering techniques on the Trp-Cage mini-protein”. In: *Biophysical Chemistry* 319 (Apr. 2025), p. 107389.

[372] Katra Kolšek, Camilo Aponte-Santamaría, and Frauke Gräter. “Accessibility explains preferred thiol-disulfide isomerization in a protein domain”. In: *Scientific Reports* 7.1 (Aug. 2017), p. 9858.